



Development of Analytical Techniques for the Investigation of an Organic Redox Flow Battery using a Segmented Cell

Mathilde Cazot

► To cite this version:

Mathilde Cazot. Development of Analytical Techniques for the Investigation of an Organic Redox Flow Battery using a Segmented Cell. Engineering Sciences [physics]. Université de Lorraine, 2019. English. NNT : 2019LORR0116 . tel-02460625

HAL Id: tel-02460625

<https://hal.univ-lorraine.fr/tel-02460625>

Submitted on 3 Sep 2020

HAL is a multi-disciplinary open access archive for the deposit and dissemination of scientific research documents, whether they are published or not. The documents may come from teaching and research institutions in France or abroad, or from public or private research centers.

L'archive ouverte pluridisciplinaire **HAL**, est destinée au dépôt et à la diffusion de documents scientifiques de niveau recherche, publiés ou non, émanant des établissements d'enseignement et de recherche français ou étrangers, des laboratoires publics ou privés.



AVERTISSEMENT

Ce document est le fruit d'un long travail approuvé par le jury de soutenance et mis à disposition de l'ensemble de la communauté universitaire élargie.

Il est soumis à la propriété intellectuelle de l'auteur. Ceci implique une obligation de citation et de référencement lors de l'utilisation de ce document.

D'autre part, toute contrefaçon, plagiat, reproduction illicite encourt une poursuite pénale.

Contact : ddoc-theses-contact@univ-lorraine.fr

LIENS

Code de la Propriété Intellectuelle. articles L 122. 4

Code de la Propriété Intellectuelle. articles L 335.2- L 335.10

http://www.cfcopies.com/V2/leg/leg_droi.php

<http://www.culture.gouv.fr/culture/infos-pratiques/droits/protection.htm>



SIMPPÉ

KEMIWATT
Your energy bankUNIVERSITÉ
DE LORRAINE

École doctorale SIMPPÉ : Sciences et Ingénierie des Molécules des Produits des Procédés et de l'Énergie

THÈSE

pour l'obtention du grade de

Docteur de l'Université de Lorraine

Spécialité "Énergie et Mécanique"

Development of Analytical Techniques for the
Investigation of an Organic Redox Flow Battery
using a Segmented Cell

*Développement d'outils d'analyse et d'une cellule
segmentée pour l'étude d'une batterie redox
organique à électrolyte circulant*

présentée par

Mathilde Cazot

Soutenue publiquement le 30 août 2019

Composition du jury :

| | | |
|--------------------|---|---|
| Rapporteurs | Mme Christel Laberty-Robert M. Yann Bultel | Professeur, UPMC, LCMCP, Paris Professeur, GRENOBLE INP, LEPMI, Grenoble |
| Examineurs | M. Chris Menictas M. Mathieu Etienne M. David Pasquier | Professeur, UNSW, Sydney, Australia Professeur, UL, LCPME, Nancy Docteur-Ingénieur, IFPEN, Lyon |
| Encadrants | Mme Sophie Didierjean M. Gaël Maranzana M. Florent Beille | Professeur, UL, LEMTA, Nancy Professeur, UL, LEMTA, Nancy Directeur Technique, KEMIWATT, Rennes |
| Invité | M. Jérôme Dillet | Ingénieur de recherches, CNRS, LEMTA, Nancy |

Laboratoire d'Énergétique et de Mécanique Théorique et Appliquée — UMR CNRS 7563
2 avenue de la Forêt de Haye, 54518 Vandœuvre-lès-Nancy

“La vérité de demain se nourrit de l’erreur d’hier”.
Antoine de Saint-Exupéry

Un Grand Merci

La thèse est un travail de longue haleine, semé d'épreuves (voire d'impasses !) mais aussi de rencontres multiples qui n'auraient jamais eu lieu autrement. Les personnes qui ont croisé mon chemin durant mon projet ont toutes, à leur manière, contribué à me faire grandir et à approfondir ma réflexion sur mon projet mais surtout sur moi-même.

À commencer par les membres du jury, qui ont pris le temps de lire le fruit de mon travail, sont venus jusqu'en Lorraine pour m'écouter, et ont fait l'effort de nourrir une discussion riche de bons conseils et de nouvelles pistes de réflexion, le tout en anglais. Je remercie les rapporteurs Christel Laberty-Robert et Yann Bultel, Mathieu Etienne le président du jury, ainsi que David Pasquier qui a corrigé de manière approfondie mon rapport, et Chris Menictas, qui a fait tout son possible pour être là le jour J.

On m'avait prévenu qu'un bon encadrement de thèse valait mille fois un bon sujet, et j'en ai saisi tout le sens dès les premiers mois. J'ai eu la chance d'être accompagnée par un trio d'encadrants hors-pair et complémentaires ; votre bonne entente m'a offert un cadre scientifique et relationnel parfait et je vous en suis véritablement reconnaissante.


Merci Sophie pour ton dynamisme inépuisable, tes nombreux conseils et ton œil de correctrice scrupuleux. Tu t'es toujours rendue disponible quand j'avais besoin d'aide, et tu n'as pas hésité à passer la blouse pour démonter la cellule !

Gaël, j'admire ta propension à partager tout ton savoir et à nous faire profiter de ton inventivité. Ta gentillesse et ta pédagogie incitent à te solliciter à chaque difficulté. Tu as toujours su rester positif et eu les mots justes pour m'encourager.

Jérôme, tu es une personne unique qui gagne à être connue ! Ton caractère bien trempé, ton dévouement et ton incroyable efficacité font de toi un allié incontournable. Je pense sincèrement que tout doctorant aurait besoin d'un Jérôme durant sa thèse.

L'aventure n'aurait pas été possible sans le soutien de Kemiwatt, et plus particulièrement de François Huber. Tu m'as offert un environnement de travail idéal pour faire cette thèse, tu m'as donné toute l'autonomie à laquelle j'aspirais, et tu n'as pas hésité à m'envoyer sur d'autres continents pour présenter et poursuivre mes travaux ! Merci pour ton coaching et ton soutien permanent. Une petite pensée également pour Mohamed qui, avec François, m'a accueillie chaleureusement chez Ionwatt pour mon stage, et qui m'a convaincue de poursuivre en doctorat. Florent, ce fut un vrai plaisir de travailler avec toi. En tant qu'encadrant technique, tu m'as accordé ta confiance tout en restant très à l'écoute, et tu as veillé à ce que mes avancées soient cohérentes avec les problématiques industrielles. Et moi qui me faisais une joie de revenir travailler avec toi... Guillaume, je te remercie de m'avoir accordé du temps pour finir la rédaction de ma thèse sereinement.

Ce fut un vrai bonheur de retrouver le dynamisme et la bonne humeur de toute l'équipe Kemiwatt à chacune de mes visites à Rennes. Je vous remercie tous pour votre bonne compagnie : Léa, la meilleure conseillère en termes d'organisation, Thibault, allié parfait pour les conférences IFBF et les longues discussions entre chimistes, Kévin et Rémi, Jérémy et William, avec qui les afterworks finissent souvent en véritable Aventure, et aussi les derniers arrivés, Guillaume O. et Nicolas. Je remercie aussi toute l'équipe MaCSE ; Didier, Florence, Solène et aussi Aurore, qui avait toujours une nouvelle saveur asiatique à me concocter. Je suis heureuse de vous retrouver pour la suite de l'aventure !

Lorsque j'étais à Nancy, la fameuse équipe Pile et plus généralement la grande famille du LEMTA m'ont offert un cadre convivial propice à la réussite de ma thèse. Merci à Fabrice Lemoine, qui m'a ouvert les portes de son laboratoire. Je me suis sentie accompagnée, soutenue et aidée tout au long de mon parcours par Assma (tous les restos et les cadeaux bien pensés pour égayer ma période de rédaction ) , Julia, Jean-Christophe, Feina qui m'a fait découvrir de nouvelles techniques de caractérisation, Olivier Lottin, Nicolas Quéromès, toujours un petit mot cordial en passant le matin par mon bureau, Kévin Mozet, Julien Boisse, ma motivation pour faire du sport après une longue journée (squash, plongée...), Jérémy Bianchin, qui a résolu mes problèmes mécaniques en un clin d'œil, et Ludo, qui a fait de même pour mes bugs informatiques. Merci aussi à Alain avec qui il fait bon bavarder, et à Franck, mon coach personnel de sophrologie ! Je remercie aussi les petites mamans du labo, Fatiha, Irène et Valérie, toujours bienveillantes et prêtes à aider.

I would like to address a special thank to Maria Skyllas-Kazacos, who, without hesitation, received me in Sydney before starting my PhD. Thanks to her and Chris Menictas, I had the chance to work and learn by their side during a few months. I was really honoured to be part of their team and discover how we do research in Down Under!

I also wish the best to Kieran, whose work in Nancy greatly contributed to the last chapter of this thesis. I thank you for all the time you spent reading my manuscript, you have been a precious ally for the last months of this PhD.

Dans la difficulté on s'entraide et crée des liens forts... Merci à tous les copains qui ont égayé mes journées de thésarde et avec qui j'ai pu partager les délicieux repas du RU. À commencer par Juan-David, que j'ai suivi assidûment sur la voie de la réussite ; je suis heureuse que nos chemins se soient rejoints. Merci pour ta présence, ta patience et ton soutien au quotidien. Julian, Associé ! avec qui je refaisais le monde entre deux chapitres, Giuseppe et tous ses câlins de réconfort, Righina, dont la porte du bureau était toujours ouverte pour aller se changer les idées, Mylène la pâtissière en chef, Arthur avec qui on ne passe pas 5 minutes sans rigoler, mon doudou Ahmad, un partenaire de choix pour l'elliptique et les pauses cafés, Olivier, Naïma, Morgan, Romain, Shirin, Mathilde, Salah et tous les autres. Ceux qui m'ont accueillie à mon arrivée, Thomas L. et Thomas G., Saïd, mais aussi Sofyane, que j'ai eu le plaisir de recroiser en conférence. Et bien sûr, mon acolyte de bureau, Axel, dont la présence m'a inspirée pour aligner toutes les pages du manuscrit, et avec qui il faisait bon râler dans les moments difficiles. Bon courage à tous ceux qui touchent à la fin de ce beau parcours !

Merci aussi aux copines jaunes Anaïs et Sophie, Camille et Mylène, Ambroise et Méné, Zahra, Boris, Elaine, Manon et Mathieu (bientôt ton tour !), Sarah, Krishnan et Peb, qui ont contribué à faire de ces 3 ans de labeur une période mémorable. Et merci à tous ceux qui se sont rendus disponibles pour ma soutenance !

En effectuant ma thèse à Nancy, j'ai eu la chance inestimable de me rapprocher à nouveau de ma petite famille vosgienne. J'ai chéri chaque instant passé auprès de vous, et j'ai réalisé combien il était précieux de se sentir aimée et entourée dans les grandes épreuves. Je remercie du fond du cœur ma Maman et ma Mamie pour tout ce qu'elles m'ont inculqué, pour leur soutien inépuisable et pour leur présence à mes côtés, même jusqu'à l'autre bout du monde. Ensemble, nous formons un trio intergénérationnel de choc qui fait toute ma force. Je vous aime tant.

CONTENTS

| | |
|---|-------------|
| Nomenclature | xiii |
| Résumé en français | xix |
| Preamble | xxix |
| 1 Redox flow battery technology | 1 |
| 1.1 The energy storage challenge | 1 |
| 1.2 The Redox Flow Battery solution | 4 |
| 1.2.1 Concept and advantages | 4 |
| 1.2.2 Existing chemistries | 9 |
| 1.2.3 Kemiwatt's industrial challenge and opportunity | 11 |
| 1.3 General understanding of the Redox Flow Battery | 12 |
| 1.3.1 Fundamentals | 13 |
| 1.3.2 Modeling | 17 |
| 1.3.3 Analytical platforms | 17 |
| 1.3.4 Internal cell instrumentation | 20 |
| 1.4 Methodology of the PhD study | 21 |
| 2 Diagnostic tools | 23 |
| 2.1 Materials and pretreatments | 24 |
| 2.1.1 Electrolytes | 24 |
| 2.1.2 Standard test cell | 26 |
| 2.2 Battery tests | 29 |
| 2.2.1 Assembly | 29 |
| 2.2.2 Cycling | 29 |
| 2.2.3 Polarization curves | 30 |
| 2.2.4 Electrochemical impedance spectroscopy | 33 |
| 2.3 Symmetric cell | 35 |
| 2.3.1 Principle | 35 |

| | | |
|----------|---|-----------|
| 2.3.2 | Impedance variation with SOC | 35 |
| 2.4 | Segmented cell | 36 |
| 2.4.1 | Internal design | 36 |
| 2.4.2 | Segmentation and local currents | 38 |
| 2.4.3 | Challenges of local potential probing | 41 |
| 2.4.4 | Assessment of the local RHE | 47 |
| 2.4.5 | Test bed | 50 |
| 2.5 | Conclusion | 52 |
| 3 | Separate characterization of the components | 53 |
| 3.1 | Electrochemical analysis | 54 |
| 3.1.1 | Electrolytes and assumptions | 54 |
| 3.1.2 | Electrochemical cell | 55 |
| 3.1.3 | Potential window and reversibility of a redox couple | 57 |
| 3.1.4 | RDE voltammetry | 59 |
| 3.1.5 | Cyclic voltammetry | 63 |
| 3.1.6 | Discussion of the results | 66 |
| 3.2 | Physico-chemical electrolyte properties | 69 |
| 3.2.1 | Conductivity | 69 |
| 3.2.2 | Viscosity | 70 |
| 3.2.3 | Material compatibility and photodegradation of catholyte | 72 |
| 3.3 | Membrane characterization | 74 |
| 3.3.1 | Membrane pretreatments: FTIR-ATR study | 75 |
| 3.3.2 | Membrane affinity with solutions | 78 |
| 3.4 | Porous electrode characterization | 86 |
| 3.4.1 | Structural observation | 86 |
| 3.4.2 | NMR analysis | 87 |
| 3.4.3 | Comparison of two materials by blocking electrode model | 90 |
| 3.5 | Conclusion | 93 |
| 4 | Half-cell characterization | 95 |
| 4.1 | Stationary porous electrode model | 96 |
| 4.1.1 | Fundamental relations | 96 |
| 4.1.2 | Analytical expression with infinite electronic conductivity | 102 |
| 4.1.3 | Electrode impedance | 103 |
| 4.1.4 | Electrode impedance in blocking electrode conditions | 103 |
| 4.2 | Global impedance of the symmetric cell: methodology | 105 |
| 4.3 | Catholyte symmetric cell | 108 |

| | | |
|----------|---|------------|
| 4.3.1 | Effect of the light exposure of the catholyte on cell impedance | 108 |
| 4.3.2 | Effect of the electrode material on cell impedance | 113 |
| 4.3.3 | R_{cell} vs SOC curves: Identification of the degradation mechanisms | 116 |
| 4.4 | Anolyte symmetric cell | 122 |
| 4.4.1 | Impedance evolution in circulation | 122 |
| 4.4.2 | Analysis of the cell overcharge | 123 |
| 4.4.3 | R_{cell} vs SOC curves | 129 |
| 4.5 | Conclusion | 134 |
| 5 | Full cell study | 137 |
| 5.1 | Standard cycling | 138 |
| 5.1.1 | Comparison standard / segmented cell | 138 |
| 5.1.2 | Parameters evolution during cycling | 143 |
| 5.2 | Influence of operating conditions | 157 |
| 5.2.1 | Strategy to investigate internal heterogeneity of battery operation | 158 |
| 5.2.2 | Current density | 163 |
| 5.2.3 | Flow rate | 169 |
| 5.2.4 | Temperature | 178 |
| 5.3 | Summary of the parameter study | 185 |
| 5.3.1 | Comparison of the impact of the three parameters | 185 |
| 5.3.2 | Development of an operational map | 186 |
| 6 | Industrial cell study | 193 |
| 6.1 | Hydraulic study | 194 |
| 6.1.1 | Model development | 194 |
| 6.1.2 | Computational results | 197 |
| 6.1.3 | Clear flow cell experiment | 201 |
| 6.2 | Flow rate optimization | 206 |
| 6.2.1 | Strategy | 206 |
| 6.2.2 | Results | 208 |
| 6.3 | Conclusion | 212 |
| | Conclusions | 213 |
| | Appendices | 217 |
| | Bibliography | 217 |

NOMENCLATURE

Subscripts

| Symbol | Meaning |
|-------------|-----------------------|
| a | anolyte |
| b | bulk / blocking |
| c | catholyte |
| ch | charge |
| dis | discharge |
| e | electrode /electronic |
| eq | equilibrium |
| exp | experimental |
| F | Faraday / faradaic |
| lim | limit |
| m | membrane |
| ox | oxidation |
| o | oxidant |
| p | peak |
| r | reducer |
| red | reduction |
| ref | reference |
| s | solution |
| theo | theoretical |
| we | working electrode |

Notation

| Acronym | Meaning |
|-------------------------|--|
| ARS | Alizarin Red S |
| CE | Coulombic Efficiency |
| CT | Charge Transfer |
| CV | Cyclic Voltametry |
| EE | Energy Efficiency |
| EIS | Electrochemical Impedance Spectroscopy |
| FT | Flow-Through |
| FTIR-ATR | Fourier-Transform Infrared Spectroscopy - Attenuated Total Reflectance |
| HF | High Frequency |
| LCOE_s | Levelized Cost Of Energy for Storage systems |
| LF | Low Frequency |
| LSV | Linear Sweep Voltametry |
| MF | Medium Frequency |
| NMR | Nuclear Magnetic Resonance |
| OFB | Organic redox Flow Battery |
| PC | Polarization Curve |
| PFSA | Perfluorosulfonic Acid |
| RDE | Rotating Disk Electrode |
| RFB | Redox Flow Battery |
| RHE | Reversible Hydrogen Electrode |
| SHE | Standard Hydrogen Electrode |
| SOC | State Of Charge |
| VE | Voltage Efficiency |
| VFB | Vanadium redox Flow Battery |

Symbols

| Symbol | Meaning | Unit |
|----------------------------------|---|-----------------------------|
| a | Developed surface area | $\text{m}^2 \text{m}^{-3}$ |
| <i>C</i> | Active species concentration | mol L^{-1} |
| <i>C_{dl}</i> | Double-layer capacity | F m^{-3} |
| <i>D</i> | Diffusion coefficient | $\text{cm}^2 \text{s}^{-1}$ |
| <i>E</i> | Electrode potential | V |
| <i>E⁰</i> | Standard redox potential | V |
| <i>E^{0'}</i> | Formal redox potential | V |
| I | Current | A |
| <i>j</i> | Ionic current density | mA cm^{-2} |
| <i>J</i> | Current density | mA cm^{-2} |
| <i>k</i> | Permeability of the porous electrode | m^2 |
| <i>k₀</i> | Standard rate constant | m s^{-1} |
| <i>Q</i> | Capacity | A h |
| <i>Q_k[*]</i> | Local capacity percentage of the total capacity | % |
| <i>R_{cell}</i> | Cell resistance | Ωcm^2 |
| <i>q̇</i> | Electrolyte flow rate | mL min^{-1} |
| T | Temperature | K |
| U | Cell voltage | V |
| <i>V_{OC}</i> | Open circuit cell voltage | V |
| V | Volume of electrolyte | mL |
| <i>v</i> | Potential scan rate | V s^{-1} |
| <i>z</i> | Number of electrons | - |
| <i>Z</i> | Impedance | Ωcm^2 |
| <i>α</i> | Charge transfer coefficient | - |

| | | |
|---------------|---|---------------------|
| ε | Electrode porosity | - |
| η | Overpotential | V |
| κ | Ionic conductivity | S m^{-1} |
| ν | Viscosity | mPa s |
| σ | Electronic conductivity | S m^{-1} |
| σ_J^* | Normalized standard deviation of the local currents | % |
| ϕ | Phase potential | V |
| ω | Angular frequency | rad s^{-1} |

Constants

| Symbol | Meaning | Value | Unit |
|----------|--------------------|--------|-----------------------------------|
| F | Faraday's constant | 96 485 | C mol^{-1} |
| R | Gas constant | 8.3144 | $\text{J K}^{-1} \text{mol}^{-1}$ |

RÉSUMÉ EN FRANÇAIS

Contexte de l'étude

Alors que l'urgence climatique ne peut plus être ignorée, et qu'un bouleversement de nos sociétés est inévitable, certaines mesures peuvent encore être prises pour éviter le pire scénario. La réduction des émissions de gaz à effet de serre est un défi majeur, qui passe par l'augmentation massive de la part des énergies renouvelables dans le mix énergétique. Ces énergies "propres" sont également intermittentes, une faiblesse qui empêche à l'heure actuelle de se passer des ressources fossiles et polluantes (charbon, pétrole, gaz).

Connecter au réseau électrique un système stationnaire de stockage permettrait de le flexibiliser et de le fiabiliser. Il agirait comme un réservoir d'énergie qui pourrait lisser la production des éoliennes ou des panneaux solaires. Le stockage stationnaire de l'énergie couplé aux énergies renouvelables permet aussi d'envisager l'électrification propre de zones isolées, telles que les îles ou les campagnes, tout en évitant d'étendre le réseau électrique déjà existant. Cette approche oblige à réinventer le paysage énergétique actuel, avec l'émergence d'une production décentralisée, de réseaux autonomes et de micro-réseaux.

Les solutions de stockage sont nombreuses mais encore peu compétitives et/ou fiables. Parmi celles-ci on trouve les batteries conventionnelles (comme le lithium-ion ou la batterie au plomb) plutôt destinées aux applications embarquées de petite ou moyenne puissance, les systèmes électrolyseur/pile à combustible pour les applications de petite ou grande puissance embarquées ou stationnaires, et les batteries redox à circulation, ou redox flow battery (RFB) pressenties pour des applications stationnaires.

Ces dernières présentent en effet l'avantage d'une capacité de stockage importante (donnée par le volume de ses réservoirs et la concentration des espèces redox), d'une mise en œuvre et d'une maintenance relativement faciles, et la perspective d'un coût de fabrication qui pourrait les rendre rapidement compétitives [1]. Bien que son principe de fonctionnement soit établi depuis longtemps, la batterie redox à circulation n'a pas connu les mêmes développements scientifiques et technologiques que les autres systèmes de conversion électrochimiques, mais revient en force aujourd'hui dans une perspective affirmée de transition énergétique.

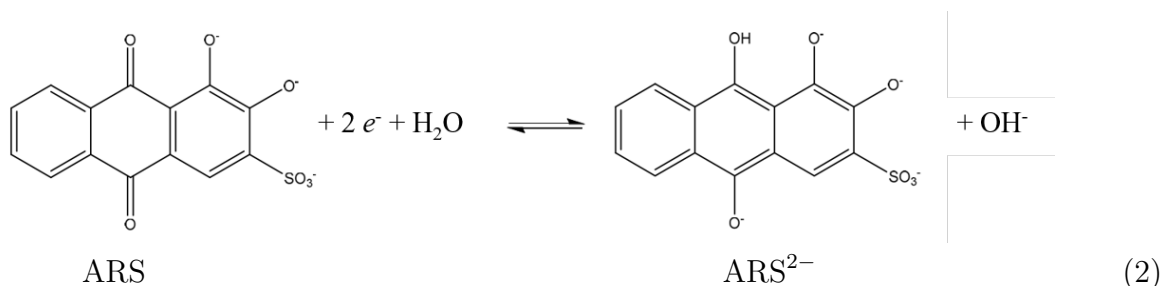
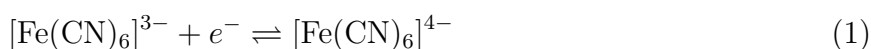
La société Kemiwatt, créée en 2014, a vocation à développer et commercialiser une technologie innovante de redox flow battery, notée RFB par la suite, basée sur des composés organiques et recyclables qui ont également un faible coût. Cette société est née à partir d'une technologie développée depuis plusieurs années par l'équipe "Matières Condensées et Systèmes Electroactifs" (MaCSE) à l'université de Rennes. Kemiwatt se positionne comme leader mondial dans

la technologie de RFB organique, depuis la réalisation de son premier prototype en 2017 puis d'un démonstrateur de 20 kW en 2017.

L'entreprise a débuté en testant l'utilisation de molécules organiques commerciales utilisées pour d'autres applications industrielles. Elle se lance désormais dans le développement de ses propres composés chimiques, dans le but de diminuer l'empreinte carbone de leur production, optimiser leur coût et augmenter leur performance dans la technologie flow battery.

L'opération scientifique "systèmes électrochimiques" du LEMTA (Laboratoire Energie et Mécanique Théorique et Appliquée) à l'Université de Lorraine développe depuis plusieurs années des activités de recherche sur la compréhension des phénomènes de transport de charges, de chaleur et de matière dans les piles à membrane échangeuse de protons. Un ensemble de compétences expérimentales permettant de caractériser les propriétés des matériaux utilisés ainsi que les phénomènes physiques qui s'y produisent a été développé. Les techniques utilisées reposent à la fois sur les outils habituels de l'électrochimie, que l'on adapte aux spécificités des cellules, et sur ceux de la thermique et de la mécanique.

La collaboration du LEMTA et de Kemiwatt à travers ce travail de thèse vise à développer une base de connaissances solide sur la technologie en cours d'industrialisation dans l'entreprise. L'objectif est notamment d'appréhender comment la chimie sélectionnée se comporte dans l'environnement batterie à électrolyte circulant et de quelle manière elle affecte les performances du système. Le premier couple redox constituant le catholyte (pôle positif de la batterie) est un composé organo-métallique: le ferricyanure/ferrocyanure (1). Celui utilisé dans l'anolyte (pôle négatif) est une molécule organique de type anthraquinone, l'Alizarin Red S (ARS) (2).



Ces molécules électroactives sont dissoutes dans une solution aqueuse alcaline contenant de la soude NaOH et de la potasse KOH. La mise au point de ces électrolytes a fait l'objet d'une thèse antérieure [2].

Une cellule unitaire de batteries redox à circulation est constituée de deux électrodes poreuses conductrices séparées par une membrane. Chaque électrode est plongée dans une solution (ou électrolyte) qui circule entre l'entrée et la sortie de la batterie. Les électrolytes contiennent des sels et les substances électroactives solubilisées qui vont réagir chimiquement au contact des électrodes. Les réactions électrochimiques, qui se traduisent par un échange d'électrons Eqs. (1) and (2), génèrent un courant et permettent de stocker puis de restituer l'énergie. Les matériaux qui composent la batterie redox sont chimiquement inertes. La membrane joue un rôle de barrière aux espèces actives mais permet le passages des cations, pour assurer l'électroneutralité entre les deux compartiments d'électrode. Le fonctionnement de la batterie est composé de deux étapes qui constituent un cycle: la charge puis la décharge. Les

réactions de réduction et d'oxydation vont se succéder dans chaque électrode de la cellule lors du cyclage.

Un schéma de principe de la cellule unitaire et des échanges ioniques et électroniques qui ont lieu en décharge est présenté sur la Fig. 1.4b.

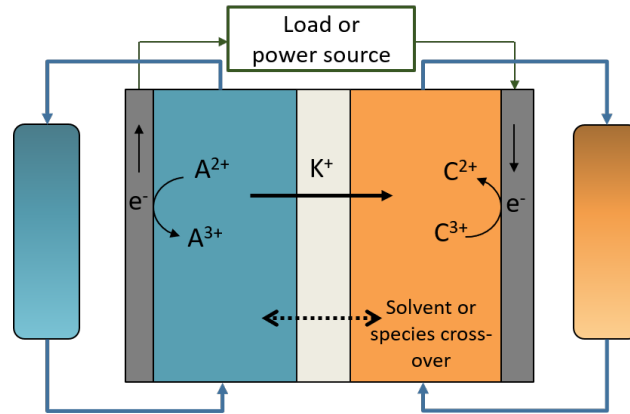
L'empilement de plusieurs cellules unitaires forme un stack, alimenté par les réservoirs d'électrolytes via des pompes. L'ensemble stack-circuits fluidiques est schématisé sur la Fig. 1.4a.

Les avantages de cette technologie sont multiples et résident dans l'utilisation d'une solution aqueuse pouvant être régénérée ou remplacée facilement, le fonctionnement instantané dès la mise en circulation du fluide, et la relation directe entre capacité électrique et volume de stockage de l'électrolyte. En effet la quantité d'énergie disponible (Joule ou Watt.heure) et la puissance développée (Watt) s'optimisent de façon indépendante. Le dimensionnement de la batterie pour une nouvelle application est très simple :

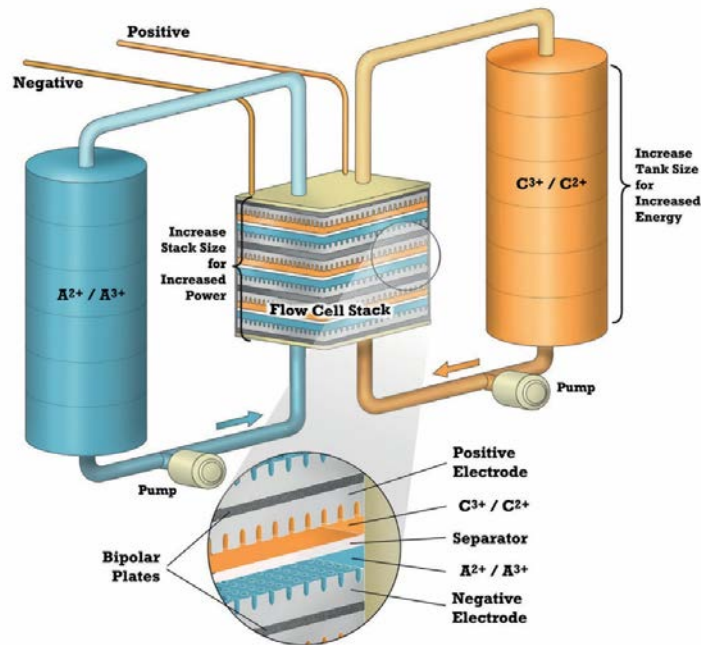
- ➔ La puissance de la pile est reliée à la différence de potentiel entre les deux couples redox et à la surface des électrodes. Augmenter la surface active et empiler plusieurs cellules permet d'obtenir une puissance plus importante. Cependant, une grande surface active pose la problématique de la distribution des électrolytes et des réactions sur toute la surface de l'électrode.
- ➔ La quantité d'énergie est liée au volume d'électrolyte et à la concentration des couples redox. Augmenter la taille des réservoirs permet de stocker plus d'énergie.

De plus, la technologie organique RFB permet de s'affranchir de l'utilisation de métaux rares tels que le lithium, le plomb, le titane ou encore le vanadium, utilisés dans d'autres types de systèmes de stockage. Leurs prix sont volatils et leur extraction a un impact écologique désastreux. Ces systèmes représentent un danger de pollution, des risques d'accidents (explosion, incendies) et nécessitent la maintenance régulière des installations.

La flow battery organique propose une alternative plus verte, fiable et robuste, qui requiert un minimum de maintenance pour une durée de vie très importante, autour de 20 ans.



(a) Flow and reactions of charge carriers during discharge of the RFB in a unit cell of the reactor



(b) General layout of a RFB

Figure 1: Representation of the RFB system, adapted from [3]

Réalisations et résultats de l'étude

Cette thèse vise à aborder la complexité de la RFB en analysant le système à tous les niveaux. Des études à différents degrés de complexités sont menées afin d'isoler l'influence de chaque composant, et d'identifier les prérequis nécessaires au bon fonctionnement de la batterie. Le travail a été effectué dans un laboratoire pluridisciplinaire et en collaboration avec l'équipe de l'UNSW (Sydney), renommée mondialement dans le domaine des RFB au vanadium [4]. Ce contexte académique riche est l'opportunité d'intégrer à l'étude des techniques de caractérisation et des plateformes analytiques inédites.

En premier lieu, les principaux composants de la cellule sont évalués séparément : les électrolytes, la membrane et l'électrode. Une analyse électrochimique approfondie a été effectuée sur les électrolytes concentrés (de l'ordre de 0.5 mol L^{-1} d'électrons) et a montré des résultats convergents, bien que les modèles utilisés soient basés sur la théorie des solutions diluées. Les propriétés intrinsèques des molécules actives ont pu être déterminées (coefficient de diffusion, cinétique de réaction).

Plusieurs prétraitements de membrane ont été examinés par spectroscopie infrarouge (FTIR) avant d'évaluer l'impact du contenu cationique de l'électrolyte sur la résistance de celle-ci. Cette dernière étude a été réalisée sur un montage de cellule spécifique.

Il a également servi à la caractérisation de l'électrode en carbone poreux. La capacité de double-couche de l'interface électrode/électrolyte ainsi que la résistance de l'électrode ont pu être estimés par une approche modèle-expérience. Enfin, l'écoulement dans l'électrode a été observé à l'échelle microscopique par imagerie par résonance magnétique (IRM). Cette première partie constitue une base de connaissance solide pour appréhender les phénomènes observés dans la batterie, et pour déterminer les matériaux idéaux à utiliser.

L'étape suivante est la caractérisation des demi-cellules de la RFB. Les électrolytes sont examinés séparément dans les conditions de fonctionnement de la RFB, en utilisant une configuration de cellule symétrique. Celle-ci est alimentée par un électrolyte mi-chargé (mélange équimolaire d'espèce active réduite et oxydée).

Cette technique permet de combler l'écart entre la caractérisation ex-situ et le fonctionnement complet de la batterie. L'étude est menée en deux étapes:

- observer l'évolution de l'impédance de la cellule par spectroscopie d'impédance électrochimique pendant la circulation de l'électrolyte durant plusieurs jours. Cela permet d'analyser la stabilité calendaire de la solution à un état de charge de 50% dans la cellule
- effectuer des cyclages de la cellule symétrique, afin d'identifier cette fois les phénomènes de dégradation lié aux opérations de charge et de décharge

Le suivi de l'impédance de la batterie dans les conditions de circulation et de cyclage est ensuite analysé.

Les deux électrolytes induisent des mécanismes différents de dégradation de performance. D'importantes limitations par transfert de matière apparaissent lors de la circulation de l'anolyte, alors que le catholyte présente une détérioration du transfert de charge. Ces observations ont été renforcées par l'utilisation de la méthode des problèmes inverses, pour déterminer les paramètres associés aux phénomènes observés. Pour ce faire, les mesures d'impédance de la cellule symétrique sont comparés à un modèle d'électrode volumique, mis au point durant la thèse à partir de la littérature [5].

Un exemple d'ajustement du modèle aux données expérimentales est présenté sur la Fig. 2. Il correspond à l'impédance d'une cellule symétrique fonctionnant en électrode bloquante, c'est-à-dire sans espèce active présente dans l'électrolyte. De ces combinaisons modèle/expérience, plusieurs caractéristiques essentielles de la batterie peuvent être déterminées in-situ, comme la constante de vitesse de réaction électrochimique, la résistance de la membrane ou encore la capacité de double-couche de l'électrode. L'effet de la concentration des espèces actives sur les performances de la cellule est également été examiné grâce à la cellule symétrique.

L'étude de la cellule entière est ensuite effectuée à l'aide un banc d'essai instrumenté, développé durant les travaux de thèse au laboratoire. Cette plateforme d'analyse permet le

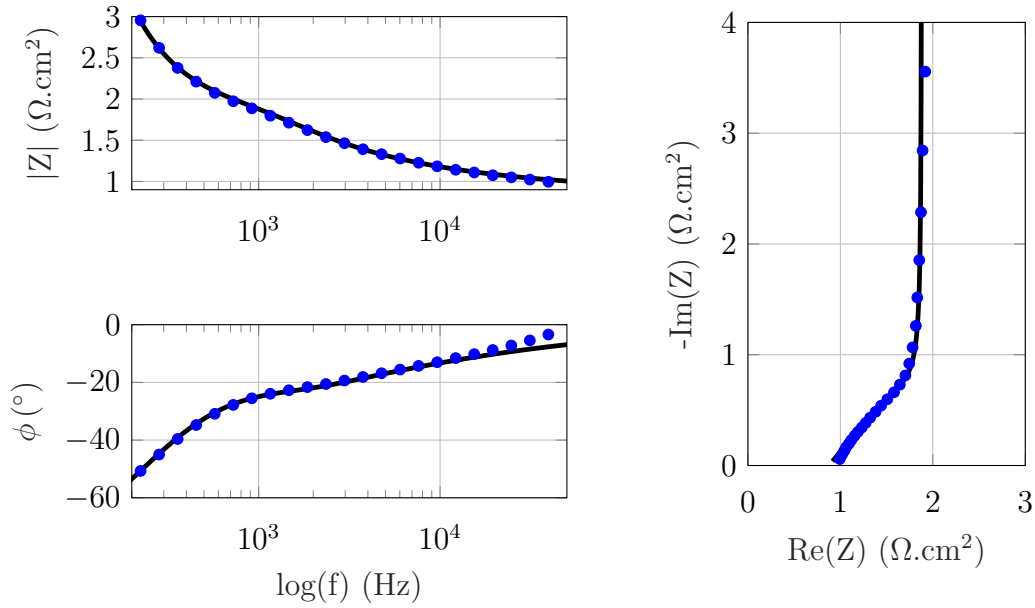


Figure 2: Représentation de Bode (gauche) et de Nyquist (droite) d’une cellule symétrique en électrode bloquante remplie de 2 M NaOH; Modèle d’électrode ajusté représenté par la ligne noire

contrôle des principaux paramètres de fonctionnement : le débit, la température et le courant. De plus, la distribution interne du courant le long du canal d’écoulement de la cellule peut être suivie au moyen d’une cellule segmentée, ce qui constitue une analyse originale du système RFB, encore très peu documentée dans la littérature.

Un effort important a été déployé pour équiper la cellule segmentée d’électrodes de référence locales à hydrogène, qui permettent le suivi des potentiels de chaque demi-cellule, comme cela est possible pour les piles à combustibles [6]. Cependant, la technique s’est avérée inappropriée pour une RFB.

La validation du banc expérimental est réalisée dans des conditions standards, avant d’examiner les performances de la batterie sur 300 cycles.

Le travail en cellule segmentée se poursuit par une étude paramétrique fine de trois variables opératoires: le courant, le débit d’électrolyte et la température. L’analyse des cycles et les courbes de polarisation (une technique de caractérisation courante des systèmes électrochimiques) permettent de comprendre comment ces trois paramètres de fonctionnement affectent la réponse globale du système. Grâce à la résolution spatiale du courant disponible, le comportement global peut être relié à des processus internes. La distribution des courants locaux est principalement évaluée par son écart-type, et fournit un aperçu inédit du fonctionnement interne de la cellule.

Des particularités se manifestent au début du processus de charge ou de décharge. Elles peuvent être expliquées par des phénomènes de potentiel de Nernst et de limitation de transfert de réactif. Grâce à la précédente caractérisation de chaque demi-cellule, certains aspects visibles à l’échelle de la cellule peuvent être associés au comportement original de l’anolyte.

Afin d’anticiper l’utilisation longue du système de stockage (sur plusieurs années dans les applications réelles), un seuil d’hétérogénéité interne acceptable en cyclage est défini. Il permet de minimiser les dégradations et donc les chutes de performances de la batterie à long terme. En combinant cette limite aux résultats de l’étude paramétrique, une carte opérationnelle

empirique est proposée: elle permet de contrôler le débit en fonction du mode de fonctionnement (charge ou décharge et intensité du courant) et de l'état de charge du système. Elle est représentée en Fig. 3.

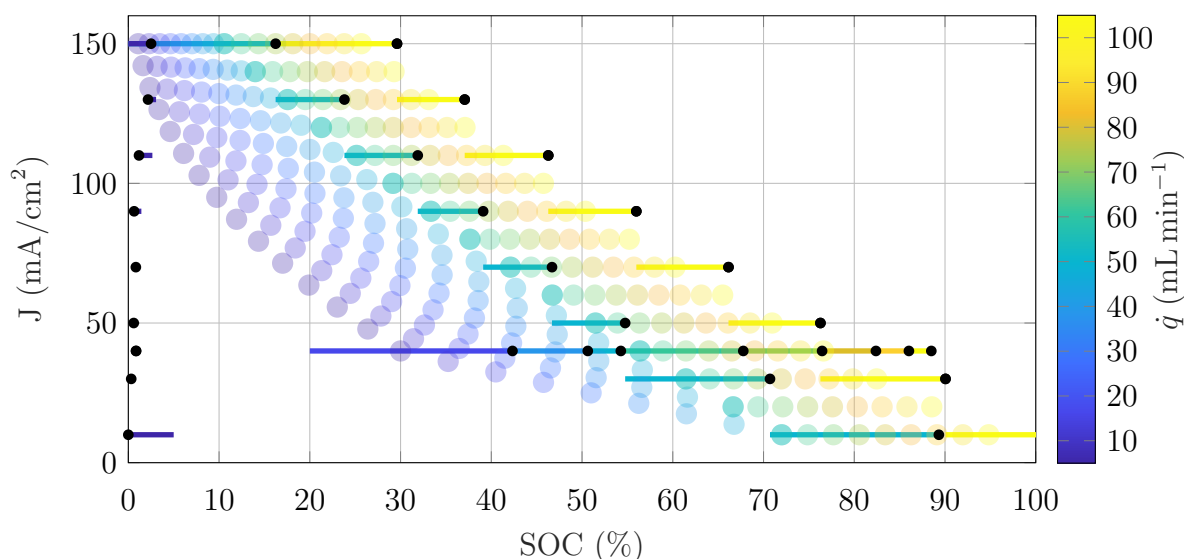


Figure 3: Carte opérationnelle de la RFB en charge, élaborée empiriquement. Elle permet une optimisation du débit en fonction du point de fonctionnement de la batterie. Les cercles noirs symbolisent les points expérimentaux, et les traits de couleur sont extrapolés entre ces points.

Cette stratégie de diminution de l'hétérogénéité interne en fonctionnement est ensuite testée sur quelques cycles et prouve son efficacité : alors que l'homogénéité de la batterie est très satisfaisante, la quantité d'énergie accessible est maintenue. La consommation des pompes peut ainsi être fortement réduite et la performance du système optimisée.

La dernière partie s'intéresse à l'aspect hydraulique du système RFB. Elle a été réalisée en majeure partie à l'UNSW (Sydney, Australie), lors d'une collaboration de 3 mois entre les deux universités. Un modèle hydrodynamique simple met en évidence l'impact majeur de l'électrode poreuse sur l'homogénéité du flux, au détriment d'une perte de charge élevée. La structure de l'électrode devient alors une caractéristique primordiale pour l'efficacité de la batterie, et ouvre de nouvelles perspectives d'étude et d'optimisation: des empilements de différents matériaux ou des structurations dans le volume de la matière seraient à considérer, afin de faciliter le passage du fluide tout en offrant une surface déployée suffisante pour les réactions.

Le design du cadre permettant l'entrée du fluide dans l'électrode est également étudié au moyen d'une maquette transparente, qui permet de visualiser l'écoulement. Plusieurs motifs de canaux d'écoulement ont été testés grâce à l'impression 3D. Ces deux approches combinées révèlent l'importance de la conception des demi-cellules, et permettent d'envisager des stratégies d'optimisation du stack de la RFB.

A tous les niveaux d'étude du système de batterie à flux, des approches non conventionnelles sont proposées dans ce travail. Un accent fort est mis sur la complémentarité des études expérimentales et de modélisation. Cette approche offre des résultats fiables et représentatifs. L'aspect multi-échelle de l'étude est primordial pour offrir une caractérisation complète. Grâce à la collaboration étroite entre l'entreprise et le milieu académique, des pistes d'améliorations

applicables industriellement émergent des différentes analyses.

La stratégie d’optimisation des conditions opératoires proposée et validée sur le banc d’étude sera reproduite sur un système d’échelle semi-industrielle: grande surface d’électrode, pompes dimensionnées, grand volume d’électrolyte. On pourra alors mesurer l’amélioration du rendement énergétique du système global grâce aux résultats empiriques tirés de cette thèse.

Plus généralement, la suite des travaux prévue en entreprise consiste à adapter les résultats à la dimension industrielle du projet, et à combiner les différents points de l’étude pour construire une approche plus systémique, dans le but d’optimiser la technologie et de garantir son déploiement rapide dans le marché du stockage de l’énergie.

La thèse est également l’occasion de sensibiliser le grand public aux problématiques énergétiques actuelles et au challenge que représente le stockage de l’énergie. La participation au concours de ma Thèse en 180s, avec l’obtention de la deuxième place de la finale régionale, et la réalisation d’une bande-dessinée signée Peb&Fox, présentée ci-après, furent des expériences de vulgarisation inoubliables et enrichissantes.

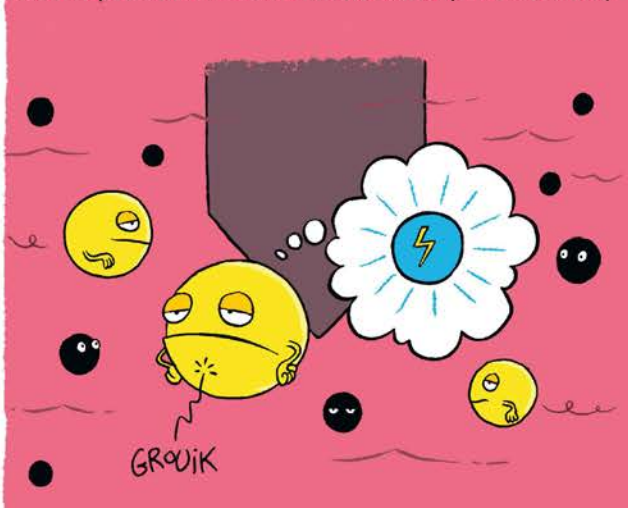
Le problème des énergies renouvelables, c'est qu'elles marchent par intermittence. Pourtant elles produisent régulièrement un surplus d'électricité difficile à stocker.



Mais ces grosses batteries que je développe contiennent un liquide qui peut la conserver grâce aux molécules qui baignent dedans.



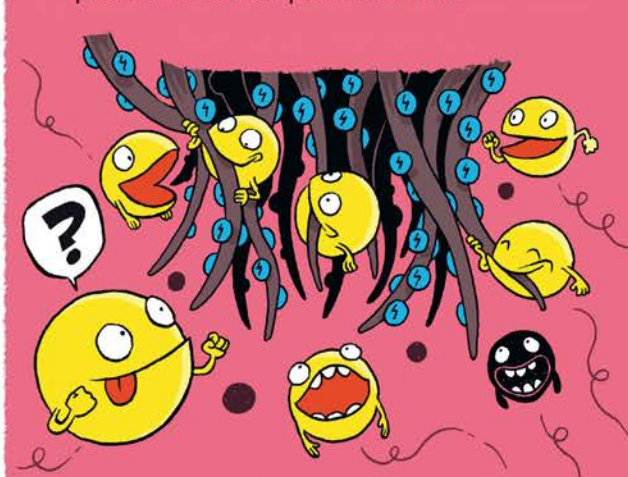
Imaginons que ces molécules sont des Pac-Mans qui attendent de pouvoir absorber des particules électriques sortant d'un bout de métal (une électrode).



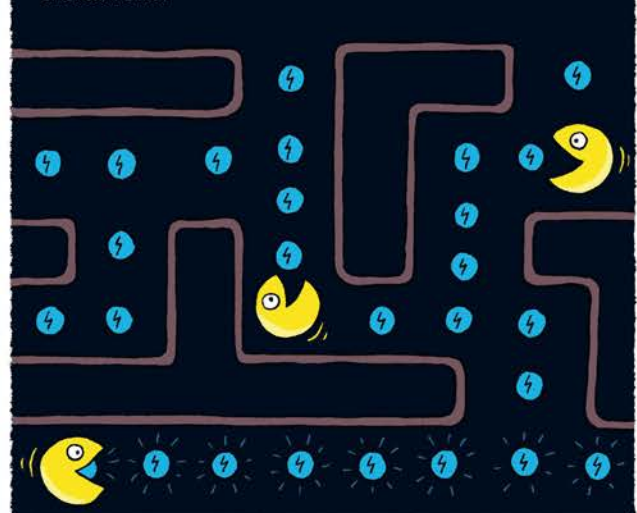
Pour charger une batterie, je connecte l'électrode à un panneau solaire : elle libère les électrons. Les molécules vont alors venir s'agglutiner autour pour se servir.



Pour contenter un maximum de molécules, je vais leur offrir plus de surface de contact en décomposant mon électrode en éléments plus fins mais bien plus nombreux !



Cette électrode alambiquée va être envisagée par les molécules comme un véritable dédale rempli d'électrons.



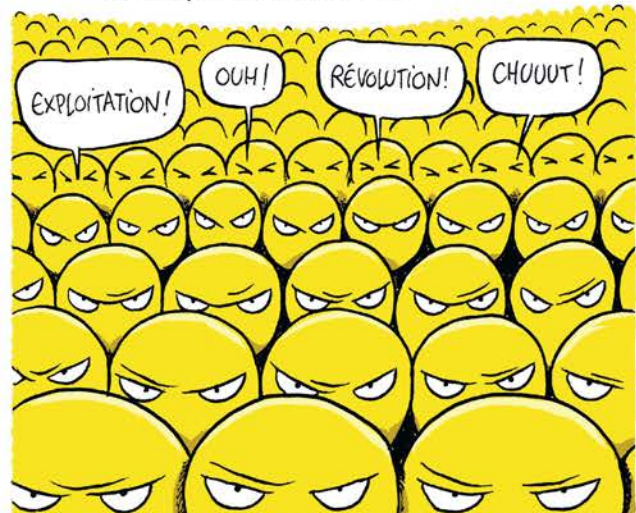
Une fois le liquide chargé, et pour que la distribution d'électricité ne s'arrête pas quand la production cesse, il faut demander aux molécules de restituer l'électron qu'elles ont capturé. Mais toutes ne le veulent ou ne le peuvent pas.



Pour optimiser le fonctionnement de ces batteries, je peux notamment rendre le labyrinthe plus accessible.



Je peux aussi augmenter la quantité de Pac-Mans pour amplifier les chances de récupérer des électrons.



JE CHERCHE AUSSI À FAIRE FONCTIONNER CETTE BATTERIE AVEC DES MOLECULES MOINS POLLUANTES QU'ON POURRAIT TROUVER DANS LA NATURE.



NOUS POURRIONS AINSI RENDRE COMPLÈTEMENT PROPRES CES NOUVELLES RESSOURCES ÉNERGÉTIQUES!



PREAMBLE

The global human population is estimated to grow to 10 billion by 2040 compared to 7.7 billion today [7]. The population growth being closely tied to economic growth, it will drive a 37% increase of global energy demand between 2013 and 2035 [8]. To meet the rise in energy consumption while facing the fossil fuel reserves depletion and the related climate crisis, huge efforts in developing renewable energy production are necessary. In their projection of global energy generation, the Australia’s national science agency (CSIRO) predicts a 4-fold rise of the renewable energy sources under a 2-degrees scenario [9], as presented in Fig. 4.

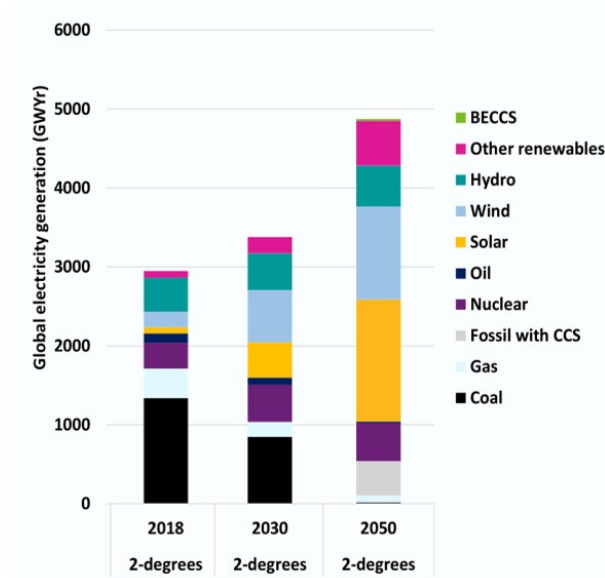


Figure 4: Projected global power generation mix under the 2-degrees scenario [9]

The transition to greener production has already started worldwide to reduce carbon emissions, Germany being one of the most popular example of this energy revolution. Nearly one-third of the electricity consumption came from renewable sources in 2015 in the country, but it is far from being run on zero-carbon electricity [10]. Nevertheless, sustainable energy is partly produced from intermittent solar and wind sources. Their variability implies the need to keep fossil-fuel plants running to meet the energy demand at all times, while on sunny and windy days Germany faces excess supply on the grid, making the electricity price go negative [11].

A buffer solution is crucially missing in the new energy markets to balance the power supply

and demand. This is precisely the role of grid-connected energy storage systems (ESS) being increasingly integrated to the electrical networks. In addition to the sustainable transition of developed countries, the electrification of emerging regions is accelerating and constitutes a crucial challenge in the current climate emergency. Microgrids combining renewable power and storage systems are an efficient solution to provide rural areas with electricity services, instead of the traditional approach of extending the existing central grid. The revamp of the existing electricity grids and the emergence of microgrids offer a booming market for stationary and grid-connected storage. Indeed, Bloomberg analysts forecast a six-fold growth of the global energy storage sector, exceeding 300 GW h of energy and 125 GW power installed by 2030 [12]. This trajectory entails a fierce race between the storage solutions to meet the demand at the low expected cost of energy storage.

The energy storage systems must store the excess of energy produced when the power supply exceeds the consumption, and feed it back into the grid during peak demand periods. Among the diverse energy storage technologies listed in Chap. 1, the redox-flow battery (RFB) is a compelling electrochemical solution for stationary applications. It offers a great flexibility of design that drives many scientific and industrial projects to investigate the potential of this technology. The state of progress of the RFB development is reviewed in the first chapter. In this context, the French startup Kemiwatt is developing a disruptive organic type of redox flow battery. The present PhD work was conducted in parallel at the company and at the Laboratory of Theoretical and Applied Energetics and Mechanics (LEMTA). A part of the work was conducted in Australia during a 3-month visit at UNSW in the team of Chris Menictas. This university is at the origin of the most famous Vanadium Redox-flow battery from the work of Maria Skyllas-Kazacos [4]. The PhD research objective was to provide an in-depth study of the electrochemical system by conceiving analytical tools to guide its industrial development.

The first step of the study was to develop an experimental platform and define characterization procedures in order to investigate the in-situ behavior of the electrochemical system (Chap. 2).

In a second time, special effort was allocated to the ex-situ characterization of the elements composing the redox flow battery (Chap. 3).

The next stage was dedicated to the separate analysis of the two electrolytes used in each side of the battery by utilizing symmetric cell layouts (Chap. 4).

Once the specificities of each electrolyte were uncovered, the battery cycling performance of the full cell was conducted in an instrumented test bench using a segmented cell. An extensive parameter study was also performed (Chap. 5).

Ultimately, several strategies were considered to advance the battery study to the industrial-cell scale (Chap. 6).

This PhD work was closely tied with the industrial context of the start-up Kemiwatt; the experiments of Chapters 3 and 4 were performed at the company, while the segmented cell tests of Chapters 2 and 5 were carried out at LEMTA and the hydraulic study in Chap. 6 was developed at UNSW. The key industrial highlights of the study are emphasized in grey inserts in the document.

1

REDOX FLOW BATTERY TECHNOLOGY

Contents

| | |
|--|-----------|
| 1.1 The energy storage challenge | 1 |
| 1.2 The Redox Flow Battery solution | 4 |
| 1.2.1 Concept and advantages | 4 |
| 1.2.2 Existing chemistries | 9 |
| 1.2.3 Kemiwatt's industrial challenge and opportunity | 11 |
| 1.3 General understanding of the Redox Flow Battery | 12 |
| 1.3.1 Fundamentals | 13 |
| 1.3.2 Modeling | 17 |
| 1.3.3 Analytical platforms | 17 |
| 1.3.4 Internal cell instrumentation | 20 |
| 1.4 Methodology of the PhD study | 21 |

1.1. The energy storage challenge

Grid-connected storage systems can support the use of renewable sources (solar, wind) and thus increase their share in energy production. Energy storage technologies must match the supply and demand, by storing the excess of energy produced by intermittent sources and supply the grid during peak periods. They must also show a long service life, the ability to withstand many charge/discharge cycles and a high energy and/or power capacity, depending on the targeting application. Several technologies are coexisting in the energy storage sector. They can be mapped according to their capacity and power ability, as presented in Fig. 1.1.

The value chain for storage contains multiple applications, going from grid services to customer energy management, and even behind-the-meter applications (that is outside the conventional network). The wide range of needs allows for the coexistence of various technologies in the storage landscape. A single energy storage installation can be further leveraged

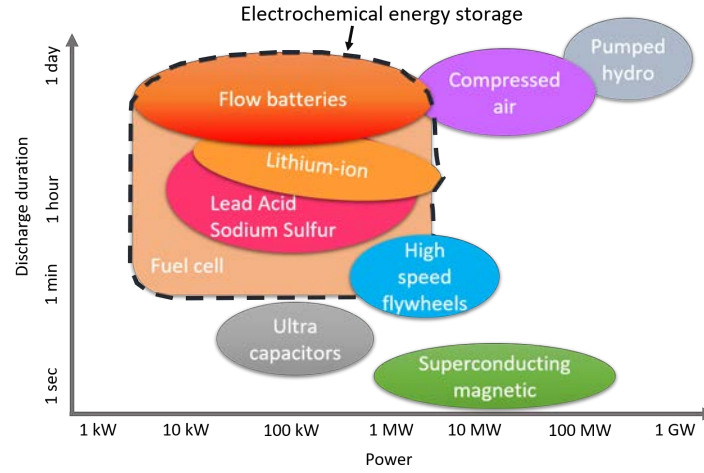


Figure 1.1: Power-Discharge duration diagram for energy storage technologies, from [13]

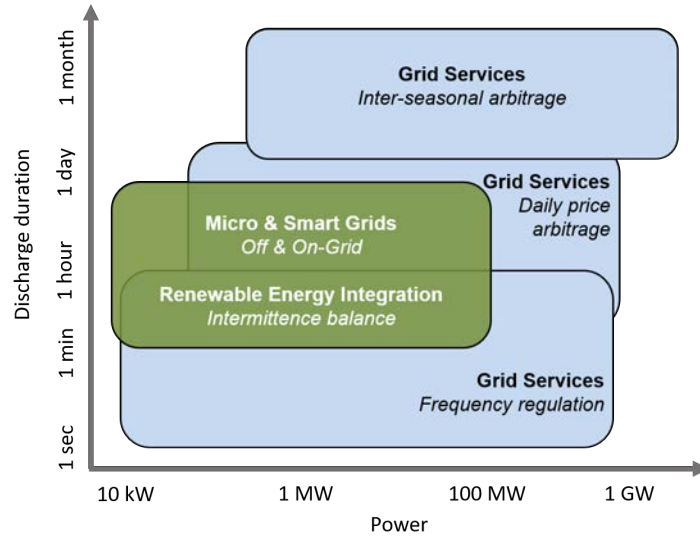


Figure 1.2: Power-Discharge duration diagram for energy storage applications, from [14]

if it delivers stacked services; several technologies are versatile, although at a lower efficiency compared to their dedicated application.

Long-duration services require substantial storage capacity and good cycling ability; they are usually referred to as energy applications. One example is the renewable time shifting to balance the fluctuations of the intermittent sources.

On the other hand, short-duration applications necessitate fast response time with high power rating; these are called power applications. It concerns frequency regulation or grid voltage stability.

Pumped hydro is one of the two large-scale (> 100 MW) technologies available today, and is by far the most commonly used worldwide [15]. The system requires an upper and a lower reservoir and reversible pumps move the water up and down according to demand fluctuations. But pumped hydro storage cannot respond fast to peak load, has environmental impacts and necessitates a specific geography to be deployed.

Compressed air storage is the other large-scale solution, but only two facilities are

working today [15]. Ambient air is compressed and stored underground, at high pressure, when excess power is available [16]. The energy is returned to the grid by feeding a turbine with the pressurized air that is heated. The technology is quite expensive and needs an underground storage.

High speed flywheels store energy by rotating a wheel, whereas **superconducting magnetic** technologies require cryogenic cooling to produce high magnetic fields [13]. Like **ultra capacitors**, these systems can store a high amount of energy and their response is very fast. However, their efficiency is good only for short discharge time. They are still under development for grid applications even if the success of such expensive solutions is uncertain.

In the energy storage field, **electrochemical energy storage** systems are key figures as they cover an area of the power/duration diagram out of reach by the preceding solutions. This group includes various technologies, such as fuel cells combined with electrolyzers, lithium-ion batteries or flow batteries. Nevertheless, a given battery chemistry is preferably paired with specific applications that maximize their efficiency. Davies et al. modelled the economic viability of several batteries by comparing their performance and revenue streams for several grid-scale services [17]. They highlighted that for all chemistries, time-shifting led to lower efficiency than frequency regulation. While Lithium ion showed the best performances of the commercial batteries tested, the sodium-ion revealed promising results, although it is still under development. This study focused on the revenue sides only for applications spanning less than 3 hours. Cost analyses, lifetime performance and larger range of applications should be included for a complete economic assessment.

Indeed, the substantial market penetration of an ESS is dictated by the so-called *levelized cost of energy* for storage systems (LCOE_s). This standardized metrics embodies the cost of ownership relative to the energy delivered by the ESS [18]. A simple form is given by [19]:

$$\text{LCOE}_s = \frac{\text{CC} + \text{MC}}{N\eta} \quad [\$ \text{ kWh}^{-1} \text{ cycle}^{-1}] \quad (1.1)$$

CC represents the capital cost per kW h invested once for the ESS installation, MC is the cost of maintenance during the entire life of the system, N the total number of cycles and η the efficiency (that depends on the application as mentioned above). Thanks to the LCOE_s indicator, Obi et al. could make the comparison of pumped hydro, compressed air and battery storage solutions [20]. The two first are undoubtedly the cheapest with an LCOE_s as low as \$ 20 MWh^{-1} , even though they are not applicable to all storage needs (e.g. medium-scale and off-grid market segments). Another parameter driving costs down is the learning rate: the technology that brings most capacity to market certainly becomes the most economical. According to the projection of Schmidt et al. [21], RFB could become the cost-leading technology for stationary applications, with prices at \$ 250 kWh^{-1} if the cumulative capacity installation at utility-scale reached 1 TW h. This situation could be achieved by 2027-2040 under a sustained pace of investment, provided that the price of raw materials do not change much. On their respective roadmap, the US Department of Energy and the European Storage Agency target a system capital cost of \$ 150 kWh^{-1} (and an LCOE_s of €10 kWh^{-1}) by 2023, to ensure the economic scalability of the battery without subsidies [22, 23].

Beyond the economic appeal, energy storage systems are increasingly valued on their environmental impact and threat, at all stages of their lifetime: installation, operation, decommissioning, and recycling.

Other minor ESS technologies exist but are not presented in this overview.

1.2. The Redox Flow Battery solution

According to the Power-Discharge duration diagrams displayed in Figs. 1.1 and 1.2, the RFB technology stands in a sweet-spot where conventional batteries cannot compete [1].

1.2.1. Concept and advantages

It is usually quantified that flow batteries outcompete lithium-ion systems for discharge duration above 3 h, that is equivalent to a discharge rate/capacity ratio of: C-rate < 0.3 [24]. Pawel evaluated the LCOE_s (1.1) for the redox-flow, the lithium-ion and the lead-acid batteries. The input parameters along with the deduced cost are detailed in Fig. 1.3. The calculation underlines that although the initial investment cost (usually called CAPEX for capital expenditure) is high, the derived cost of ownership can be the most economic over the total investment period. In this respect, the project lifetime and maintenance costs (or OPEX for operational expenditure) are the key parameters and must be assessed accurately.

| Parameter | Redox-Flow | Lithium-Ion | Lead-Acid |
|--|--------------|--------------|--------------|
| Project-specific parameters | | | |
| Installed storage power [MW] | 1.0 | 1.0 | 1.0 |
| Investment Cost [Mio. €] | 5.0 | 2.4 | 1.2 |
| C-Rate (nominal) | 0.25 | 1 | 1 |
| Utilization of usable storage capacity | 100% | 100% | 100% |
| Number of cycles per year | 365 | 365 | 365 |
| External parameters | | | |
| Energy price [€/kWh] | 0.03 | 0.03 | 0.03 |
| Storage specific parameters | | | |
| Residual value after end of lifetime (discounted) of invest cost | 15% | 0% | 0% |
| Efficiency | 70% | 80% | 65% |
| Maintenance Cost of Investment | 2% | 1% | 5% |
| Degradation storage capacity per year | 0.1% | 2.0% | 3.7% |
| Calendar lifetime | 25 | 7 | 3 |
| Usable storage capacity | 100% | 80% | 50% |
| LCOE of storage [€/kWh] | 0.338 | 1.678 | 3.072 |

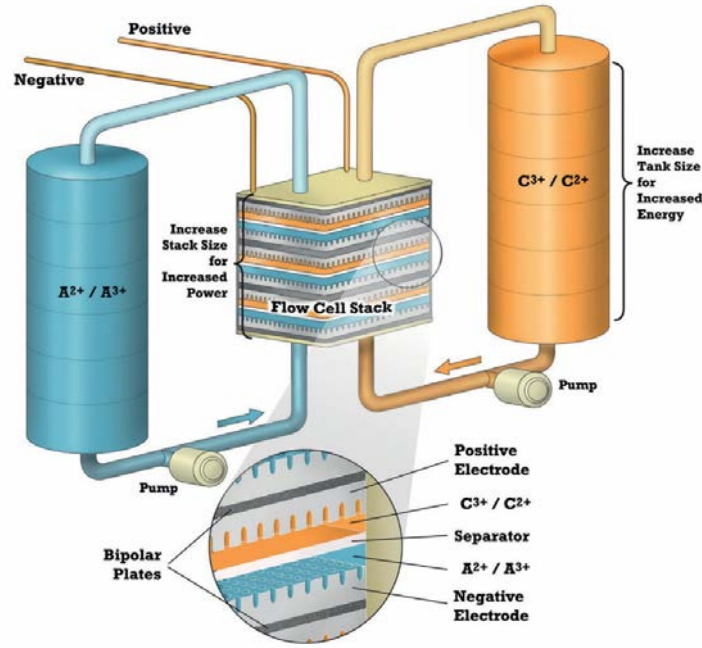
Figure 1.3: Calculated LCOE_s for three battery technologies, adopted from [18]

The author of this LCOE study detailed that the operational life and usable storage capacity were disputable, and that the C-rate value also altered the outcome of the analysis.

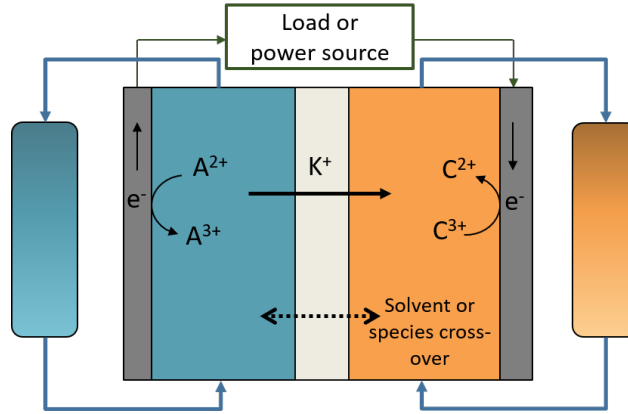
The projected competitiveness of the redox flow battery stems from its technological attributes [25]. As illustrated in Fig. 1.4a, the RFB architecture is not conventional:

- ➔ Energy is stored in two separate tanks of ionic solutions, also called electrolytes. The volume of electrolytes and their concentration in active species define the amount of energy stored in the system.
- ➔ The reactor, or stack, is connected to the reservoirs of electrolytes through a pump and an hydraulic loop. Its size, defined by the active surface area and the number of stacked cells, determines the output power of the battery.

Its design flexibility entails the dissociation of stored energy capacity and power, which



(a) General layout of a RFB



(b) Flow and reactions of charge carriers during discharge of the RFB in a unit cell of the reactor

Figure 1.4: Representation of the RFB system, adapted from [3]

makes the RFB scalable to a wide range of applications. The other appealing features of the RFB are [25]:

- a high round-trip efficiency (70 % for the energy efficiency taking into account ancillary losses), i.e. the energy charged in the battery can be almost totally recovered
- an important depth of discharge without degradation
- a long cycle life and a low-maintenance facility
- a rapid switching from charge to discharge
- safer technology than Lithium batteries (no risk of fire) for aqueous types

Nevertheless, the low energy density of the RFB prevents its use for mobile applications.

The electrolytes energy density is at best 20 Wh L^{-1} (for VFB at industrial scale, and much lower for other chemistries), in comparison to more than 600 Wh L^{-1} for Li-ion technology [26]. The above attributes actually depend on the RFB chemistry, whose major types are reviewed further (subsection 1.2.2). The basic principle of the flow batteries is described in the following paragraphs.

Like other rechargeable batteries, the RFB relies on the reversible reaction of two redox couples. They differ from solid-state batteries (NiMH, Pb, Li-ion) in that the active species are dissolved in a supporting electrolyte, which contains a salt to adjust pH (in case of aqueous solutions) and increase conductivity and solubility [27]. These reactions occur at the solid electrodes contained in the reactor and involve an electrochemical process, that is the exchange of at least one electron. The electrodes are highly-porous matrices made of graphite fibers, which offer a high developed surface area to promote the electron-exchange inside the reactor [28]. The electrodes being chemically inert during the process, RFBs feature much longer durability ($> 10,000$ cycles) than conventional batteries (Fig. 1.3), for which the internal structure is reactive. These electrochemical reactions occur at a redox potential E^0 [V] specific to the active species. The solution with the lowest potential is called anolyte (represented by the redox couple A^{3+}/A^{2+} in Fig. 1.4a), the other is the catholyte (corresponding to C^{2+}/C^{3+} in the schematic). More details on the chemical processes are given in subsection 1.3.1. During the charge of the battery, the catholyte undergoes an oxidation while a reduction occurs in the anolyte. The reverse happens in discharge. The electrolytes recirculate in each half-cell to supply the porous electrodes with reacting species. The compartments of each cell are separated by an ion-exchange membrane, as depicted in Fig. 1.4b. The latter constitutes a physical barrier for the A and C active molecules, while it is permeable to supporting salt ions of the electrolyte. The most common separators exchange cations (H^+ , Na^+ , Li^+ , depending on the electrolyte composition). This flux of charges through the membrane compensates the electron exchange at the interface of the electrode to ensure the electroneutrality of the medium. The electrons released or consumed by the chemical process pass through the electrode fibers and are then collected by external conductive plates to be sent to the external circuit, as represented in Fig. 1.4b. These collecting plates are usually made of carbon-polymer composite.

Several transfers of species happen in the membrane. Because of concentration gradients between the two half-cells, an osmotic movement of solvent occurs inside the cell. Moreover, when cations cross the membrane during operation, they tend to drag water molecules along [29, 30]. One of the electrolytes is concentrated, and the active molecules can reach their limit of solubility, involving precipitation. Even worse, since a membrane is never 100% selective, some active species can cross it [31]; it is called electrolyte cross-contamination. These electrolyte precipitation and mixing may lead to a capacity loss that is not recoverable (unless if we use the same species for both half-cells, like in vanadium batteries). The active species cross-over also contributes to a self-discharge of the battery.

The operational cell voltage is necessarily below 2V for the aqueous types of RFB. To deliver an interesting power, unit cells are piled up together and form a battery stack, as in Fig. 1.4a. In the common stack configuration, the cells are electrically connected in series and are fed by the hydraulic circuit in parallel, as illustrated in Fig. 1.5. The neighboring cells share the same collecting plate, thus called bipolar plates. They guarantee the transport of electrons between the cells.

Depending on the power rating of the system, several stacks can in turn be connected [32], either in parallel or in cascade. The latter mode entails a progressive conversion of the electrolyte

through the successive reactors; this is needed if the discharged and charged electrolyte cannot be remixed, and was the strategy of the former company Enervault for the iron-chromium chemistry [33].

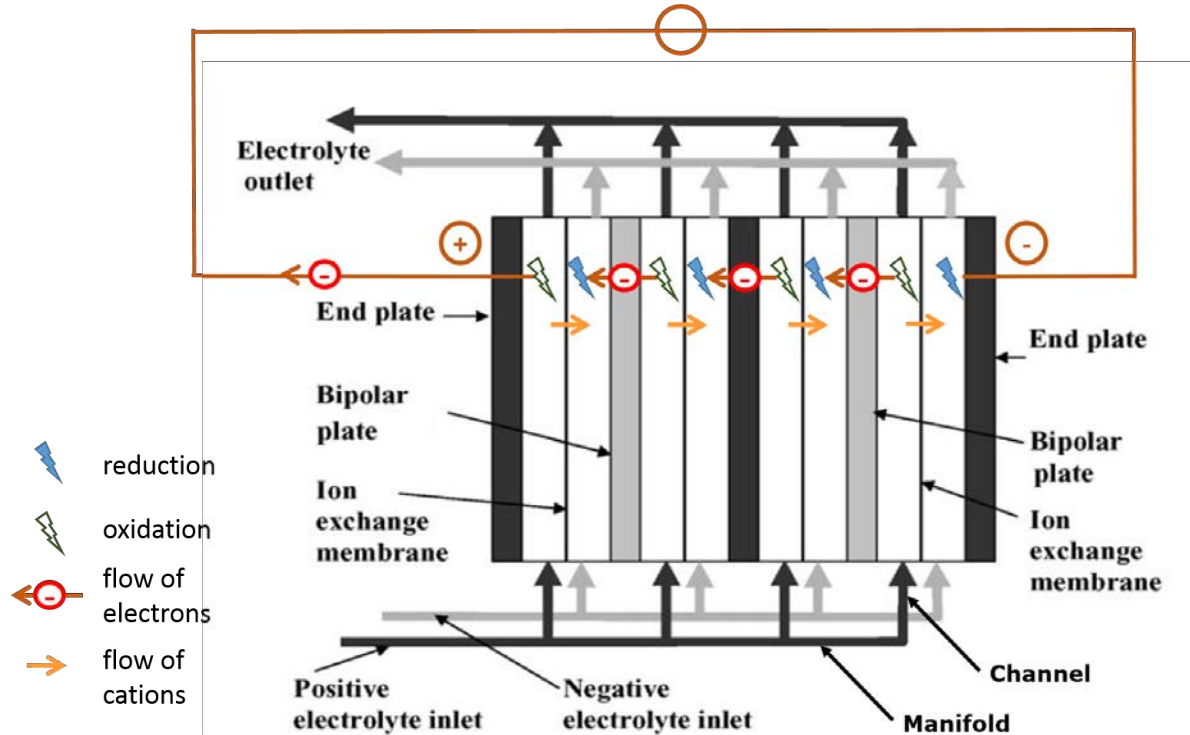


Figure 1.5: Four-cell stack and its hydraulic and electric circuit, adapted from [25] and [34]. The flow of electrons is represented during charge.

The engineering aspects of the stack are multiple.

- At the electrodes, the flow configuration can follow two main strategies to ensure an even reaction rate through the active surface [35]: the *flow-through* (FT) structure, where the electrolyte flow is directly forced through a thick porous electrode. This ensures a very good mass transport of the reactants inside the pores and towards the reactional sites, but induces substantial pressure drops particularly for high surface areas [36]. The *flow-by* configuration, inspired by the fuel cell technology, combines the use of thin carbon paper electrodes with flow field designs usually machined on the collecting plate. The pressure losses are substantially reduced but the convection inside the porous volume is poor with a non-optimized pattern, and because carbon paper has a lower porosity than felt. Interdigitated flow field is most promising to replace the conventional FT configuration [36], but its application into the industrial stack remains to be solved as it complicates the manufacturing process and adds on cost for machining the bipolar plates [37]. For both flow configurations, compression, thickness and internal structure are the parameters that must guide the choice of the electrode material.
- The flow of electrolyte must be accurately distributed among the stacks and then the unit cells to maintain uniform current and potential distribution among the cells. The reactor assembly entails the connection of the cells through the manifold and channels as in Fig. 1.5. Because the electrolyte is conductive and there is a potential gradient

between the successive cells, a leakage of current occurs through this low resistance path that represents an efficiency loss for the system. Equivalent-circuit models have been developed to investigate this shunt current phenomenon [38] and optimize accordingly the size of the stack and the internal manifolds arrangement [39, 40]. Tortuous flow distributors, long electrolyte paths and reasonably low number of stacked cells are the strategies used to circumvent shunt current losses and keep them to a reasonable amount $<1\%$ of the total stack current [32]. The increase of the hydraulic connection between the cell negatively impacts the pressure drops through the reactor and for that reason an optimum should be found.

- ➔ Side reactions can prevail in some parts of the electrode if the flow distribution is not uniform. It yields irreversible capacity loss and/or safety hazard due to gassing (due to water electrolysis). Shunt currents also trigger local parasitic reactions including corrosion of the bipolar plates which hastens the system failure [41].
- ➔ The flow of electrolyte through the long channels of the stack and the porous electrodes has an energetic cost for the system. Pump consumption must be minimized without hampering the uniform and sufficient reactant delivery inside the reactor. Pump operation is an ancillary loss that does not exist in the competing battery technologies. On the other hand, Lithium-ion suffers from substantial air-conditioning losses since its thermal management is much more critical than for RFB [42].

Gandomi et al. elaborated a comprehensive diagram of the RFB system [27], divided in 3 categories and reproduced in Fig. 1.6. It materializes the contribution of each component on the sources of inefficiencies, which are in turn related to the relevant performance metrics. In each component, the design parameters are listed with the same color coding as the numbers connecting the components to the groups of losses.

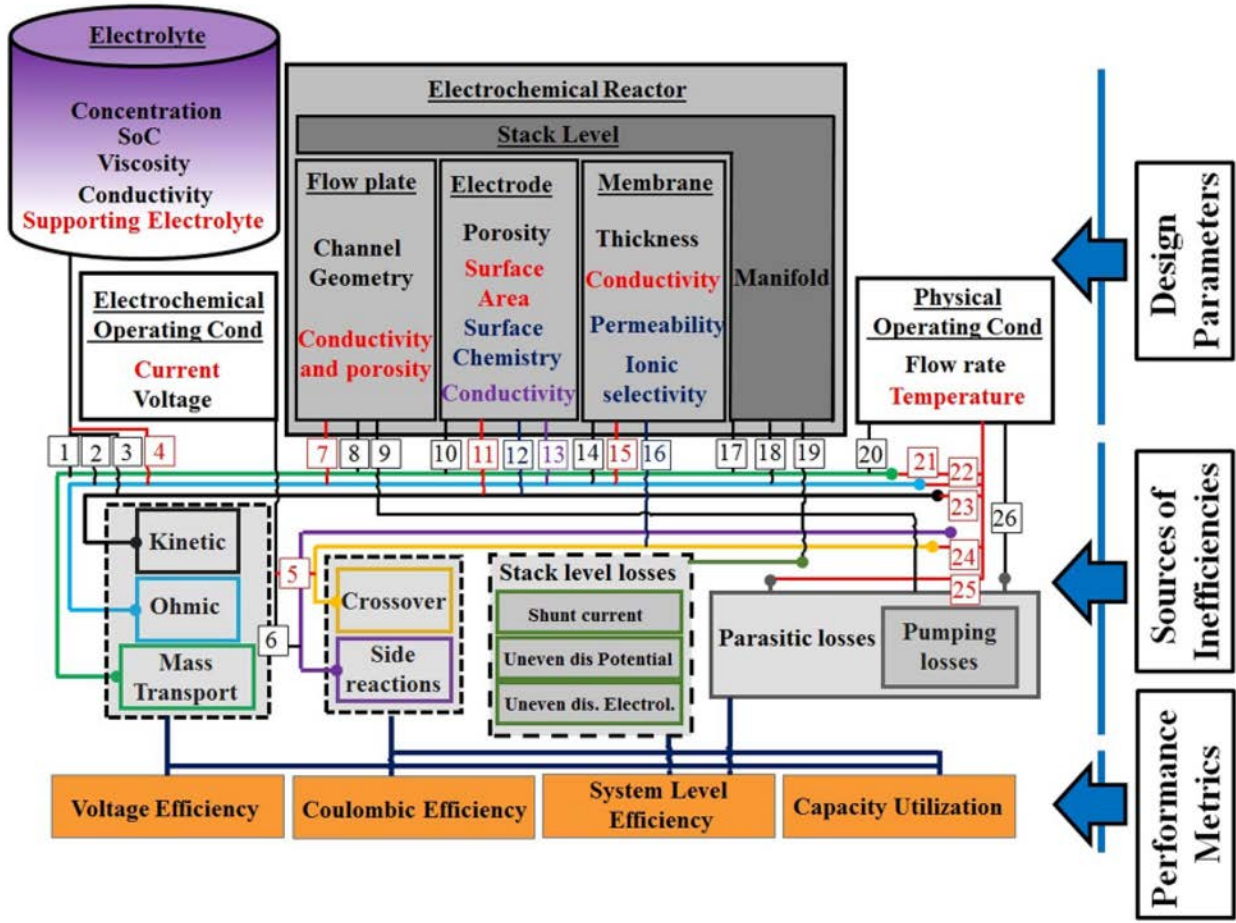


Figure 1.6: Technological diagram of the RFB system with design parameters and their interplay on the loss mechanisms and the performance metrics, adopted from [27]

Fig. 1.6 lists all the notions necessary to get a full comprehension of the RFB technology. Some of them have been mentioned above, and the others will be detailed in the following parts when necessary. The performance metrics of the third category are defined in Chap. 2. For Kemiwatt's RFB technology, the characteristics of the components are either given in Chap. 2 or experimentally determined in Chap. 3 and Chap. 4. Several loss mechanisms are assessed in Chap. 5. The influence of the operating conditions are also examined through the parameter study of Chap. 5. Ultimately, the stack-level related challenges are broached in Chap. 6.

1.2.2. Existing chemistries

Many types of RFB have been developed, each characterized by the couple of electrolytes being combined.

The earliest technology is the Iron-Chromium [13]. After NASA's initial research, the Mitsui group in Japan produced Fe-Cr systems from the mid 1980s. But this cell presents low energy density and slow reaction on the Cr side. Moreover, the Cr redox potential is close to the parasitic hydrogen evolution [16].

The most famous technology is the Vanadium flow battery, noted VFB. Its first patented

demonstration was developed by Maria Skyllas-Kazacos at the University of New South Wales in Australia in 1986 [4]. It takes advantage of the ability of the vanadium ion to exist in acidic solutions under four different oxidation states. As such a unique electrolyte constitutes both half-cells. As such, the issue of vanadium cross-over and water transfer through the membrane can be addressed by a regular remixing of the two tanks to recover the battery capacity [29]. Current VFB systems operate with 1.6 to 1.8 M electrolyte concentration. Recent progress has achieved the stabilization of 3 M vanadium solution by use of additives, and the system could be cycled for several days with no precipitation [43]. The VFB technology is being developed worldwide by companies already at the industrial level, such as UET (USA), Sumitomo (Japan), Gildemeister (Germany), RedT (UK) or Rongke Power (China). A few demonstration projects have already been undertaken, and China is underway in operating the world’s largest battery facility with Rongke Power technology (200 MW/800 MW h [44]). The current record is held by Tesla’s Li-ion battery connected to the grid of South Australia (100 MW/129 MW h [45]).

However, vanadium is a heavy-metal with high and very volatile price [46]: the vanadium-based electrolyte cost is about \$ 80 kWh⁻¹ which added to the cost of the rest of the system makes it incompatible with the target in section 1.1. Furthermore, the acidic medium causes technical challenges due to corrosion, along with environmental threat in case of leakage [32]. These downsides discredit the claimed benefits of the RFB, pretending to be a low-cost and sustainable alternative for energy storage [46]. In the last years, scientists have focused on using non-metallic and cheap molecules as electroactive species. The solvent can be aqueous or non-aqueous. Complex organic structures can also be designed to get a symmetric configuration of the RFB (as for the vanadium). These options are classified in Table 1.1 alongside their related pros and cons [47]. Dmello et al. [48] highlighted with a techno-economic model how to design an electrolyte that can advance the market penetration of the RFB technology. They constructed design maps (correlating the redox potential, the active molecular weight, the resistance in the RFB cell, and the raw material cost) to guide the material selection for viable RFB system.

Darling et al. established the feasibility of low-cost RFB systems, either by the aqueous or non-aqueous strategy [49]. They forecast substantial cost decrease for the additional contributions (labor, overhead, margin) and the balance of plant (hydraulic circuit, electronic inverter etc.); reaching 20 and 45 \$ kWh⁻¹ respectively. This involves a cost of 70 \$ kWh⁻¹ for the system itself (reactor + electrolyte), to reach the objective of 150 \$ kWh⁻¹ for the total ESS plant.

Table 1.1: Types of flow-battery electrolytes

| Electrolyte | pros | cons | examples |
|------------------------|---|--|------------------------|
| Metallic | solubility stability | price and sourcing environmental impact | vanadium [50] |
| Aqueous organic | low cost tunability | stability solubility | AQS/BQDS [51] |
| All-organic | low environmental impact no voltage window limit solubility | resistive solution low power density | Quinoxalines [52] |
| Symmetric | no cross-over issue use of low-cost separator | rare complex structure | Nitronyl nitroxide[53] |

This table does not index the so-called "hybrid" flow battery systems, involving at least one non-soluble reactant or product. The electrochemical reactions can lead to a metal deposition on the electrode, it is the case of the batteries using zinc elements, like the Zn-Fe battery developed by ViZn Energy Systems, Inc. [54] or the technology of Zn-Br developed by Redflow or EnSync [55, 56]. One electrolyte can also be a gas (called half flow-cells) or involve a gaseous species, as in the HBr/Br₂-H₂ technology, scaled up by Elestor [57]. These systems face additional areas of complexity and will not be referred to further.

1.2.3. Kemiwatt's industrial challenge and opportunity

In this context, Kemiwatt has bet on the development of aqueous alkaline electrolytes dissolving organic/organometallic species to take up the challenge of low-cost, sustainable and reliable medium to large-scale energy storage systems [58].

Organic molecules compatible with aqueous electrolytes and suitable for RFB applications can be classified in two categories: quinone molecules or radical and polymer radicals. These fully organic molecules can be combined with each other to build a complete OFB [51, 59–61]. They can also be paired with organometallic material such as ferrocyanide or ferrocene [62–66] or even inorganic couples on the other half-cell as HBr [67].

The French RFB startup was created in August 2014, from an innovative idea matured over the last decade in the MaCSE lab (Condensed Matter and Electroactive Systems), located in Rennes (France). The team of Kemiwatt is composed of ten engineers and doctors and works at transferring the technology from the lab and scaling the system up towards tens of kilowatt power supply.

The company is now competing with others in the race to develop organic flow batteries (OFB) but has been the first to reach the proof-of-concept step by building a 20 kW industrial demonstrator in 2017 (Fig. 1.7).



Figure 1.7: Kemiwatt's prototype and 20 kW demonstrator

The startup JenaBatteries (Germany) focuses on the radical type, based on the work of Janoschka et al. developed at Jena University [68, 69]. Their technology combines TEMPO and viologen active species. The electrolytes features an energy density of 8 Wh L⁻¹ and high viscosity compared to pure water 17 mPa s. The polymerization of the active species enable the use of size-exclusion separators, much cheaper and less resistive than ion-exchange membranes.

Green Energy storage (Italy) licensed the quinone-bromide technology from Harvard University [70]. Lockheed Martin Corporation (USA) also diversified in ESS, and is developing metal ligand coordination compounds for use in RFB [71].

CMBlu is the most recent company to target the industrialization of aqueous OFB, by leveraging waste products of the paper industry [72]. Their electrolytes are based on lignin molecules, as presented in the paper of Rebis et al. [73].

Leung et al. [47] comprehensively reviews all the organic molecules that have been explored so far in the field. Wedege et. al experimentally investigated the potential of 33 compounds, mostly quinone derivatives, for their use in RFB [19]. Computational screening approach has also been developed to help identifying the best performing molecules, by forecasting their redox potential and solubility [74].

In summary, organic molecules promise low cost (\$ 10-20 kWh⁻¹), sustainability and high-tunability. The downsides are a relatively low solubility 5-10 W h L⁻¹ and an important chemical reactivity that can yield capacity losses over time. Kemiwatt develops its negative electrolyte by tuning anthraquinones molecules to achieve good solubility, interesting redox potential and sufficient stability to achieve long cycle life. An Organic-Inorganic flow battery will be studied in this PhD work, based on some of the molecules currently investigated at Kemiwatt.

In a whole, RFB presents key assets to outcompete the most developed Li-ion technology for stationary applications and above 4 h of storage [25]. It can also be cycled trough the full capacity (high depth of discharge), whereas a limit is recommended for Li-ion. It has a longer assumed cycle life, corresponding to 15-20 years. The system is stand-alone with low maintenance required. It is safer because there is no risk of thermal runaway, which is one of the biggest challenges for Lithium-ion batteries along with the air cooling required above an ambient temperature of 27 °C. Finally, the organic version of RFB investigated by Kemiwatt is much more sustainable than metal-based electrolytes and has the potential to meet the target cost. The chemicals are also biodegradable, which promises a non-hazardous disposal of the system.

In the meantime, several techno-economic hurdles remain before the deep market penetration of the RFBs. The technology development is still at early stage, with only a few demonstrations available today. Projected lifetime could not be proved yet, and the material durability should be systematically tested with accelerated degradation tests, such as the one proposed by Pezeshki et al. [75]. The pump consumption represents a loss to minimize so that the system efficiency is compelling. The stack and system design must also be developed to guarantee low shunt current losses, easy manufacturing and rapid plant installation. Ultimately, the development of the organic molecules still needs investigation to master their behavior in flow conditions, verify their stability, and secure the raw material supply at a competitive cost.

1.3. General understanding of the Redox Flow Battery

The present section gives insights on the fundamentals governing the RFB system, and reviews the general understanding that has been built over the years by the scientific community, with a particular interest on the experimental/ model coupled techniques, and the instrumentation of diagnostic cells.

1.3.1. Fundamentals

The Redox-Flow Battery, such as any electrochemical reactor, relies on the reversible conversion of electrical energy into chemical energy.

a) Half-cell reaction

On each half-cell of the RFB, this transformation is permitted by the presence of a reactive species solubilized in the electrolyte, which can be reduced or oxidized at the contact of the conductive electrode. The general expression of the reaction is:



The oxidant Ox and reducer Red species form the redox couple that is characterized by its specific electrochemical properties:

- ➔ the number of electrons z it can exchange
- ➔ its redox potential E^0 [V], defined in standard conditions: $C=1\text{M}$, $T=298.15\text{ K}$
- ➔ the reaction rate constant k_0 and the apparent charge-transfer coefficient α . The second relates which reaction preferably occurs at a given potential [76].

These attributes will be determined by electrochemical analysis in Chap. 3, for the redox couples used in this PhD.

The solid electrode immersed in the electrolyte takes a potential E defined as the difference between the metal and solution phases potentials:

$$E = \phi_m - \phi_s \quad (1.3)$$

The potential is given versus a reference electrode; the one used in this PhD is the Ag/AgCl electrode. The correct writing should be E_{ref} but is omitting for simplicity.

The electrode is at equilibrium when both oxidized and reduced forms are present and the reduction and oxidation reactions are balanced: there is no net production of species. In this case, E_{eq} is defined by the bulk concentrations according to the Nernst equation:

$$E_{\text{eq}} = E^{0'} + \frac{RT}{zF} \ln \frac{C_o}{C_r} \quad (1.4)$$

The formal potential $E^{0'}$ has been conveniently introduced in practice to represent the experimental conditions of the system that deviate from the standards [77]. It incorporates some activity coefficients added to E^0 . During this PhD, the formal potential (determined in section 3.1) is used in place of the standard definition.

At the electrode surface, the forward and backward reaction rates are considered first order:

$$v_{ox} = K_{ox} C_r \quad (1.5)$$

$$v_{red} = K_{red} C_o \quad (1.6)$$

$$\text{with } K_{ox} = k_0 \exp\left(\frac{\alpha z F}{RT}(E - E^{0'})\right) \quad (1.7)$$

$$K_{red} = k_0 \exp\left(-\frac{(1 - \alpha) z F}{RT}(E - E^{0'})\right) \quad (1.8)$$

$K_{ox,red}$ are the heterogeneous rate constants of the forward and backward reactions (or oxidation and reduction). They are qualified as heterogeneous since they involve two distinct phases (solid and liquid), and directly depend on the electrode potential E .

α is defined for the oxidation reaction, considering that $\alpha = \alpha_{ox} = 1 - \alpha_{red}$.

k_0 is the standard rate constant of the reaction in m s^{-1} (that is at the formal potential $E^{0'}$). It obeys an Arrhenius dependence on temperature and on the activation energy of the reaction (E_a , J mol^{-1}):

$$k_0 = A \exp\left(\frac{-E_a}{RT}\right) \quad (1.9)$$

A is the Arrhenius constant.

The net reaction rate at the electrode is conventionally defined by the difference between the partial rates of the oxidation and reduction:

$$v^{net} = v_{ox} - v_{red} \quad (1.10)$$

This global reaction rate induces a movement of electrons related to the so-called faradaic current density j_F (A m^{-2}). Both are related by Faraday's law:

$$j_F = -zFv^{net} \quad (1.11)$$

At equilibrium, no net current passes through the electrode ($j_F = 0$) because the partial reaction rates are equal; oxidation and reduction create the exact opposite flux of charges, called the exchange current density (j_0 , A m^{-2}):

$$j_0 = zFk_0(C_o)^\alpha(C_r)^{1-\alpha} \quad [\text{A m}^{-2}] \quad (1.12)$$

j_0 depends on the concentration of the two redox species, the temperature but also the nature of the interface electrode/electrolyte through k_0 . The more the forward and backward reactions occur rapidly, the higher the exchange current density of the system is.

A net current passes through the electrode surface if one direction of the electrochemical reaction in (1.2) dominates. This is only possible when the electrode is connected to an external circuit so that the electrons can be transported towards or outside the half-cell. The electrode is deviated from its equilibrium potential E_{eq} by an algebraic overpotential, η whose sign is dictated by the net direction (positive in oxidation and negative in reduction):

$$E = E_{eq} + \eta \quad (1.13)$$

Eqs. (1.7) and (3.4) can be combined with the Nernst equation (1.4) and Eq.(1.13), before being injected into Eqs. (1.5) and (1.6). Finally, it comes that the faradaic current (1.11)

has an exponential dependence on the driving force for the surface reaction, embodied by the overpotential η . This is known as the Butler-Volmer (BV) equation:

$$j_F = j_0 \left[\frac{C_r^s}{C_r} \exp\left(\frac{\alpha z F}{RT} \eta\right) - \frac{C_o^s}{C_o} \exp\left(\frac{-(1-\alpha) z F}{RT} \eta\right) \right] \quad (1.14)$$

$C_{r,o}^s$ refers to the concentrations of the active species at the solid/liquid interface (in opposition to C defined in the bulk electrolyte). The ratio RT/zF is called Tafel slope and noted b in the following.

In practice, the concentrations of the oxidant and reducer species vary during cycling. The concentrations are expressed according to the State Of Charge of the electrolyte, noted SOC. It depicts the ratio between the species created during charge (depending on the electrolyte) and the total concentration of active species. The preceding equations expressed with SOC are developed in [section 4.1](#).

Eq.(1.14) can be simplified in two cases:

- ➔ At high overpotential, one direction of the reaction (1.2) prevails (the oxidation if $\eta \gg 0$ and the reduction for $\eta \ll 0$). One term inside the bracket of (1.14) is negligible, and BV reduces in the so-called Tafel equations. They are detailed in [Eqs. \(3.5\) and \(3.6\)](#) since they will be useful for the electrochemical analysis of [Chap. 3](#).
- ➔ At low overpotential (when $\frac{\alpha z F}{RT} \eta \ll 1$), the BV equation can be linearized (see (4.11)). This condition is verified during operation of the RFB cell and therefore the simplification is utilized in [Chap. 4](#).

b) Full cell operation

At open-circuit, the cell voltage measured between the positive and negative half-cells (containing respectively the catholyte and the anolyte) is the difference between their equilibrium potentials:

$$V_{OC} = E_{eq+} - E_{eq-} \quad (1.15)$$

V_{OC} depends on the concentration ratio of the two redox couples, according to (1.4). The subscripts c and a identify each electrolyte:

$$V_{OC} = E_{cell}^0 + \frac{RT}{z_c F} \ln\left(\frac{C_o}{C_r}\right)_c - \frac{RT}{z_a F} \ln\left(\frac{C_o}{C_r}\right)_a \quad [V] \quad (1.16)$$

The formal potential of the cell is defined by $E_{cell}^0 = E_+^{0'} - E_-^{0'}$. Consequently, one should combine redox couples with standard potentials as far as possible to get the highest RFB cell voltage.

When both electrodes are linked to an external circuit (as sketched in [Fig. 1.4b](#)), the reactional process described above happens simultaneously on the two half-cells of the RFB. The flow of current and the polarization of the two electrodes induces losses on the cell voltage U , which can be decomposed as [\[32\]](#):

$$U = V_{OC} + \eta_+ - \eta_- + \sum IR \quad (1.17)$$

The last three terms are algebraic and their sign depend on the direction of polarization (that is the sign of the current). The overpotential of each electrode contains activation and concentration overpotentials:

$$\eta = \eta_{act} + \eta_{conc} \quad (1.18)$$

A popular characterization technique of the electrochemical system allows the visualization of the contributions of (1.17). The polarization curve (PC) relates the battery voltage behavior according to the current drawn or applied to the battery. The typical PC shape in the case of a discharge is displayed in Fig. 1.8.

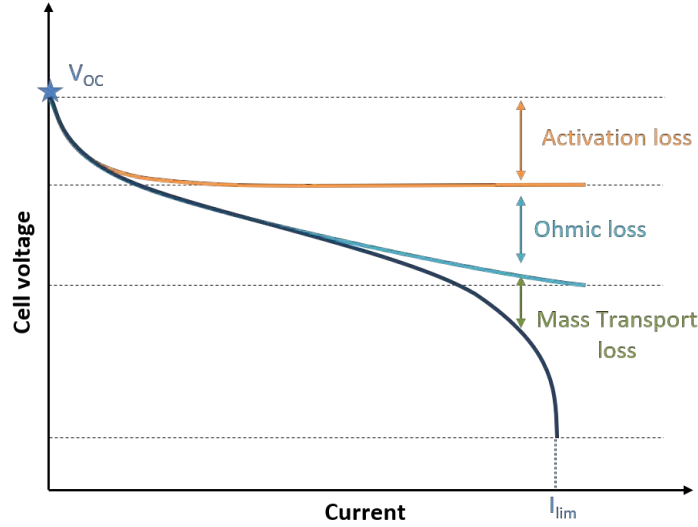


Figure 1.8: Discharging polarization curve of an electrochemical process with the three overpotential regions and their sources

When current is drawn from the device, its voltage drops from the value at equilibrium V_{OC} . Three distinct regions appear:

- ➔ If the kinetics of the reaction is sluggish, it generates a steep drop at low current identified as **Activation loss**. It corresponds to the activation overpotential η_{act} . It can be different on both electrodes, and the outcome is visible on the PC of the full cell.
- ➔ The internal resistance of the system dominates at intermediate currents, resulting in a linear **Ohmic loss** profile. It contains the ionic (membrane, electrolyte) and electronic (electrode, collecting plate) bulk resistances of the materials, alongside the contact resistances between each layer of the cell.
- ➔ When sufficiently high current is applied, a third overpotential region is caused by the reactant starvation at the reactive sites and is also called **Mass transport loss**. The current held by the battery can no longer increase; it eventually reaches a limiting threshold. The term η_{conc} embodies this process. Concentration overpotential can be reflected by a Nernst-like expression, between the bulk and interface concentration [78].

The linear section of the polarization curve is usually fitted to extract the cell resistance, noted R_{PC} . As predicated by Aaron et al. [79] and further evidenced in this PhD work (subsection 5.1.2), this resistance encompasses the three loss mechanisms described above. These losses all contribute to reducing the battery performance. As displayed in Fig. 1.6,

they are interrelated to many design parameters of the RFB. Building the best performing system signifies using highly conductive materials, active species with fast reaction rate, and maximizing the supply of electrolyte to the electrode surface.

1.3.2. Modeling

Lots of research papers about RFB are already available, but many of them deal with the vanadium technology, and they are based on modeling more than experiments [1, 80]. modeling approaches use assumptions that are not always verified. Moreover, industrial development has prevailed over laboratory research at this point, because the technology is rather easy to transfer to working systems. But to optimize RFBs and solve the remaining roadblocks to mass production, we still require scientific work for fundamental understanding.

The conventional models rely on the universal conservation laws of charge, mass and momentum combined with a model for electrochemical reaction kinetics [80]. Particularly, the processes occurring inside the porous electrode are almost always described by the approach of Newman and Tobias [5].

Shah et al. [81] proposed one of the first comprehensive models of VFB in dynamic conditions, to investigate the effects of active species concentration and electrolyte flow rate. They used an already existing model for the transport processes in the membrane that was initially developed for PEMFC [82]. By comparing its results to experimental data, the model exhibited accurate predictions under idealized scenarios. You et al. [83] proposed a simplified version of Shah's model, by assuming the following: the problem is 2D (no variation along the cell width) and stationary, the physical properties are homogeneous and isotropic, the dilute-solution case is assumed even if the technology comes with highly-concentrated electrolytes, the system is isothermal, side reactions and water mobility through the membrane are not taken into account. They were able to simulate the influence of the applied current density and the compression rate of the electrode on the performance of the cell. More recently, Gandomi et al. published a finer model describing the variables (species concentrations, flux and potentials) in the through-plane direction of the electrode [84].

Some studies extended to a three-dimensional and nonisothermal problem [85]. The heat generation by different mechanisms, such as irreversible and reversible reactions and joule heating arising from the solid and ionic resistances, were focused on.

Novel designs of the redox-flow batteries were investigated numerically to improve the efficiency along the flow and adapt the geometry with the composition change between the inlet and outlet of the reactor [86].

Models are also convenient tools for determining key operating or intrinsic parameters of the RFB system, difficult to measure or assess in-situ. To that end, the computation must be related to experimental data, obtained in specific cell configurations.

1.3.3. Analytical platforms

The literature dealing with experimental approaches is less rich than for computational studies, however some insightful set-ups allow a finer characterization of these batteries.

Due to the complexity of the flow battery systems, simplified analytical tools are required to

decouple the phenomena. Two major analytical configurations exist, using only one electrolyte and inherently ruling out cross-over related issues. They are sketched in Fig. 1.9. They enable the investigation of electrode-electrolyte combinations in representative flowing conditions and are thus more meaningful than bulk electrolysis methods, as proved in [87].

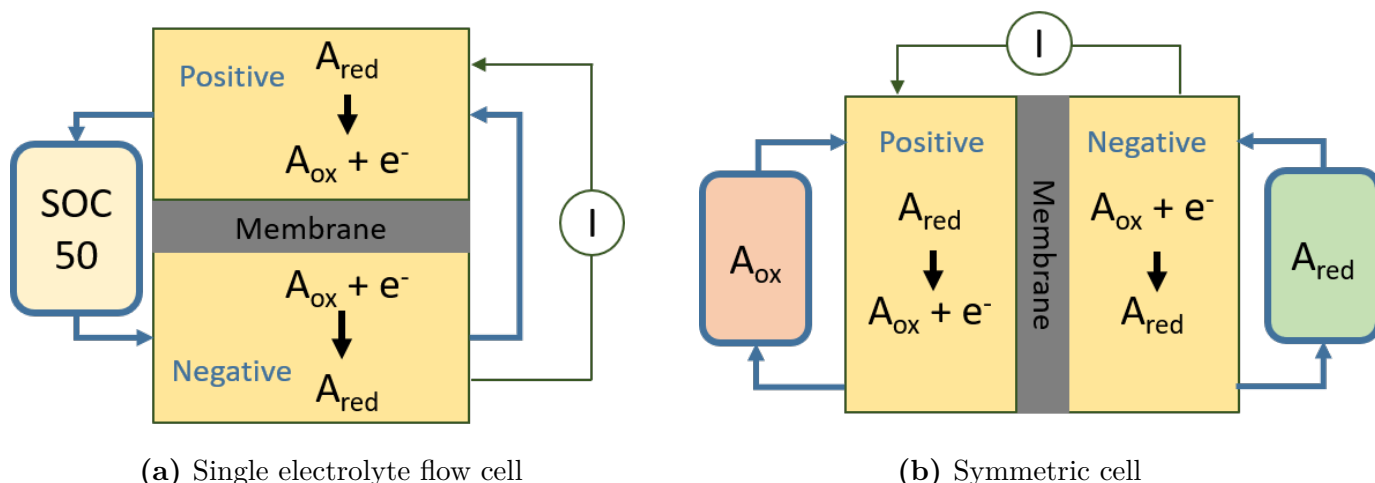


Figure 1.9: Schematics of two possible cell designs to investigate one electrolyte in a flow set-up

A *single-electrolyte flow cell* where both electrodes are fed by a common reservoir (Fig. 1.9a), is a good analytical tool to study one electrolyte in a flowing configuration at constant State Of Charge (SOC) [88–90]. The cell can be operated over a wide range of current and flow rates, while being maintained at steady-state. A *symmetric flow cell* makes the study more advanced: with separate tanks of a same electrolyte, the cell can be cycled [91, 92]. The symmetric configuration secures the electrolyte environment by removing the possibility of cross-over of the other electrolyte, and by studying the electrolyte stability on the same porous material as in the full battery [93].

The benefits and limits of these configurations made of one electrolyte are compared to full cell platforms in Table 1.2.

Aside from the standard layout (2 tanks and recirculation of the electrolyte), The 4-tank cell allows the study of the full cell with a constant concentration inlet during a single pass of the electrolyte [27]. This is particularly interesting for characterization protocols, but requires sufficiently high volumes of electrolytes. A step-by-step cycle can also be performed by changing the flow direction each time the tanks are empty on one side.

Table 1.2: Analytical cell configurations

| Configuration | Benefits | Limits |
|--------------------------------|--|---|
| Single-electrolyte cell | Steady tests (at constant SOC) Deconvolution of loss mechanisms | Change of SOC must be done in another cell |
| Symmetric cell | Cycling in flow configuration Performance and stability of one redox couple | Voltage window must be well-defined |
| Standard full cell | Cycling in practical conditions | Convolution of the two electrolytes performance Cross-over / water-osmosis |
| 4-tank full cell | Tests at constant SOC Step-by-step cycles | Large volumes of electrolytes |

Table 1.2 reviews the most common analytical configurations but other less frequent strategies can be described in the literature. Even for stack-level studies, the test platform can be adapted to improve the investigation. For instance, monitoring V_{OC} of an open-circuit cell connected in parallel to the working one is very convenient to follow the electrolytes SOC and the charge/discharge progress [94].

The above-described diagnostic platforms must be combined with characterization techniques, namely the polarization curves (PC) and the electrochemical impedance spectroscopy (EIS) [27]. These protocols will be detailed in Chap. 2. Darling and Perry were one of the first to make use of a symmetric cell in RFB. The PC characteristics proved that both electrolytes did not yield the same cell resistance [88]. Pezeshki et al. used the symmetric configuration in VFB to decouple the charge-transfer, ohmic and mass-transport overpotentials using EIS [95]. They also investigated several cell architectures by this method. With a similar methodology, Zago and Casalegno deconvoluted the mass-transport mechanisms into the diffusion and the convection contributions [96].

Goulet et al. assessed the capacity fade mechanisms of a single electrolyte in a symmetric cell, but with a capacity-limiting side (less volume of electrolyte on one half-cell) [97]. For several active materials (anthraquinones, viologen), they showed that the capacity decay was dominated by a chemical decomposition rather than an electrochemical process, since it was independent of the number of cycles.

In their work, Milshtein et al. combined the use of the single-electrolyte and symmetric configurations to validate the suitability of a redox couple in a non-aqueous RFB [93].

Several researchers have built such cells to identify the limiting electrolyte in terms of coulombic efficiency and capacity retention [91, 92] Luo and coworkers are the first to evaluate long-term cycling capability by means of a symmetric cell [92]. They unravelled the influence of the pH on the stability of the iron-cyanide redox pair $[\text{Fe}(\text{CN})_6]^{3-} / [\text{Fe}(\text{CN})_6]^{4-}$.

1.3.4. Internal cell instrumentation

The effort is also increasingly turned towards in-situ experiments and localized measurements, so that the results directly translate the real-system performance. Moreover local knowledge of the cell performance can be used for fine model validation and insightful optimization of industrial systems.

In the field of PEMFC, scientists have already investigated local phenomena. At the LEMTA laboratory, the team [98, 99] has developed a segmented fuel cell with local reference electrodes, in order to follow the current density and potential evolution inside the cell. To do so, they use a shunt resistor network and local reversible hydrogen electrode references. These works have highlighted some heterogeneities during fuel cell operation and related local ageing effects.

Attempts to observe local behavior figure among the redox flow battery literature, but advanced set-ups such as the one cited above do not exist yet. Hsieh and coworkers [100] are the first to have measured local currents by comparing two designs of segmentation: one with segments in the current collector behind the graphite end plate and one with the graphite end plate segmented itself. They found that segmenting the end plate was necessary to avoid lateral current spread in it but the poor contact resistances between the divided plate and the connectors worsened the battery performance. Clement et al. [101] used a printed circuit board (PCB) placed behind a divided flow plate. Their set-up demands a perfect mirroring between the PCB and the divided flow plate to get correct in-plane current. The tiny segments machined in the graphite composite and only maintained by a thermoset resin can jeopardize a uniform compression and results in high contact resistances. However, the set-up proved its usefulness for the system study. They demonstrated that the distributed currents reflected mass transport within the cell; the locally-resolved current diagnostics is useful to assess electrode materials or optimize the operating conditions. To get relevant and easy-to-compare data, the characterization were performed at the mass-transport limiting point.

Segmentation of the end plate was also used to measure local potential and V_{OC} measurements gave insight on the local SOC. The results were used to observe the electrode compression effect on the flow distribution of the electrolyte [102].

Becker et al. [103] used solid-phase potential probes made of carbon fibers to measure the local felt resistance at several points of the active area. They deduced the in-plane localized current densities during polarization curves. Another research group employed potential-probes between several layers of carbon paper to evaluate the through-plane current distribution inside the cell. They could deconvolute the resistances comprised in the PC for each half-cell [104]. Gandomi et al. could validated their model accuracy with a similar set of potential probes through the thickness of the electrode [84].

Another crucial point to study cell operation is to identify the losses in the system. The contribution of each component can be determined by in-situ electrochemical techniques, such as electrochemical impedance spectroscopy (EIS), combined with a reference electrode to decouple the two half-cell processes [89, 105–107]. Thanks to a dynamic hydrogen reference electrode and a set-up where the state of charge of the cell is kept constant, Sun et al. [108] showed that in a vanadium redox flow battery the negative electrode is limiting in discharge. Later on [89], they built a symmetric cell: anolyte at a state of charge of 50% was flowed on both sides. The experiment revealed how the overall cell voltage losses can be split into distinct

mechanisms: charge-transfer, mass-transfer and resistive overvoltages.

Detailed literature data are given along the PhD thesis where necessary.

1.4. Methodology of the PhD study

The PhD research objective is to meet the need of KEMIWATT to build a thorough knowledge base of its system and refine the experimental methods by developing reliable analytical tools. The results seek to help with determining the optimal design and operating conditions.

The starting point of the PhD work is the literature about redox flow batteries presented above, coupled with the expertise of the partner laboratory LEMTA in instrumentation of electrochemical systems.

The PhD study is divided into 3 main axes of research:

- * Development of specific experimental platforms to get an insight into the behavior of the system. Separate analysis (Chap. 3) and then half-cell characterization (by means of a symmetric cell layout, Chap. 4) permitted the deconvolution of the materials influence on the battery. A porous electrode model was developed and then combined so as to estimate key attributes of the system from the experimental data (Chap. 4).
- * Development of an instrumented test bench for full cell experiments to investigate the local phenomena and get a spatial resolution of the current (Chap. 2). After validation, this tool was used to perform a fine parameter study by varying alternatively the current, the flow rate and the temperature. The different tests were correlated to build operational maps adaptable to real-stack conditions (Chap. 5).
- * Investigation of industrial issues and particularly hydraulic-related aspects (Chap. 6). A reduced clear flow cell enabled the flow visualization through a typical cell stack design. A hydrodynamic model completed the study.

These three approaches are complementary and interrelated in the entire work presented in the following pages. All the diagnostics tools were developed within the framework of the PhD, and when possible, were subsequently integrated to the standard R&D procedures at the company KEMIWATT.

2

DIAGNOSTIC TOOLS

Contents

| | | |
|------------|--|-----------|
| 2.1 | Materials and pretreatments | 24 |
| 2.1.1 | Electrolytes | 24 |
| 2.1.2 | Standard test cell | 26 |
| 2.2 | Battery tests | 29 |
| 2.2.1 | Assembly | 29 |
| 2.2.2 | Cycling | 29 |
| 2.2.3 | Polarization curves | 30 |
| 2.2.4 | Electrochemical impedance spectroscopy | 33 |
| 2.3 | Symmetric cell | 35 |
| 2.3.1 | Principle | 35 |
| 2.3.2 | Impedance variation with SOC | 35 |
| 2.4 | Segmented cell | 36 |
| 2.4.1 | Internal design | 36 |
| 2.4.2 | Segmentation and local currents | 38 |
| 2.4.3 | Challenges of local potential probing | 41 |
| 2.4.4 | Assessment of the local RHE | 47 |
| 2.4.5 | Test bed | 50 |
| 2.5 | Conclusion | 52 |

This highly experimental PhD study undertakes a broad exploration of cell component behavior and response in tests that are representative of real RFB configurations. The hardware is built from materials used in the manufacturing process of Kemiwatt, but is a few cm² scale for practicality. This chapter aims to describe the components of the test cells and the battery testing protocols. It also introduces the unconventional symmetric and segmented set-ups specially developed for this thesis.

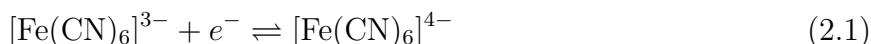
2.1. Materials and pretreatments

This section describes the general battery composition and the materials preparation used throughout this PhD thesis.

2.1.1. Electrolytes

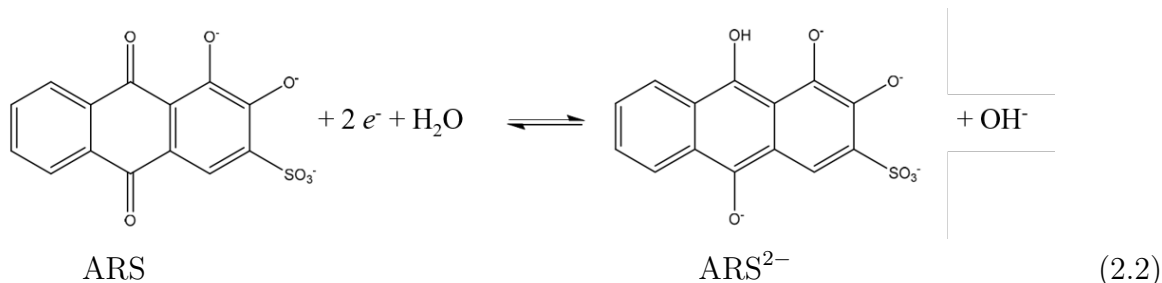
The entire study used the same pair of electrolytes. Their preparation always followed the procedure described below. The electrolyte composition is a decisive choice in RFB because it critically affects the battery performance. It is a long process to find a compatible pair of solutions that meets all the specifications. The electrolytes used here have been the subject of thorough investigations that are out of scope of this study [2]. The choice has been made to work with strong-alkaline electrolytes, neutralized around pH 13. The formulation was designed to get similar ionic concentration (of K^+ and Na^+) in both solutions, to mitigate the osmotic pressure through the membrane.

The catholyte is an alkaline solution of the iron-cyanide redox pair $[Fe(CN)_6]^{3-} / [Fe(CN)_6]^{4-}$. It is a well-known couple widely referred to in textbooks for its exemplary electrochemical behavior [109]. Several papers report its use in redox-flow batteries, especially with an organic compound on the other side [110–112]. The electrochemical reaction exchanges one electron:



The catholyte solution is synthesized by dissolving 0.5 M of the reduced species $K_4[Fe(CN)_6]$ into a solution of 0.2 M NaOH, during 2 hours of stirring.

The anolyte contains the organic molecule Alizarin Red S (ARS) or 3,4-dihydroxy-9,10-dioxo-2-anthracenesulfonic acid. It belongs to the anthraquinone group of molecules that are highly tailorable, and thus promise to meet the RFB challenges [51, 67, 70, 113, 114]. However the particular ARS has been referenced only once in a RFB application [115], but in acidic solution. Even at pH > 12, the reduced form was assessed to be not fully deprotonated [2]. A correct representation of the ARS molecule in strong alkaline medium and its associated redox reaction is:



The oxidized form ARS is dissolved in 1.2M KOH, at a concentration of 0.2M. The powder must be added slowly and the solution stirred and heated to 40 °C during 24 h to get a complete dissolution of the material. The solubility of organic molecules in water is known

to be a downside of this chemistry [47].

As specified in the reaction, an anthraquinone such as ARS exchanges $z = 2$ electrons per molecule; the solution can store up to 0.4 M of negative charges.

When measuring the amount of solid material to dissolve, one must take into account the actual purity of the powder; it usually does not exceed 80 % for the industrial ARS. The potential detrimental impact of the purity on the system is also to consider.

The standard volume used for a test is 100 mL of each solution. Therefore the capacity-limiting side is the anolyte. This configuration ensures that the cell is cycled on the total capacity of the anolyte, which eases the interpretation of the results. Anolyte properties are used in Faraday's law (2.3) to calculate the battery theoretical capacity. For this configuration, $Q_F = 1088$ mA h.

$$Q_F = \frac{C_{\text{tot}}^a \cdot V \cdot F \cdot z}{3600} \quad [\text{A h}] \quad (2.3)$$

The fresh solutions contain only one active species form corresponding to the discharged state. When the two electrolytes fill each side of the battery, the current applied to the system generates a charge of the two half-cells that takes the form of a reduction in the anolyte and oxidation in the catholyte. The State Of Charge (SOC) embodies the conversion ratio of the electroactive material between their charged and discharged forms and is thus calculated differently for each electrolyte:

$$\text{SOC}_a = \frac{C_{\text{ox}}}{C_{\text{tot}}} = \frac{[\text{ARS}^{2-}]}{[\text{ARS} + \text{ARS}^{2-}]} \quad (2.4)$$

$$\text{SOC}_c = \frac{C_{\text{red}}}{C_{\text{tot}}} = \frac{[\text{Fe}(\text{CN})_6]^{3-}]}{[\text{Fe}(\text{CN})_6]^{4-} + [\text{Fe}(\text{CN})_6]^{3-}]} \quad (2.5)$$

C_{tot} is the total active molecules concentration in the solution. It is constant providing that there is no material degradation. SOC varies between 0 and 1 but for convenience, the value of the SOC will be expressed as a percentage in the form “SOC 50”, corresponding in this case to a State of Charge of 50 %.

As the charge capacity of the two tanks are different, the electrolytes do not have the same SOC during a cycle. Other mechanisms can widen the SOC imbalance between the two sides during cycling, including among others, side reactions, degradation, cross-over or anolyte oxidation by oxygen present in the system.

It is impossible to define the strict battery SOC given that the SOC of the two half-parts will not stay equal during cycling. An apparent battery SOC will rather be used to qualify the state of the battery pertained to the total capacity accessible at a given time. This apparent capacity $Q_{\text{app}}(t)$ is relative to the history of the cycling that can degrade the capacity through diverse effects (increase of the resistance, cross-over, SOC imbalance between the two sides, material or electrolyte degradation). The accessible capacity compared to the theoretical capacity is called capacity retention. Examples of capacity retention with cycling are given in [section 5.1](#).

2.1.2. Standard test cell

A standard cell set-up of 25 cm², developed at Kemiwatt, was occasionally used during the study. Its layout has inspired the configuration of the segmented cell developed for the need of the PhD thesis and described later. The following paragraphs detail the constituents of the lab test cells.

a) Membrane

The separator used is a 80 µm Aquivion[®] membrane (E98-09S Solvay). It is a cation-exchange membrane, made of PerfluoroSulfonic Acid (PFSA) polymers. Its side chains are shorter than the widely used Nafion membrane (DuPont), as depicted in Fig. 2.1, and endow it with special properties [116].

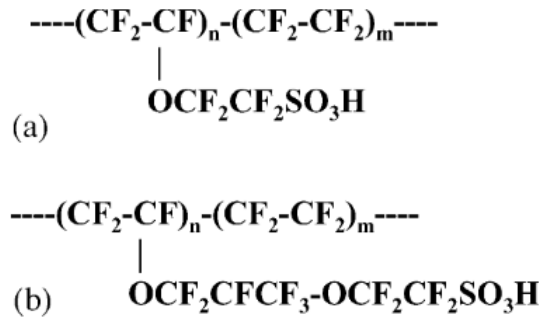


Figure 2.1: Structure of PerfluoroSulfonic Acid ionomers : (a) Short-side chains of Aquivion membrane, (b) Long-side chains of Nafion membrane. Picture from [117]

When using a polymer membrane for different chemical applications, pretreatments are usually adopted to clean and prepare the material according to its special conditions of use [118]. For the case of the benchmark membrane, a thermal pretreatment demonstrated enhanced performance in the catholyte symmetric cell; these results are detailed in subsection 4.3.1. Thereafter this membrane pretreatment was standardized for all the tests. It consists in boiling the polymer in a solution of HNO₃ 1M at a temperature of 130 °C for 2 hours. This step made more ionic sites functional and cleaned the separator. After cooling down, the polymer membrane was rinsed into baths of deionized water until the solution reached pH 7 in order to eliminate the remaining acid. The protons were finally exchanged to potassium ions by soaking the membrane into 2 baths of 1 M KOH. It was ready for a use in alkaline conditions and was stored in KOH until assembled wet in the cell. The separators that received this type of conditioning will be called “reflux membranes” in reference to the boiling conditions of this pretreatment.

b) Electrodes

The electrode material is a GFD porous graphite felt from SGL Carbon Group (reference GFD 4.6 EA), 4.6 mm thick, made from a base of polyacrylonitrile (PAN) fibers successively carbonized and graphitized. Its characteristics, available on the supplier’s website, are listed in Table 2.1. The reported electrical resistivities are surprising, as one would expect that the felt

is more conductive on the through-plane direction (\perp) than on the in-plane (\parallel). Indeed the carbon fibers are visually oriented on the through-plane direction, which gives a preferential path for electron transport.

The electrode characterization is completed in this PhD work for the special needs of the flow battery case (section 3.4). Due to its high porosity, the felt compression is a key feature of the cell assembly and alters its mechanical and electrical properties, as highlighted in Fig. 2.2 for the benchmark electrode and another thicker felt from the same supplier (GFA 6 EA, thickness 6 mm). The compression ratio applied must meet a trade-off between the liquid-transport and the electrical resistances and strongly depends on the material intrinsic features [119, 120].

Table 2.1: Electrode properties of GFD 4.6 EA, data from supplier [121]

| Properties | Units | Values |
|--|----------------------------|---------|
| Bulk density | g cm^{-3} | 0.09 |
| Area weight | g m^{-2} | 465 |
| Open porosity | % | 94 |
| Developed surface area (from BET measurement) | $\text{m}^2 \text{g}^{-1}$ | 0.4 |
| Electrical resistivity \parallel | $\Omega \text{ mm}$ | <3 |
| Electrical resistivity \perp | $\Omega \text{ mm}$ | <5 |
| Area-specific resistance (20 % compression) | $\Omega \text{ cm}^2$ | <0.15 |
| Total impurities | % | <0.05 |

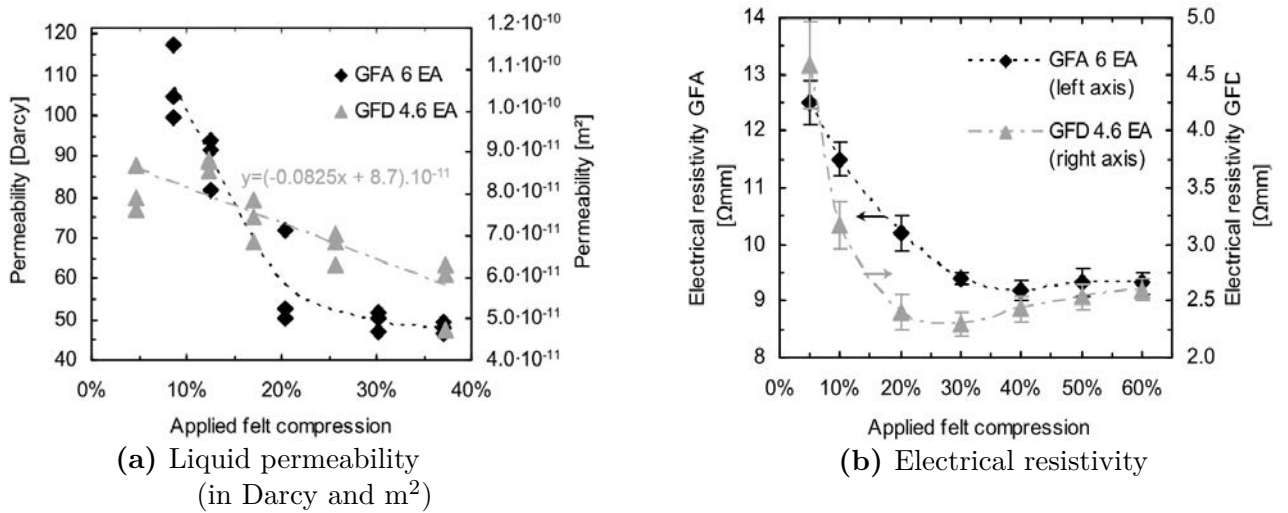


Figure 2.2: Electrical and mechanical properties variation with the applied compression ratio for two SGL graphite felts GFD 4.6 EA and GFD 6 EA, data from a supplier study [122]

It is also common practice to pretreat the electrode material to either clean it, increase its hydrophilicity or enhance the reaction kinetics at its surface by adding functional oxide groups [28]. A thermal treatment is particularly effective for the positive electrode of VFB. However, it remains difficult to assert that this pretreatment really speeds up the electron-transfer or just facilitates the material wetting and thus the accessible active surface area [123]. In the case of Kemiwatt's battery, no effect was observed with thermally-treated carbon felts. This may be explained by an outer-sphere mechanism, that is to say an electronic exchange with no chemical interaction at the surface, or an inner-sphere mechanism that is oxide-independent. The reaction rate constant k_0 of the involved species could also be too fast to be sensitive to the treatment [124]. Although no kinetics activation has been possible so far, a simple preconditioning proved to enhance the wettability.

Fig. 2.3 gives the results (capacity retention in % and pressure drops in both hydraulic circuits) of two tests run in the same conditions, except for the electrode prewetting. The set-up was a standard 25 cm² equipped with pressure sensors upstream of the cell, so that the pressure drop ΔP caused by the flow in the electrodes could be inferred.

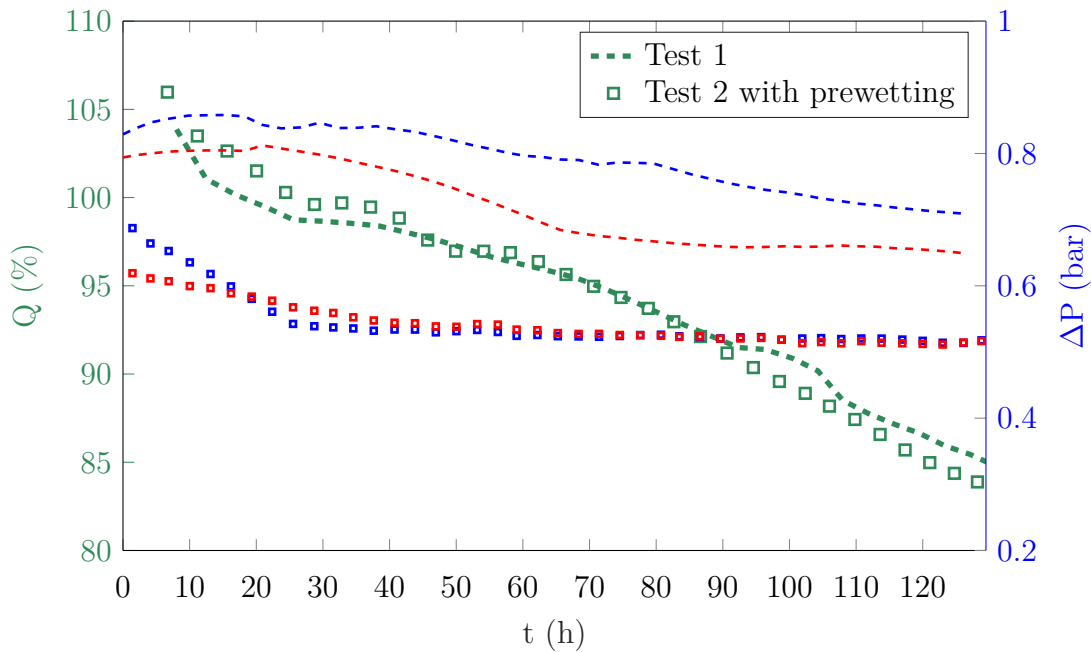


Figure 2.3: Pressure drops and capacity retentions of 2 tests, Test 2 with an in-situ prewetting of the electrodes with KOH. ΔP in red for the catholyte side and blue for the anolyte side.

In Test 2, the cell was flushed with 50 mL of a solution of 1 M KOH and then drained with air before starting the circulation of the two electrolytes. The diagram highlights a net mitigation of the pressure drops in Test 2 of -25% for the catholyte and -30% for the anolyte side, even after a hundred hours of cycling. The accessed capacity is not affected. Prewetting the electrode with the salt increases the wettability of the carbon fibers and mitigates pressure losses when the viscous solutions flow through. Due to the conclusive results from Fig. 2.3, this prewetting step was added to the standard procedure of each test launch.

c) Other components

The current collectors were made of graphite composite material, also provided by SGL. The cell was sealed with Teflon[®] gaskets, and the 3 mm PVC frames compressed the electrodes by 35%. The electrolytes flowed within the cell diaphragm pumps from KNF at a controllable flow rate of 200 mL min⁻¹. The tanks were made of polyethylene connected to polyurethane tubing (4 mm inner diameter). The flow rate relative to the small active surface area was deliberately high; it alleviates any mass-transport related problems that could be caused by the poor cell design. The 25 cm² set-up is used to study any operating parameters barring the flow rate.

2.2. Battery tests

This part details the standard procedures followed to prepare the set-up from the materials described above and perform cycling and characterizations of the RFB cell.

2.2.1. Assembly

All the components previously described were piled up between two feeder plates made of plastic. The cell assembly was tightened with a torque screwdriver to a moment of 1 N m. The cell was rinsed with a salt solution of 1 M KOH as mentioned above. The tanks were then filled with the electrolytes and the flow was started. Anthraquinones are known to be sensitive to oxygen [19]. To eliminate risk of spontaneous oxidation of the reduced form once the anolyte is charged, its hydraulic circuit was purged with inert gas during 20 minutes while the solution was flowing into the cell. It was made by bubbling nitrogen into the solution through a needle immersed in the tank. The catholyte being sensitive to light (as evidenced later in subsection 3.2.3), its tank was wrapped in foil to protect from light. After these precautions were made, the cell was ready to be used.

2.2.2. Cycling

A basic procedure was to charge and discharge the cell at constant current density, though it is different from the real-life cases where the battery system is power-controlled [17]. The operating current density, used as a standard, was 40 mA cm⁻². The voltage response of the battery was recorded over time and the charge and discharge stopped when the cell voltage reached the bounds of the safety window [0.6; 1.5 V]. This was determined to prevent side reactions and degradation of the electrolytes. “Constant-current” charges and discharges were applied successively to the RFB and constituted a cycling characterization. A small rest of 60 s was executed between each step to avoid abrupt changes of the current direction.

Performance metrics are readily available from the cycling and inform about the performance of the system.

- The total capacity accessed during a charge or discharge Q_{tot} relative to the theoretical

capacity available in the electrolytes Q_F (2.3) is called **capacity utilization**:

$$Q_u = \frac{Q_{\text{tot}}}{Q_F} \quad [\%] \quad (2.6)$$

- The **energy** stored or delivered by the battery is another interesting indicator, especially for the industrial perspective:

$$E = \int IU dt = \int P dt \quad [\text{Wh}] \quad (2.7)$$

- Efficiencies are the figures of merit to assess the battery response during a full cycle (charge + discharge) [37]. The ratio between the total discharge capacity $Q_{\text{tot, dis}}$ over the total charge capacity $Q_{\text{tot, ch}}$, expressed in Ah is called **coulombic efficiency** CE:

$$\text{CE} = \frac{Q_{\text{tot, dis}}}{Q_{\text{tot, ch}}} = \frac{\int I_{\text{dis}} dt}{\int I_{\text{ch}} dt} \quad [\%] \quad (2.8)$$

- The **voltage efficiency** EE compares the average voltage during charge and during discharge:

$$\text{VE} = \frac{\int U_{\text{dis}} dt}{\int U_{\text{ch}} dt} \quad [\%] \quad (2.9)$$

- The energy efficiency EE combines both voltage and current measures since it is the ratio of the energies:

$$\text{EE} = \frac{\int P_{\text{dis}} dt}{\int P_{\text{ch}} dt} \quad [\%] \quad (2.10)$$

The metrics defined above provide a good starting point to evaluate the high-level system yield and the ability of the system to hold and return energy. They depend on the operating conditions and the battery components. However they cannot uncover the influence of each parameter and identify the origin of the losses. The diagnostics must be supported with specific characterization tests described in the following sections. They are executed at several stages of the cycles according to the test need. The evolution of efficiency during cycling is an interesting insight of how the battery ages.

2.2.3. Polarization curves

The Polarization curve, noted PC, gives an interesting depiction of the system behavior. This characterization particularly insightful during material benchmarking or cell architecture development [90, 125]. The general description of the PC is made in subsection 1.3.1.

One consideration during the acquisition of the PC is the constant SOC of the battery; this assumption is actually not strictly met in a RFB, where the electrolyte is recirculated during characterization. To circumvent this issue, the experimental layout can be adapted to e.g. a cell-in-series or a 4-tank configuration [27], but these are constraining options. With an accurate method of acquisition, it is possible to hold the SOC almost constant during the course of the PC experiment. A number of techniques are described in the literature:

- *Stepwise method*: The first one consists of applying current steps of increasing intensity until a limiting current level, and may include a rest period between each step to

return to equilibrium. This must be done separately in charge and discharge to obtain the two parts of the PC. Aaron et al. chose to hold current during 30 s and then allowed a 2 min rest [79]. They averaged the cell potential measurements over 30 s. This method induces a continuous variation of SOC over the increase of current. The current range in which one of the overpotential phenomena dominates depends on the SOC, thus the critical domains of activation, ohmic or mass transport losses (depicted in Fig. 1.8) cannot be clearly delineated with this technique. Another downside is the determination of the voltage for each current: the average value is strongly linked to the specified current step length. This relatively arbitrary criterion of step length can strongly affect the results of the polarization curve.

- *Alternating stepwise method*: Becker et al. modified the method by using a stepwise potentiostatic mode that alternated the polarization sign at each step [103]. The cell was returned to its initial SOC after each value of overpotential tested. It constitutes an improvement in preserving a constant state during the characterization but does not overcome the problem of setting the best step length criterion. Additionally, switching the polarization from positive to negative direction might be traumatic for the system.
- *Ramp method*: Another approach is to perform a ramp of potential or current at a given rate. The polarization sign is unchanged throughout the course of the experiment and the instantaneous cell response is taken to plot the curve. One could criticize that the transient behaviour affects the results because it includes the unwanted capacitive currents. Chen et al. [104] nevertheless asserted that the linear galvanic ramping yielded the same battery response as holding current steps in their set-up.

A comparison of the alternating stepwise and ramp modes was performed on the battery studied in this PhD, to have a clear view of how each impacted polarization curve recording. The PC study was carried out in the segmented cell (described below) with electrolytes precharged at SOC 50, and a flow rate of 100 mL min^{-1} .

The current step method was performed galvanostatically with a current sign being alternated at each step. This protocol is illustrated in Fig. 2.4a by the temporal variation of U and I signals with steps of 60 s.

The influence of the current step length is noticeable, particularly at high current. The time-dependent voltage response, given in Fig. 2.4a for the 60 s time steps, illustrates the underlying problem. Since the signal is transient at each current, it is clear that averaging the response over the whole time step is not a good option. This unsteady behavior is attributed to the presence of the product species that have just been created and that play the reverse role of reagents when changing the current direction. Their transient surface over-concentration generates a lower overpotential than expected. The balance is achieved when the voltage reaches a plateau. If the current is held for too long, the SOC varies and modifies the cell voltage. This effect is prominent at high current in Fig. 2.4a. With such a varying signal, the voltage taken on to build the PC could either be an average of the last several values or the value at the level part of the signal, which can be difficult to determine. Consequently, the PC is highly dependent on both criteria of step length and calculation of the corresponding voltage. From Fig. 2.4a it can also be noted that the dynamic voltage responses for the charging or the discharging steps are not completely symmetrical: the overpotential is more pronounced in discharge than in charge. This discrepancy was also observed by Becker et al. [103], but is difficult to elucidate.

During the ramp method, the cell was also controlled in current. Fig. 2.4b depicts the protocol used: the cell was first discharged until the low voltage cut-off was reached; then the

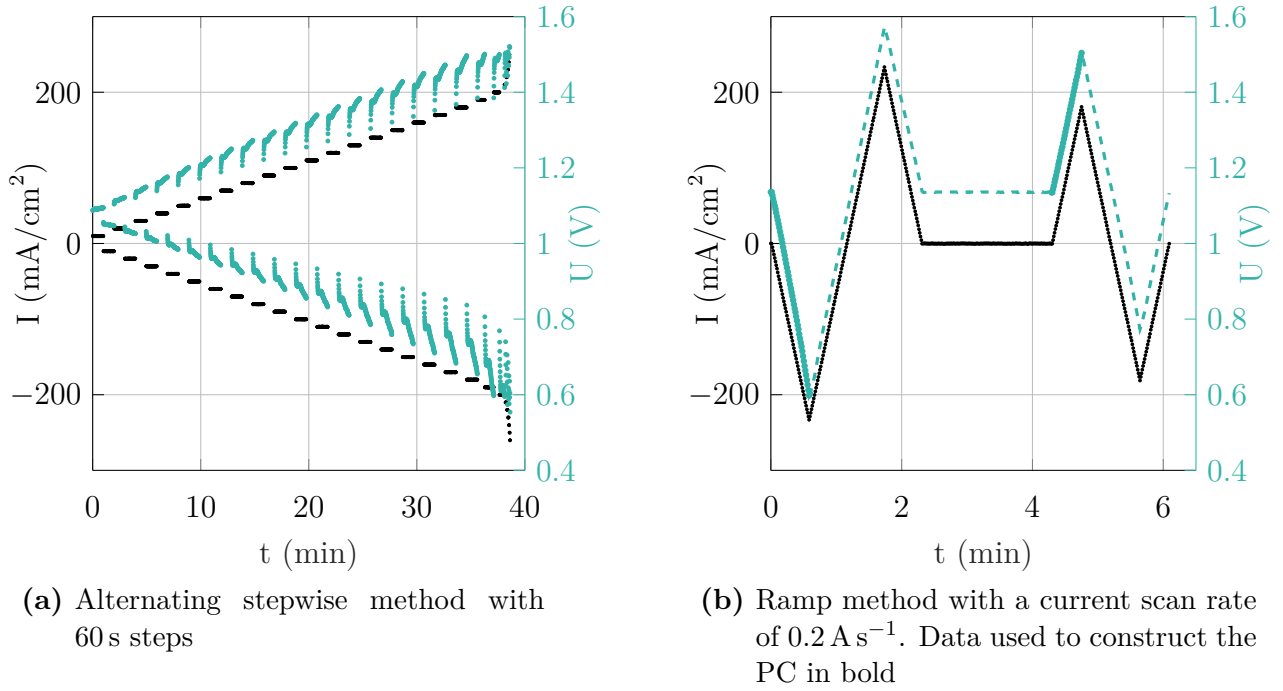


Figure 2.4: Temporal signals of current and voltage during two methods of polarization curves

ramp was reversed, and the exact opposite triangle signal was applied to return the cell to its initial SOC. After 2 min rest, the protocol was repeated in the other direction to get the positive part of the PC. The bold parts of the voltage curves represent the data used to construct the PC.

The PC characteristics deriving from these protocols are displayed in Fig. 2.5, for two ramp rates (0.2 and 0.4 A s^{-1}) and two step lengths (20 and 60 s). For the step methods, the voltage response was averaged over the 5 last points of each step (corresponding to 3 s of acquisition).

The two step methods do not yield the same response for the reasons explained above. The PCs obtained with the ramp method are slightly different from the ones built by current steps. In particular, ramping allows for a better curve resolution than the current steps. There is virtually no change between the curves at two scan rates, unless at high negative current for which the mass transport limitation appears earlier with a slower scanning. It is consistent with the fact that the SOC is more destabilized when the characterization takes longer. This low dependency relative to scan rate confirms about the small influence of transient current on the global cell response. The ramp method also eliminates the question of setting criteria of step lengths and calculation of the response value, that needs to be addressed with the step procedure. Finally, with a scan rate of 0.2 A s^{-1} , the experiment lasts for 4 min against 40 min with the slowest step method.

From these conclusions, the ramp method was selected as the standard for polarization characterization. A ramp slope of 0.2 A s^{-1} was deemed as a suitable option, as it is not too fast compared to data acquisition and at the same time allows for a rapid experiment that keeps SOC constant.

The polarization curves delineate the operating ranges where a specific source of voltage

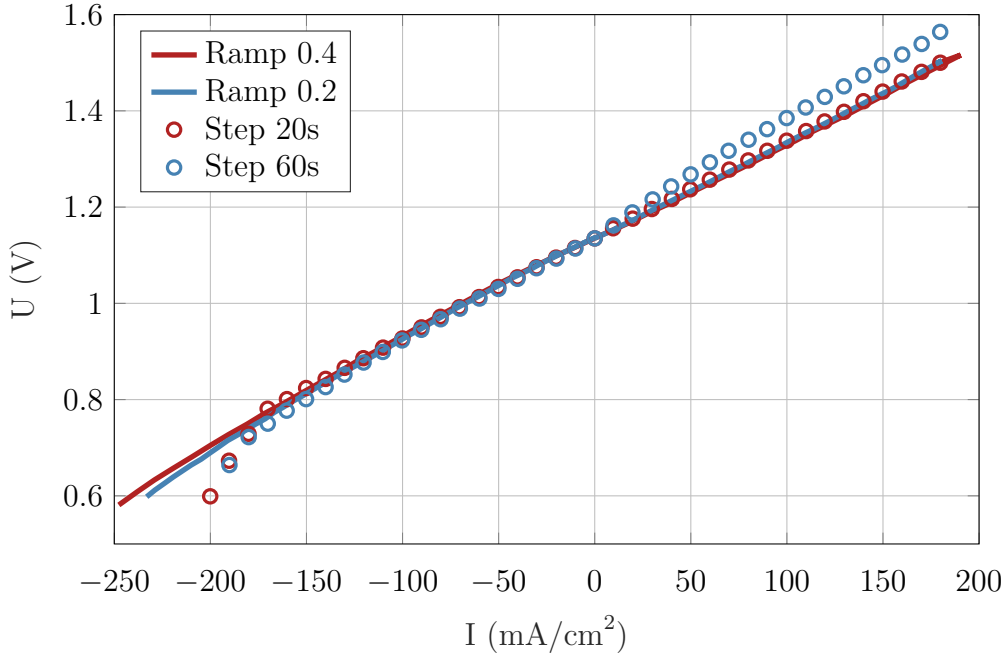


Figure 2.5: Comparison of the polarization curve ramp and step methods for two ramp rates (0.2 or 0.4 A s^{-1}) and two current step lengths (20 or 60 s)

loss dwarfs the others. A map of operating current depending on the state of the battery can be built from these results. However, it is not possible to break down the cell resistance into contributions of each voltage loss with a single PC. The Electrochemical Impedance Spectroscopy allows for identification of the limiting factors occurring at different time scales.

2.2.4. Electrochemical impedance spectroscopy

While the response to direct current during polarization curve is classically used to characterize a battery, an alternating current (AC) technique can complement the diagnostics. The Electrochemical Impedance Spectroscopy (EIS) consists of applying a small sinusoidal perturbation to the electrochemical device to make it fluctuate around equilibrium and generate a dynamic response. Current or voltage can be controlled, giving a galvanostatic (GEIS) or potentiostatic (PEIS) spectroscopy respectively. The amplitude of the input signal is constant while its frequency is swept over a wide spectrum. The output sine wave, respectively I or U , is recorded for each frequency f . If considering the galvanostatic mode, the input stimulus results in the perturbation $\Delta I(t)$ superimposed on the DC current $\langle I \rangle_t$:

$$\Delta I(t) = I(t) - \langle I \rangle_t = \Delta \bar{I} \exp(i\omega t) \quad (2.11)$$

with $\omega = 2\pi f$ the angular frequency and i the imaginary unit defined by $i^2 = -1$. In the case of a linear system, the response to the sin wave input is also sinusoidal, whose magnitude $\Delta \bar{U}$ and phase difference ϕ depend on the frequency of the stimulus:

$$\Delta U(t) = U(t) - \langle U \rangle_t = \Delta \bar{U} \exp(i\omega t + \phi) \quad (2.12)$$

These characteristics serve to calculate the transfer function of the system for each frequency investigated, called cell impedance Z for an electrochemical system (2.13).

$$Z = \frac{\Delta U(t)}{\Delta I(t)} = \bar{Z} \exp(i\phi) \quad (2.13)$$

A battery is however a non-linear system, since the Butler-Volmer relation (1.14) establishes an exponential relationship between the current and voltage. In view of the PC characteristic in Fig. 2.5, the RFB takes a linear behaviour at small currents; the assertion of considering the system linear is acceptable for a perturbation close to zero current [126]. In this case, the concentration variation of the active species stays small relative to the total concentration: $\Delta C/C \ll 1$.

This thesis used a galvanostatic spectroscopy with an AC signal amplitude of $\pm 6 \text{ mA cm}^{-2}$ around 0, to keep the SOC unchanged during EIS. The frequency was changed from 10 kHz to 1 Hz or 20 mHz, depending on whether the low frequency values were of interest. An example of signal input and output is illustrated on the left of Fig. 2.6. Potentially-controlled EIS was also tested and gave the same results. The AC signal amplitude guarantees the measurement validity: it must be small enough to assume the system linearity but sufficiently high to get a good signal-to-noise ratio.

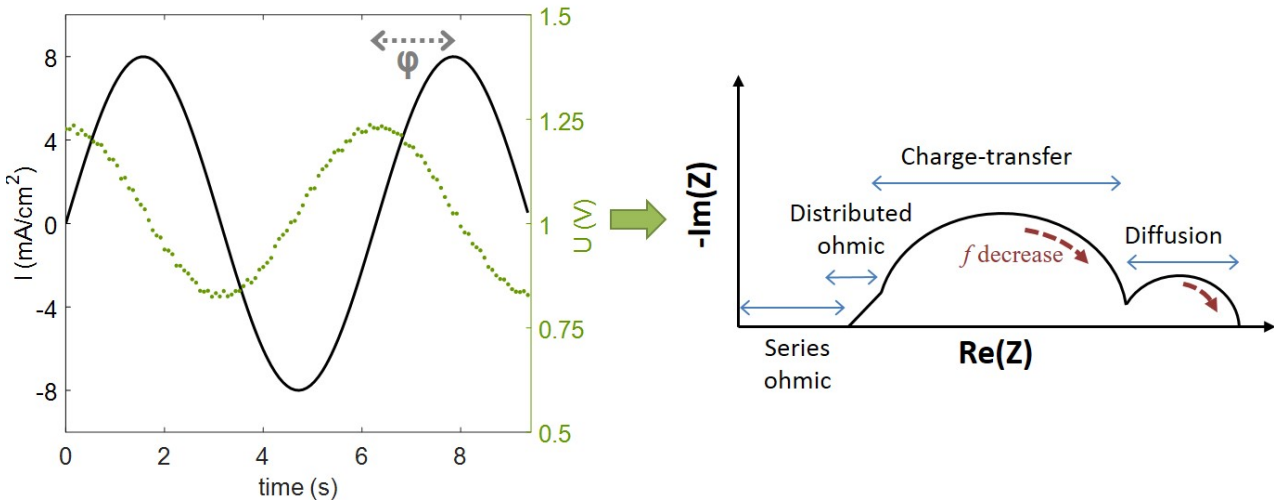


Figure 2.6: Left: Example of a RFB voltage response induced by the sinusoidal current perturbation at $f= 0.15 \text{ Hz}$. Right: Complex plan plot (called Nyquist plot) of the cell impedance from the EIS data, and detailed loss contributions

The representation of the impedance variation with the frequency can take two graphical forms, since it is a complex number:

- the **Bode plot**, giving the magnitude \bar{Z} and phase shift ϕ of Z as a function of f in a logarithmic horizontal scale.
- the **Nyquist plot** being the representation of the opposite of the imaginary part $-Im(Z)$ according to the real part of the impedance $Re(Z)$. This type of diagram does not feature the frequency but gives a very visual depiction of the results. This is the reason why it is widely used in the electrochemical community.

An example of Nyquist graph is given in Fig. 2.6 on the right. It is made of circular arcs

appearing in different frequency domains. The limiting processes account for a specific part of the spectrum as depicted on the drawing. The cell composition is actually comparable to an equivalent electrical circuit that reproduces the electrical behaviour of the impedance $Z(\omega)$, usually composed of resistances and capacitances. These electrical analogues are useful to fit the EIS shape and determine the equivalent values of the electrical components mimicking the battery response. Several models are developed depending on the cell configuration in use; they are detailed in [section 4.1](#).

2.3. Symmetric cell

As previously proposed by some authors, the use of a symmetric cell is particularly relevant to investigate one electrolyte at a time by assessing its cycling ability in the flow battery configuration [92, 97]. It is even possible to discriminate between the individual behaviors of the reduced and oxidized forms of an electrochemical couple.

2.3.1. Principle

A symmetric set-up was used in this work to investigate the electrolytes independently. The experimental results, presented in [Chap. 4](#) were analyzed and compared to a model describing the electrode to evaluate the electrolyte suitability for use in the RFB system. The next paragraphs detail the symmetric configuration used in this PhD.

Goulet et al. chose to use different volumes of solution on each side of the cell to impose a capacity-limiting side that would be responsible for any capacity fade observed [97]. In the present thesis, the strategy is different and the same volume was used on each side to have symmetrical states of progress in the conversion of the reactants.

200 mL of fresh electrolyte was first half-charged in a standard flow cell. The volume was later equally divided into the tanks of a clean cell to get the symmetric layout. Both solutions (especially the anolyte reduced species) were sensitive to air, therefore electrolyte division between two containers was made under inert gas conditions. The symmetric cell could be built either with the standard or the segmented design depending on the experiment requirements. Galvanostatic cycling of the symmetric cell could then be performed on half of the total capacity of the tank. An opposite reaction was generated at each electrode. In the case of the catholyte study represented in [Fig. 2.7](#), oxidation occurred at the positive half-cell, charging the catholyte from 50 to 100 % SOC. Reduction took place at the negative electrode; the SOC varied between 50 and 0 % on this side. It is arbitrarily considered that the global SOC of the symmetric cell evolved between 50 and 100 % during the cycles. When both tanks reached their respective extreme SOC, which should be concomitant if volumes are equal, the current polarity was reversed and applied during the same time to bring both tanks back to SOC 50.

2.3.2. Impedance variation with SOC

An innovative test developed during this study was the monitoring of the impedance variation of the symmetric cell during the charge. This particular configuration allowed fitting of the resulting curve to an analytic model in order to determine key parameters ([Sections 4.3.3](#)

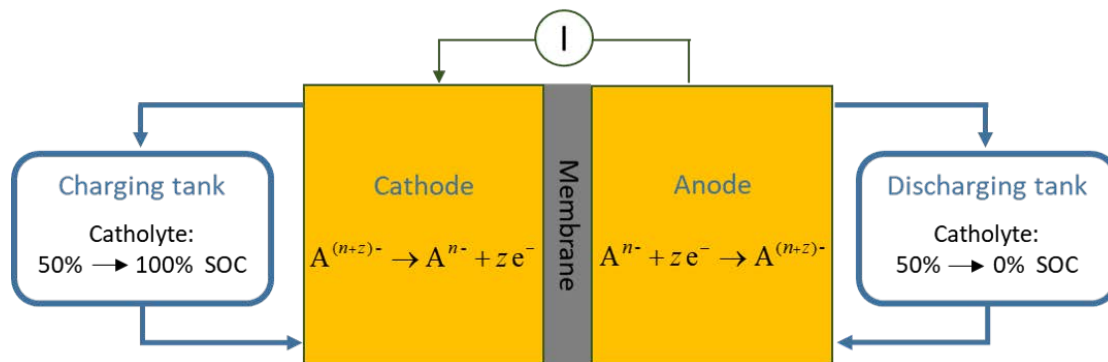


Figure 2.7: Symmetric-cell in charge, in the case of the catholyte study

and 4.4.3). To this end, the cell was sequentially charged at 40 mA cm^{-2} ; the step lengths were adapted to the state of progress of the charge to record enough points and have a fine resolution, without having a test that last too long. The charging steps (increasing the SOC by 5-10 % or less at the end of charge) were followed by a rest of 2 minutes and a GEIS measurement at high-medium frequencies: $f=[1 \text{ kHz}; 20 \text{ Hz}]$. A voltage limit of 0.9 V secured the charge before side reactions are triggered within the symmetric cell. The cell was then discharged without interruption to recover the symmetric state. This method of cycling based on charging and discharging the cell for an identical period of time is the only way to return to a similar state after each cycle. The two electrolytes showed an acceptable capacity retention during a few cycles. This allowed the assertion that each charge started from the same conditions.

2.4. Segmented cell

At laboratory scale, test cells can be equipped to get a better understanding of the system. Probing the mechanisms within an operating cell is one of the critical challenges. Literature on instrumented cells is extensive in systems such as fuel cells, but is poorer for the specific study of flow batteries. LEMTA has a considerable expertise in segmentation of electrochemical systems and has developed this diagnostic tool for more than ten years. One of the goals of the PhD work is to develop a new experimental set-up to monitor the local behavior of the cell in-situ and during cycling. It is achieved by segmenting the plate at one side of the battery and adding a local reference electrode. The cell provides current and potentials at a local scale and is embedded in a full bench to control and measure all the operating parameters. Fig. 2.8 gives a global view of the test bed developed during the PhD study.

All the elements of this experimental bench are detailed below, with a particular focus on the segmented cell layout, and the strategy developed to resolve local behavior of the RFB.

2.4.1. Internal design

The segmented cell design was based on the standard RFB test cell described earlier (subsection 2.1.2). The same pretreated membrane and porous electrode materials were used. The only difference was the nature of the current collector; but several experiments showed that it did not impact the performance (subsection 5.1.1). The active surface of the segmented cell

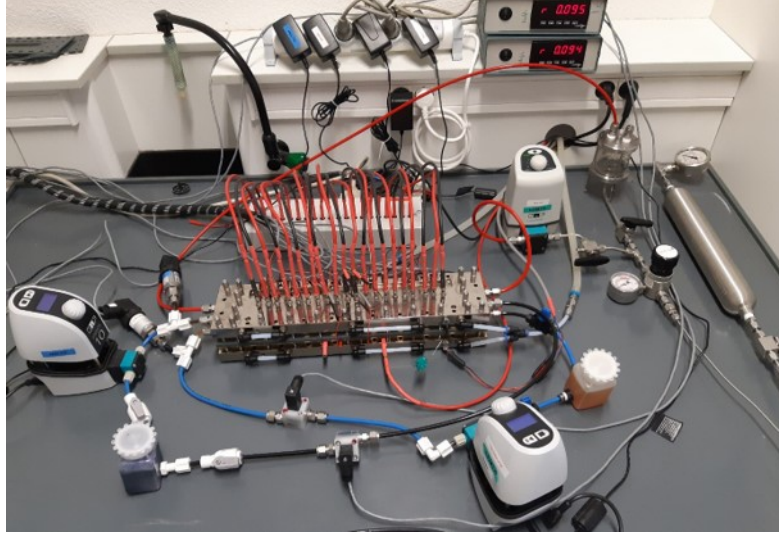


Figure 2.8: Global view of the segmented test bench for RFB study

is 30 cm long and 1.4 cm wide, giving an active area of 42 cm^2 . The cell length corresponds to the height of Kemiwatt's industrial stacks, which is a standard format for RFB batteries [127]. The essentially-1D geometrical surface ensures that local variables can be tracked along the flow inside the cell and prevents from facing flow distribution issues. Fig. 2.9 gathers the successive layers used to assemble the set-up, from left to right.

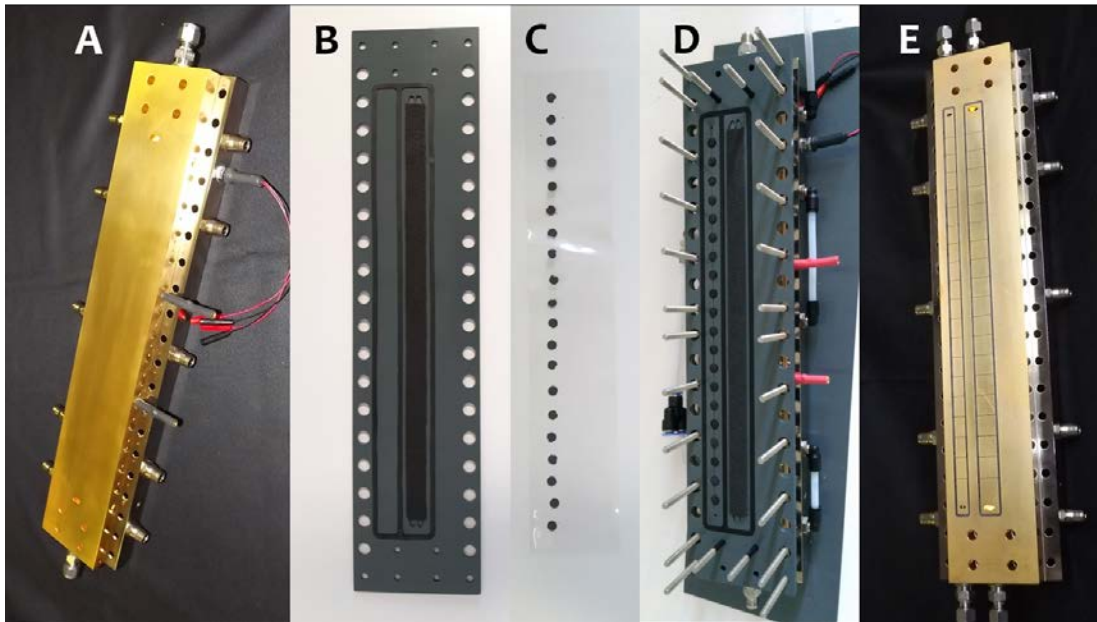


Figure 2.9: Exploded view of the layers constituting the segmented cell assembly

The non-segmented current collector (A) was a 15 mm brass plate covered with a layer of Nickel and then gilded with a $3.5 \mu\text{m}$ layer. The Ni-coat shields it from corrosion while the thin gold leaf brings a good electrical contact with the electrode. It was fastened on the back to a Nickel-coated brass clamping plate that contained the hydraulic circuit for the thermal cell control and would hold the assembly tight. At the end of this chapter, a diagram illustrates the thermal control circuit in the brass plates. These two slabs had a high thermal conductivity to

facilitate the thermal regulation. They were separated by a Kapton[®] tape ensuring electrical isolation. The PVC frame B topped the first block and held the graphite electrode, which was fed through the manifolds machined on both edges of the electrode plate. The third layer was a reflux-pretreated 80 μm Aquivion[®] membrane (C) supporting a network of reference electrodes. The latter was composed of 20 Gas Diffusion Electrode (GDE) dots of 6 mm diameter, which had been heat-pressed in line at a distance of 1 cm outside the reactive surface. GDEs are usually used in fuel cell assemblies to hold the reactions [6]. Pressing occurred during 5 min at 5 MPa and 155 °C (close to the membrane glass transition temperature T_g [117]) to guarantee a tight bond between the electrodes and the membrane. The active area of the membrane was not exposed to the hot press to avoid any structure modification in this zone. The other frame (D) supported, besides the electrode of the other half-cell, a network of 20 dots of the same porous material used as working electrodes. It would make contact between the GDE on the membrane and the end plate. The principle of the reference electrodes network is detailed elsewhere (subsection 2.4.3). The last part (E) was similar to block A, but contained two parallel sets of 20 insulated segments. They were machined in the brass slab and then surrounded with an epoxy resin that insulated them one from the other and from the surrounding block. The central set of widest segments constituted the current collector surface, with independent segments of 2.1 cm² each. The smaller segments on the left were connected to the distributed references. The thermoset resin used must comply with a stringent set of specifications: good adherence to the metal, inert compound to prevent any pollutant release, resistance to the chemicals used and to operating temperature, hardness comparable to the metal, no contraction nor porosity increase during curing.

This design has stemmed from many years of in-house developments and successive generations of segmented cell at the LEMTA laboratory. An extended chronicle of this development is detailed in [6]. The strategy of this layout along with the associated measurement techniques are explained below.

2.4.2. Segmentation and local currents

Access to the locally-resolved current density requires the measurement of the real through-plane component generated within the cell, while not disturbing the cell operation. As it was numerically demonstrated by Eckl et al. in the case of fuel cells, lateral current spread can be substantial if the solid plate behind the electrode is not segmented [128]. This was confirmed experimentally in the case of a RFB by comparing the probed internal current with or without full segmentation of the end plates [100, 129]. The accurate estimation of internal current must go along with segmentation of the solid plates constituting the back of the cell. It was asserted in former PEMFC studies that the segmentation does not need to be extended to the electrodes [130]. Nevertheless, the RFB differs from fuel cell by the presence of conductive liquid electrolytes inside the porous electrode. As a consequence, some current might spread laterally through the liquid phase [129]. Bhattarai et al. were the first ones to implement the porous electrode segmentation in a RFB [131]. They obtained slightly improved resolution with electrode segmentation. Apart from this gain, the electrode segmentation is difficult to execute and affects the internal porous structure. For these reasons this option was not considered in the PhD study.

Since the current applied on one side crosses the entire cell, it is sufficient to segment only the current collector at one end. For the same reason, the half-cell used for the localized

measurements does not affect the current [101].

The in-plane distribution of current can be collected by several ways. The four most common techniques described in the literature are the resistor network, the printed circuit board, the Hall effect sensors and the potential probes.

Their advantages, drawbacks and implementation requirements are compared in Table 2.2.

Table 2.2: Types of local current measurements approaches, inspired by [27]

| Technique | Advantages | Drawbacks and Constraints | Ref |
|------------------------------|--|--|-------|
| Resistor network | Possible individual control In-house development EIS measurements possible | Additional contact resistances Planeness of the segmented plate for uniform compression | [100] |
| Hall effect sensors | No additional contact resistance | Voltage offset depending on T Complex Appropriate for a low range of current | [132] |
| Printed Circuit Board | Low cost High spatial resolution Independent of cell design Integrable to a stack No complicated hard-wiring | Only standard geometries available EIS measurements impossible | [101] |
| Potential probes | Low cost No plate segmentation Stack implementation In-plane and through-plane distribution | Risks of leakage, special gasket design Invasive Repeatability of the probe position | [103] |

A network of *shunt resistors* can serve for data acquisition: the local current value is deduced from the potential drop across small resistors. These latter are sized according to the internal resistance of the set-up, to be able to detect the whole current component. EIS characterization can be performed locally. The shunt network is a common technique but necessitates to minimize the contact resistances for good accuracy and low impact on the cell performance.

Similarly, a network of *Hall-effect sensors* can be placed behind the current collector. The magnetic induction through the sensors provides accurate estimation but is applicable only over a low range of current. The sensors also induce a voltage offset that can fluctuate with temperature. It has so far never been applied to flow battery studies. Both shunts or Hall sensors require the individual wiring of each segment and are thus cumbersome.

Printed Circuit Boards (PCBs) can be a good alternative in terms of spatial resolution. For instance, the company S++ is well-known in the fuel cell research and industry for its off-the-shelf PCB products [133]. Thanks to low hardware requirement, these devices are meant to

be non-intrusive and easily integrated to battery stacks. Nevertheless this advantage is not really valid since the full segmentation of the end plate was deemed necessary to probe the internal current accurately [129]. For that reason, PCB tests reported in the literature are made with segmented set-ups. Since the PCB is independent of the flow field plate, it can be reused to investigate several patterns. PCBs are commercially available that makes them cheap. Contrarily, the network of resistors or sensors must be developed in-house which adds on cost, but gives more liberty in the cell design. Additionally local EIS measurement is not possible with the PCB hardware.

These three methods of shunt resistors, Hall-effect sensors and PCB require the segmentation of the end plate, which entails underlying challenges: the appropriate method of segmentation to get a plane slab and local uniform compression, the selection of insulating material that must be compatible and robust, the minimization of contact resistances between the segments and the hardware at the back.

A non-destructive approach is the insertion of *conductive potential probes* inside the active area to measure the local solid-phase potential and infer the current distribution. This technique is the least expensive and easiest because no segmentation is involved. It is however complicated to prevent from leaking around the probes, and their position is hardly reproducible.

Ghimire and coworkers proposed a slightly different approach of in-situ monitoring. They controlled each segment independently in current and recorded the individual potentials. This technique does not emulate the real use conditions of the battery. It probably induces potential gradients between segments and thus local shunt currents [102, 131].

The acidic electrolytes of VFB necessitate the use of a conductive plate, usually in graphite, between the porous electrode and the metallic current collector [101], since the direct contact of acidic solution with metal would corrode it. This configuration implies the segmentation of both the graphite plate and the current collector, which increases contact resistance and risks of uneven compression.

With the alkaline solutions used in this PhD study, such precaution is not necessary: the segmentation concerns the metallic plate only.

The specific set-up developed during the PhD thesis was equipped with a network of shunt resistors to get in-plane insight of the current distribution. A network of $5\text{ m}\Omega$ resistors was connected to the cell segments by thick wires screwed in each segmented block. The potential drops at the resistors were first amplified by a factor of 500 before being recorded; from these measurements were inferred the currents passing through the segments. Fig. 2.10 depicts the longitudinal section of the segmented set-up to make the resistors/cell connection visible.

The total electrical resistance between two segments, marked by the green path through the resistor network in the diagram, are in the order of $20\text{ m}\Omega$ including the wiring and the contact resistances. This value must be examined against the resistance in the graphite electrode represented in red. According to the material properties (Table 2.1), two successive segments are connected via the felt by a $200\text{ m}\Omega$ in-plane resistive path. It confirms that the majority of the local current would be detected by the shunt resistor and would not spread laterally in the graphite electrode.

The two edge plates were tightened before screwing the resistor network onto the segments so as to ensure a flat alignment of the segmented surface. The anolyte was always circulated in the segmented half-cell, because preliminary compatibility tests showed that a lower compatibility

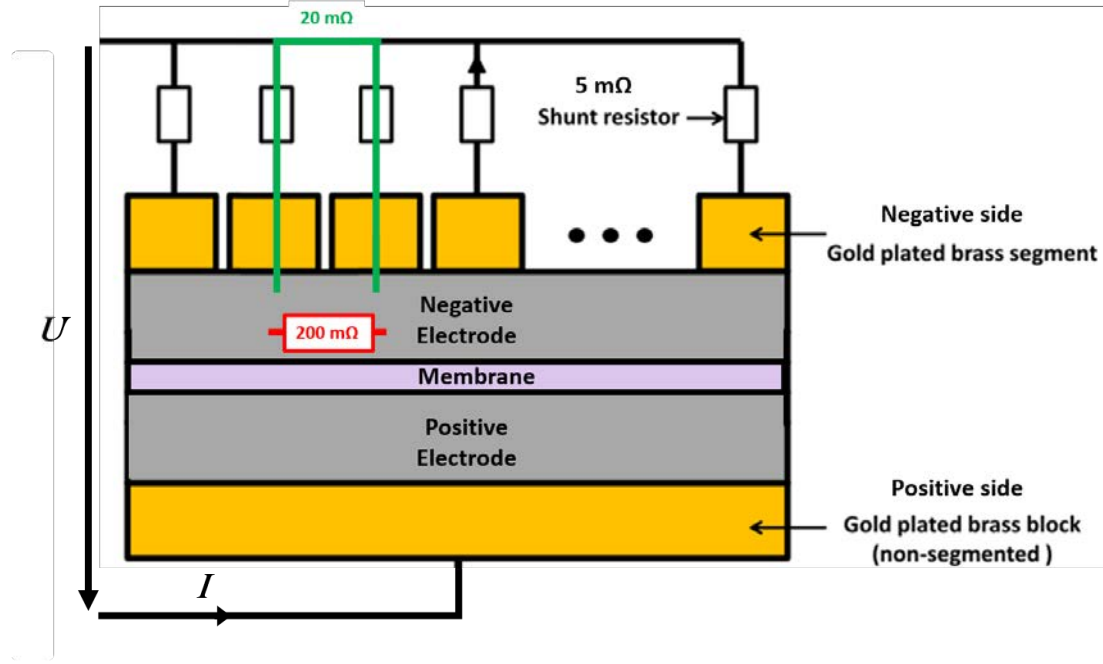


Figure 2.10: Longitudinal sectional view of the segmented cell with the network of 5 mΩ shunt resistors. The total resistance between two segmented surfaces is lower than the electrical resistance of the porous felt according to its properties Table 2.1. Adapted from [6].

between the catholyte and the thermoset resin used to isolate the segments.

2.4.3. Challenges of local potential probing

The discrimination between the negative and positive electrode potentials necessitates the presence of a reference electrode inside the set-up, since the absolute potential of an electrode is not measurable. A metal-electrolyte interface can serve as a reference electrode if its potential is stable in time, well-defined and reproducible. This condition is met when a redox couple is present in its reduced and oxidized forms in the solution and the redox-reaction at the interface is sufficiently fast that these species concentrations are at equilibrium [76]. Several real systems approach this ideal case but their suitability depends on the application. The hydrogen electrode is the best candidate for reference electrodes in aqueous solution. The hydrogen reaction takes the form of:



As the Nernst relationship spells out, the presence of protons involved in the reaction makes its actual potential a function of the pH:

$$\begin{aligned} E_{\text{H}^+/\text{H}_2} &= E^0 - \frac{0.06}{z} \log \frac{[\text{H}^+]^2}{P_{\text{H}_2}} \\ &= E^0 - 0.06 \text{ pH} \end{aligned} \quad (2.15)$$

The second line is obtained when considering a partial hydrogen pressure equal to 1 bar. The virtual condition of an ideal solution at $\text{pH}=0$ defines the Standard Hydrogen Electrode (SHE) whose potential is conventionally taken as $E^0=0\text{ V}$.

H_2 being a gas molecule, steps of dissociation and adsorption on the metal surface precede the electrochemical exchange. The metal must play the role of catalyst for these sluggish mechanisms to occur. Platinum is an effective material in electrocatalysis of hydrogen evolution, for which reason Pt particles are usually added to activate the carbon surface of the Gas Diffusion Electrodes (GDE) in fuel cells [6].

It is rather straightforward to implement a hydrogen reference electrode inside an electrochemical cell. Two strategies exist:

- The *Dynamic Hydrogen Electrode* (DHE) is made by two Pt wires in contact with water between which a small current is applied to electrolyse the H_2O molecules. The electrode hosting hydrogen evolution forms the reference.
- The *Reversible Hydrogen Electrode* (RHE) is obtained by flushing hydrogen gas on a platinum surface. This method requires an hydrogen gas supply but is at real equilibrium since no current flows through the electrode.

The hydrogen electrode must be linked to the active electrodes to be able to measure the potential difference. In a cell, it is convenient to place the reference in contact with the membrane that plays the role of ionic bridge towards the working electrodes. Fig. 2.11 gives the possible DHE positions: it can be sandwiched between two membranes or installed at the edge of the membrane layer in the vicinity of one electrode (inside or outside the active surface) [134]. The sandwich layout entails further resistive losses due to doubled membrane thickness whereas the edge-type requires a good membrane hydration between the electrode and the reference. Due to the need of hydrogen flow in the case of a RHE, the only option is the edge configuration. Fig. 2.11 represents the arrangements in the case of direct contact between the reference and the membrane.

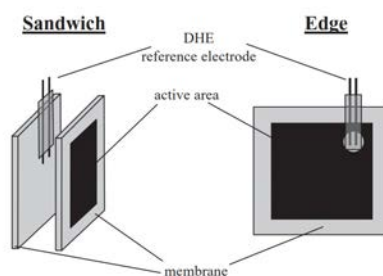


Figure 2.11: Sandwiched and edge types configurations of Dynamic Reference Electrodes (DHE) in an electrochemical cell, from [134].

One can also consider to install an external reference electrode that holds contact with the inside of the cell through a salt bridge [107]. It creates a membrane-bridge junction potential (Donnan effect) that must be accounted for in the measured potential.

The local-resolution of the half-cell potentials adds to the challenge by requiring the implementation of distributed reference electrodes. It was found easier to set a network of local RHE because DHE electrodes have several downsides: it would require as many electrical connections as the number of references, adding a second membrane layer would affect the cell performances and leakage around the Pt probes would need to be addressed.

In the segmentation design developed at the LEMTA, the access to local potentials was managed by placing a series of 20 local RHE at the edge of the active area, all fed with a unique hydrogen flow. Each RHE was built from a Gas Diffusion Electrode (GDE) (SGL 25BC type): a carbon paper loaded on one side with Platinum (1 mg cm^{-2}) and Nafion solution. It was cut into disks of 6 mm diameter and then heat-pressed onto the membrane (as visible in Fig. 2.9 C and detailed in that section). Small pieces of porous electrodes facing the GDE dots were placed in the frame (Fig. 2.9 D) to make contact with the segments on the left of the plate (Fig. 2.9 E). Finally, humid hydrogen was flowed through this channel during cell operation to keep this part of the membrane wet. The gas maintained the hydration of membrane outside the active surface. The simultaneous presence of the Pt catalyst from the GDE, the water contained in the membrane and the H_2 molecules gathered the conditions to create an hydrogen electrode. Each dot played the role of Reversible Hydrogen Electrode, from which the local potentials could be accessed. To evidence the internal layout of the segmented device regarding potential measurements, a cross-sectional view is given in Fig. 2.12.

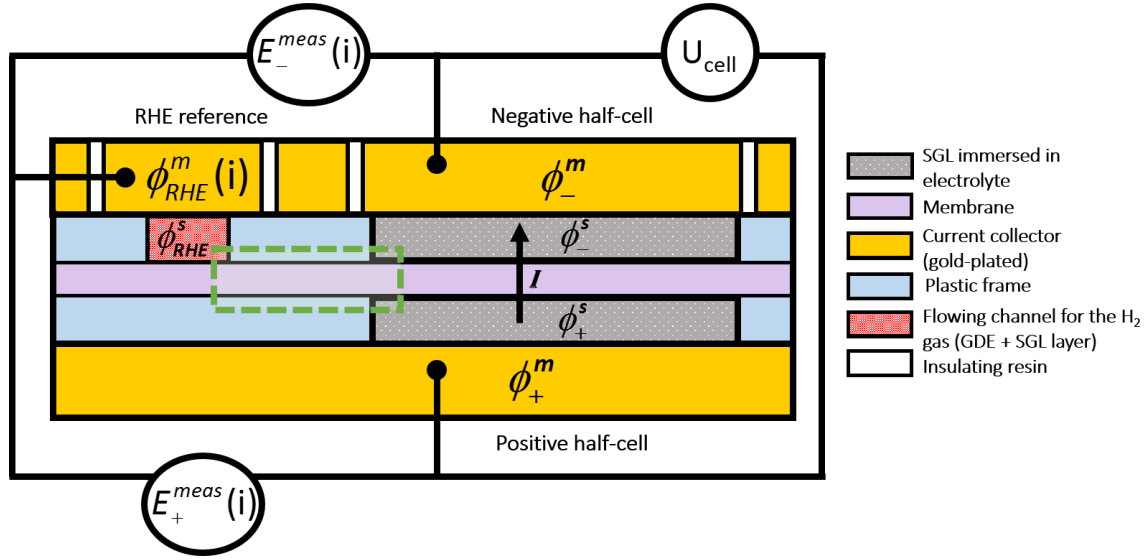


Figure 2.12: Cross-sectional view of the segmented cell and the measurement of local potentials with respect to the Reversible Hydrogen local Electrode reference. The channel of RHE (in red) is composed of one layer of GDE topped by a piece of porous SGL electrode, humid H_2 flows through the reference electrodes. The green dashed rectangle represents the zoom sketched in Fig. 2.13b. Adapted from [6].

When a metallic electrode (m) is immersed in a solution (s), there is an interfacial difference between the internal potential of the two phases. It is called the electrode potential E :

$$E = \phi^m - \phi^s \quad (2.16)$$

The voltage of a cell U_{cell} is measured between the two metallic phases at the ends of the cell, as depicted in Fig. 2.12. It is given by:

$$U_{\text{cell}} = \phi_+^m - \phi_-^m \quad (2.17)$$

Practically, the potential difference between the solid phases of the electrodes, ϕ_+^m or ϕ_-^m , and the solid phase of the local reference at the segment i $\phi_{\text{RHE}}^m(i)$ can be measured. As

Fig. 2.12 illustrates, the cell voltage can be expressed by these potential measurements:

$$U_{\text{cell}} = E_+^{\text{meas}}(i) - E_-^{\text{meas}}(i) \quad (2.18)$$

$$\text{with } E_{+/-}^{\text{meas}}(i) = \phi_{+/-}^m - \phi_{\text{RHE}}^m(i) \quad (2.19)$$

Only the reference potential has the local index i because its solid phase is segmented. The solid phase of the electrode is not necessarily segmented (only on the negative side).

The voltage can also be expressed with the potentials of the phases constituting the inside of the cell. An equivalent resistance R is introduced. It stands for the resistance of the membrane and of the two solutions, by considering predominant losses in the liquid phases and neglecting losses due to electronic transport.

$$U_{\text{cell}} = \phi_+^m - \phi_+^s - IR - (\phi_-^m - \phi_-^s) \quad (2.20)$$

I actually represents the local current $I(i)$. ϕ_+^s is also dependent on the internal position along the cell, but for simplicity sake the index $I(i)$ is removed.

In the following of this section, R will be reduced to the sole contribution of the membrane resistance R_m for simplicity sake. Chap. 4 will confirm that the major part of the ohmic losses in the cell are caused by the membrane.

When no current flows through the cell, there is no internal ohmic drop: the solution phases ϕ_+^s and ϕ_-^s of the two electrodes have the same potential. (2.20) is simplified by:

$$U_{\text{cell}}(I = 0) = E_+(i) - E_-(i) \quad (2.21)$$

Comparing (2.18) and (2.21) shows that the measured electrode potentials $E_{+/-}^{\text{meas}}$ equal the real electrode potential $E_{+/-}$ only at no current.

In the real set-up, only U and E_+^{meas} are recorded. E_-^{meas} is deduced from these records. E_+^{meas} can be decomposed as follows, by bringing out the intermediate potential phases in (2.19):

$$E_+^{\text{meas}} = \phi_+^m - \phi_+^s + \phi_+^s - \phi_{\text{RHE}}^s + \phi_{\text{RHE}}^s - \phi_{\text{RHE}}^m \quad (2.22)$$

Eq.(2.22) includes the following assumptions: the contact and bulk resistances of the solids are ignored (the potentials in the metallic and electrode solid phases are equal and homogeneous along the channel), the junction potential between the membrane and the positive electrolyte is neglected as well.

The comparison of the RHE in the segmented cell with another reference electrode (detailed in subsection 2.4.4) confirmed that their potential was close to the standard 0 V value:

$$E_{\text{RHE}} = \phi_{\text{RHE}}^s - \phi_{\text{RHE}}^m = 0 \text{ V} \quad (2.23)$$

In (2.22), the remaining entity to assess is $\phi_+^s - \phi_{\text{RHE}}^s$. To that end, a simple 2D stationary model was developed with the COMSOL Multiphysics® program. The potential distribution in the membrane and the porous electrodes was simulated according to the current applied in the cell. Current conservation through the entire domain was solved with Ohm's law (4.18) applied in each phase. The three phases were considered isotropic and homogeneous. The

conductivities of the phases were set to 10 S m^{-1} for the electrodes (which corresponds to the electrolyte conductivity) and 1 S m^{-1} for the membrane. The numerically-resolved potential distribution in the membrane sandwiched between the two electrodes is illustrated in Fig. 2.13a.

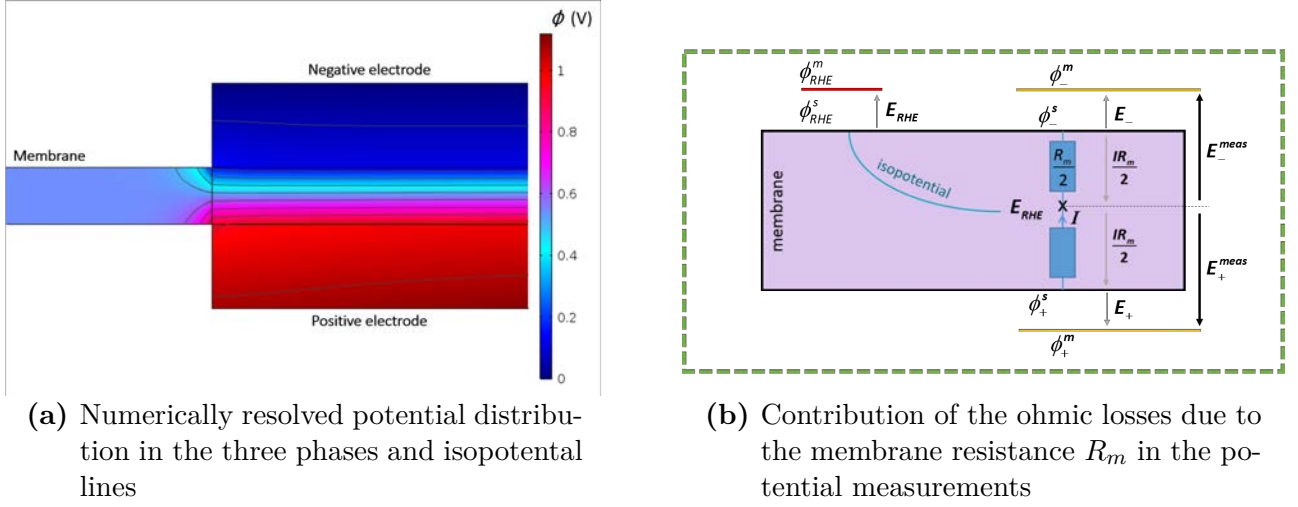


Figure 2.13: RHE in edge configuration: Schematics of the potential distribution and membrane resistive contribution in the measured potentials. Case of a perfect alignment of the two electrodes

The potential at midpoint of the membrane in the active surface expands to the rest of the membrane that is far away from the electrodes. The isopotential lines represented in black show that there is a gradient on a short distance outside the active surface. Further, the membrane takes an homogeneous potential.

Fig. 2.13b complements Fig. 2.13a by sketching the phase potentials in the electrodes and the RHE, along with the ohmic drop inside the membrane. It is a zoom in of the green dashed rectangle of Fig. 2.12. The electrolyte/metallic interfaces are represented outside the membrane by the solid lines (yellow for the two electrodes and red for the RHE).

According to the simulation, the potential of the reference E_{RHE} actually lies in the middle of the membrane. As a consequence, the membrane resistance R_m splits into two equal contributions on both sides of this midpoint. Therefore, the measured positive potential corresponds to the actual electrode potential overestimated by one half of the local ohmic losses in the membrane, as outlined in Fig. 2.13b:

$$E_+^{\text{meas}} = E_+ + \frac{IR_m}{2} \quad (2.24)$$

The negative electrode potential E_-^{meas} is deduced from the measurements of E_+^{meas} and U . Likewise, it underestimates the actual E_- :

$$\begin{aligned} E_-^{\text{meas}} &= E_+^{\text{meas}} - U \\ &= E_- - \frac{IR_m}{2} \end{aligned} \quad (2.25)$$

From this analysis, several deductions can be retained for RHE in edge-type configuration:

- ➔ The side on which the RHE is placed does not affect the signal.
- ➔ The membrane resistance induces an error on the potential values when current is passing through the cell. A correction is necessary to obtain the accurate potential. The ohmic loss can be evaluated by electrochemical impedance spectroscopy, as suggested in [134].
- ➔ In the vicinity of the active surface, the membrane potential is not uniform (Fig. 2.13a). The RHE position must observe a distance from the electrodes of at least 1.5 times the membrane thickness, so that it lies in the constant potential region. This criterion was determined by Liu et al. for a PEMFC [135].

Fig. 2.13 and the related equations (2.24) and (2.25) stem from the ideal case of perfect electrodes alignment. However, real cell assembly can feature a small misalignment δ between the two electrodes. Fig. 2.14b reproduces the membrane and electrodes of Fig. 2.12, but this time with misaligned porous electrodes. The distance between the overhanging electrode and the RHE is called L ; e_m represents the membrane thickness, equal to $80\text{ }\mu\text{m}$.

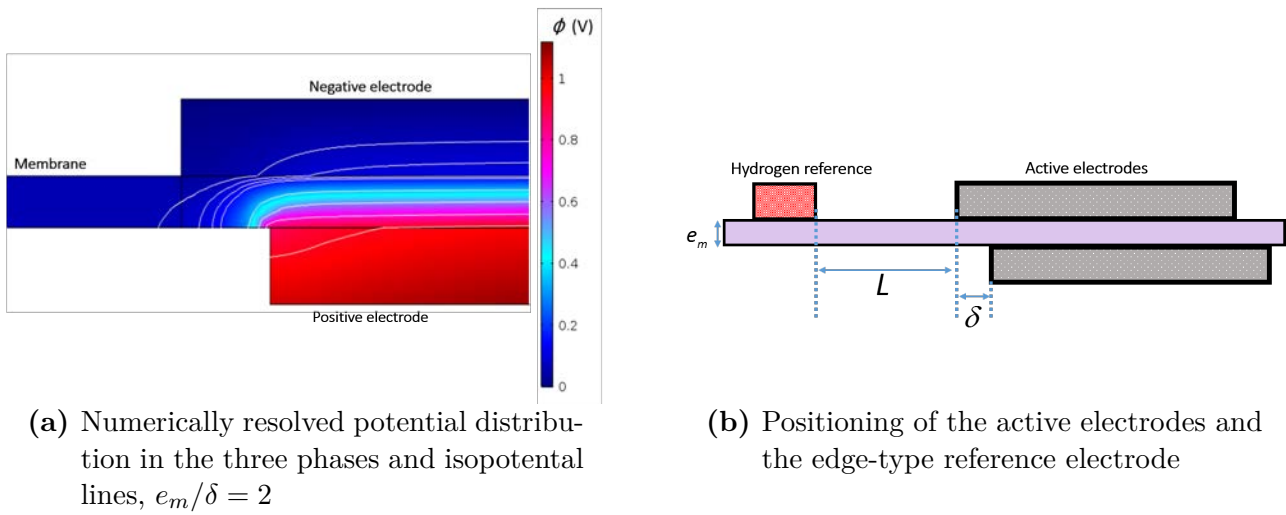


Figure 2.14: RHE in edge configuration: Schematics of the misalignment problem in the cell assembly and simulated effect on the potential distribution in the membrane

Previous papers unraveled the misleading effect of electrode positioning on the potential signal [135, 136]. Indeed, if one electrode is slightly overhanging, the potential contours will bend towards the backing electrode such that the RHE sensing point will deviate towards the potential of the electrode that sticks out. The signal will equal the negative solid phase potential when the misalignment factor δ/e_m increases above 1. Fig. 2.14a depicts the simulated potential distribution for a misalignment factor of 2. In real conditions, it would correspond to a difference of $160\text{ }\mu\text{m}$ between the two electrodes, which is impossible to control when assembling the segmented cell.

Liu et al. [135] also discovered that an additional cause for deviation of the symmetrical potential profile in the membrane was a significant difference in the kinetics of the two electrode reactions. The non-limiting side draws the RHE sensing point to its potential. This effect can hamper the measurement accuracy in fuel cells, but was not a source of error in this PhD study, where kinetics on both sides are equivalent (section 3.1).

Manufacturing of the membrane-electrode assembly in PEM fuel cells accounts for the misalignment default and thus is hard to overcome. In solid oxide fuel cells, the use of thick

separator mitigates the problem because a higher δ is acceptable to keep the misalignment factor low [135]. In redox-flow batteries, thick porous electrodes are cut and positioned by the operator during cell assembly. Non-aligned position is likely and difficult to control. The use of thicker membrane would not be an option to reduce the misalignment impact, since it would in turn impair the cell performance.

2.4.4. Assessment of the local RHE

Once all the possible hurdles were identified, verification tests were carried out in the segmented cell to assess the local potential accuracy. The segmented cell was assembled in a symmetric configuration with catholyte pre-charged at SOC 50 on both sides. It was used to quantify the RHE potential versus a standard reference and then to evidence whether the RHE sensing point detected the midpoint between the electrodes or if the geometry would query the potential probing.

Firstly, the potential taken by the RHE relative to another reference was evaluated. An auxiliary reference electrode Ag/AgCl (from Metrohm France) was immersed in one of the tanks and the potential plug of the first segment was connected to this external electrode. Fig. 2.15 displays the log of the positive electrode potentials while the cell was at rest also called Open Circuit Voltage (OCV) conditions. From now on, the numbers of the segments are noted #1 - #20 to avoid cumbersome notations.

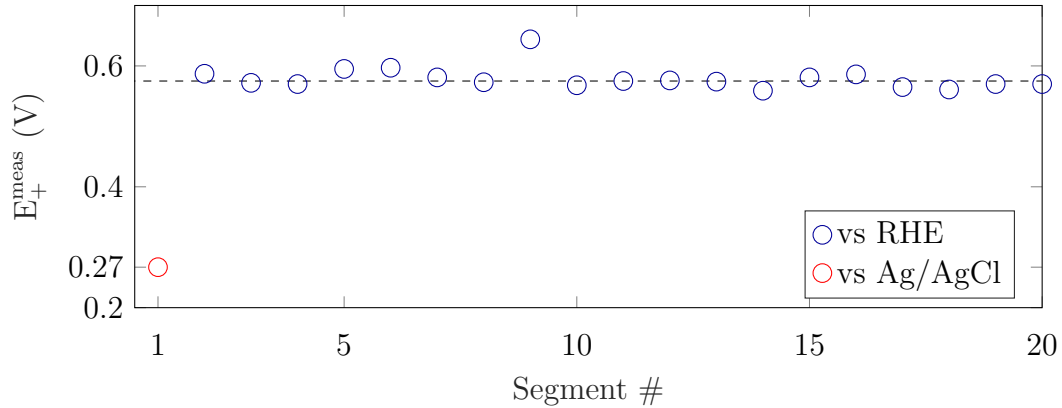


Figure 2.15: Local positive electrode potentials measured versus the local RHE at OCV, Seg. #1 measured versus an external Ag/AgCl, in a catholyte symmetric cell at rest

Seg. #1 has a potential equal to 0.267 V, representing E_+^{meas} vs Ag/AgCl. As predicted, it matches exactly the formal potential $E^{0'}$ determined for this couple during ex-situ characterization (section 3.1). The other local potentials give E_+^{meas} vs RHE; no ohmic contribution disrupted them since they were recorded without current in the cell. They are homogeneous and averaged to 0.575 V (dashed line in Fig. 2.15). The difference between potential #1 and potentials #2-20 quantifies the potential shift of the in-situ RHE compared to the external Ag/AgCl reference. Its own potential is shifted by $E_{Ag/AgCl} = + 0.23$ V from the universal SHE. The RHE implemented in the segmented cell can take a slightly different potential value depending on its experimental conditions. Thanks to the measurements in Fig. 2.15, its real

potential can be assessed:

$$\begin{aligned} E_{\text{RHE}} &= 0.267 - 0.575 = -0.31 \text{ V}_{\text{Ag/AgCl}} \\ E_{\text{RHE}} &= -0.31 + 0.23 = -0.08 \text{ V}_{\text{SHE}} \end{aligned} \quad (2.26)$$

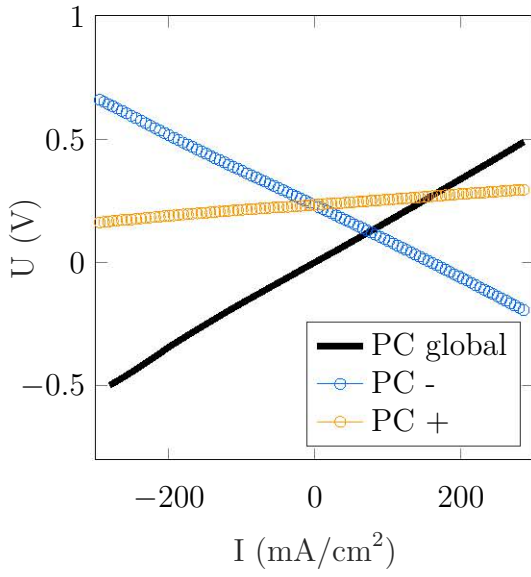
The 80 mV offset from the standard hydrogen reference is due to the non-ideal experimental conditions, in particular the pH may not be 0. The Ag/AgCl electrode served as the reference throughout the PhD study so the local potentials measured against the RHE were converted according to (2.26).

The next step was to quantify the actual potential detected at the RHE sensing point once current was flowing through the cell. In the segmented set-up, the frames holding the porous electrodes were symmetrical so that there should not be any misalignment of the two electrodes. The in-situ RHE enables to dissociate the two sides and obtain their specific characteristics.

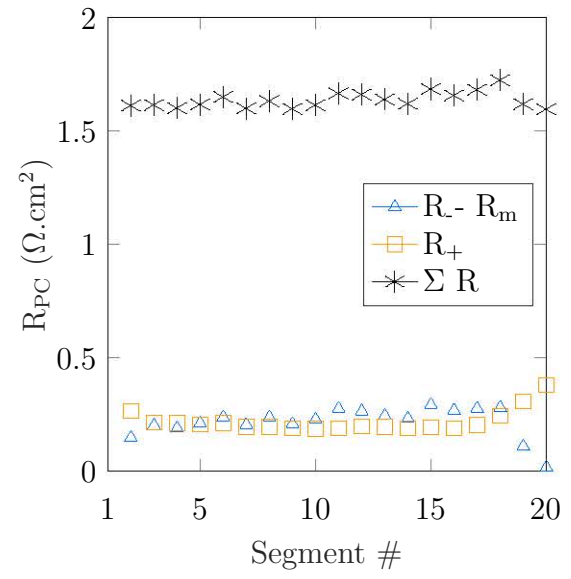
Polarization curves were performed in the symmetric catholyte cell to quantify the electrode-specific resistances. Fig. 2.16 gathers the global PC of the symmetric cell in black, and the local PCs of Seg. #5 for each half-cell, obtained by plotting $E_+^{\text{meas}}(i)$ vs $I_{\text{seg}}(i)$ in orange and $E_-^{\text{meas}}(i)$ vs $I_{\text{seg}}(i)$ in blue. The potential values have been converted in regard to the Ag/AgCl reference ahead of the plotting. Since the composition of each electrode is symmetric, their specific PC starts from the same open circuit potential and have opposite directions. While one side is charging, the other undergoes the discharge reaction. However, it comes to light that their slopes are not alike suggesting that the negative electrode is more resistive than the positive. This is unexpected in the symmetric set-up. It rather hints that the potential at the RHE sensing point is not at the middle plane between the two electrodes, as described in the previous section and illustrated in Fig. 2.14. Further experiments (described in Sections 4.3.3 and 4.4.3) attributed to the membrane an internal resistance of $R_m = 1.2 - 1.3 \Omega \text{ cm}^2$. If this ohmic drop is subtracted from the slopes of the negative PC, it gives the local electrode resistances depicted in Fig. 2.16b. Orange squares represent the positive resistances directly calculated from their raw PCs while the blue triangles give the negative resistance after correction by R_m . The sum of the three internal resistances $R_m + R_- + R_+$ is marked by black stars; their constant values prove a homogeneous reaction distribution along the channel. R_+ and corrected R_- are similar which is awaited in a symmetric set-up. Although the geometry is supposedly equivalent on both sides, the iR -correction must be entirely applied on the negative electrode because the RHE detects the potential at the positive electrode/membrane interface.

Once it was clear that the RHE sensing point detected the positive electrode potential, it was necessary to test whether this potential distribution remained similar with time. The PC was performed again after two days of circulation; the global characteristic remained unchanged from initially. Fig. 2.17 represents the local resistances derived from the local potentials during PC after circulation. Fig. 2.17a depicts the raw results whereas Fig. 2.17b presents R_- after the same ohmic-correction as done in Fig. 2.16b. It reveals that this over-corrects the negative electrode resistance for many segments. The potential distribution evolved with time and was no longer equal for all the segments. Fig. 2.17a shows an asymmetry between the inlet and outlet of the cell. It is thus impossible to know how R_m splits into the two electrodes at each segment; the resistance and by extension the local potentials are not meaningful.

To confirm that the potential distortion is caused by a misalignment of the two electrodes, new frames were machined in order to force a shift of $\delta = 3 \text{ mm}$. The positive electrode was chosen to be overhanging towards the reference, to have the opposite configuration compared to

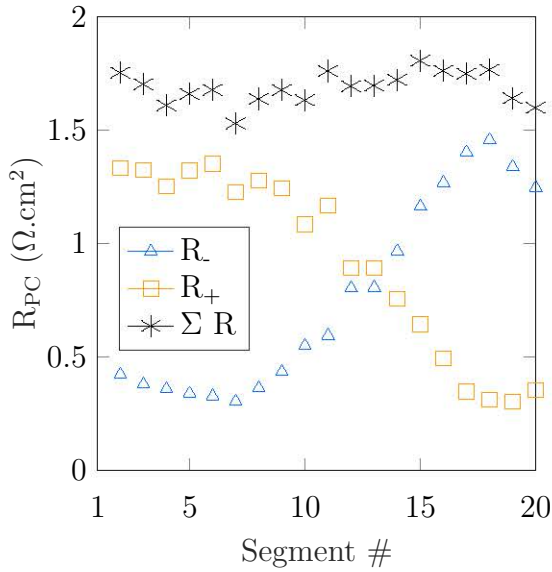


(a) Global PC (black) and Local PCs (Seg. #5) of the positive (orange) and negative (blue) electrodes

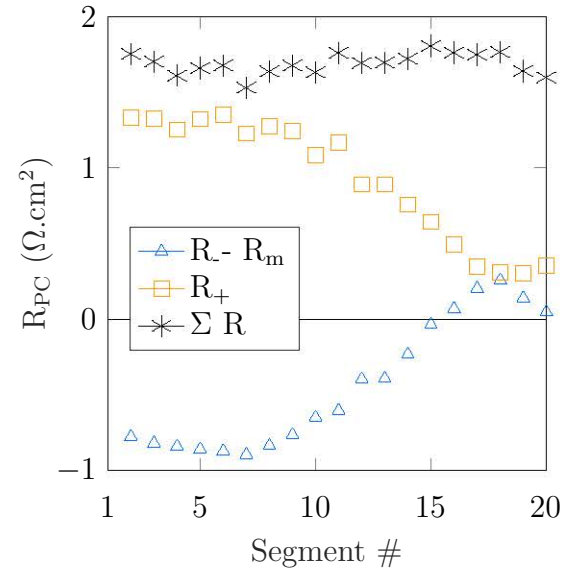


(b) Local resistances of each segment (black) and of each electrode: negative electrode resistance (blue) corrected with $R_m = 1.2 \Omega \text{ cm}^2$

Figure 2.16: Polarization curves of the two electrodes and associated local resistances in a catholyte symmetric segmented cell after iR -correction applied to the negative electrode



(a) Local resistances extracted from local PCs of each segment (black) and of each electrode



(b) Local resistances of each segment (black) and of each electrode: negative electrode resistance corrected with $R_m = 1.2 \Omega \text{ cm}^2$

Figure 2.17: Local resistances in a catholyte symmetric segmented cell after 2-days circulation without and with iR -correction of the negative resistance

Fig. 2.16. The results confirm the trend: this time the positive resistance must be iR -corrected as it was forecast. The obtained electrode resistances equal each other after the compensation, with values close those of Fig. 2.16b.

These insights negate the possibility to equip the RFB segmented cell with a reliable local reference network in edge configuration. The membrane resistance contribution to the two sides depends on the local geometry. It entails that the reference sensing point does not give access to a constant potential over time and along the cell. The RHE is not the appropriate tool for quantitative analysis and decoupling of the component contributions.

In fuel cells, the paradigm is different since membrane resistance is negligible and only one electrode is critical in the process. That is why the reference electrode could be used with the edge configuration in previous studies [6, 137].

The configuration of the local references should be redesigned to be applicable in RFB; the simplest way would be to opt for a sandwich configuration as in Fig. 2.11, but that would necessitate the use of DHE instead of RHE, and the resulting cell resistance would be compounded by the presence of two layers of membrane. The use of thinner carbon papers as porous electrodes might alleviate the alignment issue observed with the carbon felts. Ultimately, the shifted frames configuration mentioned above could be used to control the misalignment of the two electrodes. It could even be imagined to install two sets of reference on both sides of the active surface, so that each reference follows the potential of one electrode. Nevertheless, non-aligned electrodes creates distorted electric field lines and can alter the internal operation of the cell.

2.4.5. Test bed

The elements presented in subsection 2.4.1 were assembled and tightened with a torque screwdriver to 1 N m. Similarly to the standard cell, the segmented cell was rinsed with salt solution and then the anolyte circuit was purged with nitrogen gas before starting the cycling (details in subsection 2.2.1).

Fig. 2.18 depicts the fluid connections of the test bed. The two sides of the cell were supplied by parallel flows of electrolyte and the segments were numbered 1 to 20 from the flow inlet. The diaphragm pumps could provide a flow rate between 1 and 100 mL min⁻¹. Due to the narrow active channel of this segmented cell, a precautionary step was taken when using a new set-up and fresh electrolytes: the flow rate was restricted to a value of 50 mL min⁻¹ during the first cycle to lessen the pressure drops and prevent a potential packing or clogging of the felts. This was decided in view of the high viscosity of the fresh anolyte, as presented in the characterization chapter (subsection 3.2.2). After one cycle, the flow rate could safely be adjusted to the desired value.

A gauge placed after the pump measured the absolute pressure at the inlet. The atmospheric pressure (taken as 1 bar) was subtracted to this value to get the pressure drops inside the cell. A flowmeter was installed in each hydraulic circuit to verify the flow rate delivered by the pump. Parallel to the active channel, the reference channel was supplied by a 50 mL min⁻¹ flow of H₂-gas that was humidified upstream in a gas bubbler. This precaution ensured adequate wetting of the membrane in the reference electrode channel. The gas circuit was connected to a pressurized hydrogen container with a pressure regulator. The temperature-control bath generated a flow of water through the serpentine channels of the cell external slabs.

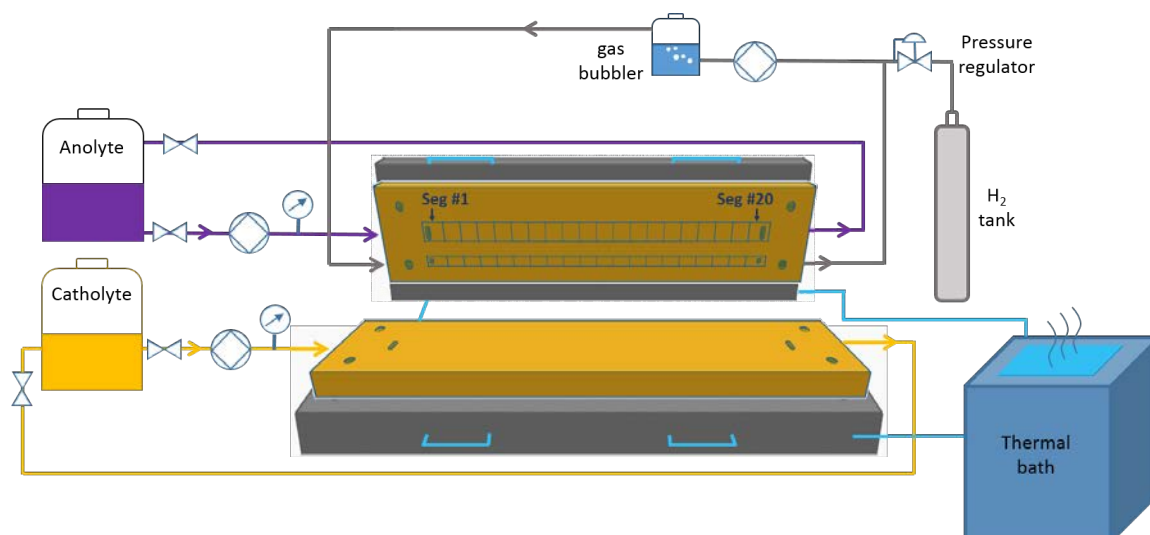


Figure 2.18: Fluid circuit drawing of the segmented cell test bed

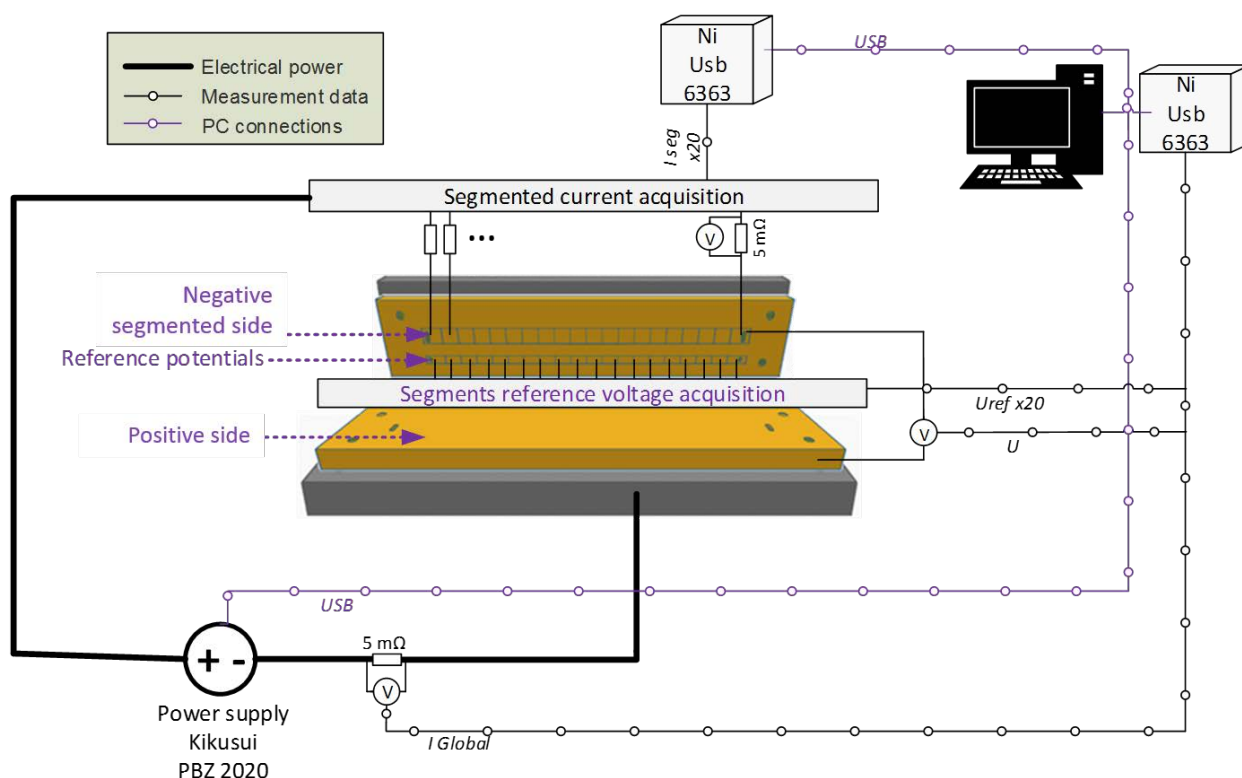


Figure 2.19: Electrical circuit drawing of the segmented cell test bed

A LabVIEW control software developed at the laboratory was used to manage the experimental facility. A schematics of the electrical installation and communication paths is presented in Fig. 2.19. The cycling and characterization steps were defined on the computer interface along with the operating conditions: pumping power, cell temperature and electrical power supply. The cell and the auxiliary devices were controlled in real time during operation. The platform collected the global and local electrical data but also the flow rate and pressure drops in each electrolyte flow path.

2.5. Conclusion

The two main battery set-ups used during the PhD study have been introduced: the standard 25 cm² test cell and the segmented cell. They are all composed of similar electrolytes and materials, described in the first part. A particular case is the symmetric configuration that was implemented either in the standard cell. These set-ups were alternatively used depending on the specific needs of the experiments. [Chap. 4](#) outlines the study of each electrolyte in symmetric configuration of the standard cell, while [Chap. 5](#) describes the full cell study by means of the segmented set-up. It can be noted that all the tests with the standard cells were performed at the company Kemiwatt, while the segmented test bench was run at LEMTA.

3

SEPARATE CHARACTERIZATION OF THE COMPONENTS

Contents

| | |
|--|-----------|
| 3.1 Electrochemical analysis | 54 |
| 3.1.1 Electrolytes and assumptions | 54 |
| 3.1.2 Electrochemical cell | 55 |
| 3.1.3 Potential window and reversibility of a redox couple | 57 |
| 3.1.4 RDE voltammetry | 59 |
| 3.1.5 Cyclic voltammetry | 63 |
| 3.1.6 Discussion of the results | 66 |
| 3.2 Physico-chemical electrolyte properties | 69 |
| 3.2.1 Conductivity | 69 |
| 3.2.2 Viscosity | 70 |
| 3.2.3 Material compatibility and photodegradation of catholyte | 72 |
| 3.3 Membrane characterization | 74 |
| 3.3.1 Membrane pretreatments: FTIR-ATR study | 75 |
| 3.3.2 Membrane affinity with solutions | 78 |
| 3.4 Porous electrode characterization | 86 |
| 3.4.1 Structural observation | 86 |
| 3.4.2 NMR analysis | 87 |
| 3.4.3 Comparison of two materials by blocking electrode model | 90 |
| 3.5 Conclusion | 93 |

The RFB system implies the continual interaction of all the constituent parts. The study of such complex energy conversion tool must begin by the separate and ex-situ characterization of each component, as undertaken in this chapter. The battery performance first relies on the electrochemical response of the electrolytes. By means of several methods, the intrinsic properties of each electroactive material are resolved. Their physico-chemical characterization follows. In a second place, the membrane is investigated by a surface technique to evaluate

several pretreatments of the material. The separator reaction to electrolyte exposure is then scrutinized by measuring its swelling and determining its conductivity in a specific symmetric set-up. In a last part, the porous electrode is visualized before being characterized again with the help of the symmetric cell configuration.

3.1. Electrochemical analysis

Analytical techniques are widely used for the initial characterization of an electrochemical system. They require a specific three-electrode set-up. A typical method is the linear sweep voltammetry (LSV): the potential of the working electrode is linearly swept with time at a controlled scan rate v , ranging from 0.01 V s^{-1} to 10 V s^{-1} . The current induced at the electrode is recorded to obtain current-potential curves, called voltammograms. The mass transport of reactants and products to the reactive surface dictates the current flowing. Two experimental conditions are distinguished: the working electrode can be stationary, giving a dynamic response of the system, or it can be a rotating disk electrode (RDE), leading to a steady-state convective method. These cases are respectively called cyclic voltammetry (CV) and RDE voltammetry. CV records inform about the reversibility of the electrochemical system (subsection 3.1.3). Fundamental relations specific to each electrochemical method have long been utilized to determine characteristics such as the diffusion coefficient of the species D , the electron-transfer rate constant of the reaction k_0 or the transfer coefficient α . In subsection 3.1.4, Levich and Koutecky-Levich equations will be applied to the RDE results. In subsection 3.1.5, the CV data will be analyzed with the methods of Randles-Sevcik, Nicholson, Gileadi and Laviron. All the results will be compared in subsection 3.1.6.

3.1.1. Electrolytes and assumptions

The electrolyte compositions analyzed in this section are equivalent to the electrolytes used in the real RFB system: the catholyte was an alkaline solution of the ferrocyanide $\text{K}_4\text{Fe}(\text{CN})_6$ at 0.5 M dissolved in 0.2 M NaOH. The anolyte was composed of 0.2 M of ARS in 1.2 M KOH. The active material concentration is noted C_1 . Another lower concentration $C_3 = \frac{1}{3}C_1$ was studied by CV for the catholyte, because the results complement the half-cell study of this side (presented later in section 4.3). In the equations, the total active species concentration is referred to as C_{tot} ; it can either equal C_1 or C_3 , depending on the solution of study.

The laws applied in the next sections assume that dilute-solution theory holds. It means that the active species (solutes) only interact with the solvent and do not influence each other [76]. This may not be true for the concentrated electrolyte systems considered here. As such, the interaction between the molecules of solutes, quantified by the ionic strength of the solution, can create ion pairs and affect the solution viscosity [2]. The standard potential of the couple deviates from the theoretical value E^0 as the non-ideal interactions increase. It is called the formal potential $E^{0'}$. This notation will be used in the following since the study focuses on concentrated solutions.

The concentrated-solution theory would be more accurate but cumbersome [1]. It was chosen in the present electrochemical analysis to apply several laws of dilute-solution theory to the real solutions used in the RFB so as to appraise whether they remain applicable and give coherent estimates.

3.1.2. Electrochemical cell

Analytical electrochemistry is performed in a three electrode set-up (Fig. 3.1). The working electrode (WE) is a glassy-carbon electrode of surface $A = 0.07 \text{ cm}^2$. The counter-electrode (CE) is a platinum wire whose surface is largely superior to A , and the reference electrode (RE) used is an Ag/AgCl electrode placed in a protective porous frit, filled with the same supporting electrolyte as the solution under study. Polishing the WE prior to each experiment is essential to remove any pollutant in order to activate its surface. It is done mechanically on a new polishing pad. The potentiostat controls the WE potential noted E with respect to the RE and monitors the current flowing between the WE and the CE to apply the potential required by the user. In other words, when a current is drawn from the surface of the electrode, the latter is deviated from equilibrium by an overpotential called $\eta = E - E_{eq}$ (E_{eq} is defined by the Nernst equation (1.4)).

This potential control in a resistive solution can lead to misleading errors that have to be minimized [138]. The compensated resistance identified as R_C in Fig. 3.1 is automatically compensated by the potentiostat. The remaining uncompensated R_U needs to be evaluated and then corrected either before the experiment or after during data post-processing, because as the control error is iR_U , it can be substantial for large current flow.

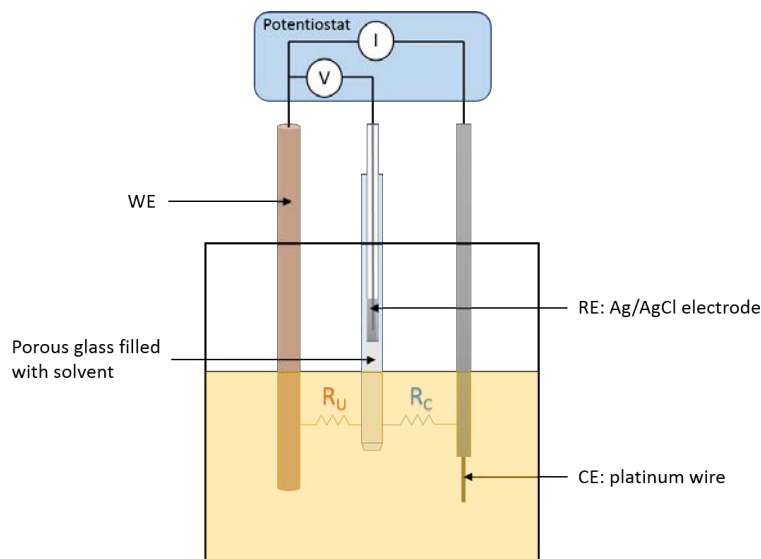


Figure 3.1: Schematic of an electrochemical cell connected to a potentiostat with representation of ohmic losses between the electrodes, adapted from [139]

When assembling a new electrochemical cell, R_U is first estimated by a current interruption measurement. The value is then taken into account during the following experiment. In spite of this precaution, the resistance might not have been compensated exactly due to measurement error (for example, the compensation applied is the average of instantaneous resistances obtained during successive current interruptions).

The data post-treatments show that the parameters estimated by several methods are scattered. It could mean that the appropriate R_U is higher or lower than its first estimate. A small resistance variation ΔR_U is added to the voltammograms data from which k_0 is determined by different ways (described later in subsection 3.1.5). This additive resistance is then changed

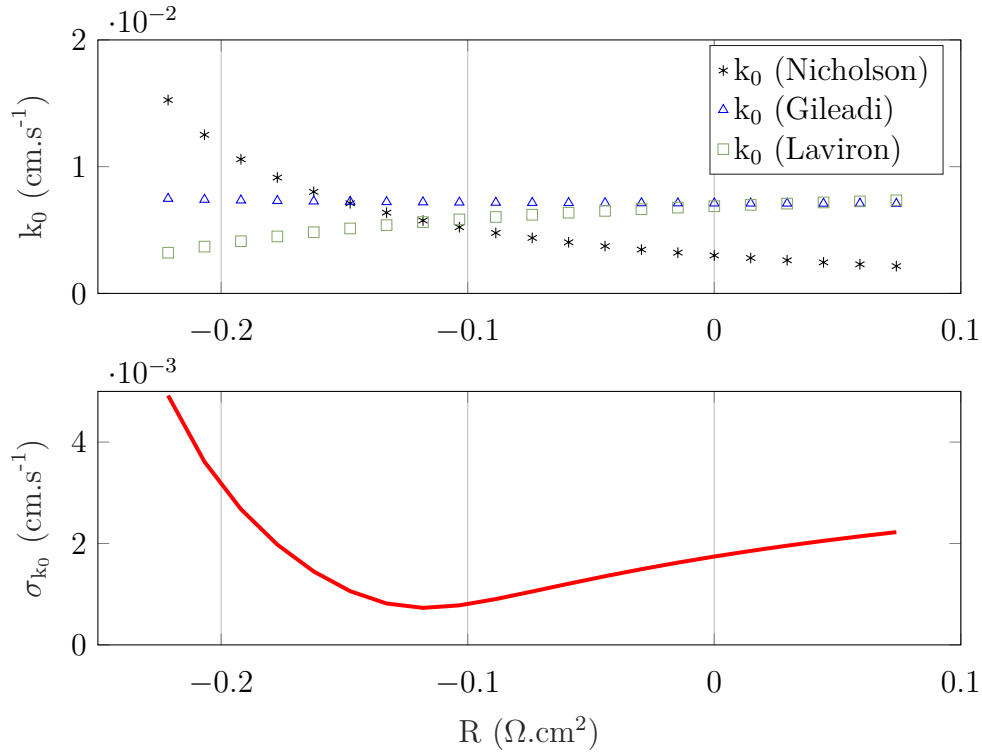


Figure 3.2: k_0 estimates from several methods (top) and standard deviation of k_0 (bottom), as a function of the additive resistance ΔR_U applied during post-treatment. Results from the catholyte analysis at C_1

over a small range of values to observe the influence on this estimate. Fig. 3.2 depicts the estimates of k_0 obtained with several laws (Nicholson, Gileadi and Laviron) as a function of ΔR_U applied during post-treatment. Their standard deviation in the bottom subplot reveals a minimum for $\Delta R_U = -0.12 \Omega \text{ cm}^2$, which corresponds to 10 % of the initial compensation R_U . The optimal ΔR_U is negative in this case: it means that the compensation prior to the experiments was too small.

Determining ΔR_U by analyzing the distribution of the estimated k_0 is the first post-treatment step for each solution under study. The total compensation (applied partly before the experiment and during post-treatment) then equates to: $R_{U_2} = \Delta R_U + R_U$. The impact of this correction on CV plots for both electrolytes is illustrated in Fig. 3.3. This post-treatment correction is small (it represents in all cases less than 10 % R_U) but useful to refine the resistive compensation of the electrochemical cell. However, it does not replace the compensation made before the data acquisition, as only translating CV by IR_U would lead to errors on the peak heights [109].

The shift of the voltammogram baseline from zero is due to double-layer charging at the electrode surface, even when no electrochemical reaction occurs. The peak current must always be measured from the baseline of capacitive current to isolate the faradaic component.

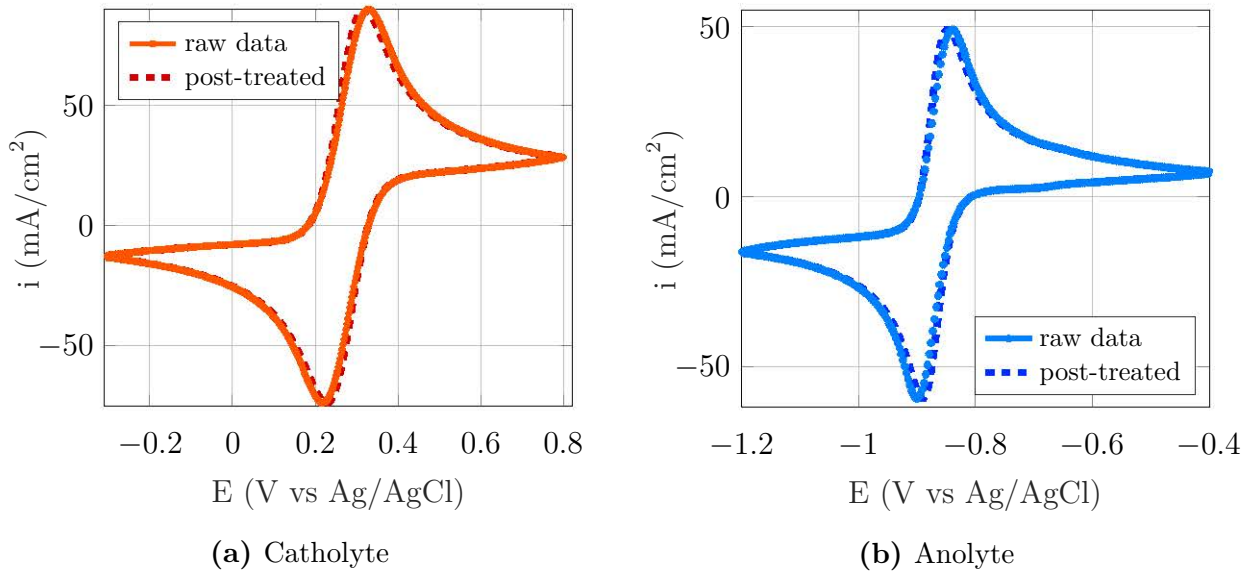


Figure 3.3: Cyclic voltammograms of the two electrolytes before and after post-treatment compensation ΔR_U , $v=100$ mV/s

3.1.3. Potential window and reversibility of a redox couple

Scanning the solution over a wide potential range shows the potential limits over which side reactions would be triggered. For an aqueous solvent the potentials at which oxidation and reduction of water occur can be calculated according to the pH. The reaction kinetics significantly alters the thermodynamic value, therefore it is better to detect the potential window experimentally in real solutions. Fig. 3.4 displays the extended CV of the 2 electrolytes. The peaks corresponding to the electrochemical couples appear in bold.

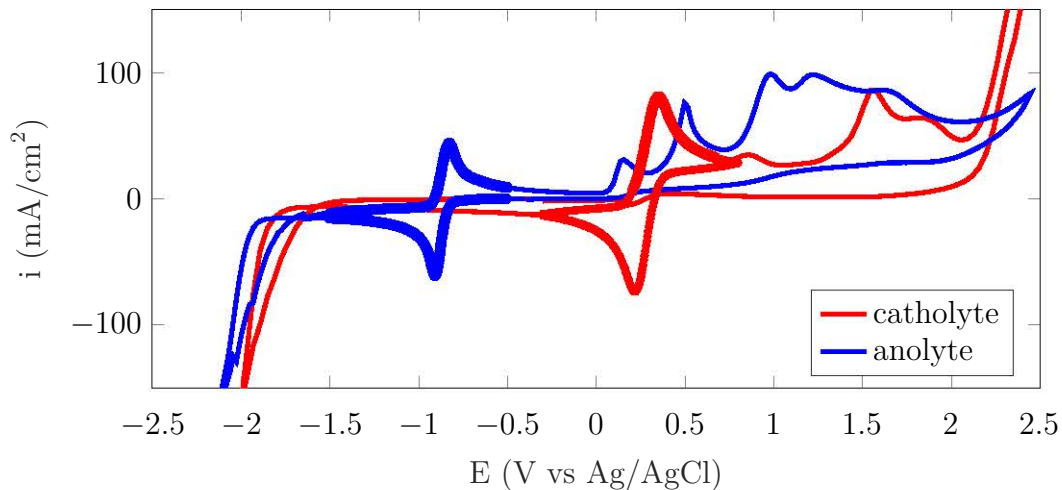


Figure 3.4: Detection of the potential windows by extended CV of the two electrolytes, $v=100$ mV/s

The plots highlight the water-splitting window: water oxidation starts at 2.1 V and its reduction occurs below -1.7 V.

An industrial perspective

The analysis validates that in this configuration of electrolytes, the gassing side reactions are unlikely in the operating window of the active species. Nevertheless, the electrolyte distribution throughout the large-surface electrode should be homogeneous, to avoid local high overpotentials and a risk to form oxygen or hydrogen from water. These parasitic reactions not only diminish the coulombic efficiency by consuming current, but also result in a safety hazard. This represents a technical hurdle of the vanadium RFB systems [140].

From 0.05 V in anolyte and 1.3 V in catholyte non-reversible oxidation peaks appear. They prove that the active materials degrade over these potentials that would be detrimental for the energy capacity. In charge, the catholyte potential must be kept lower than 1.3 V. The oxidation peaks apparent for the anolyte will be more thoroughly addressed in the half characterization in section 4.4.

A redox couple is interesting for battery applications only if it is chemically reversible that is when the reaction is possible in both directions. It is then selected according to its electrochemical and kinetic behaviors. The electron-transfer reaction is called fast when the kinetics of the process is high compared to mass transport occurring at the electrode interface. Given predefined experimental conditions (and therefore a mass transport rate), the rapidity is intrinsic to the system. The couple is also electrochemically reversible if the reaction proceeds back and forth at a similar pace; neither of the reduction nor the oxidation can be neglected. In this case the electrode assumes a potential described by the Nernst equation; it can be qualified as a *Nernstian* system [141]. The reversibility is not an intrinsic feature because it depends on the potential applied to the system. The notions of rapidity and electrochemical reversibility are linked but not exactly interchangeable although the terms are sometimes confused in literature.

The CV of a redox couple is composed of a cathodic and anodic peak when the couple is chemically reversible, and their potential position (E_p) and height (i_p) help to determine its electrochemical behavior. The following properties shed light on a reversible system [77]:

- ➔ The peak potentials E_{pc} and E_{pa} are independent from the scan rate.
- ➔ The peak-to-peak separation $\Delta E_p = E_{pc} - E_{pa}$ equals $59/z$ mV, z being the number of electrons exchanged in the reaction. The process becomes irreversible when the barrier to electron transfer is high and more important potentials from the equilibrium are required to trigger the reaction.
- ➔ The peak currents are proportional to the square root of the scan rate \sqrt{v} .
- ➔ The fraction of the two peak currents equals 1 regardless of scan rate v .
- ➔ The half potential $E_{1/2}$, calculated by the average of the two peak potentials, is a good approximate of the formal potential $E^{0'}$.

As alluded earlier, the formal potential is defined in specific experimental conditions (concentration and temperature) that deviate from the standard ones [142]. The CV results corresponding to each criterion are collected in Table 3.1. The obtained formal potentials are close to previously reported values:

- ➔ -0.9 V_{Ag/AgCl} [143], corresponding to -0.7 V_{NHE} reported in [19] for the anolyte
- ➔ 0.25 V_{Ag/AgCl} [97] or 0.5 V_{NHE} [144] for the catholyte

Table 3.1: Reversibility criteria for both electrolytes according to CV results. ΔE_p deviation from theory is put in brackets, ΔE_p and $E_{1/2}$ are calculated from CV at $v=10$ mV/s, i_p ratio is averaged over all the scan rates

| criterion | catholyte | anolyte |
|--------------------------------|--|---|
| E_p constant | yes for $v \leq 60$ mV/s | slight dependence for $v \leq 200$ mV/s |
| $\Delta E_p = \frac{59}{z}$ mV | 67.2 mV (+14%) | 31.5 mV (+7%) |
| $i_p \propto \sqrt{v}$ | yes for $v \leq 250$ mV/s (Fig. 3.10a) | yes for $v \leq 250$ mV/s (Fig. 3.10b) |
| $i_{pc}/i_{pa} = 1$ | 1.03 | 0.98 |
| $E_{1/2} \simeq E^{0'}$ | 0.27 V _{Ag/AgCl} | -0.87 V _{Ag/AgCl} |

The combination of the catholyte and anolyte species into a RFB gives an interesting cell formal potential of:

$$E_{cell}^0 = 0.27 - (-0.87) = 1.14 \text{ V}$$

The validation of at least three criteria listed above is evidence of reversibility. According to Table 3.1, the electrochemical analysis concludes on the reversibility of the molecules, which is promising for their application in the RFB system. Wedege et al. also characterized the ARS/ARS²⁻ as a reversible couple in strong alkaline conditions [19]. The extended potential scanning of the two solutions also delimits the practical voltage window that must not be exceeded to keep the risk of second reactions away. The next paragraphs target the estimation of the characteristics of each redox couple: the rate constant k_0 or the transfer coefficient α and the diffusion coefficients of the reduced and the oxidized molecule, respectively named D_{red} and D_{ox} . The electrochemical theories are introduced before giving the corresponding graph from which the estimation is made. The determined values are usually given inside the graphs, but they will only be compared and discussed in subsection 3.1.6, once all the methods have been described.

3.1.4. RDE voltammetry

The RDE voltammetry is a technique to analyze the system in steady-state. The working electrode (WE) is rotating at a controlled speed ω and creates a flow of fresh electrolyte to its surface. Convection and diffusion both govern the transport of active material: therefore the electrochemical response depends on both the rotation rate and the characteristics of the redox couple. This is outlined by the resulting voltammeteries at several rotation speeds given in Fig. 3.5 for both electrolytes.

The faster the electrode is spinning, the more reactant reaches the surface and the more current is generated. As a consequence, the plateau of limiting current appearing at large overpotential will be higher (in absolute value) at fast electrode rotation. It is worth observing that the current produced at the WE in electrochemical analysis is noted i [A] below, but corresponds to what is called the faradaic current density j_F in the full RFB cell (in subsection 1.3.1

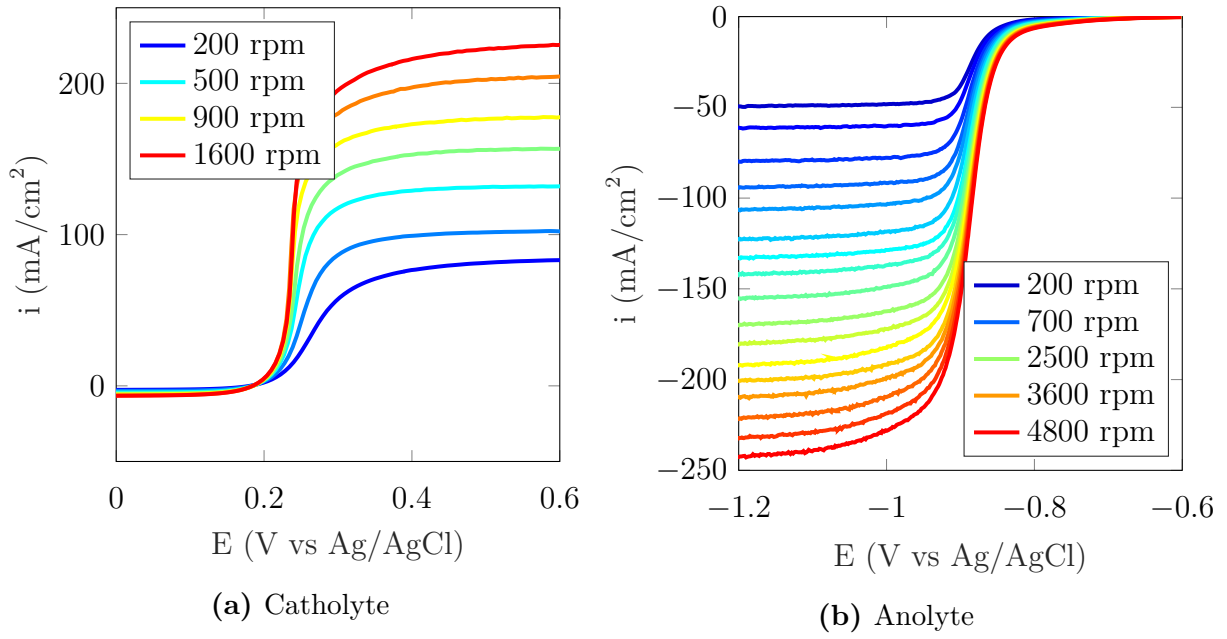


Figure 3.5: RDE voltammograms of the two electrolytes after post-treatment compensation at different rotation rates

and Chap. 4). The notation j relates to current density in A m^{-2} , expressed according to the active surface of the cell.

The limiting current collected at the RDE is caused by mass transport limitation and can be described by the **Levich law** [77]:

$$i_{lim} = 0.62 zFA C_{tot} \nu^{-1/6} D_{reactant}^{2/3} \omega^{1/2} \quad (3.1)$$

A is the electrode surface, C_{tot} the total reagent concentration, ν the solution viscosity and D the diffusion coefficient.

From the RDE voltammograms can be constructed the Levich plots, i_{lim} as a function of $\omega^{1/2}$, for the two solutions of study in Fig. 3.6. The linear regression of these curves give an estimate of the reactant species diffusivity D_{ox} or D_{red} depending on the electrolyte composition (the fresh anolyte contains the oxidant that will react, whereas it is the reducer in the catholyte).

In the transition zone before the limiting current region (at low overpotentials in Figs. 3.5a and 3.5b), the rates of electron transfer and mass transport are comparable. This case is described by the extended **Koutecky-Levich analysis** (KL) that decouples the current collected at the electrode as a kinetic and a mass transport contribution, named i_k and i_{lim} respectively [145]:

$$\frac{1}{i} = \frac{1}{i_k} + \frac{1}{i_{lim}} \quad (3.2)$$

$$\frac{1}{i} = \frac{1}{zFAK C_{tot}} + \left(\frac{1}{0.62 zFA C_{tot} \nu^{-1/6} D_{reactant}^{2/3}} \right) \omega^{-1/2} \quad (3.3)$$

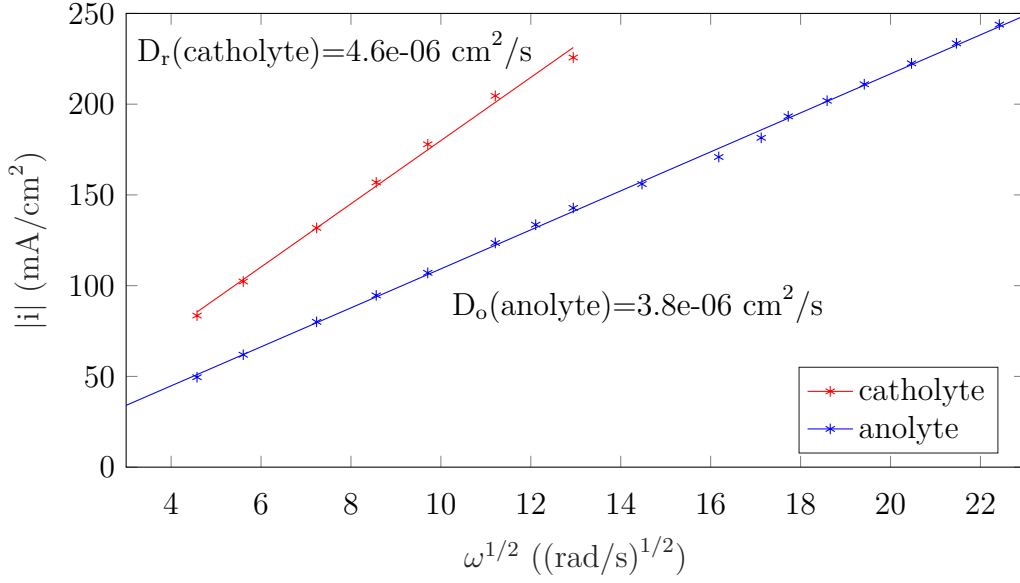


Figure 3.6: Limiting current versus square root of rotation speed for both electrolytes, fit to the Levich equation and diffusion coefficients determined from the slope, 25 °C

K is the reaction rate of the forward or backward reaction (depending on the electrode polarization). It is function of the overpotential η applied to the electrode:

$$K = k_0 \exp\left(\frac{\alpha z F}{RT} \eta\right) \quad (3.4)$$

For a given overpotential η corresponds a current i for each rotation speed tested. From Fig. 3.5 and at several low values of η , a KL line (i^{-1} versus $\omega^{-1/2}$) can be constructed. The obtained plots are linear and parallel and their y-intercept represent the component $i_k(\eta)$ at infinite rotation speed ($\omega \rightarrow \infty$). These extrapolated kinetic terms are depicted as a function of overpotential to obtain a mass-transfer corrected Tafel plot [77].

The Tafel plot is the representation of $\log(i)$ as a function of η , as illustrated in Fig. 3.7. The linear parts of the anodic and cathodic branches can be fitted with the Tafel equations. As mentioned in subsection 1.3.1, they derive from simplifying the Butler-Volmer expression (1.14) when one direction of the reaction (either reduction or oxidation) is dominating, which makes the reverse reaction rate negligible. This happens at high overpotential η . One term of the bracket in BV can be omitted that leads to, in case of uniform concentration:

$$\log |i| = \log |i_0| + \eta \frac{\alpha z F}{RT \ln 10} \quad (3.5)$$

$$\log |i| = \log |i_0| - \eta \frac{-(1 - \alpha) z F}{RT \ln 10} \quad (3.6)$$

Eq. (3.5) represents the case of dominating oxidation and (3.6) the case of predominant reduction.

As illustrated in the figure, the linear fits give access to α from the slope and k_0 from the

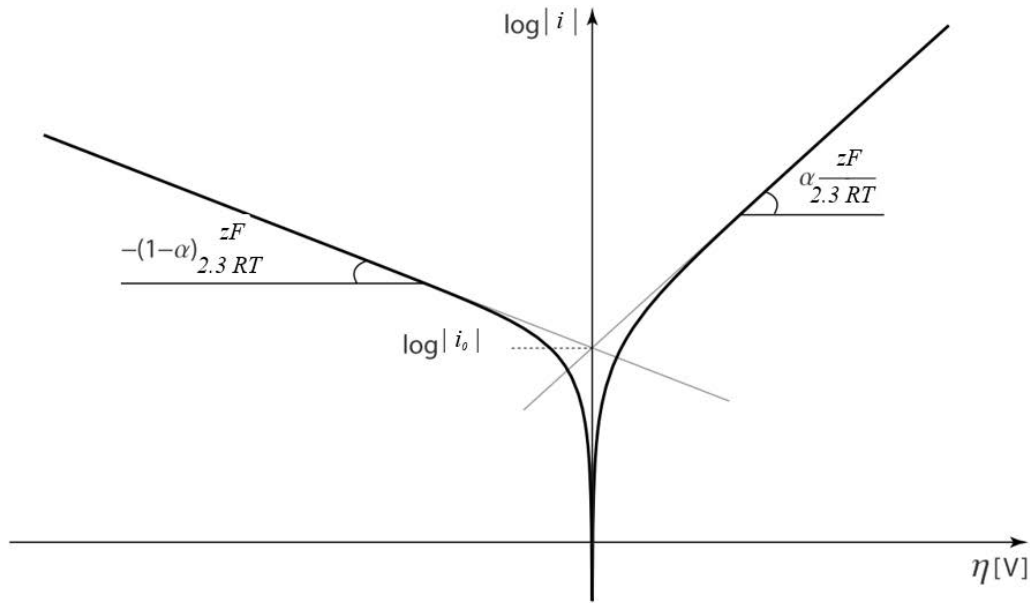


Figure 3.7: Tafel plot for anodic and cathodic branches of the current-overpotential curve, adapted from [141]

x-intercept that is equal to $\log(zFAk_0C_{\text{tot}})$. At low overpotential, the curve deviates from linearity since the approximation of one predominant reaction is no longer valid.

In practice, the Tafel plots also contain deviations at large overpotentials imposed by mass transport limitations [77]. That is why the KL analysis detailed above helps to construct a reliable Tafel plot without transport-induced distortion, and thus improves the quality of kinetic parameters estimation.

RDE requires sufficiently high rotation rates to study the charge transfer process [144]. They could not be attained in the catholyte, because high currents led to a surface pollution on the working electrode which was difficult to eliminate with the cleaning means available at the laboratory. KL study was applied to the anolyte only. The resulting curve and fitted values are given in Fig. 3.8.

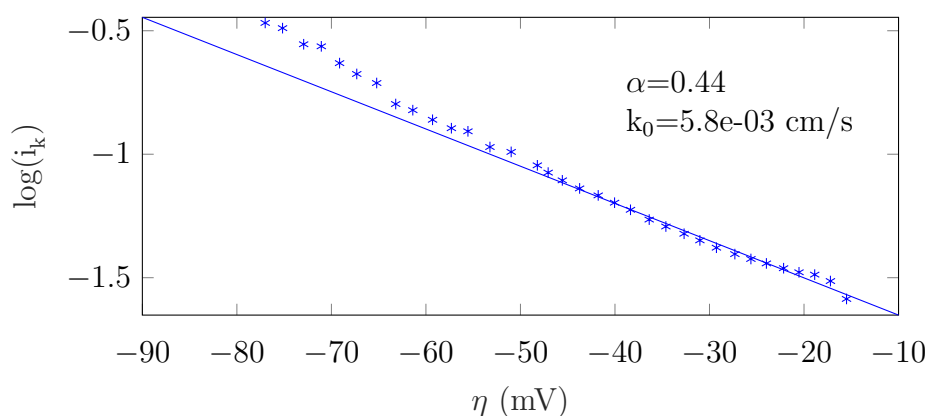


Figure 3.8: Tafel corrected plot with extrapolated i_k from KL plots for the anolyte solution; fitted Tafel line and determined α and k_0

The KL-corrected Tafel plot deviates from linearity above $\eta = -60$ mV. As underlined by Vidal-Iglesias et al., this popular Koutecky-Levich method can have some limitations [145].

RDE voltammetry is useful to determine diffusion coefficients from Levich law or to construct a Koutecky-Levich corrected Tafel plot and estimate k_0 and α . Nevertheless the parameters relate to the reaction of the species present in the solution: reduction for the catholyte and oxidation for the anolyte. The reverse reactions characteristics could not be deduced, unless the solution containing the other form of species was synthesized and the RDE study performed again. Furthermore, the Koutecky-Levich analysis could not be applied to the catholyte, because as RDE voltammetry draws large currents from the electrode, adsorbed intermediate species were created and blocked the surface. The cyclic voltammetry is another characterization procedure that allows the simultaneous study of the forth and back reactions and is less straining for the electrode. It is complementary to the anolyte analysis by RDE and is more suitable for the catholyte study.

3.1.5. Cyclic voltammetry

The CV analysis occurs at the surface of a stationary working electrode, giving the dynamic behavior of the electrochemical system. The only transport mechanism occurring at the electrode surface is diffusion. The electrode potential is swept forth and back around the formal potential of the system $E^{0'}$ at several scan rates v . The scan is repeated several times, giving the name of Cyclic voltammetry (CV) to the method. The voltammograms studied are always the second ones, when the system has reached a steady state.

Fig. 3.9 depicts the CV response for both electrolytes under varying scan rates. The oxidation and reduction peaks result from the diffusion of the species around the active surface: a faster voltage sweep reduces the diffusion layer of the reactants around the electrode so that the resulting peak current is higher, as exemplified by the two sets of curves [139].

The **Randles-Sevcik** equation relates the peak currents to the square root of the scan rate \sqrt{v} for a reversible system involving freely diffusing species (that are not adsorbed onto

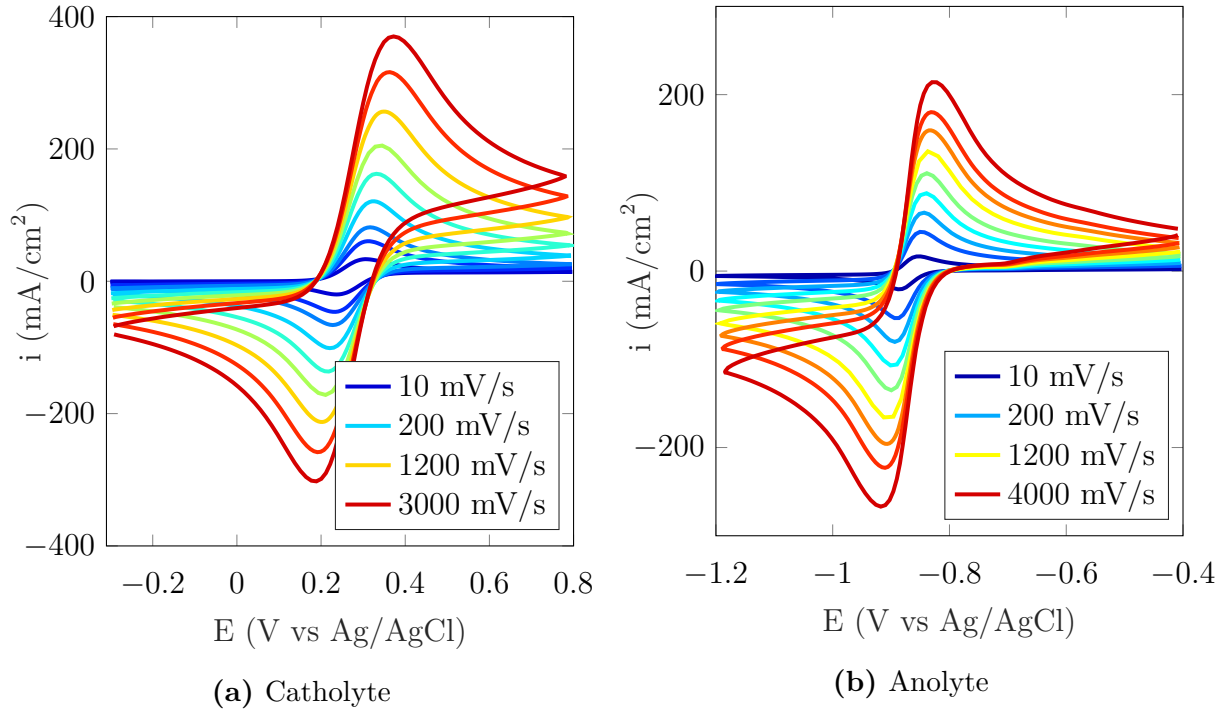


Figure 3.9: Cyclic voltammograms of the two electrolytes at different potential scan rates after post-treatment compensation

the electrode surface) [77]:

$$i_p = 2.69 \cdot 10^5 \cdot n^{3/2} \cdot AC_{\text{tot}} \sqrt{D_{\text{reactant}}} \sqrt{v} \text{ at } 25^\circ\text{C} \quad (3.7)$$

Fig. 3.10 gives the Randles-Sevcik plots (i_p vs \sqrt{v}) of the oxidation and reduction peaks (noted i_{ox} and i_{red}) for both electrolyte. They show a good linear fit at voltammetric scan rates below 250 mV s^{-1} , from which the diffusion coefficients of the respective reagents can be estimated (D_{reactant} is D_r during oxidation and D_o for the reduction reaction). The determined values are given in the legends of Fig. 3.9a; they are needed in the next relations involving the diffusion coefficient.

At higher v , the deviation from a straight line suggests a transition to an irreversible process; the mass transfer outcompetes the reaction kinetics, as stated by Matsuda and Ayabe's condition [146]. It then becomes possible to study the kinetics of the electron transfer reaction.

The **method of Nicholson** links the variation of $\Delta E_p = E_{p_{\text{ox}}} - E_{p_{\text{red}}}$ with v to estimate the electron-transfer rate constant of the reaction k_0 in the case of a quasi-reversible system [147], when ΔE_p becomes significantly higher than the theoretical reversible value $59/z$ (subsection 3.1.3). Dragu et al. developed a fitting function [148] to interpolate the tabulated values initially reported by Nicholson. By using their function, the average k_0 value obtained from the data in Fig. 3.9 is $5.9 \times 10^{-3} \text{ cm s}^{-1}$ for the catholyte, and $6 \times 10^{-3} \text{ cm s}^{-1}$ for the anolyte.

Russel et al. [149] describe the **method of Gileadi**, where the transition from reversible to irreversible process is observed when the scan rate reached a critical level v_c . This threshold is related to k_0 by the following equation:

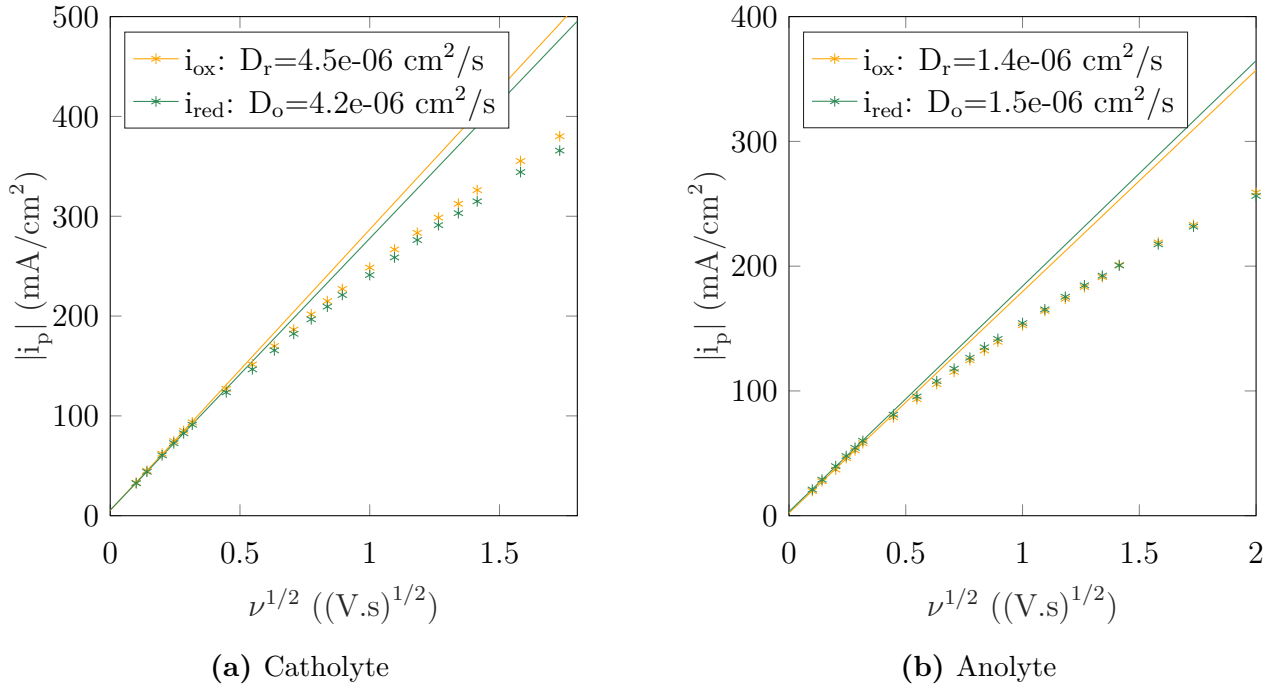


Figure 3.10: Peak current density in oxidation and reduction versus square root of scan rate fitted to the Randles-Sevcik equation and determined diffusion coefficients

$$\log(k_0) = -0.48\alpha + 0.52 + \frac{1}{2} \log \left[\frac{\alpha n F v_c D_O}{2.3 RT} \right] \quad (3.8)$$

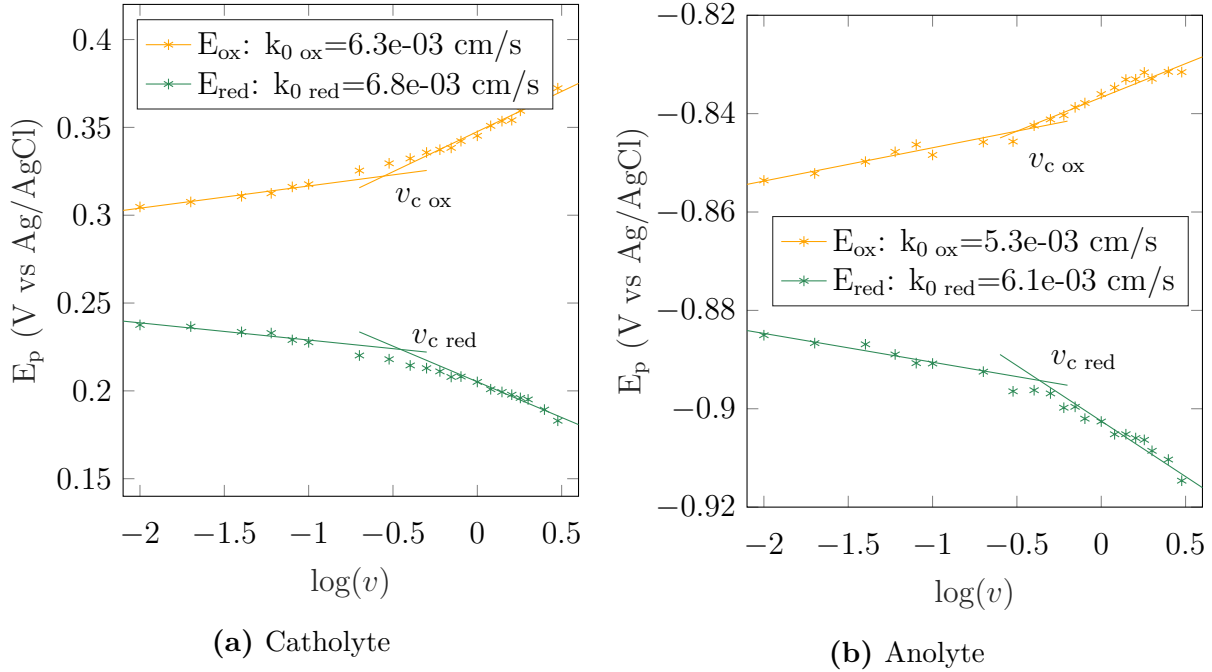


Figure 3.11: Peak potentials versus logarithm of scan rate and determination of the critical scan rates at the intercept of regression lines at low and high v ; k_0 obtained according to the method of Gileadi (3.8)

Fig. 3.11 shows the determination method of the critical scan rate from Gileadi for the two electrolytes, and the corresponding k_0 deduced with (3.8).

For a totally irreversible reaction, i.e. for $v \geq v_c$, the peak current i_p and the peak potential E_p are directly linked by the following equation, sometimes referred to as **Laviron's method** [77]:

$$i_p = -0.227nFAC_{\text{tot}}k_0 \exp \left[-\frac{\alpha nF}{RT}(E_p - E^{0'}) \right] \quad (3.9)$$

The plots of $\ln(i_p)$ with respect to $E_p - E^{0'}$ from Laviron's method are represented in Fig. 3.12 for the two electrolytes. Being the analogy of the Tafel curves in the RDE analysis (Fig. 3.7), the Laviron curves can be fitted with (3.9) to estimate α and k_0 from the slope and the intercept, respectively. This method is only applicable to scan rates above v_c to be in irreversible conditions.

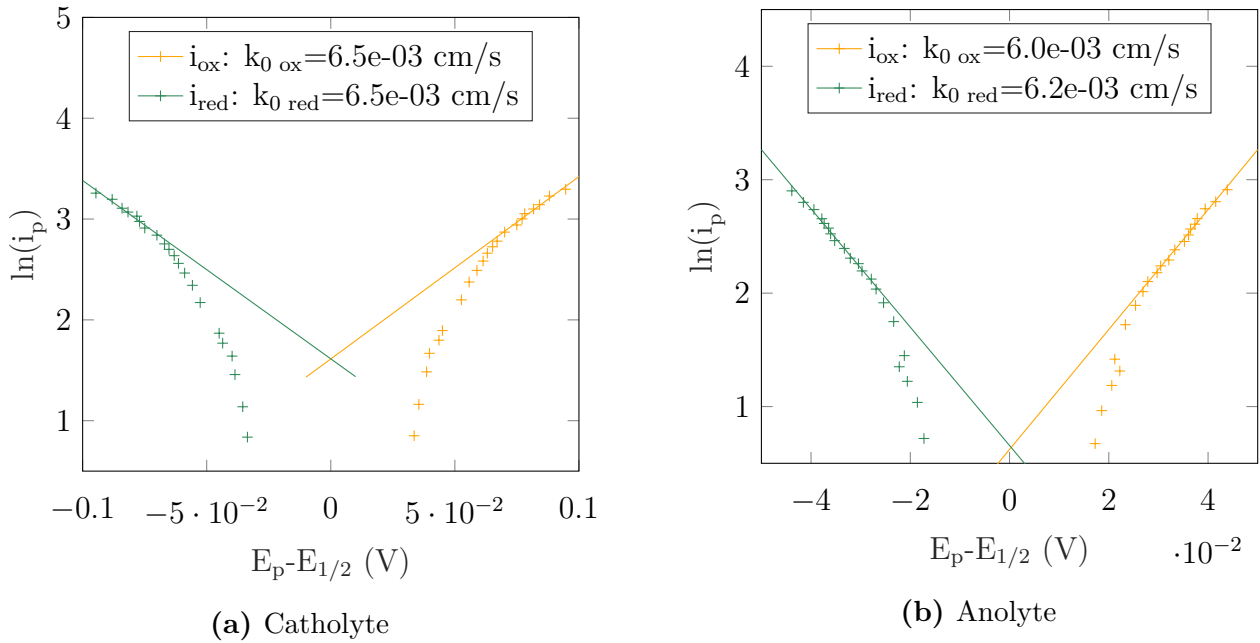


Figure 3.12: Peak current densities versus difference between E_p and $E_{1/2}$, and fitting line at when the system becomes irreversible; determined k_0 from Laviron's equation (3.9)

Only a few points can be fitted at high overpotentials in the case of the catholyte Fig. 3.12a. The anolyte curves show a larger linear region, making the fit more reliable Fig. 3.12b.

3.1.6. Discussion of the results

The stationary RDE and dynamic CV techniques can both lead to the determination of the parameters k_0 , α and D_o/D_r , so that one method can be used to confirm the estimates obtained from the other. The detailed results corresponding to each method are summarized in Table 3.2 for the catholyte and Table 3.3 for the anolyte. For the relations giving access to the parameters of both reactions, the first value before the “/” relates to the oxidation (D_r , $k_{0 \text{ ox}}$ or α_{ox}) and the second one to the reduction process (D_o , $k_{0 \text{ red}}$ or α_{red}).

Table 3.2: Detail of the parameter estimations from all the electrochemical methods applied to the catholyte of concentration $C_1 = 0.5$ M

| Parameter | Levich | RS | KL | Gileadi | Nicholson | Laviron |
|---|--------|---------|----|---------|-----------|----------|
| D_0 ($\times 10^6$ cm ² s ⁻¹) | 4.6 | 4.5/4.2 | | | | |
| k_0 ($\times 10^3$ cm s ⁻¹) | | | | 6.3/6.8 | 5.9 | 6.5/6.5 |
| α | | | | | | 0.49/0.5 |

Table 3.3: Detail of the parameter estimations from all the electrochemical methods applied to the anolyte of concentration $C_1 = 0.2$ M

| Parameter | Levich | RS | KL | Gileadi | Nicholson | Laviron |
|---|--------|---------|------|---------|-----------|-----------|
| D_0 ($\times 10^6$ cm ² s ⁻¹) | 3.8 | 1.4/1.5 | | | | |
| k_0 ($\times 10^3$ cm s ⁻¹) | | | 5.8 | 5.3/6.1 | 6.0 | 6.0/6.2 |
| α | | | 0.44 | | | 0.34/0.33 |

In the case of the catholyte, the methods match each other to give similar estimation of each parameter. As for the anolyte, the determination from CV and RDE do not tally for the diffusion coefficient. The advective flow of electrolyte could for instance avoid adsorption of the species at the WE, while for CV the phenomenon would be observed. Such adsorption process was detected for the ARS by Schumacher et al. [150].

Moreover in Table 3.3, Laviron's method gives α_{red} and α_{ox} , determined from each branch of the polarization (Fig. 3.12b). The fits lead to a similar value of 0.34, while it is usually considered that the sum of the two transfer coefficients equal unity ($\alpha_{\text{red}} + \alpha_{\text{ox}} = 1$). As explained by Fletcher in his review [151], it is not necessarily the case for a multi-electron transfer reaction, which can justify the finding for the anolyte.

For both couples, since there is no marked contrast between the forward and backward reactions characteristics. Therefore, the values obtained for a given parameter were averaged without distinction between oxidant/reducer or oxidation/reduction.

This led to the global estimates summarized in Table 3.4 for both electrolytes. The results obtained for the diluted catholyte ($C_3 = 0.17$ M) are also listed in the table.

Table 3.4: Summary of the determined parameters from the electrochemical analysis of the concentrated electrolytes at 2 different concentrations

| Parameter | catholyte C_1 | catholyte C_3 | anolyte C_1 |
|---|-----------------|-----------------|-----------------|
| D_0 ($\times 10^6$ cm ² s ⁻¹) | 4.43 ± 0.2 | 4.55 ± 0.35 | 2.23 ± 1.36 |
| k_0 ($\times 10^3$ cm s ⁻¹) | 6.4 ± 0.33 | 5.4 ± 0.47 | 5.9 ± 0.32 |
| α | 0.5 | 0.55 | 0.37 |

α is close to 0.5 for the catholyte, independently of the concentration. The diffusion coefficient is not influenced either by concentration and equals 4.5×10^{-6} cm² s⁻¹. On the other hand, k_0 decreases by approximately 15 % after dilution by 33 %, suggesting a possible small correlation between kinetics and amount of electroactive material. This outcome is insightful for the half-cell characterization of the catholyte (subsection 4.3.3).

The two electrolytes have equivalent kinetic rates, but the anolyte species are twice as slow regarding diffusion, certainly stemming from a higher electrolyte viscosity as shown later in subsection 3.2.2. The facile kinetics of both electrolytes compared to alternatives such as vanadium solutions (reported values vary between 1×10^{-6} to 8×10^{-4} cm s⁻¹ [152]) are promising for the use in RFB and eliminate the need of electrode activation or the use of catalysts [28].

Electrochemical characterizations of the ferri-ferrocyanide system are numerous in the literature. The electron transfer rate constant on a glassy carbon electrode for a diluted solution presented in [109] ($5.9\text{--}6.3 \times 10^{-3}$ cm² s⁻¹) complies with the present values. The author also suggests faster kinetics with low active species concentration because it reduces the number of adsorbed species. Another paper supports the same theory; it shows an increase of k_0 thanks to higher salt concentration and attributes it to an ion-pairing effect that prevents the adsorption on the electrode [153]. This effect can explain why with more concentrated salt and lower reactive species concentration than our solution some papers report much higher rate constants [92]. Zhang et al. [154] shed the light on the influence of the solution viscosity on k_0 and D (ν explicitly appears in the Stokes-Einstein expression of diffusivity (3.12)). For a viscosity close to the catholyte ($\simeq 1.5$ mPa s) (subsection 3.2.2), the measured diffusion coefficients agree with the values in Table 3.4. The ones obtained for a solution with viscosity of water corresponds to other studies with low concentrated solutions, implying low viscosity [91, 92, 109]. Several papers agree on a transfer coefficient close to 0.5 [144, 154]. The range of reported k_0 values for $[\text{Fe}(\text{CN})_6]^{3-}/[\text{Fe}(\text{CN})_6]^{4-}$ is very large, from 4.7×10^{-3} cm s⁻¹ [155], to 0.32 cm s⁻¹ [92]. Some works have evidenced that the measurement was very sensitive to the experimental conditions (electrode preconditioning and material, electrolyte composition, pH...) [153, 156, 157].

The ARS is much less studied for its electrochemical capabilities. Wedege et al. reviewed it as a potential candidate for RFB application [19]. They also characterized it as quasireversible. Zhang and coworkers [115] are the only one who tested its suitability in RFB; they determined consistent values of $k_0 = 3.6 \times 10^{-3}$ cm s⁻¹ and $D = 2.1 \times 10^{-6}$ cm² s⁻¹. These characteristics are usually equivalent for similar anthraquinones [67, 113, 114] and their reversibility are justified by a transfer coefficient close to 0.5 (0.43 – 0.47 in [67]).

All the results obtained during this analysis are related to the glassy carbon surface of

the working electrode. The in-situ characteristics will certainly deviate from this preliminary estimation since the electrode material does not have the same composition (it is in graphite) nor the same structure (it is porous), and the hydraulic driving forces are different. The use of a porous electrode in electrochemical analysis is questionable because the theory cannot really apply, and the results depend on many other parameters, such as the electrode wetting [158]. In this PhD, the rate constant k_0 was assessed in-situ by means of parameter determination from modelling and EIS measurements. This methodology is presented in Chap. 4.

Electrochemical analysis possesses many laws applicable to Rotating Disk Electrode or Cyclic voltammetries to characterize a redox couple. The present study intended to extend these relations pertaining to the dilute-solution theory to concentrated electrolytes. It was revealed that all the methods still converge to give coherent estimates of the kinetic features of the ferri/ferrocyanide and ARS/ARS²⁻ pairs. The values determined herein also match with literature. Moreover, the workable voltage window to respect for each electrolyte was defined.

Concerning iron-cyanide species, pollution of the electrode by adsorbates was obtained during RDE voltammetry, making the technique poorly reliable to examine the catholyte. Cyclic voltammetry was shown appropriate. A slight dependence of the kinetic rate constant to the concentration of active species was substantiated with the catholyte; this trend had already been described in the literature.

3.2. Physico-chemical electrolyte properties

Not only the electrochemical properties are key for a suitable electrolyte but also its physico-chemical properties. This section focuses on the conductivity of the solutions along with their viscosity. The way these features evolve with cycling are also observed. A last section concentrates on the catholyte stability over time under various storage conditions.

3.2.1. Conductivity

The ionic conductivity influences the performance of the battery since it takes part in the porous electrode resistance (see the model developed in section 4.1). The better the conductivity, the lower the ohmic losses in the liquid phase. However, a high conductivity also drives unwanted mechanisms, such as shunt current in a battery stack [39].

The conductivity of the bulk electrolyte named κ_b is easily measurable. It is to be distinguished from the effective conductivity κ once the liquid fills the porous electrode that will be of interest when modelling the RFB cell (Sections 3.3.2 and 3.4.3 and Chapter 4). The two are linked by the geometrical factor of the electrode defined by the ratio of the porosity over the tortuosity ε/τ . The Bruggeman correction $\varepsilon^{1.5}$ is usually utilized in the RFB field (this approximation is appropriate for highly-porous materials [159]):

$$\kappa = \frac{\varepsilon}{\tau} \kappa_b = \varepsilon^{1.5} \kappa_b \quad (3.10)$$

The device used to evaluate κ_b was a CDC566T Hach conductivity cell with 4-pole platinum sensor and integrated temperature sensor, which was connected to an analytical conductivity

meter. The temperature during the measurement is important due to the logarithmic-T dependence of the conductivity. The ionic conductivities of the two electrolytes are presented in Table 3.5, for the fresh solutions (at SOC 0) and after having been used in a battery (at approximately SOC 50). The temperature is given in brackets.

Table 3.5: Measured conductivities of the two electrolytes for several aging and SOC conditions

| κ_b mS cm ⁻¹ / (T) | catholyte | anolyte |
|--------------------------------------|---------------|---------------|
| fresh solutions (SOC 0) | 170 (26.4 °C) | 162 (23.6 °C) |
| aged solutions (SOC 50) | 168 (25.4 °C) | 163 (25.7 °C) |

The ability of a charged species i to move in a solution under an electric field is called mobility u_i . The Nernst-Einstein equation relates it to the diffusion coefficient D_i :

$$u_i = \frac{D_i}{RT} \quad (3.11)$$

The coefficient D_i , also called diffusivity, depends on the surrounding solution properties, i.e. its temperature T and viscosity ν , and the radius of the particle r according to the Stokes-Einstein expression:

$$D_i = \frac{k_B T}{6\pi\nu r} \quad (3.12)$$

with the Boltzmann constant $k_B = 1.38 \times 10^{-23}$ J K⁻¹.

The ionic conductivity κ of a solution is calculated after the mobility and concentration of each charge carrier (with z_i its algebraic number of charges):

$$\kappa = \frac{F^2}{RT} \sum_i z_i^2 D_i C_i \quad (3.13)$$

This relation actually belongs to the infinite dilute solution theory and accordingly overestimates the real conductivity at higher concentration because of non-negligible ion interaction effects or important viscosity that directly influences the diffusivity (3.12) [119, 160, 161]. For this reason, the experimental values of ionic conductivity will be used in the subsequent models to guarantee their accuracy. During the catholyte symmetric study described later in subsection 4.3.3, two other active species concentrations were tested, making the electrolyte conductivity vary. The dependence of κ_b with C is described in this part.

The pH was also measured with a sensor. Both electrolytes have a pH=14.

3.2.2. Viscosity

The research on electrolyte suitable for RFB endeavours to stabilize the highest possible active species concentration to increase the system power density. A rich solution involves in turn downsides, such as viscous properties. It is particularly critical with molecules like quinone

compounds [19]. Rheological behaviors were examined with a rotating disk rheometer with a shear rate increasing from 1 to 100 s⁻¹. The geometry used was a cone-plate configuration (cone of 6 cm and 2°).

Fig. 3.13 presents the viscosity relative to shear rate of the two electrolytes at 20 °C, for fresh (SOC 0) and aged solutions after 100 cycles (at approximately SOC 50).

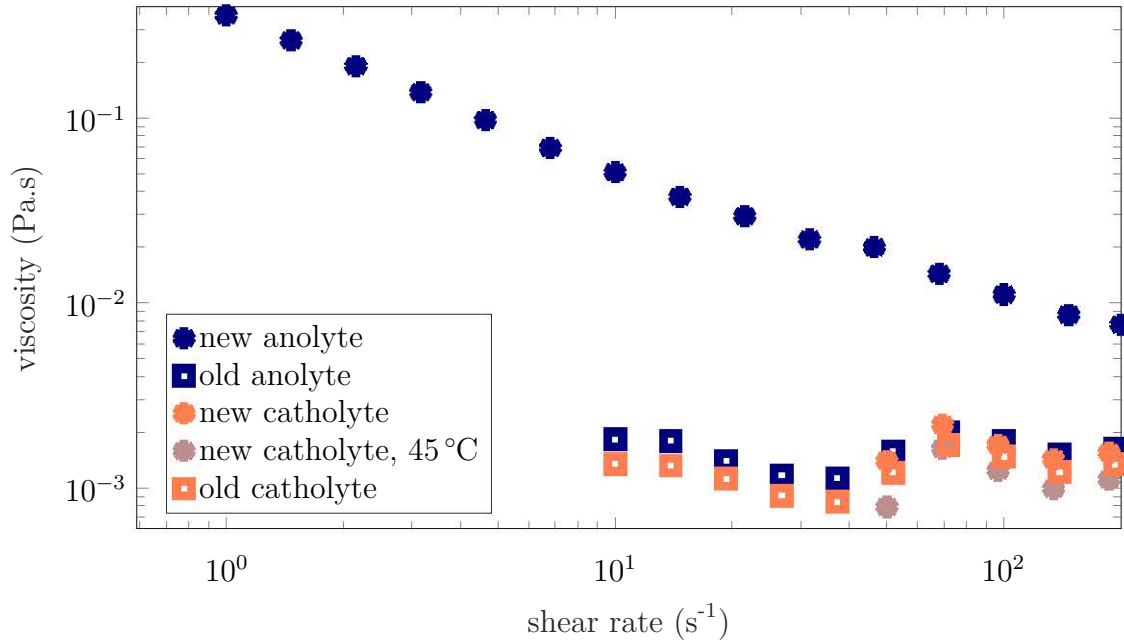


Figure 3.13: Viscosity according to shear-rate for the two electrolytes at 20 °C (unless specified) ; fresh or aged solutions

Fresh solution of anolyte exhibits shear thinning over the whole range of shear rates. It is a characteristic response of a fluid with internal network structure, e.g. a suspension whose particle aggregation is progressively broken by the increasing shear [162]. In their review, Wedege et al. [19] listed the Alizarin Red S as a molecule inducing thixotropy in alkaline conditions. Thixotropic behavior that goes along with shear-thinning, defines the aptitude of the liquid to reform its internal network and recovers its high viscosity after shearing. This is undesirable for RFB applications where the electrolytes are often kept still for extended periods in the reservoirs.

Nonetheless, this feature vanished after cycling the anolyte in a battery. It either suggests that molecules interaction building a structured network evolved during aging or that solid particles initially present were dissolved. The pressure drops variation observed in the cell and detailed later (subsection 5.1.2) certainly stems from this structural evolution. A rapid microscopic observation of the fluid pinpointed the presence of particles in the fresh anolyte. The nature of the dispersion, relative to the particle size (colloids are < 1 µm, suspension are > 1 µm), could however not be resolved and would require extended analysis, by filtration for instance.

With this insight, it was chosen to keep a low flow rate when launching a new segmented cell with fresh anolyte, as it is described in the previous experimental chapter (subsection 2.4.5).

The catholyte rheology is not as critical and does not vary with aging. It is similar to a Newtonian fluid with constant viscosity, and a slim decrease is observed at higher temperature.

Overall, the viscosity of the catholyte and old anolyte lies between 1 and 3 mPa.s.

3.2.3. Material compatibility and photodegradation of catholyte

The photo-sensitivity of the iron-cyanide chemical has long been known in view of all the scientific papers mentioning it [163–166]. The photolysis (breakdown of the molecule by the action of light) mechanisms have been partially identified in the literature, but depends on many environmental conditions (pH, excitation wavelength [166, 167]).

During the PhD, a long-term storage test was conducted over 1.5 years to investigate the influence of the environmental factors on the stability of the catholyte. Several aliquots of solutions of ferrocyanide or a mix of ferri/ferrocyanide (catholyte at SOC 0) were placed in glass flasks, with air as the gas phase above the liquids. The flasks were hermetically closed to avoid evaporation. Pieces of the different pretreated membranes (pristine, converted or reflux-treated) or a stainless steel bolt were added in several flasks to unveil their influence on the aging of the solution. Half of the samples were installed behind a window while the other half was completely protected from light. The list of experiments is summarized in Table 3.6. The resulting observation given in the table for each flask refers to the numbered pictures presented in Fig. 3.14.

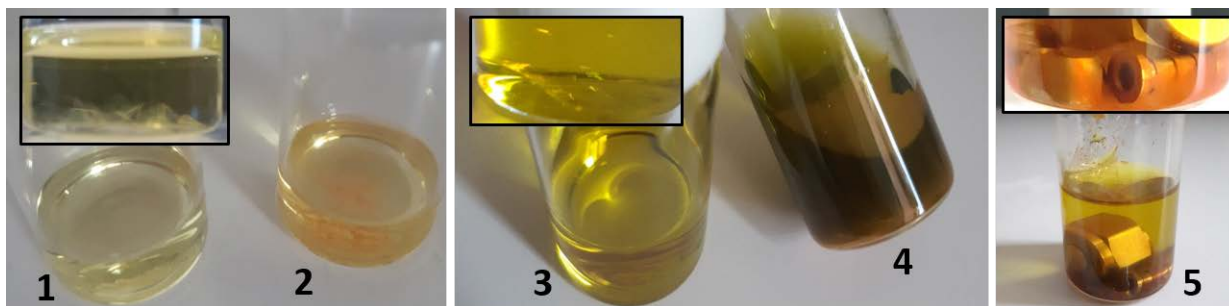


Figure 3.14: Pictures of the several observed forms of catholyte aging after 1.5 years storage. 1: Transparent sediment flakes, 2: Orange particles, 3: Small floating transparent crystals, 4: Orange deposit on the glass + green solution, 5: Orange sediment flakes

Table 3.6: Summary of the observed forms of aging of the catholyte after 1.5 years according to its storage conditions. Numbers refer to the pictures of Fig. 3.14.

| | ferro | ferri/ferro | ferri/ferro + membrane | ferri/ferro + stainless steel | ferri/ferro + membrane + stainless steel |
|-------|-------|-------------|---------------------------|----------------------------------|--|
| Dark | 1 | 3 | 3 | 5 | 5 |
| Light | 2 | 4 | 4 | 5 | 5 |

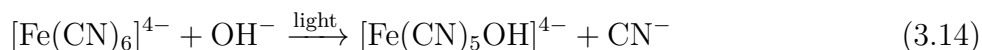
The comparison of all the solutions pinpoints the strong influence of light on the iron-cyanide chemical and the substantial effect of its contact with stainless steel. Ferrocyanide kept under dark showed a significant sediment of transparent flakes as visible in the inset of picture 1 in Fig. 3.14. Since no color change was noticeable, the flakes likely illustrate the

precipitation of $[\text{Fe}(\text{CN})_6]^{4-}$ without degradation. Instead, some orange thin solid particles were formed quickly after a few days under sunlight (picture 2) with no transparent sediments. The formation of the solids was substantial after 10 days of light exposure but tempered over time, as after 1.5 years the amount of apparent solids did not grow in the same proportions. This observation correlates with the findings of Kuhn et al. [165]. They evidenced that the irreversible photolysis rate of ferrocyanide (3.15) was hampered by a high concentration of free cyanide ions in the solution, leading to the conclusion that production of iron(III) hydroxide mitigates with time because of an increase of $[\text{CN}^-]$ during the first days of degradation.

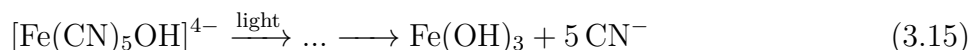
Regarding the mixture of ferri/ferrocyanide, it contained thin needle-like crystals in suspension when stored in the dark, as illustrated in the inset of picture 3. The transparency and limited amount of the particles (compared to the sediments in ferrocyanide alone) suggest that they were caused by the precipitation of ferrocyanide. It comes that dissolved $[\text{Fe}(\text{CN})_6]^{3-}$ is more stable than $[\text{Fe}(\text{CN})_6]^{4-}$. However, under light exposure the catholyte at SOC 50 displayed a serious degradation: the glass walls and the bottom of the flask were covered with an orange solid layer and the solution took a greenish shade (picture 4). The formation of precipitate and the change of color was detectable after a few days of light exposure and worsened inexorably over time. The flasks containing a piece of membrane (pristine, converted or treated) had the same aspect than the flasks without membrane, under light or in the dark. The contact with whichever treated membrane has obviously no effect on the photo-sensitivity of the catholyte.

The last material compatibility inspected was with stainless steel bolts, a material that might be present in the final system process. In that case, the result did not depend on the light exposure nor the presence of a piece of membrane: in whichever conditions, the contact of the solution with stainless steel produced large orange flakes, as shown in picture 5, while the bolt did not appear corroded. The photoproducts of picture 4 look different from this degradation, as if the photolysis was hindered by the presence of a metallic object. A characterization of the products is however required to confirm that the degradation pathway is really dissimilar with metallic contact or under sunlight. The solids in pictures 1 and 5 have a comparable color but a different form.

Since no decomposition was detected in the dark (unless in presence of stainless steel), catholyte is not sensitive to oxygen. The light was confirmed destructive for iron cyanide. Shirom et al. evidenced the photoaquation process that ferrocyanide is subjected to in alkaline solution when exposed to UV above a certain wavelength [164]:



The aquated species $[\text{Fe}(\text{CN})_5\text{OH}]^{4-}$ is the primary step of photolysis and is reversible. Other research proved that this hydrated complex could undergo sequential substitutions to release all the remaining cyanide groups by extended UV-exposure, at high pH or by the presence of a photocatalyst TiO_2 that oxidizes the free cyanide groups [165, 166]. This would eventually form a red-brown precipitate of iron(III) hydroxide $\text{Fe}(\text{OH})_3$:



Ferricyanide is considered as more stable under light than ferrocyanide [167].

The small orange precipitates observed in the ferrocyanide under sunlight are likely $\text{Fe}(\text{OH})_3$

(picture 1 in Fig. 3.14). However, the mix of ferri/ferrocyanide features another degradation process under light. The ferricyanide could also be photosensitive, as already mentioned by [168], although to a lesser extent than ferrocyanide. Intermediates photoproducted complexes of both forms of iron cyanide could be formed and interact with each other to precipitate. The turbid aspect of the solution and the deposit visible on the glass implies that there is not a unique photolysis mechanism occurring when both iron cyanide forms are present.

The photodegraded solutions of ferrocyanide and ferri/ferrocyanide were placed in the dark for a month: the precipitates did not dissolve back substantiating that the decomposition beyond the first photoaquation step (3.14) is not reversible.

Regarding the degradation in contact with metal, it can be speculated that a metal-iron cyanide complex, such as Prussian Brown $\text{Fe}^{\text{III}}[\text{Fe}^{\text{III}}(\text{CN})_6]$ referenced in [169], could be formed subsequent to the release of metallic ions from the stainless steel. This is purely hypothetical and could be confirmed by further chemical characterization.

This long-time storage experiment demonstrates the photosensitivity of both forms of the iron-cyanide. Solid iron(III) hydroxide is doubtlessly created from $[\text{Fe}(\text{CN})_6]^{4-}$, while in the mix of reduced and oxidized catholyte the photoproducts seem diversified: they alter the color of the solution and form a deposit on the glass. In the dark, ferrocyanide precipitates over time without apparent degradation. Finally, the contact of catholyte with stainless steel triggers as well some precipitation.

An industrial perspective

Key learnings for manufacturing stem from the catholyte stability study. The fresh catholyte should be protected from sunlight during storage since its degradation is fast and irreversible. After an extended period of storage, the solution should be stirred before starting the circulation in the battery with the aim of redissolving the precipitates. The contact with metal, even stainless steel, is deleterious and should be avoided in the hydraulic circuit of the catholyte.

The storage study of the catholyte should be completed by three analyses:

- The monitoring of solution volume to detect any evaporation; this mechanism could particularly explain the transparent crystals formed in the dark (case 1 and 3 of Fig. 3.14).
- The characterization of the solutions and/or the precipitates to uncover the nature of the degradation (by UV-visible or IR spectroscopy).
- The electrochemical signature of the stored solutions, useful to detect a decrease of active species concentration or the formation of new electroactive species.

3.3. Membrane characterization

The membrane plays a key role in a redox flow battery operation but also represents the largest expense item in a stack. This component must be scrutinized in order to improve its efficiency, choose the best material structure and thickness and adapt a pretreatment process that makes it suitable in regards to the specific application. Many features define the membrane

and must be taken into account in the effort of selecting the best separator: ionic conductivity, water uptake/swelling, diffusivity, chemical mechanical and thermal stability, perm-selectivity, water permeability etc.

The PhD study restricted to a predefined type of perfluorosulfonic acid (PFSA) ionomeric membrane: the 80 μm Aquivion[®] membrane E98-09S supplied by Solvay; it was chosen as a good compromise of cost, thickness and performance in Kemiwatt's battery. The membrane characterization section focuses on assessing several pretreatment processes by infrared surface analysis of the membrane, before examining the membrane behavior in solution and its affinity with cations, by means of a specific symmetric cell coupled with EIS model.

3.3.1. Membrane pretreatments: FTIR-ATR study

While manufacturers advise pre-cleaning as a precaution to remove any remaining contaminant from production, a thorough pretreatment is crucial to leverage the separator relative to its application. The suppliers of the most-used Nafion[®] membranes recommend to expand the sheets of material in deionized water so that they do not swell and wrinkle uncontrollably during operation. For applications such as batteries, they can be firstly rinsed in high purity acid solution to take contaminants away [170]. In practice, it is difficult to assemble a stack of cells with pre-wetted membranes, for that reason this step cannot be integrated to the industrial level. Literature on the specific Aquivion[®] ionomer is scarce. A first approach was thus to replicate widely applied Nafion[®] pretreatments to the benchmark membrane used in this study since they have a similar structure (Fig. 2.1). Three preconditioning types were tested:

- ➔ a conversion into alkaline form, by soaking the membrane in three successive baths of 1 M KOH, during 24 h in each bath. The samples treated with this procedure will be called "KOH-converted" in the following.
- ➔ a boiling treatment into 3 wt % H_2O_2 during 2 h, before rinsing it in deionized water and changing it into the desired cationic form (K^+). These membranes will be named " H_2O_2 -treated". The hydrogen-peroxide treatment is typical with Nafion[®] [171] and seeks to eliminate any organic contamination.
- ➔ an acidic treatment in 1 M HNO_3 at a reflux temperature of 130 °C during 2 h, followed by rinsing bathes of deionized water until the solution reaches pH 7, and a storage into a solution of 1 M KOH. It mimics some procedures applied on Nafion[®] membranes [95], by being slightly under the glass transition temperature of the Aquivion[®] ionomer ($T_g = 165^\circ\text{C}$ [117]). This type of conditioning will be referred to as "reflux-treated" membranes below.

Samples of KOH-converted and reflux-treated membranes were used in the test of long-term catholyte storage described earlier. The contact of the electrolyte with any type of membrane did not alter the aging observed (subsection 3.2.3).

The three pretreated samples were then installed into a flow cell to compare their performance with a pristine ionomer. The H_2O_2 -treated membrane caused an unequivocal mixing of the electrolytes according to the immediate color change of the catholyte tank. The same observation recurred with several samples, although no defect was visually detectable: the hydrogen peroxide undoubtedly degrades the short-side chains of the Aquivion. It led to the rapid rule-out of the H_2O_2 preconditioning for this membrane. The other treatments improved the cell operation; their effects were investigated in symmetric cells to discriminate the interactions

with each electrolyte. The results are detailed in [subsection 4.3.1](#).

To complete the observation made in symmetric cells ([Chap. 4](#)), the treated samples were examined ex-situ to diagnose how the preconditioning impacts the chemical structure of the ionomer. A surface analysis was performed with the Fourier transform infrared–attenuated total reflectance (FTIR-ATR) spectroscopy. The instrument used was a VERTEX 80v spectrometer from Bruker with a spectral resolution of 0.2 cm^{-1} . The samples were positioned on the PLATINUM ATR (also supplied by Bruker) that is a single-reflection diamond ATR material. This technique is based on the infrared (IR) excitation of a solid and the detection of the transmitted radiation signals according to the beam wavelength. This interferogram is subsequently converted in a IR-absorbance spectrum using Fourier transformation. The absorption bands being characteristic to the molecular bonds within the solid, they allow to identify the sample molecular structure. The low penetration of the IR beams into the material makes the FTIR a surface analysis tool well-suited for membrane examination. Other investigations from FTIR spectra are presented in [subsection 4.3.1](#).

[Fig. 3.15](#) compares the KOH-converted and reflux-treated membranes spectra to a pristine sample.

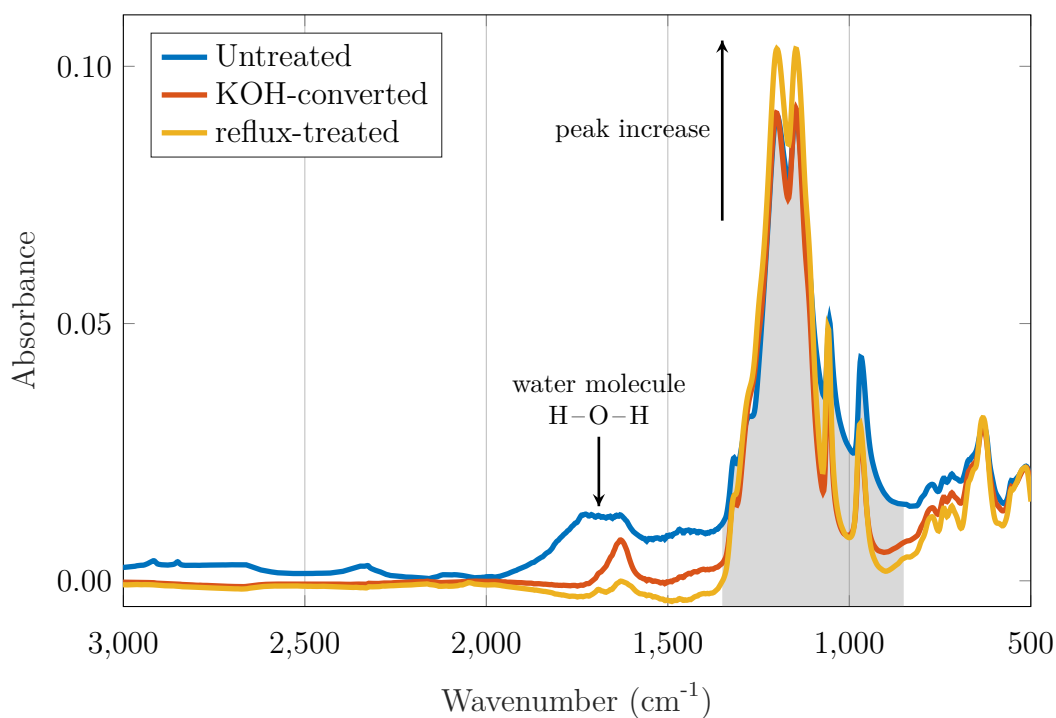


Figure 3.15: ATR-FTIR spectra of Aquivion[®] membranes untreated, after KOH-conversion, after reflux treatment. Gray shaded area highlights the Aquivion[®] bands ($900 - 1350\text{ cm}^{-1}$)

The stretches between 900 and 1350 cm^{-1} correspond to the fingerprint of Aquivion[®] membranes according to published literature [172]; the zone is shaded in gray in the chart. The highest peaks at 1150 and 1200 cm^{-1} pertain to the $-\text{CF}_2$ group while the 1050 cm^{-1} band is assigned to $-\text{SO}_3^-$. The peaks between 1500 and 1800 cm^{-1} are related to the vibration of the water bending $\text{H}-\text{O}-\text{H}$. In the pristine membrane, the wide stretch evidences the presence of water (at 1630 cm^{-1}) and of its deformation into oxonium ion at 1730 cm^{-1} [173]: these bands reveal that all the ionic sites are not protonated. It relates to the conversion protocol followed

by the manufacturer, being first an immersion in an alkaline solution and then in strong acidic condition [172]. The latter step did not acidify completely the membrane according to the absorption spectrum. On the contrary, once the membrane was carefully converted into KOH at the laboratory, a single peak remains: all the sites could be deprotonated.

After reflux treatment, the intensity in the water region ($1500 - 1800\text{ cm}^{-1}$) is lower and could be associated with unequal relative humidity of the samples that were not stored in the same humid conditions. The most noticeable feature is the increase of the main stretch around 1200 cm^{-1} , while with the simple KOH conversion it remained unchanged. It could be the sign of an activation of more functional sites in the acidic environment at a temperature close to the ionomer T_g , by reprotonating the end of the side chain that was left fluorinated after the manufacturing process ($-\text{SO}_2\text{F}$ converted to $-\text{SO}_3\text{H}$). The exact mechanism was not confirmed yet, but the acidic treatment led to outperformed cell results that could partly be due to improved ion-exchange capacity. More generally, the spectra of the two conditioned separators are cleaner than the pristine sample confirming that the treatments contributed to the removal of residual pollutants.

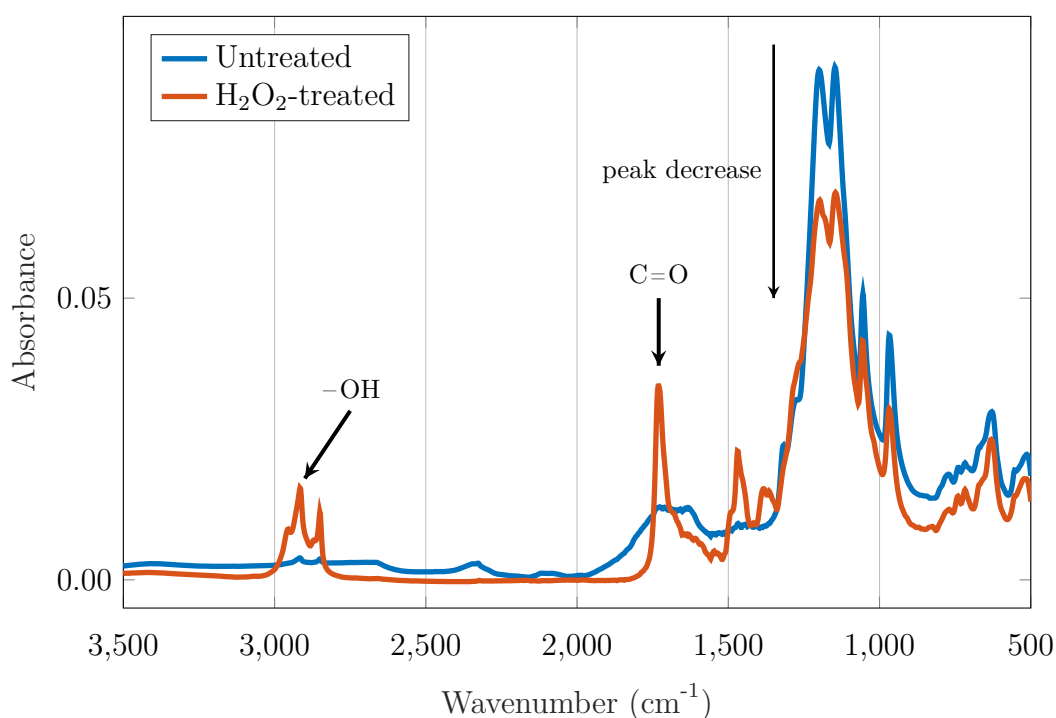
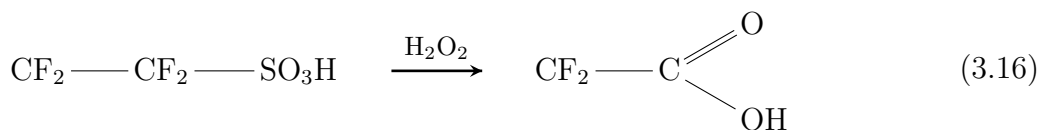


Figure 3.16: ATR-FTIR spectra of Aquivion® membranes untreated, and after H_2O_2 treatment

The spectrum of the H_2O_2 -treated membrane shows more differences with the pristine Aquivion® in Fig. 3.16. First, the ionomer band decreased significantly. It is accompanied with the apparition of two new stretches around 1700 and 2800 cm^{-1} , which are characteristic of the carboxylic group bendings [174]. The degradation process triggered by H_2O_2 could be hypothesized as the following reaction:



The ion-exchange functional groups being degraded, the membrane would afterwards be permeable to any chemical; it would clarify why an immediate cross-over was obtained when using these samples in the RFB cell. PFSA degradation is currently explained in the literature by radical attack of the polymer chains [175]. The radicals are formed by the simultaneous presence of H_2O_2 and metal ions (the mixture is known as the Fenton reagent), while H_2O_2 itself is supposedly not a strong enough oxidant to degrade the polymer substantially. More analyses would be necessary to confirm the herein proposed mechanism, and to perceive why H_2O_2 alone impairs Aquivion® but not the Nafion® structure (since it is commonly utilized for pretreatment). It could also be explained by the presence of metal ions pollutants in the commercial Aquivion® ionomer.

An industrial perspective

The hydrogen peroxide at high temperature has injurious effects on the Aquivion® membrane. The anthraquinone molecule composing the anolyte is usually used in chemical processes to synthesize H_2O_2 by oxidation with air [176]. The contamination of the RFB system by small amounts of oxygen represents a risk of membrane deterioration by H_2O_2 , even though the probability of forming this chemical in the operating conditions of the battery was not evaluated.

The implementation of membrane pretreatment into the battery manufacturing needs to be envisioned to leverage the material performance and durability. The first analysis evidences a cleaner separator after pretreatment which could be beneficial for the system. Further results will confirm the positive effect of membrane pretreatment on performance.

The pretreatment itself can alter the membrane composition and ATR-FTIR is an appropriate characterization tool to assess it. The analysis could however not highlight a difference between KOH-converted and reflux-treated membranes. Cell testing will complement the study in the next chapter (subsection 4.3.1). Concerning membrane characterization, the next step is to evaluate its behavior relative to the solution it is immersed into.

3.3.2. Membrane affinity with solutions

Various aspects of PFSA behavior not only depend on its structural arrangement, but are controlled by the environmental conditions in which the membrane is used: surrounding solution, temperature, mechanical stresses etc. In this section, the influence of the cationic form of the benchmark membrane on its transport properties is evaluated. Three categories of electrolyte constituents are liable to cross the membrane: the water, the solvent ions and the active molecules. The transport of water and ions will be broached separately in the following, although it is clear that the mechanisms are closely related and cannot be treated one by one.

a) Water in membranes

The water transport in the membrane is activated by three driving forces:

- ➔ a difference of solute concentration between both sides of the membrane; this chemical gradient is referred to as osmotic pressure and the related movement is osmosis.
- ➔ a thermal gradient, called thermo-osmosis effect.
- ➔ an electrical gradient through the membrane. This electro-osmosis mechanism is particularly conspicuous in batteries applications.

Several advanced diagnostic techniques exist to study the water mobility through the membrane and discriminate each driving force, but this topic lies beyond the scope of this PhD study [118].

The observation of membrane swelling gives an overview of its affinity with water. The material was immersed in several aqueous solutions to measure its in-plane size variation before and after swelling with a digital caliper. The results relative to the nature of the salt are given in Table 3.7 for the Aquivion® membrane.

Table 3.7: In-plane swelling of 80 μm Aquivion® membrane after 1 day of submersion in several aqueous solutions (measurements with a digital caliper)

| | 0.5 M HNO_3 | 0.5 M NaOH | 0.5 M KOH |
|--------------|----------------------|---------------------|--------------------|
| swelling (%) | 25 | 19 | 8 |

The solvent and in particular the nature of the cation affects the water uptake of the material, since the studied PFSA is a cation-exchange membrane. At equal concentration, it is observed that the smaller the cation in solution the more water uptake. Swelling entails that the hydrophilic paths of the membrane expand: it can reasonably be expected that the more the membrane swells, the easiest the transport of water and cations is [118]. The ionic conductivity κ_m of the membrane embodies its ability to transport positive charges in the through-plane direction. The flow of ions generates an ionic current, necessary for the operation of the battery. Experimentally, the membrane resistance R_m represents a significant part of the total cell resistance that can be accessed in-situ with EIS measurements. It is defined as:

$$R_m = \frac{e_m}{\kappa_m A} \quad [\text{S m}^{-1}] \quad (3.17)$$

where e_m is the membrane thickness (80 μm) and A the active surface area of the cell.

To highlight the correlation between membrane swelling and conductivity, two reflux-treated membranes, one dry (at ambient relative humidity conditions) and one pre-wetted in 1 M KOH , were subsequently assembled in a symmetric cell filled with catholyte at SOC 50. The cell resistance was determined by EIS at high frequency. Table 3.7 compares the swelling of the membrane and the cell resistance obtained with the dry and the wet samples.

Table 3.8: Comparison of the cell resistance with a reflux-treated membrane assembled either dry or pre-wetted and correlation with its swelling

| | Dry membrane | Wet membrane |
|---|--------------|-----------------------|
| Swelling by prewetting | 0 | +12 % vs dry |
| R_{cell} ($\Omega \text{ cm}^2$) | 1.78 | 1.58 (−11.2 % vs dry) |

The obtained value depends whether the membrane was mounted dry or wet. In particular, the gain in resistance with a wet membrane (−11.2 %) perfectly matches its swelling in the potash: 12 % compared to its dry dimensions. Indeed, when tightened in dry state, the membrane can no longer swell in all the directions when getting in contact with the solution. This mechanical constraint hinders the in-plane expansion of the hydrophilic domain. On the other hand, when the membrane is pre-wetted, its hydrophilic pathways have already been enlarged and the tightening keeps them open; the ionic conductivity of the membrane is higher.

An industrial perspective

Since the membrane resistance is directly correlated to its swelling, it would be appealing to assemble the battery with already prewetted membranes. But the stack being stored in a dry state before utilization, the membranes would inevitably dry and shrink. Their contraction under mechanical stress might weaken them or even tear them. Furthermore, it is practically not conceivable to assemble a stack of about 50 cells on a production line with wet membranes, although advised by suppliers. There would be a risk of sliding of the layers of the cells or the membranes would retract before being tightened in the correct position.

b) Cations in membrane: analysis by blocking electrode model

As already evidenced with the influence of ions on the water uptake, the transport of water and ions are highly coupled. Indeed, ions crossing the membrane also drag a number of water molecules with them, depending on their hydration shell. The cell resistance measurement used above is refined to correlate the membrane resistance R_m with the cationic composition of the solution flowing in the cell. The sodium and potassium ions were of interest since they enter in the electrolytes compositions (subsection 2.1.1). In the ensuing paragraphs, the method along with the results are described.

A porous electrode model in specific blocking electrode conditions, that is when no active species are present in the solution, was developed during the PhD study. For convenience, the full demonstration of the model is detailed in the next chapter, in section 4.1. The equations used in this membrane characterization are given below:

$$Z_{\text{cell}}(\omega) = 2 Z_b(\omega) + R_{\text{HF}} \quad (3.18)$$

$$\text{with} \quad Z_b = \beta_1 \frac{1}{\sqrt{i\omega\beta_4} \tanh \beta_1 \sqrt{i\omega\beta_4}}$$

$$\text{and} \quad R_{\text{HF}} = R_{\text{solid phase}} + R_{\text{contact}} + R_m$$

Two factors characterizing the electrode/electrolyte system were introduced:

$$\beta_1 = \sqrt{\frac{L}{\kappa}}$$

$$\beta_4 = LC_{\text{dl}}$$

The total impedance of the symmetric cell Z_{cell} is a function of the signal frequency ω imposed during EIS measurement. It depends on the high-frequency resistance of the cell containing the parameter of interest R_m . Z_b is the analytical expression of the electrode impedance in blocking conditions. L is the electrode thickness and C_{dl} the double-layer capacity characterizing the electrode/solution interface. κ is the effective solution conductivity in the electrode. The ionic resistance $L/\kappa = \beta_1^2$ represents the total electrode resistance in $\Omega \text{ cm}^2$ for the blocking conditions and is called R_b . The solid conductivity of the porous matrix is indeed considered infinite (see section 4.1).

Eq.(3.18) was fitted to EIS measurements on several symmetric cells with the goal of estimating the parameters R_m and κ from this model. These values were determined for several solution compositions to assess the membrane conductivity depending on its cationic form.

A symmetric cell assembled with a reflux-treated membrane was first filled with 2 M NaOH on both sides. Controlled volumes of 2 M KCl were progressively added to the solution, to make the cation ratio Na^+/K^+ vary while maintaining the total salt concentration constant to 2 M. KCl salt was selected to provide the potassium cations instead of the potash KOH, because its level of purity (100 %) being higher than the KOH (86.5 %), any risk of membrane pollution was then excluded. At each cationic ratio, the solution was circulated during several hours with periodic EIS measurements to observe the stabilization of the spectrum, with a flow rate of 200 mL min^{-1} . The average time needed for stabilization was 4 hours. The last spectrum obtained for each electrolyte was processed for interpretation.

From the impedance spectra obtained for all the solution were extracted the underlying values of R_m and κ (contained respectively in R_{HF} and β_1). For the blocking electrode, R_{HF} stands at the spectrum intercept (or extrapolated intercept) with the real axis in the Nyquist chart. As the solid phase and contact resistances are not affected by the nature of the electrolyte, the term $R_{\text{solid phase}} + R_{\text{contact}} = 0.09 \Omega \text{ cm}^2$ (measured in a dry cell) was subtracted from the total measurement to isolate R_m .

The Nyquist and Bode plots and the fits obtained from (3.18) for the cell filled with 2 M NaOH are illustrated in Fig. 3.17. They follow the typical shape of a blocking electrode impedance (see section 4.1). The fit is therefore highly accurate. Yet the low frequency line attributed to capacitive response is not completely vertical. This tilt underlines a small faradaic current created by parasitic reactions such as carbon oxidization or water reaction.

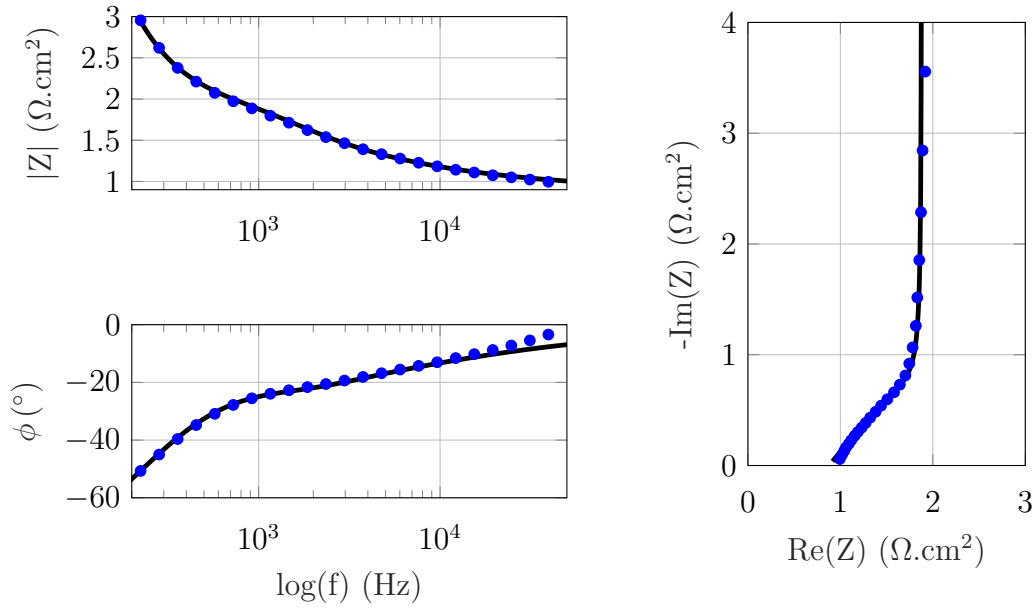


Figure 3.17: Bode plots (left) and Nyquist plots (right) of a blocking symmetric cell filled with 2 M NaOH; Fitted model (3.18) depicted by the black lines

The resistance variation with the Na^+/K^+ ratio of the solution is outlined in Fig. 3.18. It evidences the membrane resistance dependence on the cationic charge carriers: R_m increases with the addition of K^+ in the salt (from left to right on the diagram). This reveals that the K^+ ions are less mobile in the membrane than the Na^+ , and from the Na^+ -form to the K^+ -form, the membrane resistance increased by at least 30 %. These findings show a good agreement with the results presented by Shi et al. [177] and by Kusoglu et al. [118]. These authors reported that the ionic conductivity of Nafion[®] membrane in K^+ -form is lower than in Na^+ -form. They also reported the very complex effects on the membrane behavior in high concentrated electrolyte solutions containing multiple cations and anions.

After the cell impedance stabilized with the 2 M KCl salt, the membrane (noted memb.1) was substituted by another pretreated sample (memb.2); the data relative to this sample are represented by pink bars in Fig. 3.18. The membrane 2 showed a higher resistance of $1.88 \Omega \text{ cm}^2$. When the solution is changed back to pure NaOH (from right to left on the chart), the detected R_m follows a decrease similar to with membrane 1, but cannot reach a value as low as before, even after several hours of circulation. The hysteresis response alludes to an “historical effect” of the membrane exposure to mobile cations. If first soaked in a salt containing sodium ions, the membrane will keep a low resistance even when the surrounding is later replaced by K^+ ions. On the other hand, a membrane directly exposed to K^+ displays a higher resistance even with the presence of sodium charge carriers thereafter. The resistance discrepancy between the two samples is more acute in 2 M KCl than in 2 M NaOH. This suggests that the membrane cannot be fully converted to another cationic form by the sole driving force of diffusion at room temperature.

From the fitted membrane resistances the corresponding membrane conductivity can be deduced with Eq.(3.17). The data points used are the ones corresponding to the first measurement of each membrane, before progressive addition of the other ion: membrane 1 gives the point for 2 M NaOH (far left blue bar) and membrane 2 is used for the 2 M KCl salt (far right pink bar). The corresponding conductivities are given in Table 3.9 along with values from the

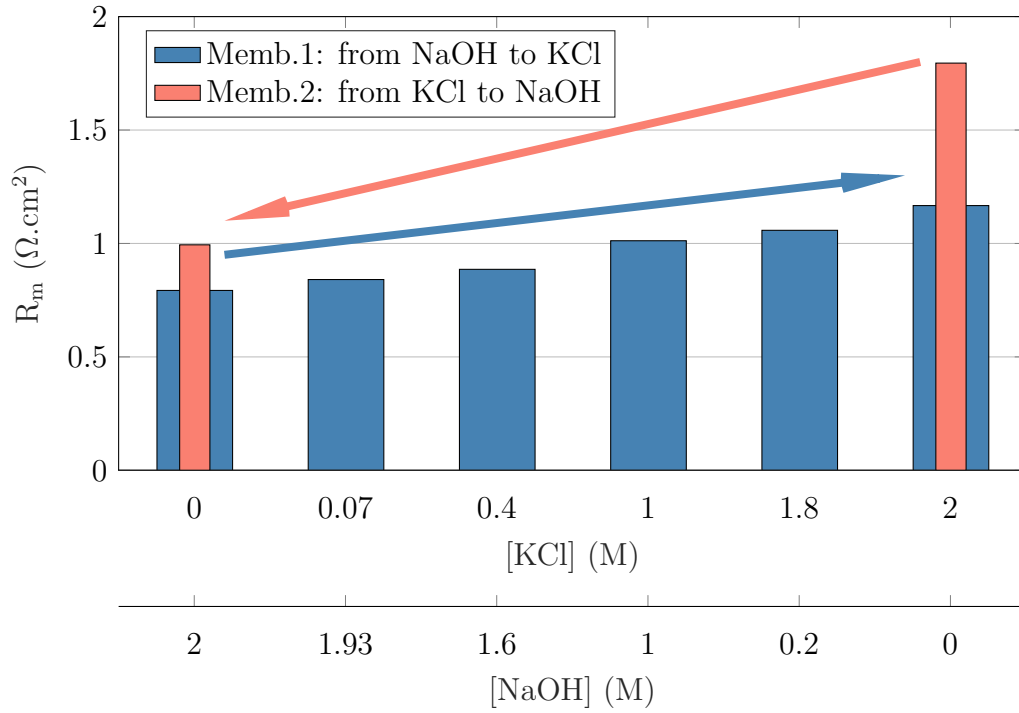


Figure 3.18: Resistance of the reflux-treated membrane determined by model fitting (Eq. (3.18)) in a symmetric cell; variation with NaOH/KCl concentration. Membrane 1 in blue (resp. membrane 2 in pink) was first in contact with NaOH (resp. KCl) before being progressively replaced with KCl (resp. NaOH).

literature measured in close conditions.

Table 3.9: Membrane conductivity from model fitting (Fig. 3.18) and comparison with reported values

| $\kappa_m (\times 10 \text{ S m}^{-1})$ | 80 μm Aquivion [®] (this study) | 178 μm Nafion-117 [178] | 110 μm Aquivion [®] [179] |
|---|--|---------------------------------------|--|
| 2 M NaOH | 10.1 | 11 (in NaCl) | — |
| 2 M KCl | 4.5 | 6.8 | 5.2 (in 2 M KOH, 80 °C) |

The values obtained from fitting the blocking electrode model are equivalent to reported values for a Nafion-117 membrane or a 110 μm Aquivion[®] in similar electrolytes [178, 179], although some experimental conditions and the measurement techniques are different.

The results draw the conclusion that not only the choice of the material for the separator is critical, since one ionomer can display enhanced performances with a specific cationic charge carrier. The supporting electrolyte must be composed in regard to the active material but also the nature of the membrane. Nevertheless, the experiment did not exactly mimic the real battery configuration since no current was drawn from the cell and conclusions need to be moderated with respect to this. Indeed, the migration and electro-osmotic mechanisms induced

by a potential gradient in the cell certainly alter the transport through the membrane [180].

The bulk ionic conductivities of 2 M NaOH and 2 M KCl measured at 25 °C are respectively 26.5 S m^{-1} and 18.7 S m^{-1} . The substantial difference stems from the anion, OH^- being much more conductive in solution than Cl^- (and K^+ is only slightly more mobile than Na^+ in water) [181]. To verify the impedance model predictions, the effective ionic conductivities are extracted from the fits and presented in Fig. 3.19. These effective estimates actually enclose the disturbance generated by the porous geometry of the electrode. Their divergence from the bulk conductivity equals 0.8-0.85. By using the classic Bruggeman correction factor $\varepsilon^{1.5}$ to relate the bulk and effective conductivity as in (3.10), the porosity of the felt compressed at 35 % was estimated to $\varepsilon = 90 \%$. The value is coherent with the material open porosity of 94 % (from SGL data). Bruggeman equation is controversial for use in non-spherical particles and low porous media, because it was proven to underestimate tortuosity [159, 182]. Nevertheless, for the highly porous electrode used in the PhD work, Bruggeman correction is validated by the preceding results.

Fig. 3.19 highlights a progressive increase of the effective ionic conductivity with the Na^+/K^+ ratio increment. The variation is not perfectly linear since the dilute solution theory cannot be strictly applied to these highly-concentrated solutions. The pink bars correspond to the second membrane experiment; as expected, the fitted ionic conductivity values are reproducible (within $\pm 5 \%$), thus confirming the accuracy of the model.

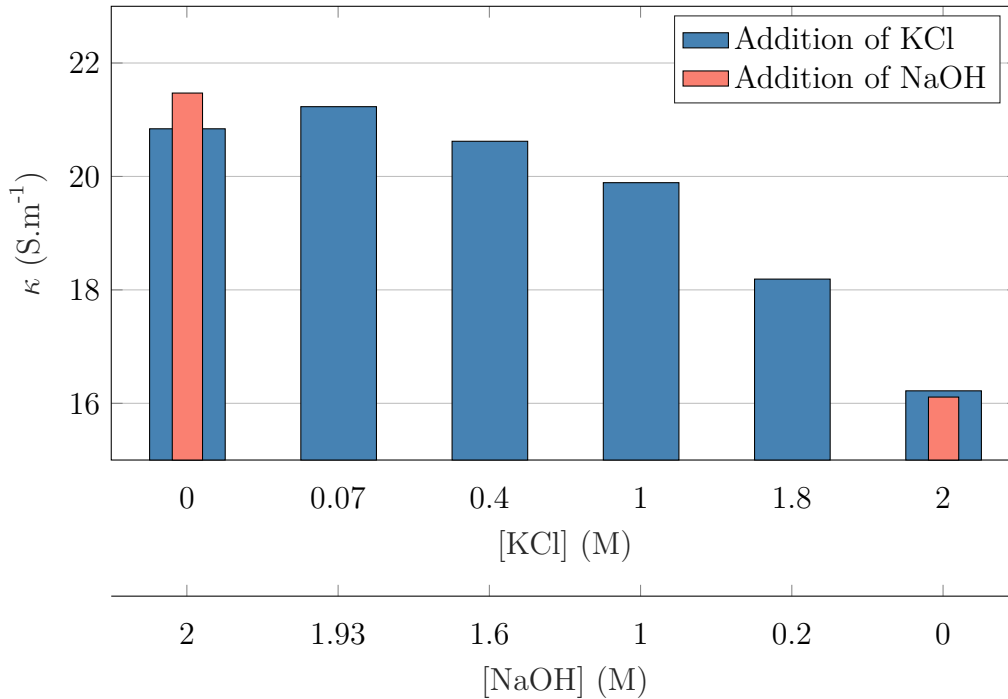


Figure 3.19: Effective ionic conductivity of the solution determined by model fitting (Eq. (3.18)) in a symmetric cell: variation with NaOH/KCl concentration

An industrial perspective

The use of alkaline solutions impedes the separator performance, since transport of K^+ or Na^+ is more than six times lower in the membrane compared to protons present in acidic

VFB [183]. On the other hand, vanadium ions are positively charged and can easily enter the membrane. The consequence is twofold: the presence of vanadium inside the separator decreases its conductivity [127] and their cross-over implies a loss of battery capacity [180] that must be managed by electrolyte remixing over time [184].

In summary, the overall transport properties of a membrane depend on its structural arrangement, but also on the surrounding solution. They are controlled by two interactions:

- The mobile cation (in solution) - fixed anionic site (in membrane) electrostatic affinity
- The solvation energy between the cation and water molecules

As the cation radius rises ($H^+ < Na^+ < K^+$), its hydration decreases [118]; it is typically considered that Na^+ is surrounded by 5 molecules of water while K^+ only by 3. The bigger and less hydrated the cation, the stronger is its interaction with the SO_3^- sites of the membrane. And the higher the affinity cation/sulfonate groups, the less mobility and water uptake in the membrane. This interplay between the solution and the ionomer justified the above observations:

- The membrane swells more in NaOH than in KOH, because Na^+ drags more water with itself and makes larger hydrophilic pathways through the membrane
- The membrane conductivity is enhanced in the Na^+ cationic form, since electrostatic interaction is weaker and cationic transport facilitated

The same mechanisms account for a contrasting consequence regarding solution conductivity. Indeed the conductivity of Na^+ in water is lower than K^+ because its larger hydration shell reduces its mobility [181].

Results are rather straightforward when comparing the membrane behavior for several fully-exchanged cationic forms. However, when it comes to view the membrane as an interface with a complex electrolyte where multiple cations coexist, the mechanisms are more intricate. As brought out by the non-reproducibility of the results when the membrane is first soaked in a salt containing Na^+ and then K^+ or in the reverse order, the competition between the different ions will depend on the interactions in the mixture and within the membrane.

c) Active species in membranes

According to Xie et al. [183], the type of pretreatment affects more the membrane permeability to active species than its ionic conductivity. However, after cycling the membrane in a RFB test cell, they showed that all types of pretreated membranes converged to a single permeability value, as if the pretreatment only had a provisional influence that charge/discharge cycles would overwrite.

The membrane permeability relative to its preconditioning was not tackled in the PhD thesis, but a specific experiment was conducted on the pristine 80 μm at the company Kemiwatt. The trend shows a very low permeability of both forms of anolyte and of the catholyte reduced form. The permeability of the catholyte oxidant $[Fe(CN)_6]^{3-}$ was however found critical to meet the threshold of CE=99.992 % determined by [185] to achieve 1250 cycles with less than 20 % capacity fade. These tests only took into account the diffusion force; electro-osmosis or migration could play a significant role in active species cross-over.

In summary, competing functionalities appear in a battery application: the transport of desired cations must be best while being restrictive for the active material. Simple tests give a first insight on the transport mechanisms through the membrane but cannot fully represent the intricate picture of the separator in practical applications. From the presence of many different species in solution could emerge other interactions with the membrane. The transport drivers are also multiple in the real system: diffusion, migration, osmosis (due to the difference of ion concentration and ionic strength through the membrane) and electro-osmosis. The half-cell and full cell tests of the next chapters [Chapters 4](#) and [5](#) will address the electrolyte/membrane interaction more globally.

3.4. Porous electrode characterization

The full understanding and optimization of the use of a porous felt in a flow battery application begins with the knowledge of its *structural characteristics*, that is to say: pore size distribution, fiber diameter, total surface area, porosity, tortuosity, isotropy, but also its *physical properties*: electronic conductivity, liquid permeability, electrochemically active surface area, the two aspects being closely tied [186]. The first section visualizes the structure of the material by microscopy before examining the flow behavior thanks to the NMR technique. The last part presents a method to characterize the electrode in flowing conditions; two types of standard materials are compared.

3.4.1. Structural observation

The porous electrode used in the RFB cell has a specific structure difficult to characterize. A first approach is to observe it with microscopy techniques. This section compares the pictures of two porous materials:

- Material A: A pre-carbonized felt made of polyacrylonitrile (PAN) fibers: this precursor is graphitized in furnaces above 1000 °C by the manufacturers to obtain the final graphite felt
- Material B: The SGL carbon felt GFD 4.6EA, the benchmark electrode of the PhD study

Material A is a non-conductive polymeric structure; it is suitable for the NMR study detailed in the next section. That is why there is an interest of evaluating the internal arrangement of this precursor, comparatively to the actual porous structure composing the battery.

[Fig. 3.20](#) depicts the two materials side by side, observed with two magnification factors. Felt B features a more periodic structure visible at smallest magnification, with holes regularly distributed on the surface (remnant of the manufacturing process). The two samples were supplied by different manufacturers which can account for their dissimilar aspect. Felt A looks more dense, although it could be an optical bias since it reflects less light. At higher magnification, the structures look comparable. It is impossible to conclude about porosity on a simple observation.

A more powerful optical microscope was used to look at the materials unitary components, the fibers. [Fig. 3.21](#) presents the picture of materials A and B, along with the material C, a thermocouple wire with known diameter of 25 μm . Indeed, the optical device was developed at

the laboratory, hence its magnification is not precisely known. Sample C served as a reference to evaluate the sizes of the fibers. The comparison gives an average diameter of $11\text{ }\mu\text{m}$ for the precursor A, and smaller fibers of $6\text{ }\mu\text{m}$ for the carbon felt B. This observation was expected since the solid likely loses volume during the process of carbonization.

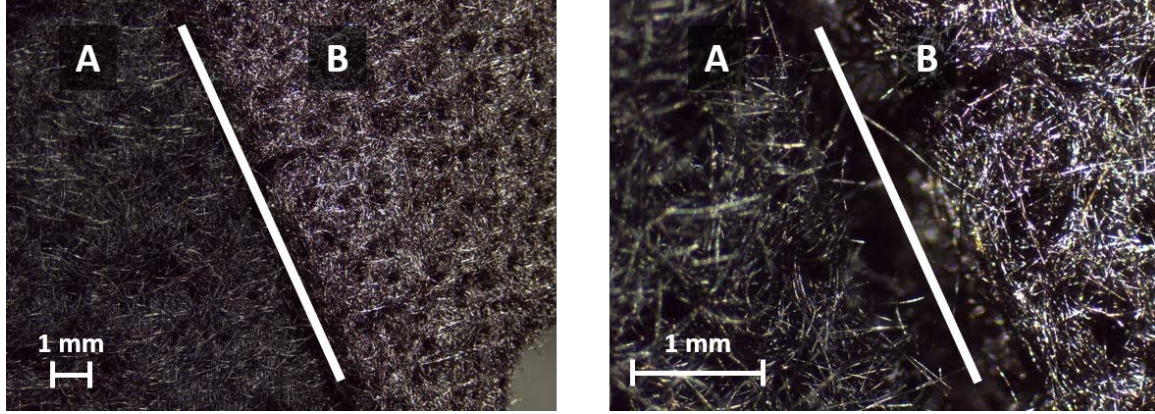


Figure 3.20: Porous materials observation through a binocular microscope at two magnification factors.

A: PAN felt precursor, B: carbon felt from SGL

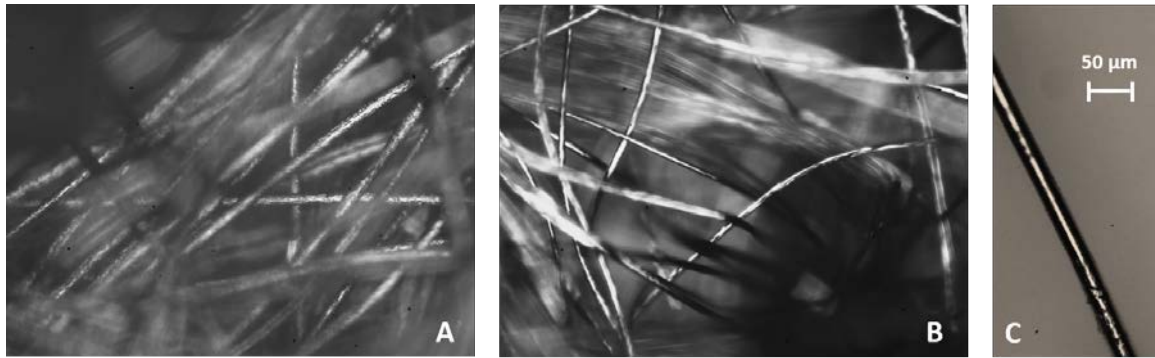


Figure 3.21: Porous materials observation through a light microscope

A: PAN felt precursor, B: carbon felt from SGL, C: Comparison with a wire of known diameter $25\text{ }\mu\text{m}$

Given the structural difference between the two materials A and B, it is deduced that the results from the NMR study described hereafter cannot be immediately extrapolated to the real battery cases, but can give a qualitative insight of the internal flow behavior.

The pore size distribution and the developed surface area are other crucial aspects of the material to assess. Exploratory experiments of nitrogen adsorption were unsuccessful during the PhD, but other advanced methods of microscopy or tomography could give reliable data. Nevertheless, disparate results are given in the literature [186], and physical techniques do not diagnose the actual electroactive surface area of the graphite electrode [187].

3.4.2. NMR analysis

The flow through the pre-carbonized porous material (Material A) could be observed at the small scale thanks to Nuclear Magnetic Resonance (NMR) measurements. Imaging NMR

(noted MRI) is a non-intrusive spectroscopy technique suitable for studying the dynamic flow behavior in the volume of an opaque material, such as the porous electrode, by direct marking (no tracer injection) of water molecules [188]. The final graphite felt (Material B) could not be used because its conductivity is not compatible with this characterization method (it would interfere with the signal). NMR technique provides a nearly ideal tracer method by marking and tracking the molecules in their movement. In this experiment, the protons of water molecules are excited by a magnetic field and their signal informs on the advective molecular displacement. The average velocity field can be deduced in the three spatial dimensions of the sample. An example of the use of MRI for flow study is given in [189].

Flow measurements were conducted with a Bruker spectrometer (Fig. 3.22) (Bruker Avance III 600Wide Bore) providing a static magnetic field of 14.1 T (proton resonance frequency at 600 MHz) equipped with a micro-imaging probe (MicWB40). The measurements were performed at room temperature (25 °C).

The probe inserted in the spectrometer is also shown in Fig. 3.22) on the right. A piece of electrode was placed in the tube and held compressed to 30 %. Plastic tubing fed the porous medium with water from bottom to top, as depicted by the blue arrows on B. The water flow was controlled by a syringe pump (Teledyne Isco 500D).

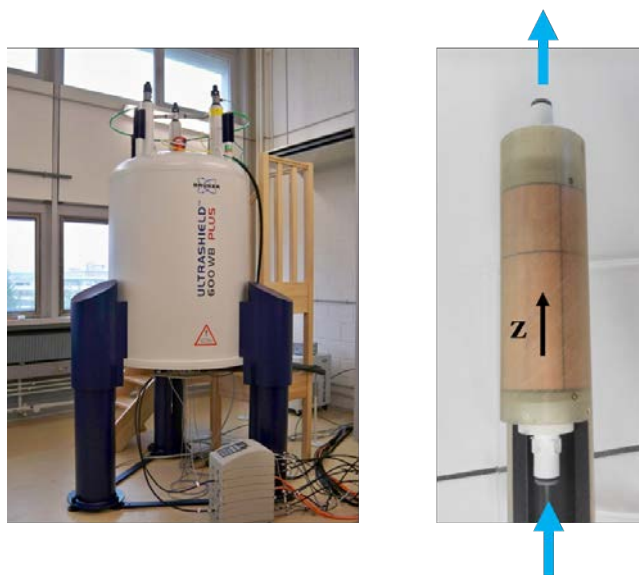


Figure 3.22: 600 MHz NMR equipment (left) and test tube holding the compressed felt (right). The arrows depict the flow of water through the sample

Magnetic Resonance Imaging (MRI) consists in constructing spatially-resolved pictures from NMR velocity measurements. The spatial resolution of the images is a pixel of $78 \times 78 \mu\text{m}$, with a depth in the sample of $500 \mu\text{m}$. The sensor is placed at half height of the test tube, to be far from the inflow. Static or dynamic imaging of this section of the porous material is presented below.

Dynamic images in Fig. 3.23 present the profiles of the velocity magnitude v_z along the z -axis (flow direction), at three different flow rates. The sum of each voxel velocity over the entire section corresponds to the control value of flow rate, with a difference $< 7\%$. This validates the accuracy of the velocity estimation with NMR. Inside the rectangle (corresponding to the section of the porous material), dark blue areas highlight dead zones, where no movement of

water molecules is detected. Dead zones clearly appear at the two highest flow rates, in the bottom of the material, which makes the flow rather heterogeneous throughout the section.

The average local velocity magnitude and relative standard deviation is, for the 3 flow rates:

- 10 mL min⁻¹: $\bar{v}_z = 0.43 \text{ cm s}^{-1}$, $\sigma^* = 72 \%$
- 20 mL min⁻¹: $\bar{v}_z = 0.85 \text{ cm s}^{-1}$, $\sigma^* = 58 \%$
- 30 mL min⁻¹: $\bar{v}_z = 1.18 \text{ cm s}^{-1}$, $\sigma^* = 54 \%$

In light of the relative standard deviations, the flow heterogeneity through the porous section is huge. Although preferential paths and dead zones are more visible at increased fluid stream, the relative σ^* decreases.

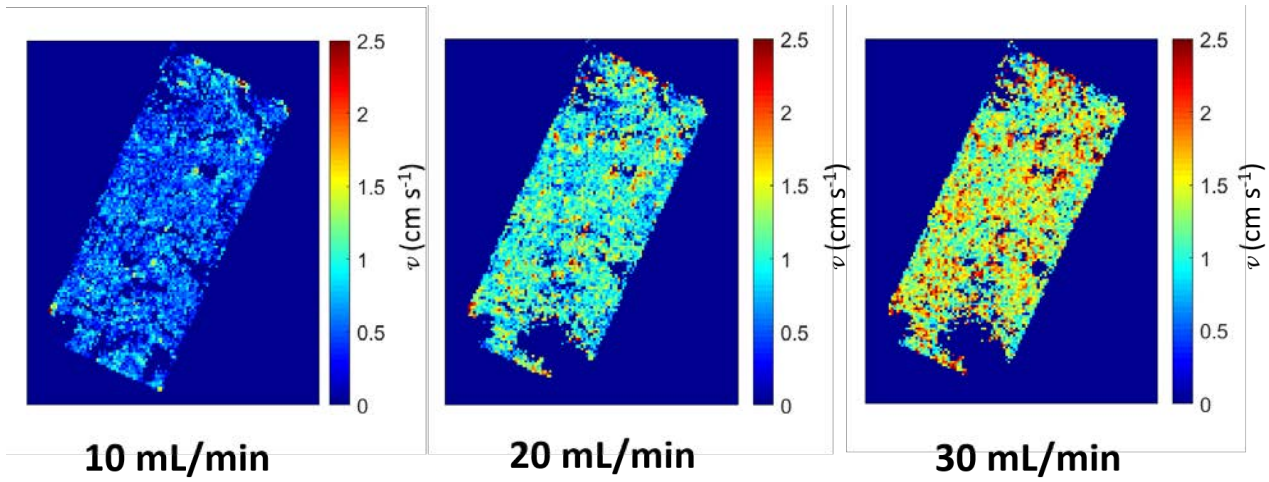


Figure 3.23: Velocity magnitude profiles across the porous material in the flow direction (along z -axis) for three flow rates

The large dead zones detected in some regions are likely caused by gas bubbles trapped inside the pores. This is all the more possible that the material is highly hydrophobic. Static imaging allows the detection of the water filling the material. The upper-left image in Fig. 3.24 is the static image of the section: the gray-white zones contain water, while the fluid is absent in dark areas. Two small bubbles are clearly visible on the lower-left and upper-left corners (circled in red). The same zones are disturbed in the dynamic image below (corresponding to the flow rate of 30 mL min⁻¹). The lower-right hand side of the electrode is filled with water, but a large dead zone is detected: there is certainly an important bubble upstream that cannot be detected, but which disrupts the flow pattern in this region.

The set-up was left under circulation at 30 mL min⁻¹ for one day. The static and dynamic pictures of the material are given in Fig. 3.24 on the right-hand side. The gas bubbles in the static image are strictly identical as initially. However, the dead zones in the bottom have been reshaped but have not been mitigated with extended circulation. The characteristics of the velocity profile evolved slightly. After circulation, the average local magnitude is slightly lower at $\bar{v}_z = 1.08 \text{ cm s}^{-1}$, which induces an increased dispersion of the distribution: $\sigma^* = 60 \%$.

Other sections of the test tube were imaged and similar occurrences (bubbles and important heterogeneity) were detected along the height of the tube. Finally, complementary tests showed no further evolution of the flow distribution after one week of circulation, even under an important flow rate of 100 mL min⁻¹.

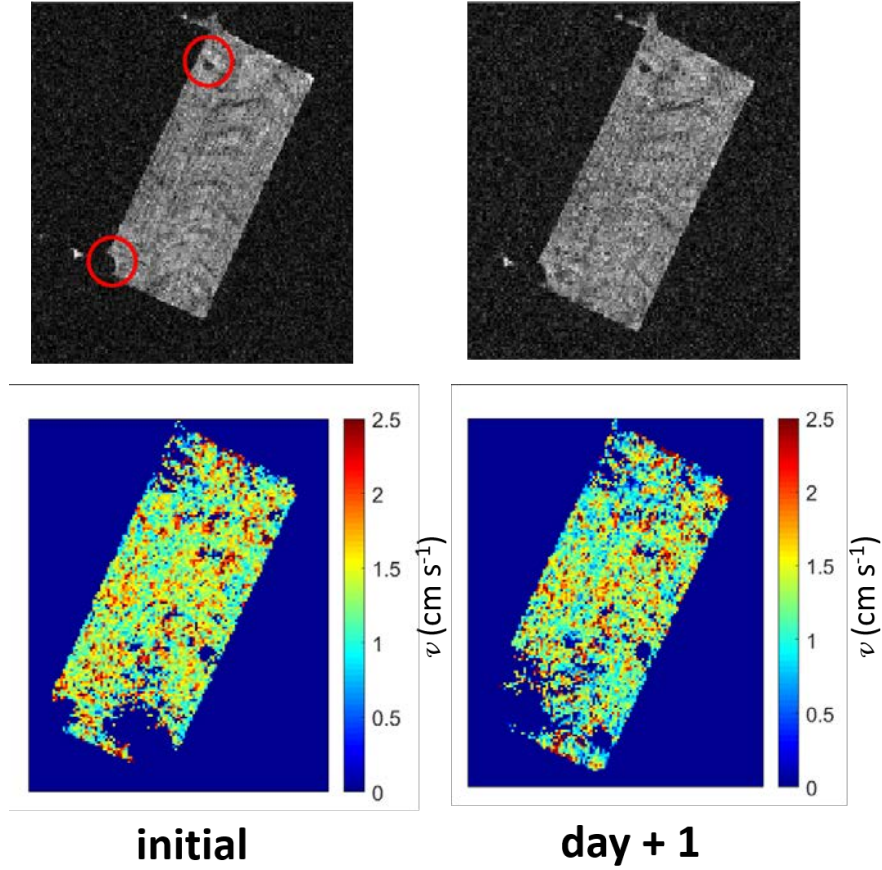


Figure 3.24: Water static images (top) and velocity magnitude v_z profiles (bottom) initially at 30 mL min^{-1} (left) and after one day of circulation (right)

The conditions of the NMR experiment are different from the real battery environment: the material is the pre-carbonized version of the graphite electrode, and the fluid is pure water instead of the real electrolytes. Nevertheless, it is observed that the flow heterogeneity is significant in the section of the porous matrix, mainly disrupted by residual air bubbles. They cannot be eliminated by the sole circulation of fluid, even after a long period. The heterogeneity even seems to be intensified. This poses the question of how to remove the bubbles from the pores to avoid dead areas. Indeed they could induce local overpotentials and side reactions, prevent from the full utilization of the developed surface of the electrode, and increase the pressure drops induced by the flow through the porous matrix.

3.4.3. Comparison of two materials by blocking electrode model

In the literature, some RFB cells are built from an electrolyte flow field machined in the end plate, associated with thin carbon paper electrodes [32]. This section aims at comparing the benchmark electrode with a typical carbon paper material used in these configurations to foresee the effect of the electrode type on the cell performance. To this end, the same strategy as presented in subsection 3.3.2 was applied. The blocking electrode impedance model of (3.18) was fitted to the impedance measurements of several symmetric cells, so as to determine the electrode resistance called $R_b = \beta_1^2$, along with the double-layer capacity C_{dl} characterizing

the electrode/solution interface.

Three configurations of porous electrode were tested:

- the benchmark carbon felt GFD (supplied by SGL Group) that is 4.6 mm thick with a porosity of $\varepsilon = 0.94$.
- one layer of Sigracet[®] GDL 38AA carbon paper, 0.3 mm thick, also provided by SGL Group. The open porosity of the carbon paper is 82 % (manufacturer's data).
- two layers of the GDL carbon paper

All the assemblies were compressed with the same ratio of 33 %. By solid volume conservation, the porosity is 90 % for the compressed felt and 73 % for the compressed paper. Electrodes were used as received, but once assembled the cell was rinsed with 2 M NaOH before starting a new test. Since paper electrodes were used in this test, the 25 cm² cell was assembled with gilded brass plates in which 30 parallel channels (cross-section of 0.4 mm²) had been machined. The conductive solution used was 2 M NaOH that circulated in the cell at a flow rate of 200 mL min⁻¹ to minimize mass transport limitation.

The EIS Nyquist plots obtained for the three configurations of symmetric cell are depicted in Fig. 3.25. The fitted models from (3.18) are represented by the black lines. The carbon felt test has already been used and presented in the previous subsection 3.3.2.

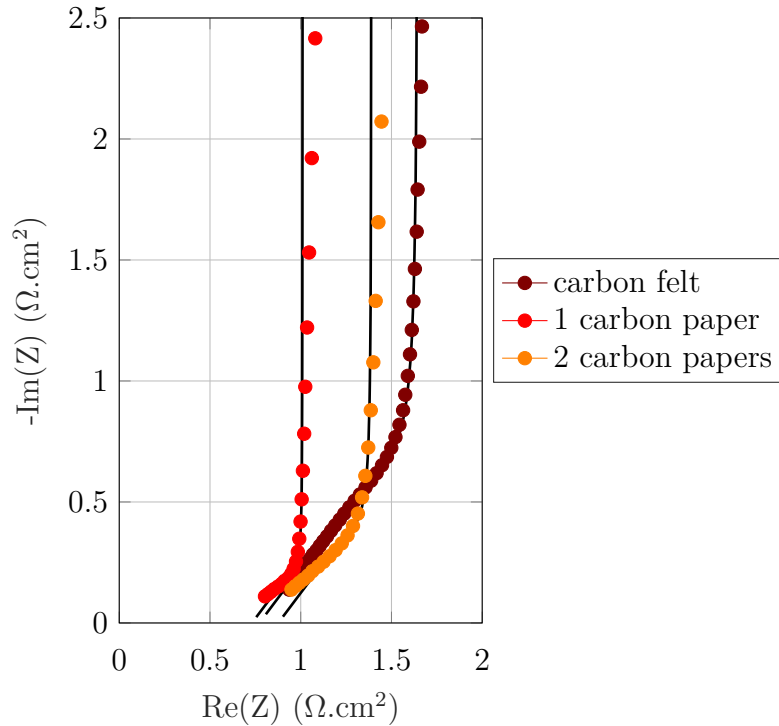


Figure 3.25: Nyquist plots of a blocking symmetric cell filled with 2 M NaOH for three electrode configurations; Fitted model (3.18) depicted in black line

The double layer capacity estimated with the model is small and nearly constant for the three electrode configurations. The values lie between 6×10^{-4} to $12 \times 10^{-4} \text{ F cm}^{-2}$. The discrepancy originates from a non-ideal capacitive behavior at low frequency, as represented by the vertical line tilt, mostly visible on the red plot. By relating this estimation to the electrode samples weights (measured beforehand), the average gravimetric double layer capacity value was found to be about $20 \times 10^{-3} \text{ F g}^{-1}$. Rabbow et al. correlated the active surface area of a

carbon felt to its total surface area and its gravimetric electrochemical double-layer capacity [187]. They reported an electrochemical double-layer capacity of $30 \times 10^{-3} \text{ F g}^{-1}$ for PAN-based carbon felts with a comparable total surface area (the one used in the PhD work is $0.4 \text{ m}^2 \text{ g}^{-1}$ according to SGL data). The value reported by Rabbow et al. is consistent with the present estimation. It is however worth mentioning that the double-layer capacity not only relates to the electrode material but mainly depends on the ionic composition of the solution filling the porous structure. As such, the value estimated from the symmetric cell might not be completely the same with the RFB electrolytes. As expected, the spectra display a similar membrane resistance for any electrode nature (see subsection 3.3.2 for the membrane resistance obtained with the fit).

Table 3.10: Extracted electrode resistance and equivalent ionic conductivity obtained in a symmetric cell for three electrode configurations (Fig. 3.25)

| | Carbon felt | 1 layer of carbon paper | 2 layers of carbon paper |
|---|--------------------|----------------------------|-----------------------------|
| Compressed electrode thickness L (m) | 3×10^{-3} | 0.2×10^{-3} | 0.4×10^{-3} |
| Electrode resistance $R_b = \beta_1^2$ ($\Omega \text{ cm}^2$) | 1.44 | 0.42 | 0.77 |
| Effective ionic conductivity κ (S m^{-1}) | 21 | 5 | 5 |

The estimated electrode resistance and the corresponding effective ionic conductivity are gathered in Table 3.10 below along with the electrode thickness. The electrode resistance unsurprisingly varies according to the electrode material mostly because of its thickness. Since it is almost doubled when measured for one or two layers of carbon paper, the resulting ionic conductivity is independent of the number of carbon layers, which is coherent. Nevertheless, the obtained value of 5 S m^{-1} constitutes only 20 % of the real solution conductivity, whereas the fraction should obey $\varepsilon^{1.5}$ (62 % for the carbon paper). On the contrary, the resulting electrode resistance from the carbon felt matches Bruggeman correction as already mentioned in subsection 3.3.2.

This irregularity observed with carbon paper could be ascribed to the effect of the flow field machined in the end plate. The parallel channels would behave as an electrode of thickness equal to the channel depth (0.4 mm), and thus alter the electrode resistance detected. Indeed, considering the total thickness of carbon paper and channel results in an effective conductivity close to the predicted value of 17 S m^{-1} . On the other hand, the channel influence was not detected for the carbon felt. The felt being a soft material, it can partially fill the void spaces of the channels once compressed. It is also thicker and more porous than the carbon paper: the bypass flow in the channels is insignificant thanks to a low pressure drop through the electrode, as asserted by [95].

In summary, the flow field / carbon paper configuration gives higher ionic electrode resistance (comparatively to its thickness) than the carbon felt. As for its suitability for hosting a redox reaction, it will be discussed in a following test (subsection 4.3.1) by adding some active material to the symmetric set-up, to activate the faradaic behavior of the electrodes (Fig. 4.10).

The symmetric cell set-up in blocking conditions can be coupled to the electrode impedance model so as to determine key factors of the electrode/electrolyte entity, inaccessible by ex-situ approach: the double-layer capacity or the porosity/tortuosity ratio of the structure.

It must be noted that the electrode resistance deduced with the blocking configuration R_b is not representative of the real battery, that is in presence of an electrochemical reaction. In the latter case, the charge-transfer resistance (evaluated in [Chap. 4](#)) is much lower than the electrode resistance, since the reactions happen in the full volume of the electrode so that the ions should not cross the entire thickness of the material.

3.5. Conclusion

Several characterization tools are capable of advancing the development of a complex system such as RFBs. Key information like electrochemical kinetics, membrane resistance or electrode porosity are readily accessed by straightforward and time-saving methods. Some other analytical techniques, unusually used in the RFB literature, have been introduced in this chapter: the FTIR spectroscopy could readily dismiss a type of membrane pretreatment, while the NMR analysis provided insightful depictions of the flow distribution in the electrode, and underpinned the challenge of draining the gas bubbles away.

Nonetheless, the ex-situ techniques generally overlook the complexity of the final object. For instance, the results give a glimpse of material interaction that will play a key role in the overall system. The elements determined thanks to the separate analysis approach are the cornerstone of RFB development and will guide the next investigations.

4

HALF-CELL CHARACTERIZATION

Contents

| | |
|---|------------|
| 4.1 Stationary porous electrode model | 96 |
| 4.1.1 Fundamental relations | 96 |
| 4.1.2 Analytical expression with infinite electronic conductivity | 102 |
| 4.1.3 Electrode impedance | 103 |
| 4.1.4 Electrode impedance in blocking electrode conditions | 103 |
| 4.2 Global impedance of the symmetric cell: methodology | 105 |
| 4.3 Catholyte symmetric cell | 108 |
| 4.3.1 Effect of the light exposure of the catholyte on cell impedance | 108 |
| 4.3.2 Effect of the electrode material on cell impedance | 113 |
| 4.3.3 R_{cell} vs SOC curves: Identification of the degradation mechanisms | 116 |
| 4.4 Anolyte symmetric cell | 122 |
| 4.4.1 Impedance evolution in circulation | 122 |
| 4.4.2 Analysis of the cell overcharge | 123 |
| 4.4.3 R_{cell} vs SOC curves | 129 |
| 4.5 Conclusion | 134 |

The RFB cell being a complex system involving at the same time two electrochemical reactions, a methodology to investigate separately each electrolyte in a flow cell is developed. As already introduced in the diagnostic tools chapter, a particular symmetric set-up is used. The Electrochemical Impedance Spectroscopy (EIS) technique is extensively employed in this chapter. For a in-depth interpretation of the cell response, a 1D stationary model is developed in the first part. It describes the porous electrode as the superposition of the solid and liquid phases whose interface hosts electrochemical exchanges. Through specific considerations, the model leads to an analytic expression of the electrode impedance that can be compared with experiments. The studies of the catholyte and the anolyte in symmetric cells are detailed in the last two sections of the chapter.

4.1. Stationary porous electrode model

A porous electrode is a matrix of solid conductor whose pores are filled with an electrolytic solution. The intimate contact between the two phases entails a complex and heterogeneous distribution of the phenomena through the depth of the electrode. To efficiently describe the behavior of such system, it is paramount to develop a reliable macroscopic model by overlooking the exact geometric detail. The model presented in this section relies on the porous electrode description of Newman and Tobias [5].

4.1.1. Fundamental relations

The modeling domain is the porous electrode of one half-cell of the battery between the membrane and the current collector, as schematically represented in Fig. 4.1. Without convection of electrolyte inside the cell, the problem is one-dimensional in the through-plane direction along the x -axis. The properties are considered uniform and the domain is assumed isothermal. The system is in steady state by considering no net reaction in the electrolyte: the concentrations are constant. The current collector only conducts electrons; it is a barrier for the electrolyte. The membrane can only be crossed by the supporting salt cations K^+ and Na^+ ; neither the active species nor the electrons pass this boundary. We consider a general electrochemical reaction exchanging z electrons, taking place at the interface between the electrolyte and the carbon fibers of the porous electrode:

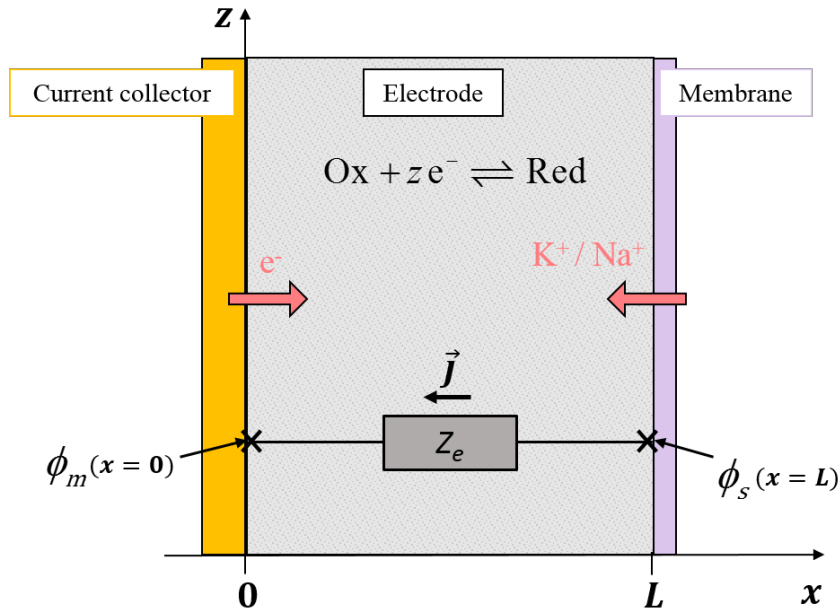


Figure 4.1: Schematic of the half-cell geometry considered for modeling

a) Electrode potential

As already introduced in subsection 1.3.1, the electrode potential is defined locally by the difference of the solid and liquid phases potentials (1.3). In the battery, the voltage drop observed through the thickness of the electrode, that is between the solid phase potential at the collector and the electrolyte potential at the membrane as depicted in Fig. 4.1, is caused by several loss mechanisms. The electrode impedance Z_e is introduced to represent these losses inside the electrode, according to the total current density applied to the battery J (A m^{-2}):

$$Z_e = \frac{\phi_m(x=0) - \phi_s(x=L)}{J} \quad (4.2)$$

b) Faradaic processes

When a current passes through the battery, the electrode is deviated from its equilibrium potential E_{eq} by an algebraic overpotential, η whose sign is dictated by the net direction (positive in oxidation and negative in reduction):

$$E = E_{\text{eq}} + \eta \quad (4.3)$$

As detailed in subsection 1.3.1, the relation between the faradaic current induced by the electrochemical reactions and the overpotential is given by the Butler-Volmer equation:

$$j_F = j_0 \left[\frac{C_r^s}{C_r} \exp\left(\frac{\alpha z F}{RT} \eta\right) - \frac{C_o^s}{C_o} \exp\left(\frac{-(1-\alpha) z F}{RT} \eta\right) \right] \quad (4.4)$$

The oxidized and reduced species concentrations can be expressed with the State Of Charge (denoted SOC) of the electrolyte and the total active species concentration (subsection 2.1.1). In the case of the catholyte it comes:

$$C_o = C_{\text{tot}} \text{SOC} \quad (4.5)$$

$$C_r = C_{\text{tot}} (1 - \text{SOC}) \quad (4.6)$$

It leads to the exchange current density of the catholyte j_{0_c} (in this case $z = 1$):

$$j_{0_c} = F k_0 C_{\text{tot}} (\text{SOC})^\alpha (1 - \text{SOC})^{1-\alpha} \quad (4.7)$$

This is reversed for the anolyte (which exchanges $z = 2$ electrons):

$$j_{0_a} = 2 F k_0 C_{\text{tot}} (1 - \text{SOC})^\alpha (\text{SOC})^{1-\alpha} \quad (4.8)$$

The faradaic reaction occurring in the pores of the electrode is located at the solution/solid interface. If averaged over a representative volume element of the electrode, j_F gives rise to a volumetric flux of charges represented by the divergence of the ionic current j :

$$\frac{dj(x)}{dx} = a j_F(x) \quad (4.9)$$

The coefficient a ($\text{m}^2 \text{m}^{-3}$) is the surface of the pore walls per unit volume of the total electrode and is called the specific surface area.

The porous electrodes used in flow batteries have a very important surface area, in the order of $10^3 - 10^5 \text{ m}^2 \text{m}^{-3}$ [186]. With a typical operational current density $J = 0.1 \text{ A cm}^{-2}$ assumed uniform in the volume of an electrode of thickness $e = 1 \text{ mm}$ and in steady-state, (4.9) becomes:

$$j_F = \frac{J}{ae} \approx 0.1 - 0.001 \text{ A cm}^{-2} \quad (4.10)$$

In the case of a uniform concentration in the pores (that is $C^s \approx C$), (1.14) can be linearized if $\frac{\alpha z F}{RT} \eta \ll 1$, and leads to:

$$\begin{aligned} j_F(x) &= j_0 \frac{zF}{RT} \eta(x) \\ &= \frac{j_0}{b} \eta(x) \end{aligned} \quad (4.11)$$

With typical values of $k_0 = 10^{-5} \text{ m s}^{-1}$ and $C = 500 \text{ mol m}^{-3}$, it gives:

$$\frac{j_F}{j_0} = \frac{1}{b} \eta \approx 10^{-4} \quad (4.12)$$

With $0 \leq \alpha \leq 1$, the linearized form (4.11) is thus justified.

c) Conservation of charge

During the electrochemical reactions, the amount of charges leaving the solid phase is equal to those entering the liquid, as a consequence of electroneutrality. This charge conservation in the volume of the porous electrode links the local ionic and electronic current densities j and j_e to the total current density J :

$$j(x) + j_e(x) = J \quad (4.13)$$

$$\frac{dj(x)}{dx} + \frac{dj_e(x)}{dx} = 0 \quad (4.14)$$

At the membrane interface ($x = L$), the ionic current collected is the current density applied to the battery (J , A.m^{-2}), whereas at the current collector ($x = 0$) there is no ionic current:

$$\begin{cases} j(x)|_{x=0} &= J \\ j(x)|_{x=L} &= 0 \end{cases} \quad (4.15)$$

The opposite boundary conditions apply to the electronic current density:

$$\begin{cases} j_e(x)|_{x=0} &= 0 \\ j_e(x)|_{x=L} &= J \end{cases} \quad (4.16)$$

In absence of concentration gradient within the electrolyte, the movement of charge species under an electric field is given by Ohm's law:

$$j = -\kappa \frac{d\phi_s}{dx} \quad (4.17)$$

The same correlation applies in the solid phase:

$$j_e = -\sigma \frac{d\phi_m}{dx} \quad (4.18)$$

κ and σ are the effective conductivities of respectively the solution filling the pores and the porous matrix (S m^{-1}), taking into account the geometrical factor of the electrode ε/τ as defined in subsection 3.2.1.

d) Analytical expression of the electrode resistance

The set of equations is resolved to get an analytical expression of the electrode impedance that can be compared to the experimental measurements.

Combined with (4.11), Eq. (4.9) gives:

$$\frac{dj(x)}{dx} = a \frac{j_0}{b} \eta(x) \quad (4.19)$$

According to (4.17) and (4.18), the derivative of (4.19) is:

$$\frac{d^2j(x)}{dx^2} = a \frac{j_0}{b} \frac{d(\phi_s - \phi_m)(x)}{dx} \quad (4.20)$$

$$\frac{d^2j(x)}{dx^2} = a \frac{j_0}{b} \left[-\frac{j(x)}{\kappa} + \frac{j_e(x)}{\sigma} \right] \quad (4.21)$$

With (4.14), the following second-order equation of $j(x)$ is obtained:

$$\frac{d^2j(x)}{dx^2} = a \frac{j_0}{b} j(x) \left[\frac{1}{\kappa} + \frac{1}{\sigma} \right] - a \frac{j_0 J}{b \kappa} \quad (4.22)$$

The global solution of such an equation has the form of:

$$j(x) = A \cosh(x\sqrt{K}) + B \sinh(x\sqrt{K}) \quad (4.23)$$

with $K = a \frac{j_0}{b} \left[\frac{1}{\kappa} + \frac{1}{\sigma} \right]$

According to the boundary conditions from (4.15), the ionic current density expression is:

$$\frac{j(x)}{J} = \frac{\sinh\left(\frac{\lambda x}{L}\right)}{\sinh \lambda} + \frac{\kappa}{\sigma + \kappa} \frac{\sinh \lambda - \sinh\left(\frac{\lambda x}{L}\right) - \sinh\left(\lambda\left(1 - \frac{x}{L}\right)\right)}{\sinh \lambda} \quad (4.24)$$

$$\text{with} \quad \lambda^2 = a \frac{j_0}{b} \left(\frac{L^2}{\kappa} + \frac{L^2}{\sigma} \right)$$

From this expression and by using Ohm's laws given in Eqs. (4.17) and (4.18), an analytic solution of the electrode impedance defined earlier can be deduced. It is only a resistance noted R_e in the present case of no dynamic perturbation of the electrical signals:

$$R_e = \frac{\phi_m(x=0) - \phi_s(x=L)}{J} \quad (4.25)$$

$$R_e = \frac{L}{\sigma + \kappa} \left[1 + \frac{2}{\lambda \sinh \lambda} + \left(\frac{\sigma}{\kappa} + \frac{\kappa}{\sigma} \right) \frac{1}{\lambda \tanh \lambda} \right] \quad (4.26)$$

This expression is rearranged to make the SOC apparent, along with three parameters specific to the electrode/electrolyte combination :

$$R_e(\text{SOC}) = \beta_1^2 \frac{1}{1 + \frac{1}{\beta_3}} \left[1 + \frac{2}{\lambda \sinh \lambda} + \left(\beta_3 + \frac{1}{\beta_3} \right) \frac{1}{\lambda \tanh \lambda} \right] \quad (4.27)$$

$$\text{with} \quad \lambda^2 = \beta_1^2 \beta_2^2 \text{SOC}^\alpha (1 - \text{SOC})^{1-\alpha}$$

In (4.27), three parameters that characterize the system electrode/electrolyte are defined:

→ β_1 and β_3 involving to the conductivities of the solid and liquid phases:

$$\beta_1 = \sqrt{\frac{L}{\kappa}}$$

$$\beta_3 = \frac{\kappa}{\sigma}$$

→ β_2 the ratio between the exchange current density (except the factor “SOC”) and the Tafel slope:

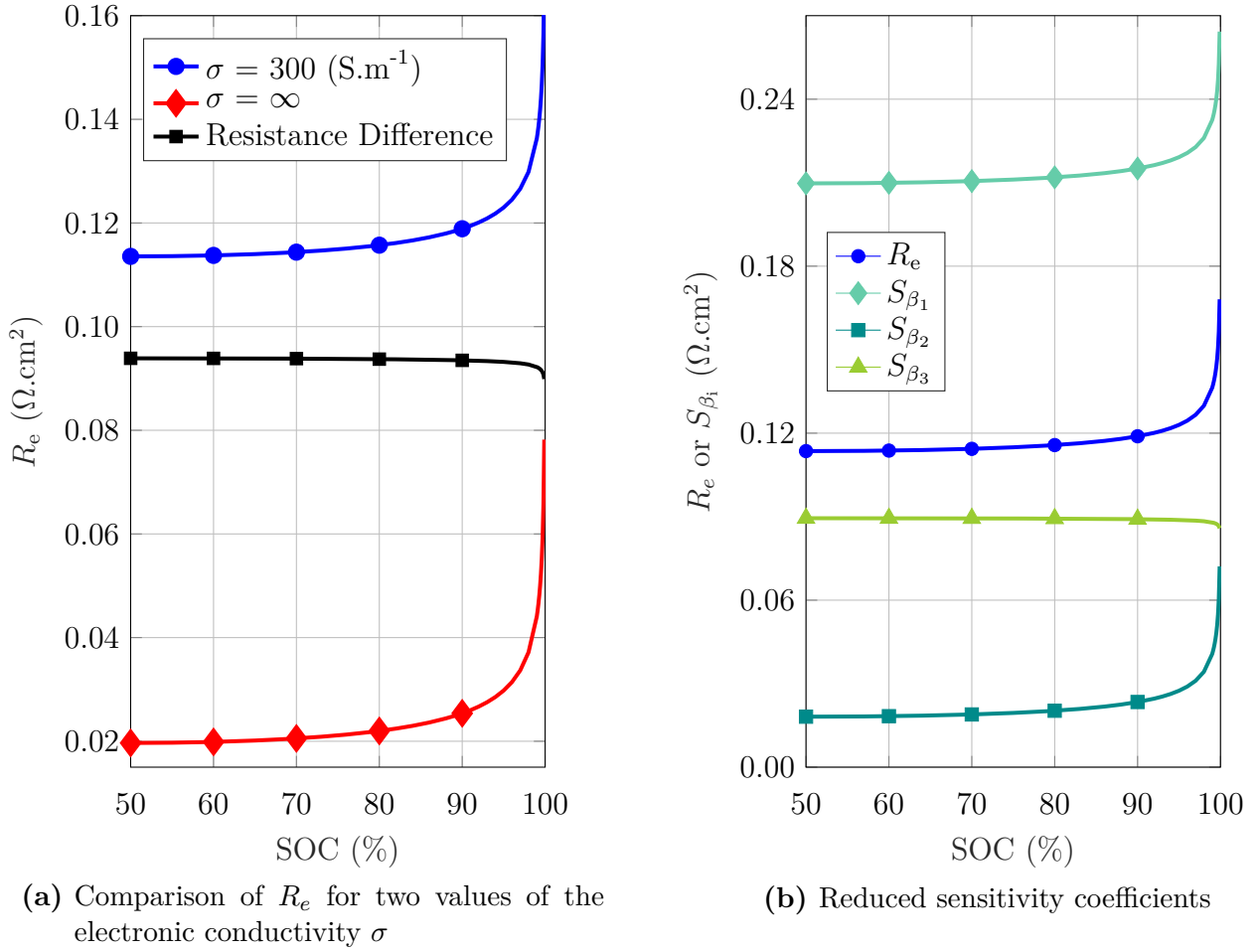
$$\beta_2 = aL \frac{zFk_0 C_{tot}}{b}$$

In the porous electrode, the ionic conductivity is usually much lower than the electronic conductivity : $\kappa \ll \sigma$. The electrode resistance (4.26) is calculated for the two cases of $\sigma = 300 \text{ S m}^{-1}$ or $\sigma = \infty$ (so that $\beta_3 \approx 0$). The results are respectively the blue curve and the red curve of Fig. 4.2a. The typical values listed in Table 4.1 were utilized to calculate R_e .

Table 4.1: Typical values of the parameters involved in R_e (4.26)

| L m | C_{tot} C=mol m ⁻³ | k_0 m s ⁻¹ | κ S m ⁻¹ | T K | a m ² m ⁻³ | α |
|--------------------|------------------------------------|----------------------------|-------------------------------|----------|---------------------------------------|----------|
| 3×10^{-3} | 0.5×10^3 | 15×10^{-5} | 15 | 300 | 100×10^3 | 0.5 |

As presented in Fig. 4.2a, the electrode resistance increases as the SOC changes from 50 to 100%. It would be the same between 50 and 0%. The resistance is obviously higher if the solid phase conductivity is not infinite. The black curve depicts the difference between the resistance calculated with finite and infinite solid conductivity: it is almost constant (except at SOC close to 100%). This means that neglecting the solid phase resistance only shifts the curve downward without reshaping it.

**Figure 4.2:** Calculation of the electrode resistance model R_e (4.27) as a function of SOC with the typical values of Table 4.1

Before using the porous electrode model for parameters determination, a preliminary sensitivity analysis must be carried out. Dimensionless sensitivity coefficients are introduced to be able to compare them:

$$S_{\beta_i} = \beta_i \left. \frac{dR_e}{d\beta_i} \right|_{\beta_j}$$

The sensitivity coefficients of β_1 , β_2 and β_3 are presented in Fig. 4.2b (right) as a function of the SOC, for the set of parameters given in Table 4.1 and $\sigma = 300 \text{ S m}^{-1}$.

The graph reveals that R_e is sensitive to all parameters. However, since S_{β_1} and S_{β_2} are proportional, the two parameters cannot be deduced simultaneously from the resistance measurement. The sensitivity to β_3 is nearly constant, which confirms that the solid phase resistance can be regarded as an additional term to the electrode resistance at infinite σ . In the following, the electronic conductivity σ is considered much larger than the ionic conductivity: the solid potential ϕ_m is then assumed uniform.

4.1.2. Analytical expression with infinite electronic conductivity

By considering $\sigma \rightarrow \infty$, the previous resolved expressions are simplified. The analytic form of $j(x)$ (4.24) reduces to:

$$\frac{j(x)}{J} = \frac{\sinh(\lambda x)}{\sinh(\lambda L)} \quad (4.28)$$

$$\text{with} \quad \lambda^2 = \frac{a}{\kappa} \frac{j_0}{b}$$

In this regard, the expression (4.26) of the electrode resistance is simplified by:

$$R_e^{\sigma \rightarrow \infty} = \frac{1}{\lambda} \frac{1}{\kappa \tanh(\lambda L)} \quad (4.29)$$

If the ionic conductivity $\kappa \rightarrow \infty$, (4.29) tends towards the charge-transfer resistance R_{CT} :

$$R_{CT} = \frac{b}{a j_0 L} \quad (4.30)$$

Since $\beta_3 = 0$ with an infinite σ , the resistance expression as a function of SOC (4.27) becomes:

$$R_e(\text{SOC})^{\sigma \rightarrow \infty} = \frac{\beta_1}{\beta_2} \frac{1}{\sqrt{\text{SOC}^\alpha (1 - \text{SOC})^{1-\alpha}} \tanh\left(\beta_1 \beta_2 \sqrt{\text{SOC}^\alpha (1 - \text{SOC})^{1-\alpha}}\right)} \quad (4.31)$$

Eq. (4.31) will be used to analyze the experimental results; the exact methodology is described in section 4.2.

4.1.3. Electrode impedance

At the interface between the electrode and the electrolyte, the species in solution arrange into several layers to form with the metal an electrically neutral system [76]. This behaves like a capacitor that is characterized by the double-layer capacity of the interface C_{dl} ($F m^{-3}$) (depending to both the electrode material and the ionic composition of the solution). In addition to charge-transfer reactions and the related faradaic current j_F , the reorganization of the charges at the surface of the solid fibers induces a capacitive current.

By considering this interface property, (4.9) becomes a function of x and t :

$$\frac{\partial j(t, x)}{\partial x} = a j_F(t, x) + C_{dl} \frac{dE(t, x)}{dt} \quad (4.32)$$

If the concentrations are constant (when no net current flows through the electrode), it comes:

$$\frac{dj(t, x)}{dx} = a j_F(t, x) + C_{dl} \frac{\partial \eta(t, x)}{\partial t} \quad (4.33)$$

The capacitive processes occur within short periods of time and can be neglected in long time-scales experiments. They are however of importance during the dynamic perturbation by Electrochemical Impedance Spectroscopy measurements (subsection 2.2.4). In this specific application, the electrical variables (current and potential) are a superposition of a constant value (depending on the position inside the electrode) and a dynamic signal whose frequency is modulated with time. They can be written as the product of these two components: $F(t, x) = f(x) \exp(i\omega t)$, with the angular frequency $\omega = 2\pi f$ (and i the imaginary unit).

Therefore, combined with (4.11), the spatial part of Eq. (4.33) gives:

$$\frac{dj(x)}{dx} = \left[a \frac{j_0}{b} + i\omega C_{dl} \right] \eta(x) \quad (4.34)$$

The resolution is similar to the previous case. By introducing a new parameter $\beta_4 = LC_{dl}$, the electrode impedance can be extended to:

$$Z_e(\omega, SOC) = \frac{\beta_1}{\beta_2} \frac{1}{\sqrt{SOC^\alpha(1 - SOC)^{1-\alpha} + i\omega\beta_4} \tanh\left(\beta_1\beta_2\sqrt{SOC^\alpha(1 - SOC)^{1-\alpha} + i\omega\beta_4}\right)} \quad (4.35)$$

The electrode impedance simplifies to the electrode resistance at DC current, that is when $\omega \rightarrow 0$. As such, the value of R_e stands at the intercept of the x-axis in the Nyquist representation.

4.1.4. Electrode impedance in blocking electrode conditions

As it was presented by Gaumont et al., the impedance model can be simplified to the specific case of $\beta_2 = 0$ when no faradaic reaction occurs in the pores; it is referred to as blocking conditions [137]. The blocking electrode impedance, noted Z_b is only a function of

the frequency:

$$Z_b = \beta_1 \frac{1}{\sqrt{i\omega\beta_4} \tanh \beta_1 \sqrt{i\omega\beta_4}} \quad (4.36)$$

Z_b depends on the ionic conductivity of the electrode via β_1 and on the double layer capacity in β_4 .

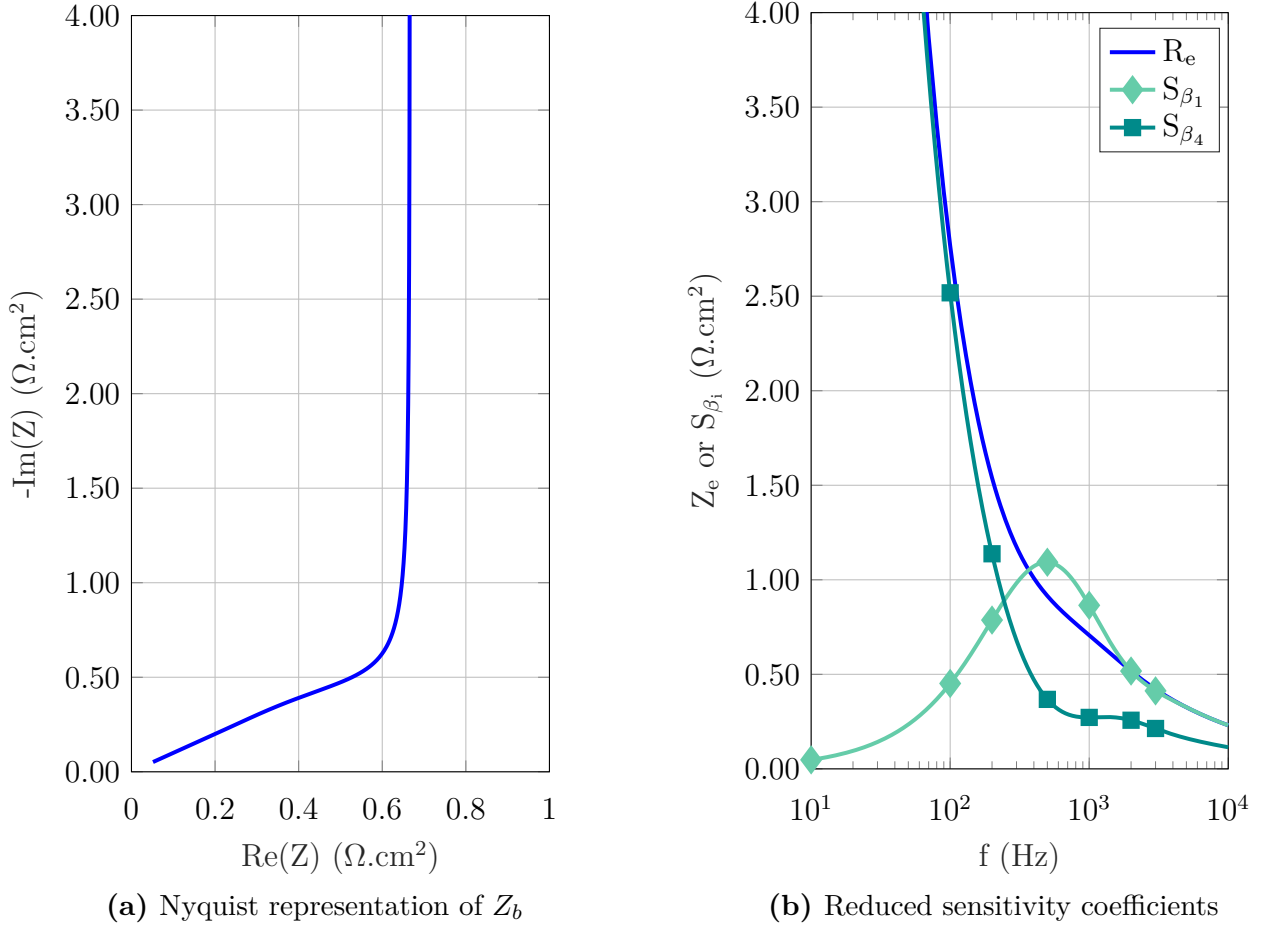


Figure 4.3: Calculation of the blocking impedance model Z_b (4.27) as a function of frequency with the typical values of Table 4.1

Fig. 4.3a displays the Nyquist plot of the blocking electrode impedance Z_b (4.36) for the standard parameters (Table 4.1) giving $L/\kappa = 2 \Omega \text{cm}^2$ and for $LC_{\text{dl}} = 6 \times 10^{-4} \text{F cm}^{-2}$. With an infinite solid conductivity, the electrode impedance tends towards 0 at very high frequency. When decreasing the frequency, the electrode impedance can be approximated by $Z_b \approx \beta_1 \frac{1}{\sqrt{i\omega\beta_4}}$: as a consequence the Nyquist plot features a 45° slope in the high-medium frequency region. At low frequencies, the electrode behaves like a pure capacity and appears as a vertical line in the Nyquist chart (it is a semi-circle with infinite diameter): $Z_b^{\omega \rightarrow 0} \approx \beta_1 \frac{1}{i\omega\beta_4}$.

The sensitivity analysis of the impedance magnitude $|Z_b|$ depending on the frequency is shown in Fig. 4.3b. The electrode impedance is sensitive to both β_1 and β_4 . At low frequencies the impedance is only sensitive to the double layer capacity while at medium frequency the ionic resistance is most influential. This analysis shows that both parameters β_1 and β_4 can be deduced simultaneously from the impedance measurement providing that it is performed over

a wide range of frequencies.

In the present study, the model was applied to a symmetric cell filled with the supporting electrolyte to force the blocking conditions at the electrodes. This approach served in the characterization chapter to determine the membrane resistance R_m for several salt compositions (subsection 3.3.2) and to evaluate the electrode resistance in these conditions, noted $R_b = \beta_1^2$ (subsection 3.4.3).

The same blocking electrode model was applied by Malifarge et al. to derive electrode physical characteristics such as the pore tortuosity from the determination of the effective ionic conductivity κ in β_1 [182].

This section developed the porous electrode model in two specific conditions:

- when the electrode impedance is a pure resistance and can be expressed as a function of SOC of the electrolyte filling the pores. With the assumption of infinite solid conductivity, R_e depends on the two parameters β_1 and β_2 as given in (4.29).
- when capacitive processes are not negligible and the electrode is in blocking conditions (no electroactive material present). In this case the electrode impedance Z_b is expressed as a function of the frequency of the electrical signal (4.36) and is sensitive to β_1 and β_4 .

The two electrode models were used to determine some intrinsic parameters of the electrode by comparison with experimental data. The method is described in the next section.

4.2. Global impedance of the symmetric cell: methodology

Models of electrode impedance in specific conditions were developed above to obtain analytic expressions including intrinsic features of the electrodes. However, these equations describe what happens in one electrode of the cell, while it is the full cell that can be experimentally characterized.

To be able to compare model and experiment, a specific set-up was used: the symmetric cell (described thoroughly in section 2.3). The composition of the electrolyte of both sides was the same. For both the anolyte and the catholyte, the following hypotheses were stated:

- α is equal to 0.5
- the oxidation and reduction are first order in the reactants and their respective rates can be expressed with the common parameter k_0 (Eqs. (1.5)–(1.7) and (3.4))

These hypotheses were partly confirmed by the results of the electrochemical analysis for both electrolytes (section 3.1).

As previously mentioned, the resistance of the electrode solid phase is considered as additive to the total impedance so that with the contact resistances between the materials and the membrane resistance, they constitute the high frequency component of the cell impedance R_{HF} . The sum of the solid phase and contact resistance $R_{\text{solid phase}} + R_{\text{contact}}$ was experimentally assessed in a dry cell assembled without membrane and with two porous electrodes at a compression ratio of 35 %. The value of $0.09 \Omega \text{ cm}^2$ was measured with a four-probe milliohmeter. In the subsequent results, this amount can be subtracted from R_{HF} so as to isolate the membrane resistance R_m . It must be noted that the junction potential at the electrolyte-membrane interface was neglected.

With the above assumptions, the impedance of the symmetric cell Z_{cell} contains the two electrodes impedances and the high-frequency resistance. It can be written as:

$$Z_{\text{cell}}(\omega, \text{SOC}) = 2 Z_{e/b}(\omega, \text{SOC}) + R_{\text{HF}} \quad (4.37)$$

$$\text{with} \quad R_{\text{HF}} = R_{\text{solid phase}} + R_{\text{contact}} + R_m$$

In (4.37), the electrode impedance considered is either Z_e or Z_b , depending on the experimental conditions. In both cases, Z_{cell} contains several variables that can be determined by fitting the model to the data points obtained with the symmetric set-up. The sensitivity of Z_{cell} regarding R_{HF} is constant with SOC and thus uncorrelated with the parameters in $Z_{e/b}$. The experimental data fitting by the model was performed by a non-linear least square method implemented in Matlab with two different algorithms: trust region reflective and Levenberg-Marquardt [190].

In the case of the blocking electrode conditions, the influence of the supporting electrolyte and of the electrode material on the resistances are explored through the impedance model Z_b (4.36). The parameters β_1 (related to electrolyte conductivity), β_4 (representing the double layer capacity) and R_m contained in the impedance expression can be extracted concomitantly from the fitting. The results of these experiments are displayed in the previous chapter of material characterization (subsection 3.4.3).

In the presence of active species, the equation of Z_e (4.35) is used. The focus is put on the parameter β_2 to seek an in-situ estimation of $a.k_0$, the product of the reaction rate and of the specific surface area. The actual active surface area being hard to determine for porous materials, the two factors cannot be evaluated separately [123]. β_1 being correlated to β_2 , it is estimated by preliminary conductivity measurements. It is also possible to estimate the membrane resistance R_m .

A typical Nyquist spectrum of the cell impedance, obtained with the catholyte symmetric cell is presented in Fig. 4.4. The cell was built in this case with carbon paper electrodes; the catholyte was at SOC 50; the spectra obtained for two flow rates are compared.

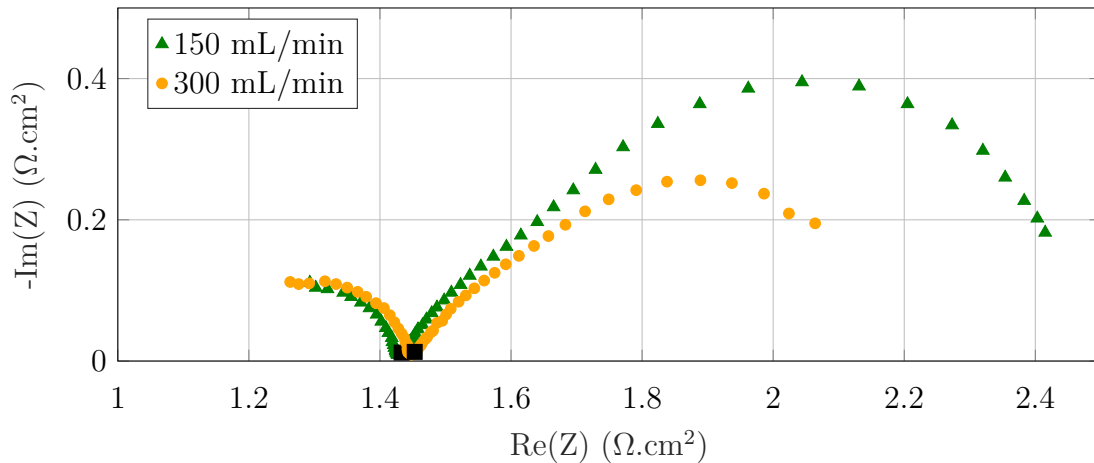


Figure 4.4: Complex Impedance spectrum of the symmetric cell at SOC 50 with carbon paper electrodes for 2 flow rates. The black square show the value at 100 Hz.

It is clear that the real component of Z_{cell} prevails over the imaginary part. They are

composed of two successive semi-circles:

- The small arc at frequencies higher than 100 Hz (left side of the spectrum) relates to the solid/liquid interface where the electrochemical reaction happens; it is usually associated with an equivalent RC circuit accounting for the charge-transfer resistance and the double-layer capacity of the electrode. Even at the highest frequencies tested this loop stays open because of a low double-layer capacitance value.
- A large loop was obtained at the frequencies lower than 100 Hz (right side of the spectrum). It can be ascribed to mass transfer limitations by diffusion and advection. The variation of the low frequency loop observed for two flow rates in Fig. 4.4 underpins this theory. This part of the impedance plot is not described by the electrode model developed earlier. Pezeshki et al. presented an analytical EIS model also accounting for the whole spectrum [95]. The mass-transport resistance associated to the LF region depends on the active surface area of the electrode, the diffusion and the concentration of the reduced and oxidized forms of the active species.

The relevant part of the spectra for this study is the high to mid-frequency range. The impedance at 100 Hz, outlined by the square in Fig. 4.4, represents the sum of R_{HF} and of twice Z_e , according to (4.37). It is actually a pure resistance at that frequency. Thus, the simplified electrode resistance expression (4.29) is adequate to interpret the experimental data instead of its complex form (4.35).

Since the high-frequency loop remains open within the range of possible frequency scanning, R_{HF} value is not readily available from the plot; fitting the impedance model to the R_{cell} vs SOC curve paves the way for decoupling the two resistive elements R_{HF} and R_e . The spectrum obtained with carbon paper reaches the x-axis at almost a single point (the square) between the two loops. However, the use of carbon felt induced a level section of several points between the 2 semi-circles (comparison of spectra with the two electrode materials available in subsection 4.3.1). The mid-frequency resistance was thus obtained experimentally by averaging the real part of (Z_{cell}) over several frequencies:

$$\begin{aligned} R_{\text{cell}}(\text{SOC}) &= \overline{\text{Re}} [Z_{\text{cell}}(50; 200 \text{ Hz})] \\ &= 2R_e(\text{SOC}) + R_{\text{HF}} \end{aligned} \quad (4.38)$$

The standard deviation of the measurements at mid-frequency was insignificant, inducing an error of less than 5 %. To keep the test short, the scanned frequencies were restricted to the values of interest (between 50 and 200 Hz).

This section introduced how the porous electrode models detailed before and the experimental EIS data of a symmetric cell could be combined to determine in-situ some important features of the system: the membrane resistance R_m , the double-layer capacity C_{dl} and the kinetic product $a.k_0$. All the results relating to blocking electrode conditions were used in the previous chapter to characterize the membrane and the electrode (Sections 3.3.2 and 3.4.3).

The next two sections relate the findings from this method in the case of the catholyte symmetric cell and then the anolyte symmetric cell.

4.3. Catholyte symmetric cell

The catholyte behavior in a RFB configuration was scrutinized by means of the symmetric cell configuration. The catholyte, composed by 0.5 M $[\text{Fe}(\text{CN})_6]^{4-}$ in 0.2 M NaOH, was half-charged before use in the symmetric set-up. In a first part, the investigation focused on the electrolyte interaction with the other materials of the cell (membrane and electrode) during the circulation of the solution. In particular, the effect of photodegradation of $[\text{Fe}(\text{CN})_6]^{3-}$ / $[\text{Fe}(\text{CN})_6]^{4-}$ on the battery performance was examined. The catholyte was then protected from light to outline the performance evolution during cycling.

4.3.1. Effect of the light exposure of the catholyte on cell impedance

The stability of the catholyte depends on its environmental conditions. It was revealed in a previous chapter (subsection 3.2.3) that direct contact with metal or light exposure triggered a catholyte degradation along with formation of precipitates. Metallic components were totally removed from the set-up by the exclusive use of plastic connectors. During the manufacturing process of the system, large volumes of liquids are stored in standard Intermediate Bulk Containers (IBCs) that can either be made of opaque or clear plastic. It is crucial to comprehend how light affects the performance of the catholyte. The ensuing discussion assesses the effect of photodecomposition in the context of RFB. To that end, the reservoirs of electrolyte were not protected from sunlight during the tests of this section.

a) Experiment

A catholyte symmetric cell was used to compare the in-situ performances of three types of membrane preparation: the pristine, the KOH-converted and the reflux-treated membranes. This experiment completes the previous ex-situ analysis of these membranes by FTIR-ATR (subsection 3.3.1).

The cell was filled with a catholyte pre-charged at SOC 50; the tanks containing the catholyte were not protected from light in this part. This set-up was left under circulation at 200 mL min^{-1} for an extended period during which the cell impedance was followed.

Fig. 4.5 exhibits the Nyquist plots obtained with the three membranes before long-duration circulation, along with the spectrum recorded after 200 h of electrolyte flow with the pristine membrane.

The only difference between the initial curves is the HF behavior (that is above 10 kHz): this is ascribed to interference from the electrical hardware since no physical reason was found to explain it and because the spectrum in this range of frequency was not repeatable, even with the same set-up. The HF data excluded, the initial spectra feature the exact same shape with a small shift on the x-axis: unsurprisingly, the type of membrane only affects the pure resistive component of the cell. After circulation with untreated membrane, the plot essentially has the same shape: it has been shifted to higher resistance values, with only a minor increase of the charge-transfer loop.

This suggests that a performance degradation is observed during circulation and is predominantly attributed to the membrane resistance, which equates to the diminution of its conductivity.

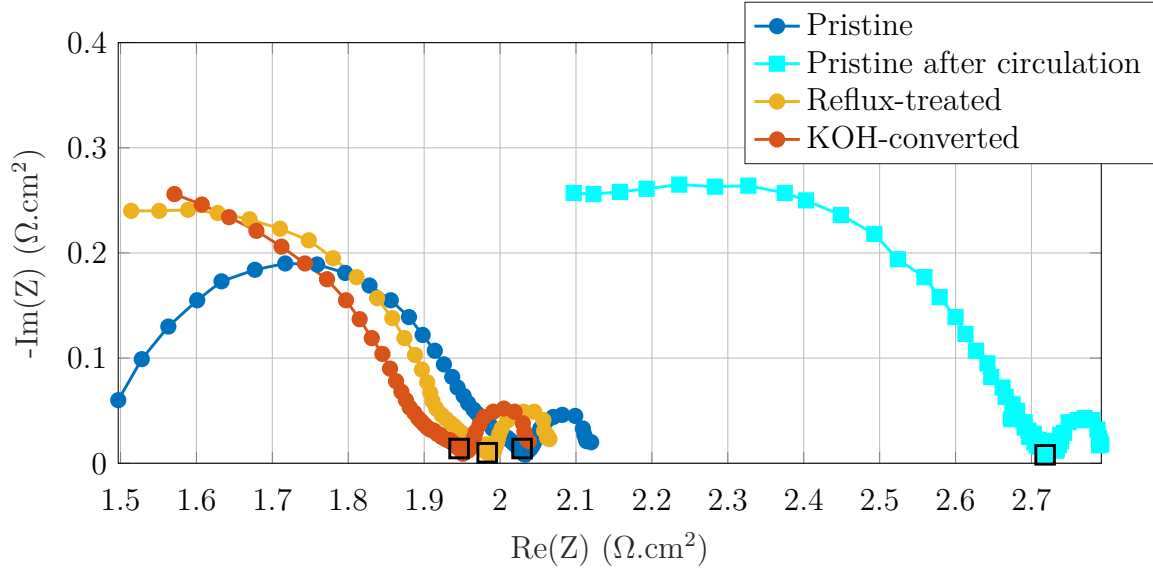


Figure 4.5: Comparison of the Nyquist plots in a symmetric cell with several types of membranes, for the frequency range [20 mHz;10 kHz]. \square : datapoint at $f = 100$ Hz

b) Cell impedance evolution with circulation

To get a clear view of the performance degradation during circulation, the mid-frequency resistance (at $f = 100$ Hz) noted R_{cell} is displayed as a function of circulation time for the three types of membranes in Fig. 4.6. The horizontal scale is cut after 160 h for better observation as the values for the pristine membrane stabilized after that time.

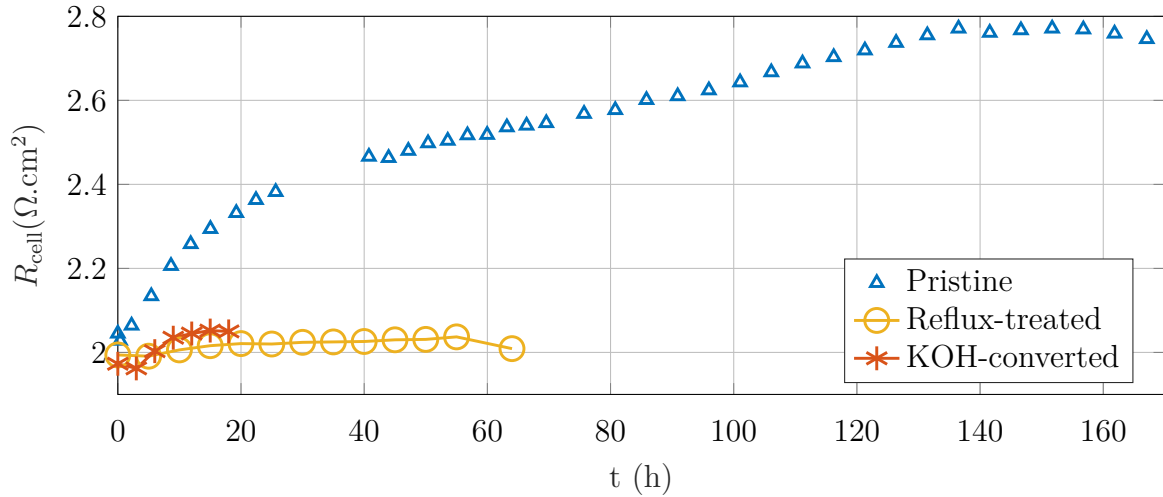


Figure 4.6: Evolution of the cell resistance (real part of the cell impedance at 100 Hz) of a catholyte symmetric cell during circulation of electrolyte with three types of pretreated membranes

The resistance was initially similar for all the membranes, around $1.9 \Omega \text{ cm}^2$. A significant performance degradation was measured in the case of the pristine membrane: R_{cell} increased by 40 % in one week. The reflux-treated membrane gave a nearly constant impedance, while the evolution of the converted membrane was slightly above: membrane cleaning in alkaline

solution seems to mitigate the performance degradation, although the experiment was not run for long enough to certify this. Yet the photolysis of catholyte is not influenced by the type of membrane in contact with the solution, as demonstrated in the long-duration stability test in subsection 3.2.3. It means that the membrane pretreatment only changes how the degradation products affect the cell resistance.

During the 200 h of circulation with the pristine membrane, the results outline three zones with different kinetics. The degradation rate is more pronounced for the first 15 h, then declines before leveling after 140 h. Kuhn et al. evidenced that the photolysis rate inversely depended on the free cyanide concentration in solution [165]. As such, the complete ferrocyanide dissociation is faster at the beginning and slows down over time; it could correlate with the decrease in slope detected after 15 h circulation in Fig. 4.6.

A further test substantiates the implication of the membrane in the observed degradation. After the circulation, the untreated membrane was swapped with a new pristine sample and the cell impedance could recover its initial modulus of $1.9 \Omega \text{ cm}^2$ at 100 Hz. The plateau detected in Fig. 4.6 might illustrate a saturation of the membrane with pollutants or the shortage of pollutants themselves.

The occurrence of such a resistance increase (of about 40 %) could be reproduced under several other conditions, as listed in Fig. 4.7 under the red arrow. On the other hand, specific experiments retained the performance or could bring the system back to its original impedance; they are represented in green in Fig. 4.7.

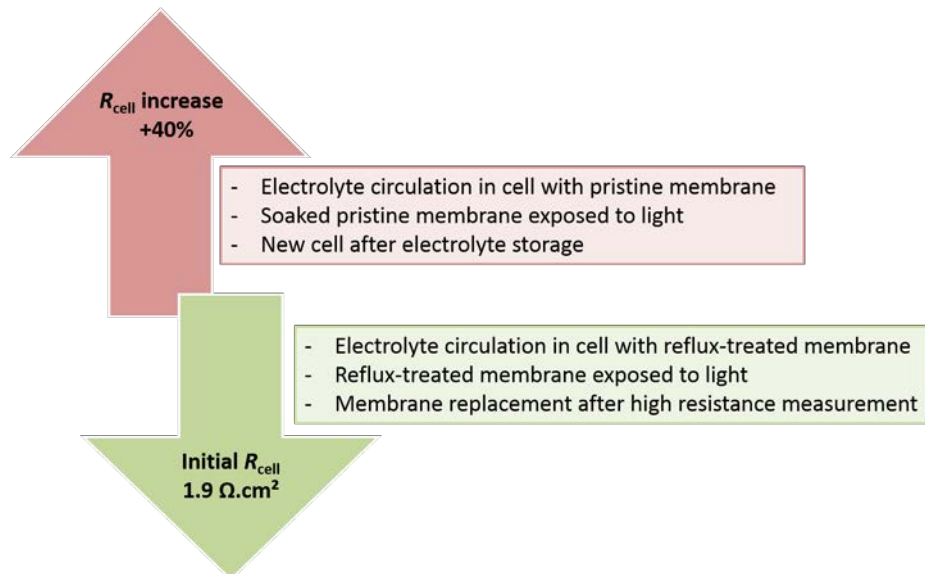


Figure 4.7: Classification of the catholyte symmetric tests in two categories: the ones causing a cell impedance increase of +40 % and the ones keeping or reducing the impedance to its initial value of $1.9 \Omega \text{ cm}^2$

The repeatability of the measurement with the same sample of membrane was tested: a cell with low initial impedance was pulled apart to remove the membrane. The latter was either directly re-assembled into the set-up, or stored in dry/water/KOH conditions, for one minute to several hours. Whichever circumstance was chosen, the observation was similar: with an untreated membrane, reassembling the cell worsened its impedance of 40 % compared to initially. With a reflux-treated membrane the initial performance was however maintained. It

evidences that the exposure to light “pollutes” the membrane that has already been in contact with the catholyte, but only if it is untreated.

Another experiment was performed to investigate the electrolyte photodegradation during storage. A freshly prepared electrolyte at SOC 50 was stored during 1, 5 or 15 days in transparent plastic tanks. Afterwards, a clean cell containing an untreated membrane was connected to the stored electrolyte: the impedance took a high value of $2.5 \Omega \text{ cm}^2$ after 1 day and $2.7 \Omega \text{ cm}^2$ after 5 or 15 days. By replacing the membrane with another pristine sample, the performance recovered its standard value of $1.90 \pm 0.05 \Omega \text{ cm}^2$. It seems that the photodegradation products were trapped in the membrane, making it highly resistive. Once the pollutants were captured in the first membrane, the cell performance could be retrieved by the single replacement of the separator.

In summary, the photolysis of the catholyte entails an increase of cell resistance with a pristine membrane certainly through the lessening of the membrane conductivity. The electrolyte alteration has no consequence on a reflux-treated membrane, and it is more difficult to conclude for the KOH-converted membrane. The catholyte degradation completely saturates the pristine membrane with pollutants after 120 h of circulation or external storage in unprotected conditions, or immediately after the direct exposure of the membrane soaked with catholyte to light. It could be hypothesized that during circulation, the pollutants are produced in the tank: they are progressively carried towards the membrane and as a consequence the resistance increase is delayed. On the contrary, exposing the soaked membrane to light alters the catholyte that it contains. As the pollutants are created into the material, their impact on the impedance was observed immediately afterwards. Changing the polluted membrane allowed for the recovery of the initial impedance (corresponding to the “pristine” spectrum in Fig. 4.5); the electrodes and other components of the cell were not polluted by the photoproducts.

c) Post-mortem FTIR-ATR analysis of the membranes

A thorough post-mortem analysis of the different pretreated membranes might unravel why they are unequally sensitive to the photoproducts of the catholyte. After use in the symmetric cell, one distinction was visible: all the untreated membranes presented a blue frame on the rim of the active surface, as exemplified in Fig. 4.8 by the letter B. The coloring did not vanish even when cleaning the membrane with water or KOH. On the other hand, the treated membranes were completely clear.

The FTIR-analysis of the untreated membrane after use is shown in Fig. 4.9; the two zones of the active surface (A) and the blue stain (B) were analyzed. Solutions of ferrocyanide (catholyte at SOC 0) and of a mixture of ferrocyanide/ferricyanide (catholyte at SOC 50) were previously analyzed with the IR technique to determine their band positions. As also reported in the literature, ferrocyanide gives rise to a peak at 2044 cm^{-1} and ferricyanide vibrates at a frequency of 2118 cm^{-1} [191]. The characteristic peak of Prussian Blue at 2090 cm^{-1} was clearly identified in the colored rim of the membrane [191]. This pigment is produced in the presence of iron(III) salt and ferrocyanide [192]. In the case of an excess of Fe(III), it gives insoluble blue precipitates:



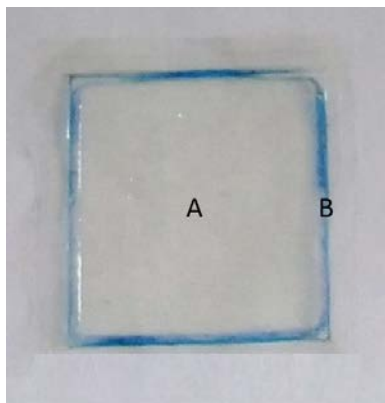


Figure 4.8: Picture of a pristine membrane after use in a catholyte symmetric cell, and the two zones analyzed in FTIR-ATR

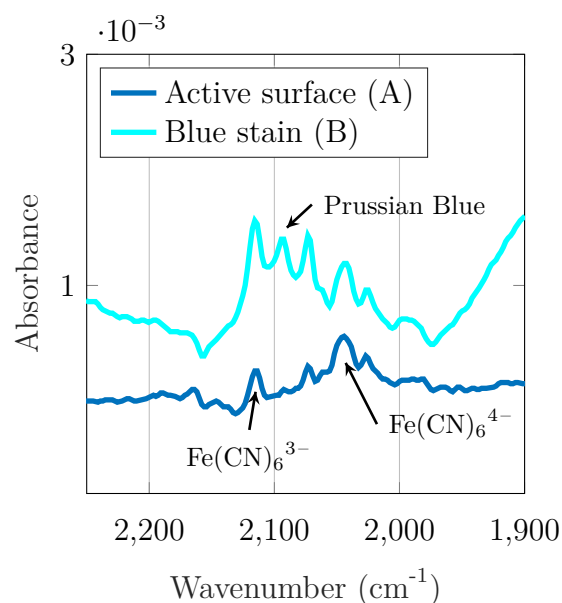
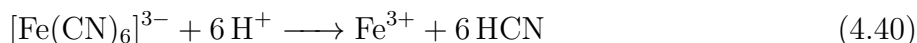


Figure 4.9: ATR-FTIR spectra of two regions of a pristine membrane whose analyzed areas are pointed in Fig. 4.8

Detection of the Prussian Blue band on the stain of the membrane implies that Fe(III) was formed in the cell. Indeed, under strongly acidic conditions, such as close to the pristine membrane that was still in protonic form, the decomplexation of the ferricyanide can be total:



As for the ferrocyanide, it is more stable. Poisonous hydrogen cyanide gas is released in this reaction: the contact of the catholyte with strong acid must be circumvented by converting the membrane before use. Insoluble Prussian Blue was present only at the rim of the active surface of the membrane, because it was the unique zone where ferric ions could be produced in excess: protons were rapidly washed away and replaced by other cations everywhere in the membrane except close to the edge where H^+ could diffuse from the dry part of the membrane (outside the seal) and locally create many ferric ions. Fe(III) precipitated into blue solid with ferrocyanide. Once the pigment was formed, it stayed trapped in the membrane because of its high stability. Elsewhere, the protons in the membrane might have triggered the formation of soluble Prussian Blue that diluted into the catholyte; it was not detected at the surface of the membrane.

Three peaks at 2025, 2073 and 2165 cm^{-1} in the active surface remain unidentified : according to [191] they likely stem from reaction intermediates of the catholyte during the charge-transfer step that adsorb onto the electrode. This complex band signature substantiates the complexity of the electrochemical behavior of the iron-cyanide pair and confirms the possibility of strongly-adsorbed intermediates. However the active surface spectrum in Fig. 4.9 is not specific to the pristine membrane; the same bands were also recorded on the two other pretreated membranes after use.

Therefore, FTIR-ATR analysis ascribes the origin of the blue rim of the pristine membrane to formation of Prussian Blue. But the results are not meaningful to account for the different behavior in a cell containing photo-decomposed catholyte. The reason for the resistance increase of the untreated membrane in contact with the photoproducts could lie in the thickness of the separator where the IR surface technique cannot penetrate.

An industrial perspective

Light exposure can be minimized in a real RFB system, but analyzing the performance of the different membrane pretreatments in contact with the catholyte photoproducts demonstrates the stability of the reflux-treated membrane. One could forecast that this type of membrane would also be robust against other pollutants. The reflux process is constraining but secures the performance of the membranes. By unraveling the real benefit of this pretreatment, a simpler method which is as effective could be designed. The membrane should at least be pre-converted to alkaline form, since its use as-received leads to undesired Prussian Blue formation (by degradation of active species) and HCN release. Since handling wet materials complicates the stack assembly, it is worth considering placing the membranes after pretreatment in a humid chamber that regulates their relative humidity and avoid uncontrolled contraction of the material during drying. Once their water content regulated, they are ready for assembly. The membranes manufacturers are ready to adapt a pretreatment of their materials corresponding to KEMIWATT's needs, once the company orders sufficiently large amounts of membranes.

This first part of symmetric cell study highlights the importance of membrane pretreatment on the performance evolution during circulation of the catholyte. Its photolysis clearly affects the membrane resistance when this material is used as-received. An appropriate pretreatment mitigates the membrane sensitivity to pollutants. Since the underlying mechanism of resistance increase could not be clarified, the membrane was never used as-received in the next steps of the PhD: the 80 μm reflux-treated membrane was chosen as the standard for the following experiments. Moreover, the effect of light exposure was suppressed by keeping the catholyte protected at all times.

4.3.2. Effect of the electrode material on cell impedance

This part follows on from subsection 3.4.3. The impedance of a cell filled with a supporting salt was monitored during the addition of active species for the purpose of observing the transition from a blocking electrode to an active electrode hosting electrochemical reactions.

a) Experiment

The experience was performed in a symmetric cell with a flow rate of 200 mL min^{-1} . The cell was first filled with a solvent of 2 M NaOH; $[\text{Fe}(\text{CN})_6]^{4-}$ powder was then added on one side of the cell to reach a concentration of 0.5 M of ferrocyanide. This step is denoted by “ferro” in the legend of the following figures. One, and then both sides of the cell were replaced with a solution composed in equal proportion of the ferri/ferrocyanide species (0.25 M of each form)

corresponding to the catholyte at SOC 50. These steps are mentioned as “ferri/ferro”. During all these successive additions of active species, the cell set-up remained the same.

This protocol was applied to a cell assembled with carbon felts (4.6 mm). The first and last solution configurations were also tested on another cell, this time assembled with one layer of carbon paper at each electrode (300 μm). In both cases the porous electrodes were compressed at 35 %, and the assembly was rinsed by circulating NaOH prior to starting the test. After each modification of solution composition, EIS measurements were repeated over a few hours to detect when the system was at equilibrium. The Nyquist plots evolution relative to the electrolyte composition is given in Fig. 4.10a with carbon paper electrodes and in Fig. 4.10b in the case of carbon felt. The mention of “d+1” indicates the spectra obtained after 1 day of circulation. The squared data point out the impedance at 100 Hz.

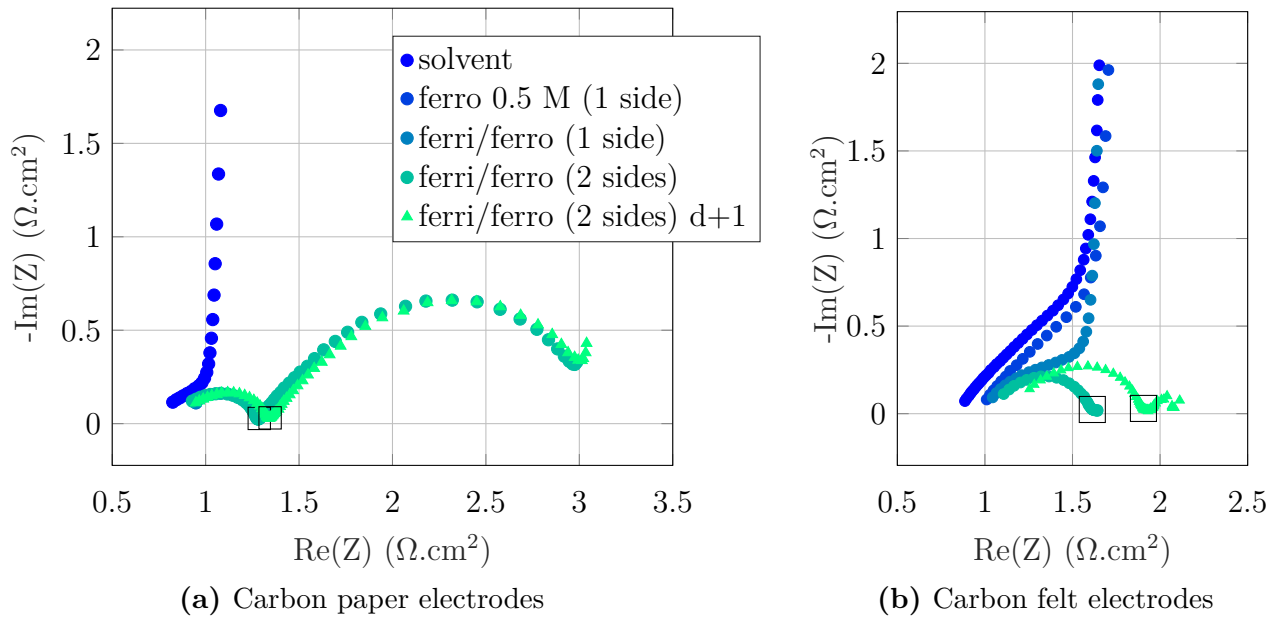


Figure 4.10: Impedance spectra evolution of a symmetric cell with addition of catholyte active species. Uniform legend for both cases. \square : datapoint at $f = 100$ Hz

It can be observed that the addition of the active species tends to increase the cell resistance. Indeed, the counter-ion of ferrocyanide was K^+ , so that this increase relates to the aforementioned influence of the cation on R_m . The left graph highlights that the 45° slope remained even with the presence of ferrocyanide on one side but faded away when this side was filled with a mixture of ferri/ferrocyanide. It gave way to a circular shape that still terminated vertically. It was only when both sides of the cell were supplied with a redox couple that the full semi-circle replaced the blocking electrode line at decreasing frequency. The diagram on the right gives evidence that a similar evolution was observed with carbon paper. Nevertheless, the final complex impedance plot obtained for the two electrode materials is different.

b) Comparison between carbon felt and carbon paper electrodes

The ohmic cell resistance resolved at the high-frequency intercept is lower with the thinner carbon paper. The EIS shape at high frequency also exhibits a facilitated charge transfer with carbon paper. This matches the suggestion of Pezeshki et al. that the activity of the

graphitized paper is greater than the carbon felt in VRFB [95]. On the other hand, Darling et al. determined similar charge-transfer resistances for both types of electrodes [36]. They were however in different conditions (they studied vanadium electrolytes and heat-treated the porous materials before use).

At low frequency, the response of the two types of electrode is also contrasting. With carbon felt, the shape of a tiny loop can barely be noticed while with the carbon paper configuration, the low frequency loop dominates the spectrum. This underpins the difference of resistance already detected in subsection 3.4.3.

This second semicircle is often put down to critical mass transport limitation that is mitigated by increased electrolyte velocity within the pores. This can be achieved by changing the flow rate as already highlighted in Fig. 4.4 but is also a consequence of the porous structure. The carbon paper features concurrently a reduced thickness and porosity compared to the felt. As asserted by pressure drop measurements in [95], this hinders the portion of the solution flowing through the electrode. The electrolyte instead bypasses the porous material via the channels. On the contrary, the structure of the carbon felt facilitates the electrolyte penetration into the pores, reduces the bypass flow in the channels and promotes a uniform electrolyte distribution. The mass-transport property was also found to be slightly better for a carbon felt than for carbon paper in the work of Darling and Perry [36].

Aside from the porous structure itself, several external factors can account for the discrepancy of the two electrodes responses at low frequency. The critical diffusion loss observed with the carbon paper could also be amplified by the flow field geometry employed in the PhD study; the parallel channels have already proved to be inefficient compared to other designs such as serpentine or interdigitated, because of lack of forced convection within the electrode [36]. Furthermore, Maranzana et al. evidenced that concentration oscillation could also create parasitic effects in the low frequency semicircle and lead to an overestimation of the mass transport losses [193]. This oscillation may spread along the parallel channels from the inlet to the outlet, and thus be exacerbated with the carbon paper layout. Finally, the diaphragm pumps used for the study could also interfere with the signals at low frequency.

c) Cell impedance evolution with circulation

The complex impedance spectrum was recorded again after one day of circulation in the two cell configurations. The spectrum is strictly unchanged with carbon paper electrode Fig. 4.10a. As with the porous electrode, the mid-frequency resistance symbolized by the square increases notably, by almost 20 %.

Complementary tests not presented here confirmed a systematic increase of the cell resistance of about 10 % during the first day of circulation with carbon felt after what it stabilized, while it remained nearly constant when the cell was composed of carbon paper. Deeper analyses are required to elucidate this phenomenon, even though several hypotheses can already be put forth: a contaminant could be released from the felt and block some of the membrane ionic sites, or the electrolyte interaction with the felt could impede the electrode activity. It should be noted that this 10 % increase was not detected in the previous section when catholyte was exposed to light. The important pollution of the pristine membrane dwarfs the small effect of the electrode.

When protected from light, the electrode material becomes influential; a small resistance increase is observed with carbon felt while carbon paper prevents it. This observation reiterates that the choice of material and their compatibility with the electrolyte are key to achieve the best performances.

The next section makes use of the porous model to analyze the degradation phenomena occurring inside the symmetric cell fed in catholyte.

4.3.3. R_{cell} vs SOC curves: Identification of the degradation mechanisms

After the materials assessments of the previous sections, the catholyte symmetric cell was built with a reflux-treated membrane and carbon felt electrode. The characteristic curve R_{cell} vs SOC was recorded in several conditions: at several days of circulation and after one week cycling, but also for several active species concentration. The results are analyzed with the help of the electrode impedance model, in order to identify the mechanisms impacting the cell performance.

a) Difference between circulation and cycling

With the purpose of unraveling the resistance increase observed with carbon felts during circulation, the cell impedance spectra was followed relative to the SOC of the ferri/ferrocyanide electrolyte, by applying sequential charges to the symmetric cell. Fig. 4.11 shows R_{cell} as a function of the SOC at several days of circulation, which is defined in (4.38) as the real part of the mid-frequency impedance. During the first three days, the cell was only charged and discharged in the purpose to record the curve R_{cell} vs SOC. Test 1 reports the response of the freshly assembled cell and Test 2 and 3 after respectively 1 and 3 days of circulation. Test 4 depicts the evolution after 5 days of cycling (equating to 100 cycles).

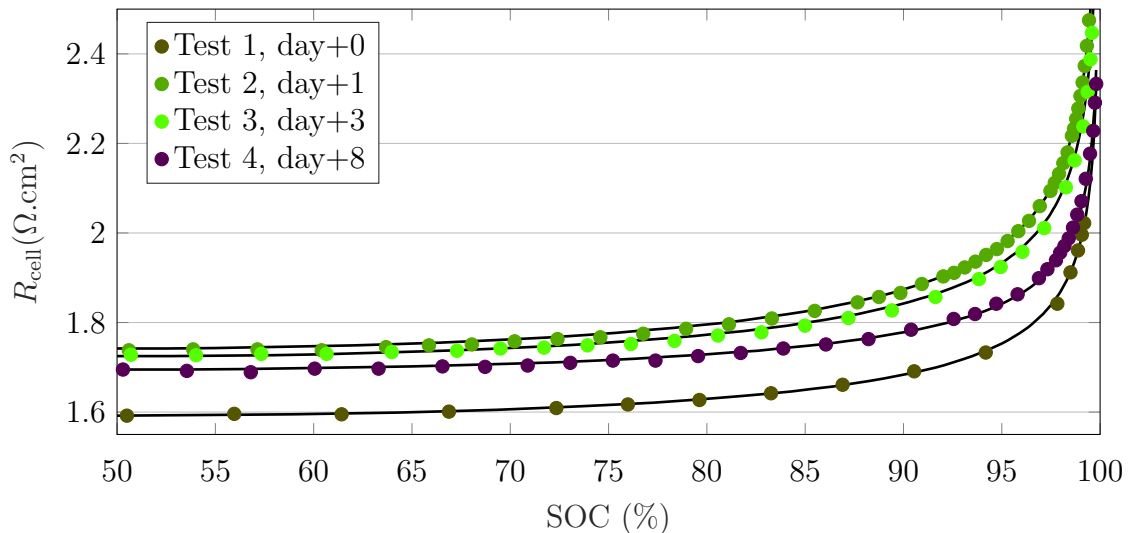


Figure 4.11: Mid-frequency resistance of the catholyte symmetric cell as a function of the SOC and fitted curves (black lines), during 3 days of circulation (Test 1-3) and after 100 cycles (Test 4)

All the experimental curves show the same characteristic shape as the model curve in

Fig. 4.2a, with a curvature appearing at high SOC. If the hypotheses considered in the model are correct (section 4.2), the curves would take a symmetrical shape if extended between SOC 50 and 0.

As already detected in the previous section with porous electrodes (in Fig. 4.10b), the cell resistance substantially increased by 10 % after a few hours of flowing, making the curve move upwards between Test 1 and Test 2. The 3 days of circulation slightly reshaped the curve (Test 3) with no further resistance increase. The data points were fitted to (4.31) and (4.37) to derive the variables R_m and $a.k_0$ by the least squares method; the model fits are depicted by the black lines in Fig. 4.11. Their estimates are represented according to the time of cell operation in Fig. 4.12. They reveal that the detected resistance increase was actually not caused by the performance degradation of the membrane since R_m is almost constant between day 0 and 3. The major contribution actually lies in the diminution of $a.k_0$ by 2 within the first day; the fitted value stabilized afterwards.

The membrane resistance is $1.2 \Omega \text{ cm}^2$ at day 0. As the total R_{cell} is $1.6 \Omega \text{ cm}^2$ at SOC 50, it can be inferred from (4.38) that the resistance of one electrode R_e is $0.2 \Omega \text{ cm}^2$ in operation. It is indeed much lower than the value under blocking conditions R_b , determined in subsection 3.4.3.

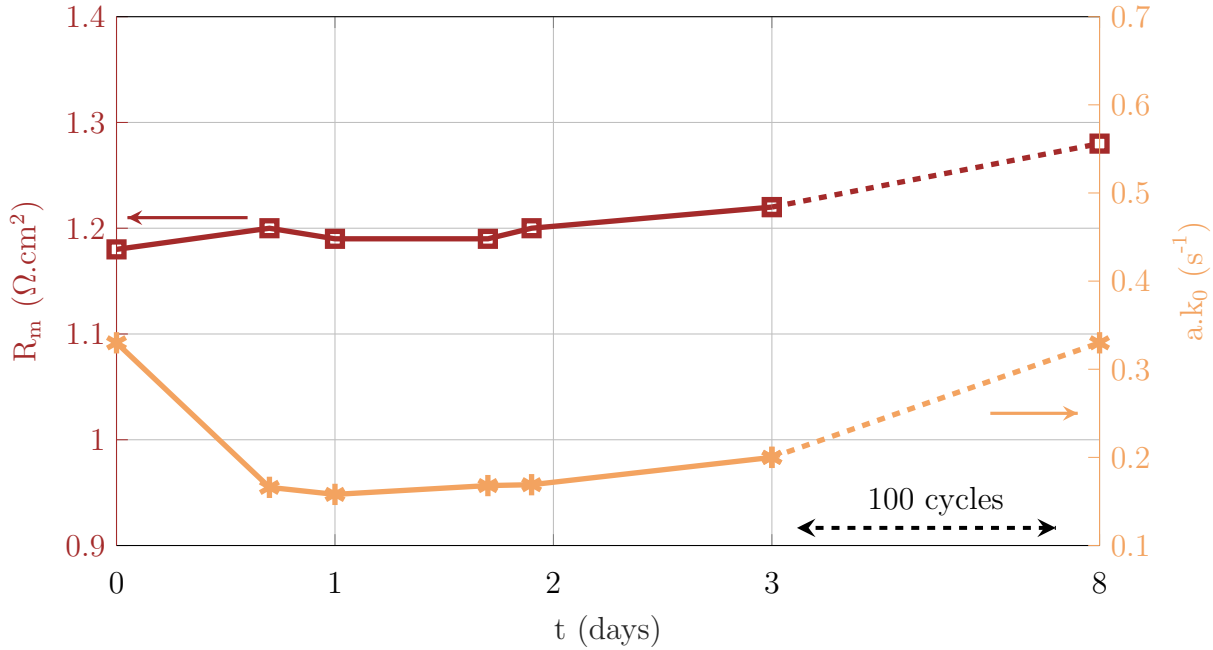


Figure 4.12: Determined parameters R_m and $a.k_0$ from model fitting of Fig. 4.11 and their evolution during circulation and after 100 cycles (represented by the dotted portion)

In light of the parameter determination, the justification of the performance degradation observed with porous electrodes can be refined: the electrolyte circulation impairs either or both of the total active surface area a and the reaction rate constant k_0 , at the electrode level. Surface functional sites can be blocked or even degraded by a mechanism specific to this catholyte/electrode material coupling, since it was not observed at the surface of the carbon paper after 1 day (Fig. 4.10a). This resistance deterioration was very reproducible and seemed to be triggered by the sole circulation of the solution through the volume of the electrode. It occurred even though the electrode material was previously rinsed with solvent. This mechanism may be explained by the presence of a persistent pollutant from manufacturing at the surface of the fibers (but the remaining impurities are $< 0.05 \%$ according to the supplier)

or by the surface condition of the material.

As far as it is known, no published paper reports a compatibility issue between the iron-cyanide pair and a carbon felt that would happen even without current drawn from the system. Possibly correlated explanations found in the literature concern electrochemical reaction or battery cycling. On the electrode itself, Derr et al. observed with a VRFB an early degradation during the first 20 cycles that they partly attributed to the electrochemical degradation of the carbon felt [194]. Cycling gives rise to corrugated surface accompanied by a loss of fiber surface area. In their study, the loss of active surface was not reversible. The $[\text{Fe}(\text{CN})_6]^{3-}/[\text{Fe}(\text{CN})_6]^{4-}$ couple also presents a complex reaction process that involves adsorption phenomena on the electrochemical surface, as reported with a gold [195] or a platinum electrode [196]. The existence of intermediate forms of the active species was also suggested by the IR analysis of the used membranes. They featured several peaks close to the catholyte signal (Fig. 4.9). It is likely that even without external current stimulation, some active molecules adsorb and occupy the active sites of the graphite.

After the 100 charges/discharges cycles, the characterization curve (Test 4) shifted downwards and its shape evolved slightly. The model fitting (Fig. 4.12) points out that the kinetic product $a.k_0$ recovered a high value. It signifies that kinetics diminution observed during circulation is reversible: flowing current through the cell could unlock the functional groups of the electrode or wipe away the active material that had been adsorbed. In the meantime, the membrane resistance extended of about 9%: the cycling, unlike the circulation of electrolytes, increases the membrane resistance. The membrane may be broke in at the start of the cycling or could be gradually polluted; this depends whether its performance stabilizes or further deteriorates in the long term, which cannot be confirmed at this stage. The suggestions developed herein would require further analysis such as ex-situ characterization to be confirmed.

It is worth mentioning that the information on capacity retention is still missing in Fig. 4.11. The cycling could partially modify the SOC of the two electrolytes. A small capacity fade was observed during 100 cycles, being however less than the rate of 0.2% per cycle announced by Luo et al. [92] for the same electrolyte. They concluded about the instability of the ferricyanide/ferrocyanide redox couple in alkaline conditions. They used a similar set-up, with the only difference being their solutions initially at SOC 100 and 0, so that they cycled them through the entire capacity of each tank. The divergence of the results found herein with their work is the resistance evolution during cycling; while they displayed increased ohmic losses with time (not quantified but visible on their cyclic voltage curves), results of Test 4 in Fig. 4.11 demonstrate no cell-level degradation after 100 cycles. They proposed a mechanism of hydrolysis that could account for the capacity decay, yet did not correlate it with the resistance increase observed in their voltage curves. Furthermore, they did not mention any precaution against light exposure, while the degradation of potassium ferrocyanide by light has long been known [164].

In subsection 4.3.1, the effect of light on catholyte was revealed detrimental to the cell performance because of an important increase of R_m when the membrane was in contact with the photodegraded catholyte. It could account for the resistance increase observed by Luo et al., which accompanies their capacity loss due to ferri/ferrocyanide photolysis. That is why the electrolyte was protected from light exposure throughout the study described here, to prevent any UV-triggered deterioration. The cell resistance remaining low after the cycles negates an important pollution in the cell nor a species precipitation that would reduce ionic conductivity.

The exact explanation of apparent capacity fade must be addressed with complementary study and longer cycling. A likely hypothesis is the effect of active species crossover through the membrane, since at the charged state of the symmetric cell, the concentration gradient of ferrous and ferric forms is highest. Preliminary tests conducted at Kemiwatt diagnosed a critical membrane permeability for the less negatively charged ferricyanide form, as also alluded to in [114].

The use of the R_{cell} vs SOC plots identified the mechanisms entailing the measured performance degradation. With a carbon felt electrode, the kinetic product $a.k_0$ dropped after a few hours of catholyte circulation, and the cycling slightly raised the membrane resistance.

b) Influence of the electrolyte concentration

The method was also applied to study the influence of the active species concentration in the electrolyte. Indeed, some published works mention a dependency of k_0 with electrolyte composition. Kawiak et al. found a strong correlation between $[\text{Fe}(\text{CN})_6^{4-}]$ and the rate constant, being higher for the lower concentrations [197]. They attributed the phenomenon to the partial blocking of the active surface by insoluble complexes. Beriet et al. stated that the cation association to ferrocyanide (and ferricyanide to a lesser extent) prevented the formation of these adsorbed species, and thus the kinetics was boosted with more concentrated supporting electrolyte [153]. Another possibility was raised by Zhang et al.: the solution viscosity, which inevitably changes with its composition, can also influence the kinetics of the reaction for $\text{Fe}(\text{CN})_6^{3-/4-}$ [154].

Subsequent to Test 4 (after 8 days of circulation and cycling), the reservoirs were diluted two times with 0.2 M NaOH, to reach lower active species concentrations. This experiment is referred to as “cycled set-up”, since it is performed on the aged symmetric cell. After each dilution, the characterization curve R_{cell} vs SOC was recorded. Fig. 4.13 overlays the plots for the three concentrations: $C_1 = 0.5$ M, $C_2 = \frac{2}{3} C_1$ and $C_3 = \frac{1}{3} C_1$. The measured conductivity for each dilution is given in Fig. 4.14. The corresponding fitted parameters (fitted model in black in Fig. 4.13) are represented as a function of concentration in Fig. 4.15.

For this aged set-up, the model fit to the experimental data attributes almost no change to R_m nor to $a.k_0$ after dilution (dashed lines in Fig. 4.15). This establishes that the cell resistance increase only stems from the diminution of the exchange current density (since it is proportional to the active concentration) and the lower electrolyte conductivity, whose measurement was input to the model. As observable in Fig. 4.14, the variation of κ is close to linearity with $[\text{Fe}(\text{CN})_6]$; when diluting the concentration by $\frac{2}{3}$ ($C_3 = 0.17$ M), the conductivity was divided by 2, and the electrode resistance worsened by +22 % (at SOC 50). In the catholyte, the active species concentration actually dominates over the supporting electrolyte ($C_{\text{NaOH}} = 0.2$ M) and as a consequence are the main contributors of the solution conductivity.

The determined $a.k_0$ decreases linearly with the concentration but to a small extent; it reduced by 15 % between C_1 and C_3 . The dependency of the in-situ k_0 regarding $[\text{Fe}(\text{CN})_6]$ or the ratio between supporting salt/active species is possible but disputable in this test. However, these parameters should be varied to a larger extent to detect the potential effect and reproduce the literature findings [153, 197].

The dilution experiment was replicated with a new symmetric cell and freshly prepared electrolyte. The parameters determined for this test correspond to the “new set-up” results of

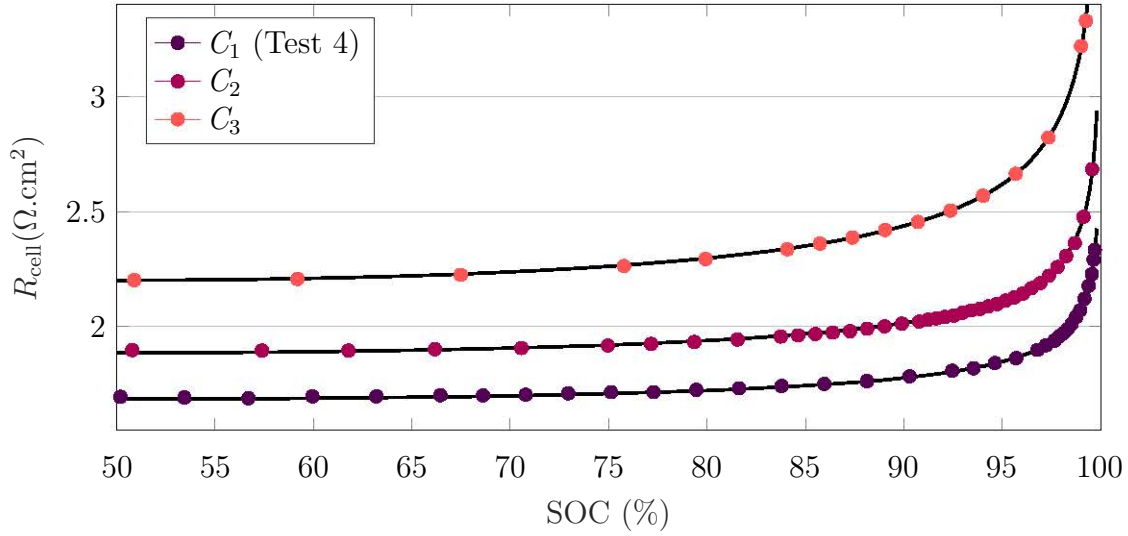


Figure 4.13: Mid-frequency resistance of the catholyte symmetric cell as a function of the SOC and fitted curves (black lines). Three active species concentrations $C_1 = 0.5 \text{ M}$, $C_2 = 0.33 \text{ M}$, and $C_3 = 0.17 \text{ M}$ obtained by successive dilutions in the cycled set-up.

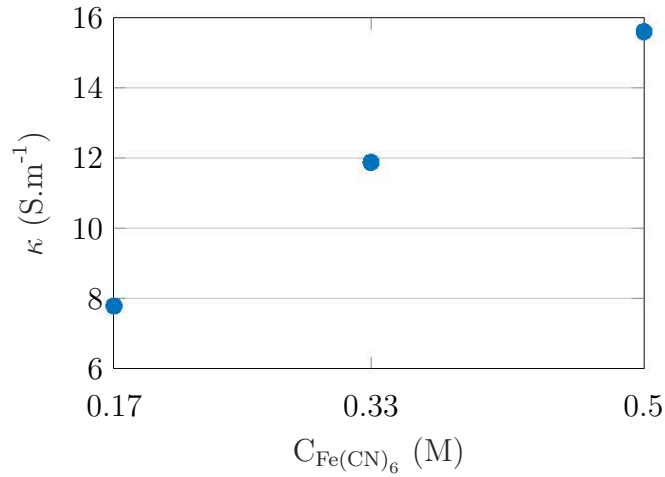


Figure 4.14: Measured catholyte conductivity (at SOC 50) as a function of active species concentration

Fig. 4.15. For $C_1 = 0.5 \text{ M}$, the membrane resistance equals $1.2 \Omega \text{ cm}^2$ which is very reproducible with the former set-up before cycling (days 0 to 3, Fig. 4.12). The product $a.k_0 = 1.4 \text{ s}^{-1}$ is one order of magnitude higher than with the previous cell, but this discrepancy is attributed to the specific surface area a that could vary between two samples of electrode.

The fitting with the new cell underlines a clear evolution of both R_m and $a.k_0$ with the 3 concentrations tested. R_m decreases when diluting the active material with NaOH. The potassium being the counter-ion of the iron-cyanide, the dilution implies an increase of the Na^+/K^+ ions ratio. As demonstrated earlier in subsection 3.3.2, this can account for an enhanced membrane conductivity. This effect was not observed on the cycled membrane; R_m had already stabilized at a higher value of $1.3 \Omega \text{ cm}^2$ and could not recover an enhanced performance by changing its ionic form.

Regarding the kinetic product $a.k_0$, it reduced by 75 % after the two dilutions in the new

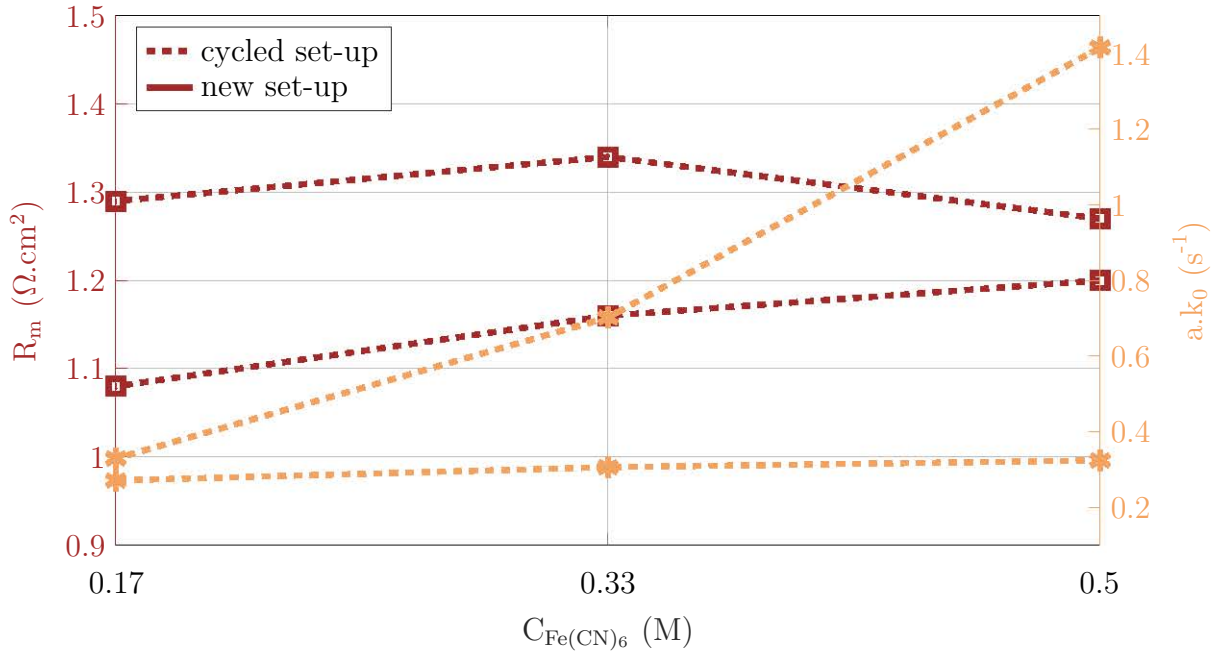


Figure 4.15: Determined parameters R_m and $a.k_0$ as a function of active species concentration. Model fitting of the cycled set-up results (Fig. 4.13) in dashed lines, and results obtained with a new set-up in solid lines.

cell. A significant portion of this variation certainly relates to the decrease observed during circulation with the carbon felt material ($a.k_0$ decreased by 50 % in Fig. 4.12). Indeed, the experiment of successive dilutions having a run time of several hours, the time-dependent effect could not be eliminated. Excluding this side effect, $a.k_0$ still varies of around 25 % with concentration. It agrees with the small decrease detected with the aged set-up. It is impossible to attribute it to either a or k_0 at this stage, since these two characteristics could not be dissociated.

The method of fitting the characteristic curve R_{cell} vs SOC of the catholyte symmetric cell was fruitful to identify the degradation mechanisms during either circulation or cycling. The results underline a process reducing the active surface area or hampering the electron-exchange kinetics. This phenomenon manifests with the sole electrolyte circulation in the electrode and is specific to this porous material. A further test at several catholyte concentrations suggests an intricate interplay between the electrode and the electrolyte that alters the reaction kinetics. Adsorption of intermediate complexes is a viable hypothesis already contemplated in the literature. This electrode pollution seems reversible. On the other hand, cycling the cell slightly increases the membrane resistance. This modification appears to be permanent. These performance degradations observed with a set-up protected from light are still one order of magnitude lower than the membrane pollution by photoproducts. Finally, a small capacity decay was observed during cycling, however not correlated to material degradation at first glance. It was speculated to be a cross-over issue.

4.4. Anolyte symmetric cell

The anolyte composed of 0.2 M ARS in 1.2 M KOH charged at SOC 50 was used to build a symmetric cell. The behavior of this electrolyte is notably different from the observations with the catholyte although not more elementary. Several tests were carried out with the anolyte symmetric cell and are sorted hereafter in three sections: the cell impedance evolution during circulation, the characterization curves R_{cell} vs SOC and their fitting at two concentrations, and the pressure drops monitoring obtained with the segmented set-up. Existing literature and complementary ex-situ tests were used to clarify the intricate response of this electrolyte.

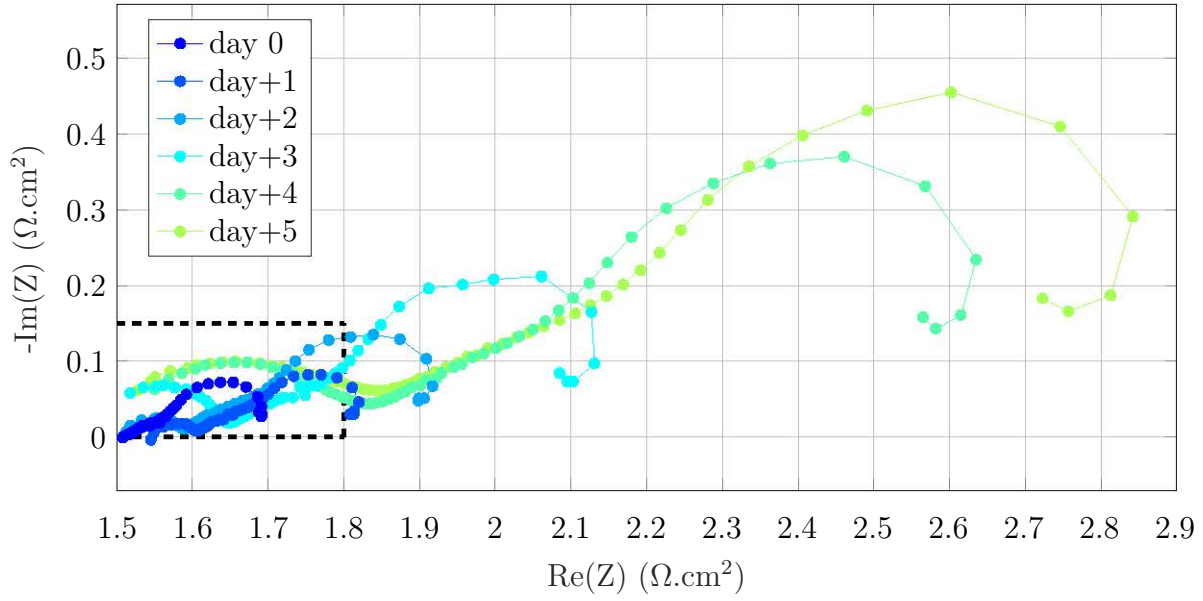
4.4.1. Impedance evolution in circulation

The half-charged anolyte was placed in the two compartments of a new cell without exposing it to air to prevent self-discharge. The resistance of the catholyte symmetric cell significantly showed a dependence on the membrane pretreatment (subsection 4.3.1); the effect on the anolyte was tested similarly. It proved that unlike the catholyte, the anolyte was not sensitive to the type of treatment applied to the membrane. Besides, taking out the membrane and exposing it to light and air did not affect the resistance measured afterwards. For consistency with the catholyte study, the reflux-treated membrane was selected as the standard for the next experiments.

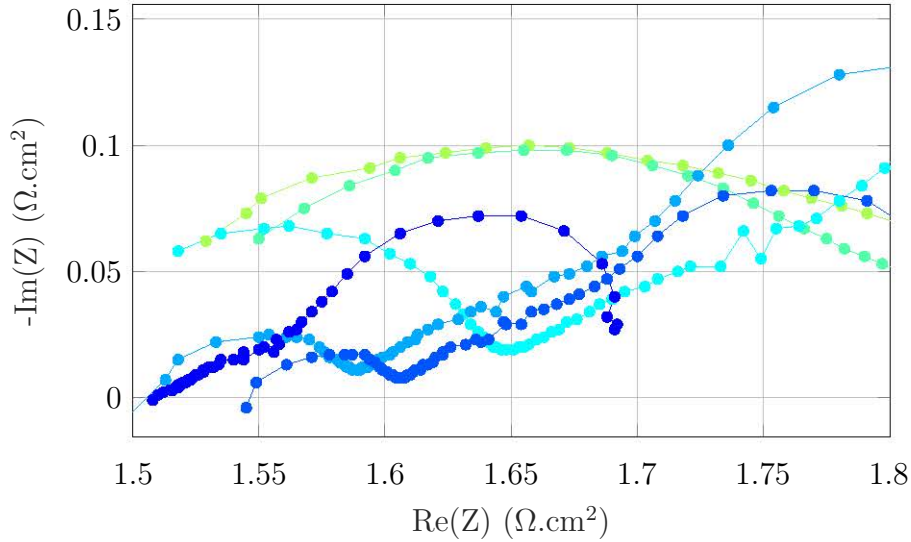
The anolyte symmetric cell was left in circulation for several days with a regular EIS data record to unveil any degradation. Fig. 4.16a compares the Nyquist plots of the anolyte cell at several days of circulation, with a zoom on the first part of the chart in Fig. 4.16b.

The comparison of the spectra evidences a gradual increase of the two loops between day 2 and 5, while after the first day of circulation the plot was only shifted on the x-axis. After day 4 the medium-frequency position, i.e. between the two loops, stabilized to a value corresponding to a 20 % increase compared to day 0 (from 1.55 to 1.84 $\Omega \text{ cm}^2$). Although the HF loops do not close over the range of tested frequencies, the high-frequency resistance did not seem to degrade with circulation.

On the other hand, the complex plane plots suggest that the mass transfer is considerably impaired when circulating a solution of fresh anolyte at SOC 50 in the cell: the LF loop size extending by almost 70 %. It is accompanied with a less critical hampering of the charge-transfer mechanism (revealed by the expansion of the HF loop). The two processes are possibly linked: it could be suspected that some active species progressively adsorb onto the carbon fibers, or that the electrode plays a role of filtration of small solid particles. These mechanisms would complicate the transport of the active species into the pores, generating an increased LF loop. This speculation is reinforced by the singular rheological behavior of the fresh anolyte (subsection 3.2.2). Another consequence would be the partial obscuring of the active surface area that would translate into a higher charge transfer resistance. Finally, the decrease of the active species concentration or their diffusion coefficients would worsen the mass transport resistance, according to the analytical EIS model developed by Pezeshki et al. [95]. A refined examination post-mortem of the electrode, along with an electrochemical and rheological characterization of the circulated anolyte would help on predicating the underlying process.



(a) Global view



(b) Zoom on the dashed rectangle in Fig. 4.16a

Figure 4.16: Evolution of the Nyquist plots obtained with the anolyte symmetric cell at several days of circulation, for the frequency range [20 mHz;10 kHz]

4.4.2. Analysis of the cell overcharge

The electrochemical analysis of the anolyte in the previous chapter uncovered the presence of oxidation peaks above the formal potential of the couple (around 0.05 and 0.5 $V_{Ag/AgCl}$ in Fig. 3.4). These non-reversible reactions could be triggered during deep discharge of the RFB cell. At the industrial scale, this could happen if local overpotentials are more important in some regions of the electrode (due to a heterogeneous flow distribution) or because of shunt current effects. The symmetric cell is a relevant tool to assess the consequences of such circumstances. It was built in the segmented set-up. This section focuses on the impact of the upper voltage bounds during charge of the symmetric cell.

When exceeding the standard limit of 0.9 V (set for the symmetric cell tests), the ARS in the negative side underwent a overcharge (or over-reduction) and at the same time the positive compartment was subjected to a surcharge (or over-oxidation). The cell was gradually charged at 40 mA cm^{-2} by current steps of varying lengths interrupted by small open circuit periods, to be in the same conditions as when recording the R_{cell} vs SOC curve. The electrolyte was flowing at a rate of $\dot{q} = 50 \text{ mL min}^{-1}$ to prevent high pressure drops. The upper voltage maximum was set to $U = 1 \text{ V}$ in Cycle 1, and then raised to $U = 1.2 \text{ V}$ in Cycle 2. After each charge, the cell was discharged by constant voltage steps at $U = 0$ and -0.2 V until the current reduced to less than 5 mA , to return to the initial SOC 50 on both sides.

During Charge 1, the cell voltage evolved normally until reaching the 1 V limit; the capacity accessed corresponded to 60 % of the theoretical capacity ($Q_F = 1650 \text{ mA h}^{-1}$). This was due to the choice of setting a fairly low flow rate and the possible presence of residual oxygen in the set-up. Consequently, the symmetric configuration was certainly lost after Charge 1.

The cell voltage curve recorded during Charge 2 is displayed in Fig. 4.17. Only the measurements during charging periods are represented in this curve, not the open circuit steps, which causes the small transitions identifiable every 5 min in the graph. Charge 2 showed a peculiar voltage profile with a large and flat plateau appearing at 1.05 V before the upper limit of 1.2 V .

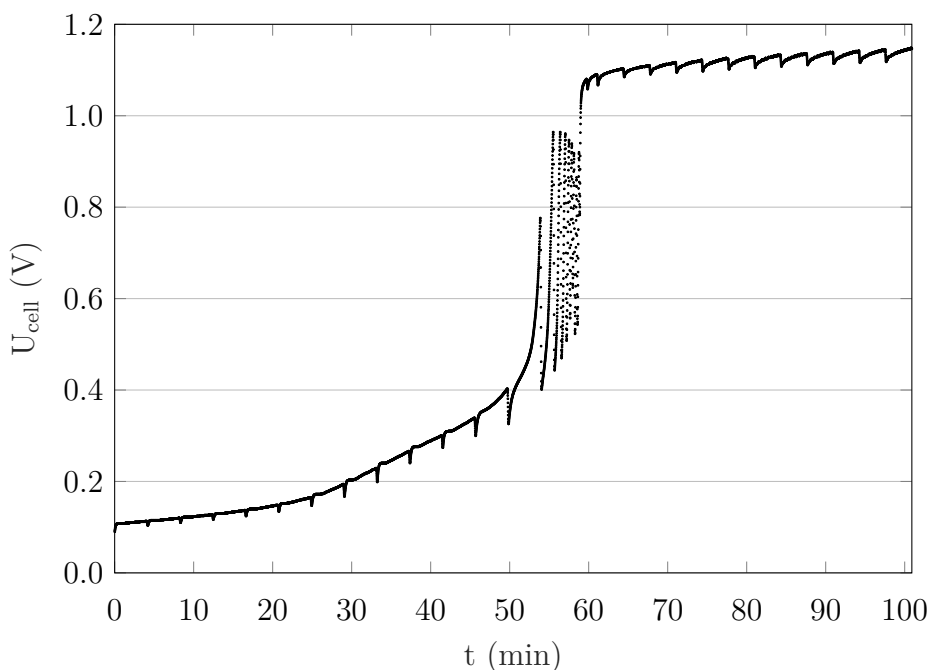


Figure 4.17: Cell voltage during over-charge of the anolyte symmetric cell (Cycle 2)

The potential jump in Charge 2 occurred after the same charging time as for Cycle 1. It is a direct consequence of a depletion of the reactants in the electrolyte; the charging current can no longer be sustained by the reactions. However, in the case of Charge 2, U could reach a level section after a leap of $+0.9 \text{ V}$. As such, the charge continued until it was stopped manually at 100 min: at that moment the capacity matched Q_F . In view of the voltage profile, the charge could have been maintained for longer since no new limitation seemed to rise.

According to the local potentials records of the segmented cell, the steep cell voltage increase is caused by the positive electrode, which holds the ARS oxidation (solution varying between

SOC 50 \rightarrow 0). This could evidence that a secondary reaction is triggered when the positive side is over-discharged. On the other hand, the negative electrode that hosts the reduction only presents a linear potential decline. One can speculate that a side reaction occurs alongside the ARS reduction in this half-cell, giving the possibility to charge the negative electrode during an extended period without disruption (water reduction into H_2 is unlikely, since it was neatly triggered only below -1.7 V according to the preceding electrochemical analysis Fig. 3.4). It is also likely that the symmetry between the compartments was shifted after Cycle 1, and that the negative side could be reduced for a longer time than the oxidation at the other half-cell.

As the potential measurements could not be validated in Chap. 2, they are not presented. An external electrochemical analysis of the used electrolytes was deemed necessary to investigate on the internal processes and confirm the speculation from the local potentials.

An aliquot of each solution was taken off to examine it in the electrochemical cell by cyclic voltammetry (CV), whose principle was already exposed in section 3.1. The CVs of the fresh anolyte compared to the over-reduced and over-oxidized solutions from the symmetric cell are displayed in Fig. 4.18a.

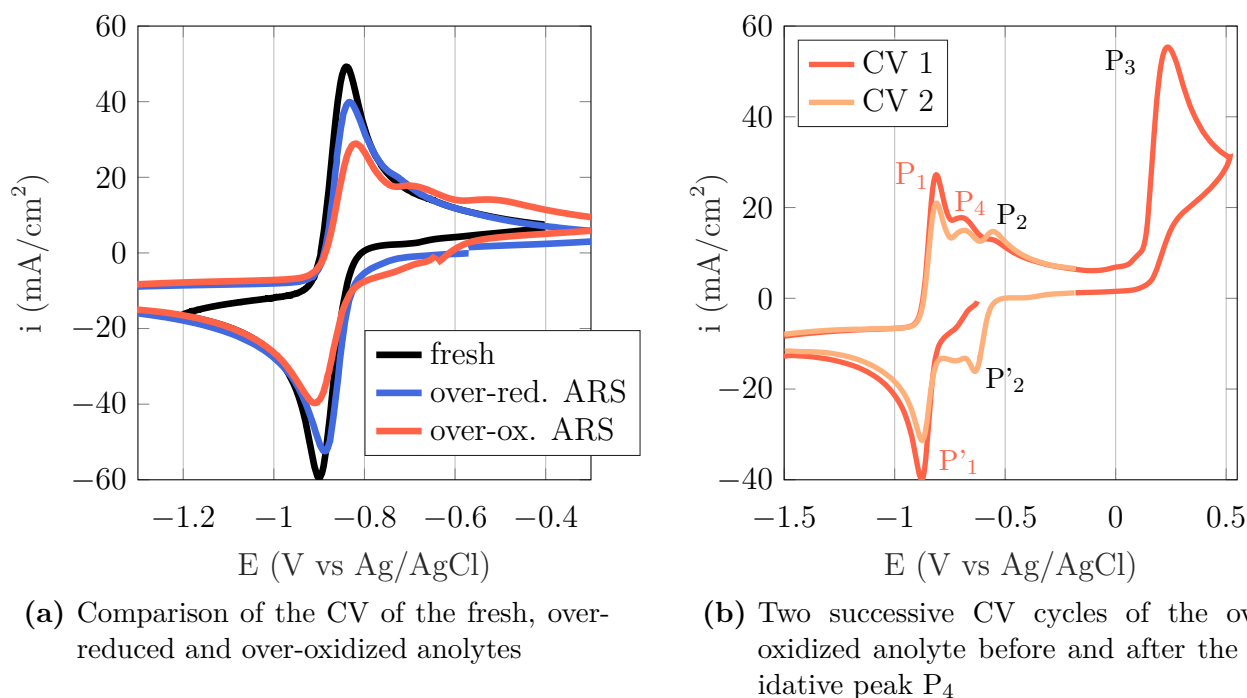


Figure 4.18: Cyclic voltamograms of the anolytes used in the symmetric cell after over-charge, recorded with a potential scan rate of $\nu=100$ mV/s

The two peaks in reduction and oxidation are smaller for the cycled solutions, which evidences a loss of concentration (difficult to quantify with the CV technique). Apart from the peak height, the over-reduced form has essentially the same signal as the fresh ARS. A very small positive shoulder is detected at -0.69 V (noted as P_4 in Fig. 4.18b). On the other hand, the over-oxidized solution features a more pronounced peak at this potential, and a distinctive third oxidation peak appears at -0.55 V, which will be referred to as P_2 . These features indicate the presence of new molecules; however due to the size of these spikes, the species are in very small concentrations. In summary, the over-reduced anolyte presents a new system P_4 and the over-oxidized version features P_4 along with a third cathodic peak P_2 .

The voltage scanning range was extended towards the positive potentials to mimic the overcharge conditions in the positive electrode of the symmetric cell. In Fig. 4.18b, “CV 1” is the signal of the over-oxidized solution just after sampling from the tank of the battery. The scan started at -0.6 V in the negative direction and at -1.5 V, the potential was reversed towards positive values. The second cycle obtained subsequently to this positive scan is superimposed and called “CV 2”. When reaching higher potentials, a prominent cathodic spike (P_3) rises at 0.23 V. It is in a distance of 1 V from the standard oxidation peak of the anolyte (P_1 at -0.8 V). This gap closely equals the cell voltage step measured during overcharge (Fig. 4.17). It substantiates that the mechanism produced ex-situ in this electrochemical analysis is the same as in the overcharging symmetric battery.

When reversing the scan direction, no reduction peak corresponding to P_3 was detected, which suggests an irreversible reaction. Back to the zone of ARS activity, the waves P_2 at -0.55 V and P'_2 at -0.63 V are larger in CV 2 than in CV 1. This testifies the appearance of new reversible species in the wake of the oxidation happening at 0.23 V. As for the initial signature of the anolyte (P_1 and P'_1) and the small shoulder P_4 , they faded in favor of the new peaks. This analysis underpins the theory of an irreversible degradation process of the ARS during over-oxidation, from which originates a new electrochemically active and reversible substance. The signals being near the original ARS response, the by-products must have kept the anthraquinone skeleton with different functional groups. CV analysis performed in section 3.1 underlined that the response of the fresh anolyte is really stable if the electrode potential E is kept under 0 V. The appearance of the new redox system P_2 / P'_2 is evident when extending the scan to 0.5 V: after several CV cycles, the ARS initial signature completely vanished. It shows that the ARS alteration is rapid, total and irreversible at slightly positive potentials.

In other scientific applications, the ARS electrochemical properties were assessed by CV. Although in acidic or neutral conditions, an equivalent degradation path was evidenced during over-oxidation [150, 198–200]. Schumacher et al. proposed that the anodic peak P_3 corresponds to the oxidation of one or two of the ARS hydroxyl groups into ketone groups [150]. The scheme of this process is represented in Fig. 4.19. The product proposed in the drawing is a 4-ketone molecule that gives rise to a new redox couple reacting at P_2 and P'_2 , whose exact form is still unknown.

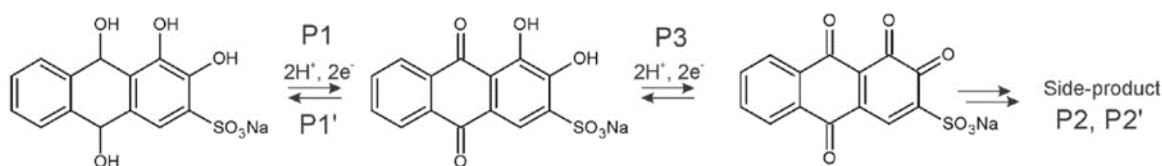


Figure 4.19: Proposed ARS modification processes responsible for the new peak potentials detected in CVs of Fig. 4.18b (P_2 , P'_2 and P_3), adopted from [150]

The authors also claimed that the new ARS form adsorbed onto the active surface in a polymeric product. Dadpou et al. [200] underpinned this statement by showing that the ARS by-product inhibited the surface of a glassy carbon electrode by adsorbing in a multilayer arrangement. These mechanisms can justify the charge-transfer and mass-transport resistances being compounded during circulation in Fig. 4.16.

A similar theory ventures the formation of radicals that bind together to form dimerized

structures. These by-products are an assembly of two anthraquinones exchanging two electrons. This was evidenced by [201] in the case of alizarin: one of the possible dimeric configurations is displayed in Fig. 4.20.

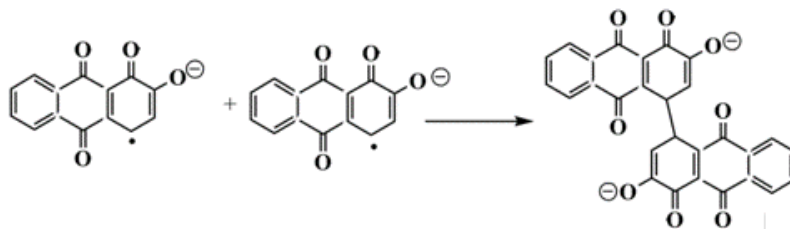


Figure 4.20: Example of formation of a dimer from radicals of alizarin, adopted from [201]

Whatever the pathway of ARS degradation by over-oxidation, the electrochemical signature of the product certifies that it exchanges two electrons (peak-to-peak separation of the CV is 59/2 mV), at a higher formal potential of -0.6 V [2].

To supplement the investigation, the pressure drops recorded in the two compartments of the symmetric cell were analyzed. The data of Cycle 1 and 2 are presented on the same graph in Fig. 4.21. The dotted lines delimit the charge and the discharge for the two cycles. Due to the extended upper voltage limit, Cycle 2 last longer than Cycle 1.

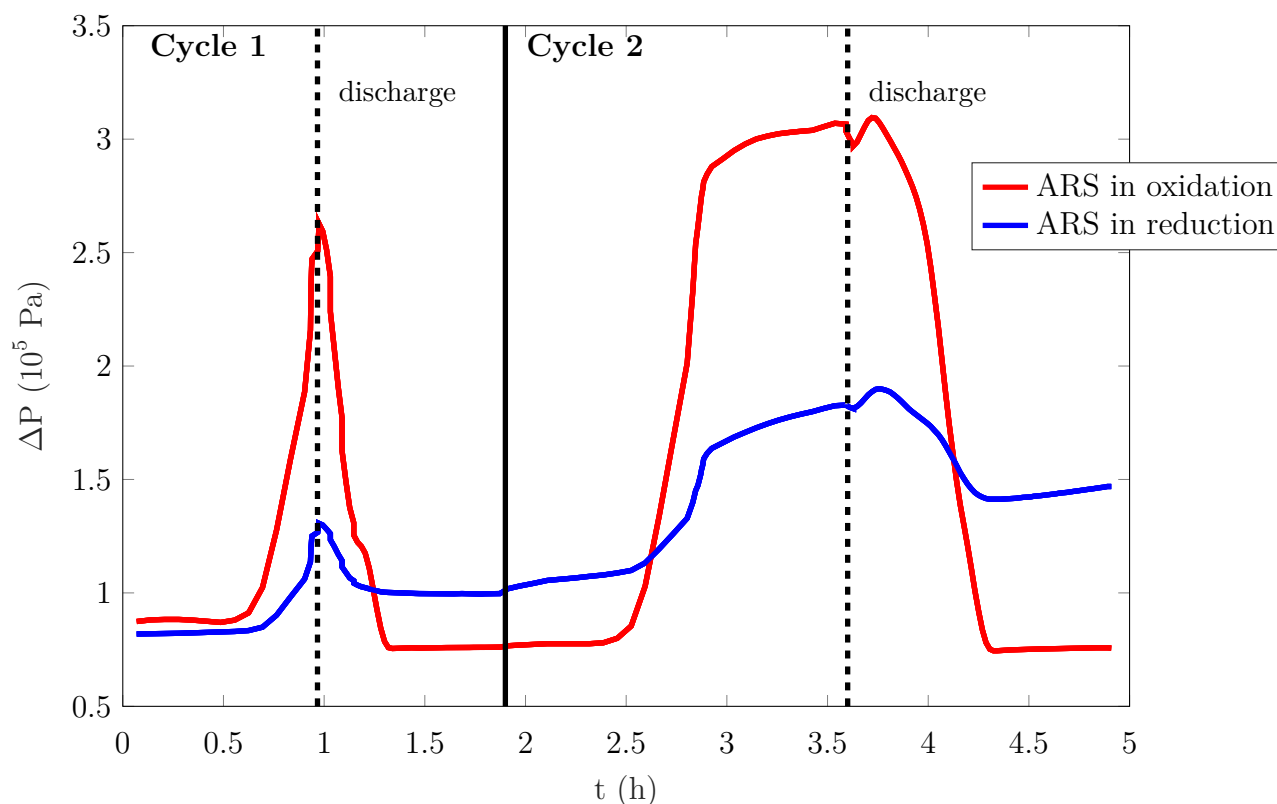


Figure 4.21: Pressure drops in both compartments of the anolyte symmetric cell during 2 cycles with different upper voltage limits (Cycle 1: $U = 1$ V, Cycle 2: $U = 1.2$ V) flow rate at $\dot{q} = 50 \text{ mL min}^{-1}$

At the end of Charge 1, the pressure drop of the ARS in oxidation reaches a peak: the solution is back at SOC 0. As already evidenced during the rheological study (subsection 3.2.2),

its viscosity is important in this state. Shortly after the start of discharge, the pressure drop regains a low value, even smaller than initially. During Cycle 2, the same trend is observed for this half-cell. Even after holding the ARS in its oxidized form during 1 h, the solution recovers its fluidity and ΔP is further reduced compared to Discharge 1.

The plateaus in both pressure drops (between 2.8 and 3.6 h) match with the overcharge of the battery, and the level potential detected in Fig. 4.17.

A contrasting behavior is highlighted in the electrode hosting the reduction. At the end of Cycle 1, the pressure drops have slightly increased. When holding the cell in overcharge (Cycle 2), the pressure drops aggravate on this side. The two successive cycles actually doubled the ΔP of the ARS in charge.

When replacing the porous electrodes of the symmetric cell but keeping the used solutions, the pressure drops of the negative side reduced significantly. In that respect the issue came from the partial clogging of the electrode rather than a viscous liquid. It can be ascribed to the formation of solid precipitates or small gas bubbles that obstructed the pores and hindered the circulation of electrolyte. Since the ARS electrochemical signal was reduced in Fig. 4.18a, it supports the hypothesis of active species precipitation in over-reducing conditions.

An industrial perspective

The initial ARS form is not stable in over-reduction nor in over-oxidation. The option to intentionally over-oxidize the molecule into its by-product could be considered. Yet this new compound presents drawbacks: its formal potential being higher, the battery output power will be decreased against a given catholyte. If the radical formation is the correct scenario, it also reduces the number of exchanged electrons to one per molecule and deteriorates the energy density accordingly. Finally, the presence of highly reactive chemicals such as radicals might perpetrate chain degradation of the other materials (membrane, electrode).

As such, the voltage window of the battery must be appropriately delimited to mitigate degradation in over-oxidation and precipitation in over-reduction. Beyond that, the homogeneity of reactions throughout the large active surface of the stack is essential to prevent high local overpotentials and side-reactions.

By appraising simultaneously the results from the CV signatures and the pressure drops, general conclusions can be drawn:

- The over-oxidation of the anolyte, happening in discharge, degrades the molecule when it is driven above 0.23 V. The degradation pathway, even though not certainly identified, generates a new redox couple reacting between -0.63 and -0.55 V. This form leads to reduced pressure drop that suggests a more fluid solution. This structural modification is irreversible.
- The over-reduction of the anolyte that occurs in charge does not trigger a neat side reaction; the charge can be maintained without potential decline. This could be explained by the presence of oxygen inside the circuit, triggering the oxidation of the freshly reduced ARS. The reduction however reduces the anolyte concentration. In light of the pressure drops rise, it can be hypothesized that insoluble species are formed or that ARS is precipitated.

- ➔ Regardless of the side from which comes the electrolyte, another electrochemical signature is detected in the used solutions. It stands very close to the potential of the initial ARS. Its formation is certainly not related to the overcharge of the symmetric cell. At that stage, the origin of this signal could not be identified.

The severe consequences of overpotential on the ARS being already pinpointed, a strict voltage window for the anolyte symmetric cell was decided accordingly, as $[-0.2 ; 0.9 \text{ V}]$. It was made sure that within this voltage window, the pressure drops did not rise on the positive side and that no gas evolution could be detected.

Finally, the anolyte being very sensitive to oxygen, it is a challenge to assemble a perfect symmetric cell with electrolytes at SOC 50 on both sides. The experiment should be carried out in a glove box.

4.4.3. R_{cell} vs SOC curves

The characteristic curve R_{cell} vs SOC of the anolyte symmetric configuration was performed analogously to the catholyte study, by respecting the aforementioned safe voltage boundaries. This test gives peculiar plots. As a primary step, the first section of the plot fitted with the standard model developed in section 4.1, before proposing a new approach accounting for two successive reactions.

a) One-reaction model

The cell was charged by sequential current steps interspersed with small rests and EIS measurements. The real component of the cell impedance was averaged for the three medium frequencies $[50; 200 \text{ Hz}]$, as explained in the method section 4.2 (typical Nyquist plots of the anolyte symmetric cells were charted in Fig. 4.16). Fig. 4.22 displays the curve obtained for two concentrations $C_1 = 0.2 \text{ M}$, $C_2 = \frac{2}{3} C_1$.

With dilution, the conductivity of the anolyte increased (measured values reported in Table 4.2): this partly explains that the curve C_2 is shifted downwards. The presence of ARS molecules certainly diminish the solution conductivity since they make it more viscous (subsection 3.2.2). The effect of ferro/ferryanide is different, as the evolution of the catholyte conductivity (and with it the R_{cell} vs SOC) was opposite with dilution (subsection 4.3.3). This correlates to the lower diffusion of the ARS compared to ferro/ferryanide, as determined in subsection 3.1.6.

Furthermore, the shape of the plots deviates from the response observed with the catholyte. As it is, the electrode impedance model previously developed cannot account for this complexity. The process taking place inside the electrode can rather be interpreted as the outcome of two contributions, which could refer to successive reactions. Nevertheless, fitting the first portion of the curves (below SOC 85) with the model of one reaction (Eqs. (4.31) and (4.37)) is possible, providing a few rearrangements. If the SOC of this portion is normalized between 50 and 100 % and if the total concentration is moderated by 0.85 (portion of the species reacting during this first reaction), the black fitted lines in Fig. 4.22 are obtained. These fits provide the determined parameters of Table 4.2.

The membrane resistance estimates are higher than in the catholyte symmetric cell Fig. 4.15, for a similar ionic conductivity of the two solutions at C_1 . This could underpin a small pollution

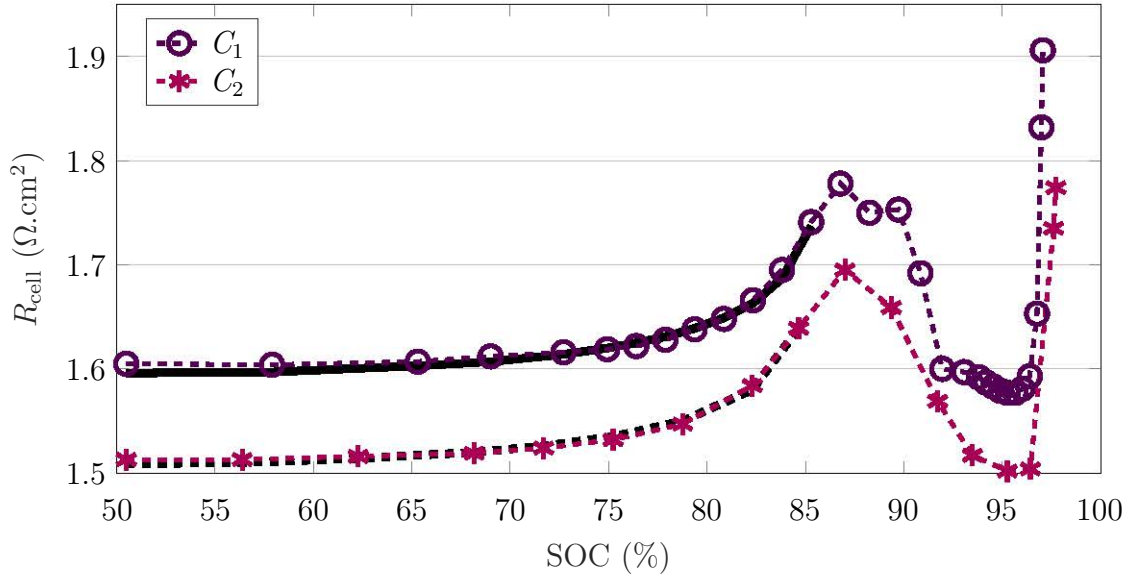


Figure 4.22: Mid-frequency resistance of the anolyte symmetric cell as a function of the SOC for two active species concentrations $C_1 = 0.2$ M and $C_2 = 0.13$ M. Black lines show the fits of the first parts with the porous model considering one reaction (Eqs. (4.31) and (4.37)).

Table 4.2: Measured conductivities (at SOC 0) and determined parameters from the fits of Fig. 4.22 for two anolyte concentrations

| | κ (S m ⁻¹) | R_m (Ω cm ²) | $a.k_0$ (s ⁻¹) |
|-------|-------------------------------|----------------------------|----------------------------|
| C_1 | 15.6 | 1.45 | 3.0 |
| C_2 | 18.1 | 1.37 | 4.3 |

of the membrane by the anolyte. It also depends on the amount of free cations of the solution; it is certainly lower for the ARS molecule that needs to be deprotonated at high pH (subsection 2.1.1). The product $a.k_0$ is higher than with the catholyte (between 0.4 and 1.4 s⁻¹). The active surface area a could change with the electrode sample used, but it certainly represents a negligible percent of the total active surface, supposedly tremendous for these highly-porous electrodes (0.5 m² for one electrode used in the 25 cm² standard cell, according to the supplier's data in Table 2.1). Since the two redox couples have equivalent reaction rate constants (section 3.1), the difference probably substantiates the catholyte adsorption on the graphite fibers as it was already alluded several times earlier.

The evolution of R_m and $a.k_0$ with concentration is appreciable. These two parameters contribute to the diminution of the resistance curve at C_2 . For the membrane resistance, it is logically lower at improved electrolyte conductivity (C_2): more ions are free because less ARS molecules need to be deprotonated, and thus improve the transport of charges in the membrane. The reaction kinetics coefficient is also enhanced by 30 % at lower concentration. Two main reasons can be hypothesized:

- ➔ The anolyte adsorption on the surface is mitigated.
- ➔ In the diluted solution, the portion of free OH⁻ ions is more important since less hydroxyl groups (on the ARS structure) need to be deprotonated. This slightly rises the

pH of the solution, and can in turn modify the reaction kinetics of the ARS molecule. The tests at two concentrations should be repeated by maintaining a constant pH to confirm this assumption.

An industrial perspective

The outcomes of the anolyte symmetric cell show a notable improvement of two key features of the cell at lower active species concentration. This uncovers the intricate trade-off between electrolyte energy density and battery performance. The optimization of the electrolyte formulation must be addressed carefully by appreciating its impact on other attributes of the system.

Generally, the fitting of the first data points gives coherent estimates of the intrinsic parameters, but does not consider the anolyte behavior over the whole range of SOC.

b) Two-reactions model

The model is refined to examine the theory of two successive reactions. It is conjectured that the current is at first generated by a dominant chemical (numbered 1) until it is almost totally consumed. It entails a cell resistance increase and thus a higher cell voltage. At this potential threshold, reached around SOC 85 according to the experimental curves, a subsidiary reagent (numbered 2) present in lower concentration takes control of the end of charge. It is considered that species 1 and 2 represent partial fractions of the total concentration, and both involve the exchange of two electrons.

The passage between the two chemical processes must be smooth since the experimental curve is continuous; to this end a transition factor γ is integrated to the model. It equals 1 when the ionic current is produced by reaction 1 and 0 when the current is produced by reaction 2. The partial fraction of the two chemicals relative to the total active material concentration is represented by χ . The variation of γ with SOC depends on χ and on another parameter d that demarcates the transition zone between the two reactions:

$$\gamma = 1 - [1 + \exp(-d(\text{SOC} - \chi))]^{-1} \quad (4.41)$$

The shape of the transition factor is represented in Fig. 4.23. The values $\chi = 0.83$ and $d = 60$ were chosen to adapt the model to the spike observed experimentally in R_{cell} vs SOC. However, the actual potential from which reaction 2 is triggered is uncertain, as well as how long the first reaction is significant during the charge.

After having introduced γ , the total current J produced at the electrode can be expressed as:

$$J = \gamma J_1 + (1 - \gamma) J_2 \quad (4.42)$$

With $J_{1,2}$ the partial ionic current density of each reaction.

From Ohm's law (4.17) and with ideal infinite conductivity of the solid phase, the potential gradient in the electrode $[\phi_m(x = 0) - \phi_s(x = L)]$, as defined in section 4.1, depends on both

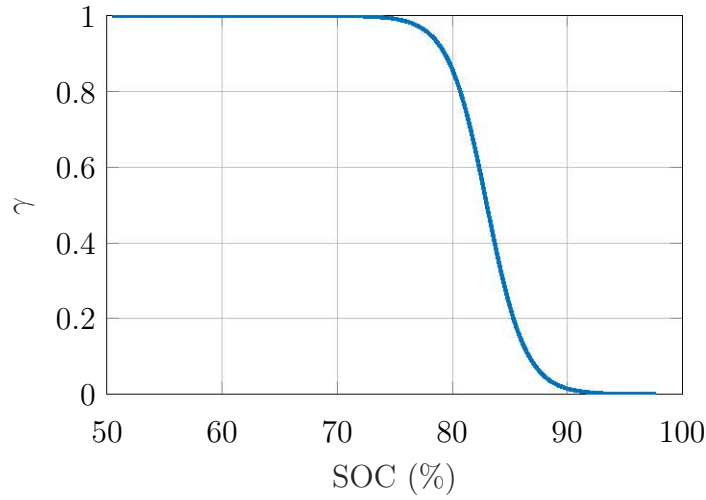


Figure 4.23: Transition function γ versus SOC describing the change from reaction 1 to reaction 2 in the two-reaction model used for the anolyte symmetric cell

partial current densities:

$$J_1 = [\phi_m(0) - \phi_s(L)] \kappa \lambda_1 \tanh(\lambda_1 L) \quad (4.43)$$

$$J_2 = [\phi_m(0) - \phi_s(L)] \kappa \lambda_2 \tanh(\lambda_2 L) \quad (4.44)$$

$$\text{with } \lambda_k^2 = \frac{a}{\kappa} \frac{j_{0_k}}{b} \quad (4.45)$$

From the above expressions of the total and partial current densities and according to the definition of R_e (4.25), the electrode resistance associated with two simultaneous reactions, called R'_e , is:

$$R'_e = \frac{1}{\gamma \kappa \lambda_1 \tanh(\lambda_1 L) + (1 - \gamma) \kappa \lambda_2 \tanh(\lambda_2 L)} \quad (4.46)$$

Eq.(4.46) is actually the equivalent resistance of an electrical circuit composed of two resistive compounds in parallel.

The following equation allows a comparison with the experimental data:

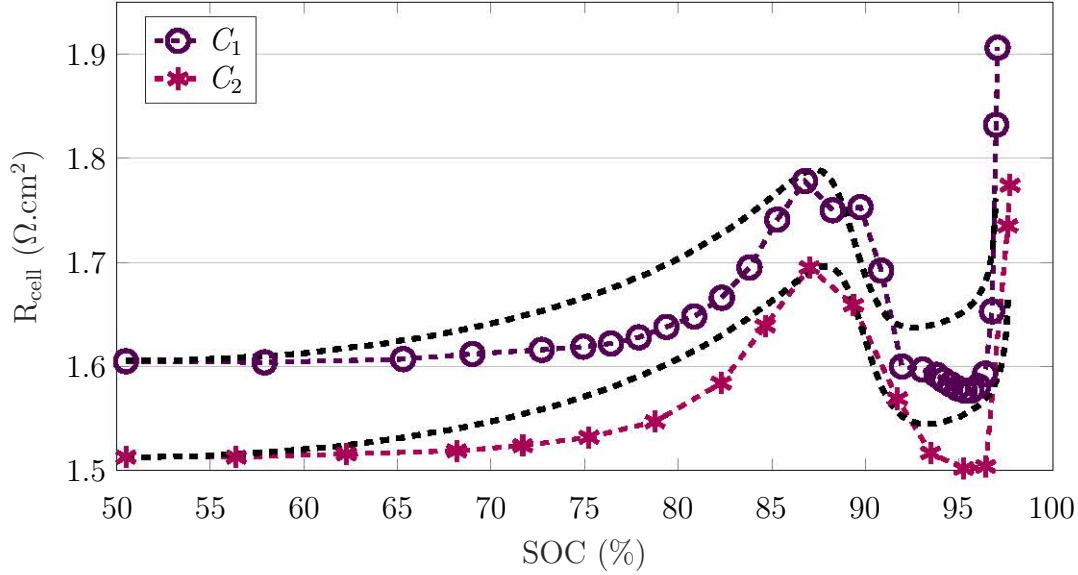
$$R'_{\text{cell}} = 2R'_e + R_{\text{HF}} \quad (4.47)$$

The input variables of the model are the total concentration and the ionic conductivity. The unknown parameters, being α_1 , α_2 , $a.k_{0_1}$, $a.k_{0_2}$, and R_m cannot be determined all at once by model fitting. A set of values detailed in Table 4.3 was chosen to optimize the trend of the black plots in Fig. 4.24.

Even though the electrode model is not accurate throughout the SOC range, the similarity with the experimental shape is promising. The values used for the kinetic products $a.k_0$ would imply that the successive reactions involved have very different kinetics. The experimental plots show similar fashion and spike position. The successive reactions certainly keep the same

Table 4.3: Parameters used for the two-reaction model to obtain the curves of Fig. 4.22, for two anolyte concentrations

| $\alpha_1 = \alpha_2$ | $a.k_{0_1} \text{ (s}^{-1}\text{)}$ | $a.k_{0_2} \text{ (s}^{-1}\text{)}$ | $R_{m, C_1} \text{ (}\Omega \text{ cm}^2\text{)}$ | $R_{m, C_2} \text{ (}\Omega \text{ cm}^2\text{)}$ |
|-----------------------|-------------------------------------|-------------------------------------|---|---|
| 0.5 | 0.08 | 65 | 1.5 | 1.4 |

**Figure 4.24:** Mid-frequency resistance of the anolyte symmetric cell as a function of the SOC for two active species concentrations $C_1 = 0.4 \text{ M}$ and $C_2 = 0.27 \text{ M}$. The resistance model considering two successive reactions (4.47) calculated with the parameters in Table 4.3 is represented with black lines.

characteristics independently of the total concentration of active species. As a consequence, repeating the test at other concentrations could give enough experimental data to fit with the two-reactions model, and the unknown parameters could be accurately determined.

The anolyte reactional mechanisms require deeper investigations to be described thoroughly. The choice of the symmetric cell is questioned for this purpose: since the ARS does not have the same behavior in charge and in discharge as exemplified in subsection 4.4.2, the electrodes of the symmetric cell cannot be described by the same impedance model. The spike at SOC 85 is likely caused by the electrode in oxidation in view of the preceding conclusions. Another difficulty stems from the modification of the ARS response over cycling, as it is shown in detail later (subsection 5.1.2).

The scenario of two successive reactions is still hypothetical: another possibility could be a two-steps reaction, each of which involving one electron. Nevertheless, the appearance of another electrochemical signal in the CVs of the previous section (Fig. 4.18a, P_4) reinforces the theory of two coexisting species, each exchanging 2 electrons. According to mass spectroscopy and NMR analysis performed at Kemiwatt on a fully-aged anolyte solution, the new chemical could have the structure depicted in Fig. 4.25: it corresponds to the ARS with one hydroxyl group removed. Its electrochemical properties and behavior in a RFB cell could be compared with the anolyte features to confirm that it is the second molecule.

Although the ARS signature is very stable in cyclic voltammetry with no decrease of peak intensity, complementary tests performed at Kemiwatt revealed that holding the chemical in its reduced form for an extended period led to the appearance of the anodic peak P_4 and its cathodic twin (Fig. 4.18). It underlines the chemical reactivity of the reduced molecule. This also entails that cycling the battery within a constrained window of operation (below SOC 85) does not prevent from the formation of the second form of the ARS. This was confirmed by cycles with restricted voltage limits performed at the company: the degradation process appeared anyway.

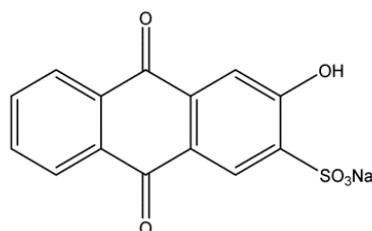


Figure 4.25: Proposition of the aged structure AQ-2-OH-3-SO₃ obtained from the reduced form of ARS [2], determined by mass spectroscopy and NMR analyses

An industrial perspective

Despite the strict voltage window determined in the previous section, the anolyte features an unusual reactional behavior in the symmetric cell, suggesting the successive reaction of two forms of the molecule. The consequences on the system can be binary:

- As illustrated by the R_{cell} vs SOC curve, the transition to a second reaction increases the resistance and could provoke a premature charge or discharge cut-off. It would prevent the access to the total capacity of the battery. Furthermore, the two forms of ARS may have different kinetics, as suggested by the kinetic parameters chosen in the model, complicating the task of system optimization. The interaction between the two structures could create local disturbances inside the pores or at the carbon fibers, giving rise to dead zones and limited surface of reaction.
- The coexistence of two active molecules can be positive for the system, by stabilizing for instance the electrolyte over a wider range of temperature, or enhancing the species solubility.

4.5. Conclusion

According to the Nyquist plots of anolyte and catholyte symmetric cells (Fig. 4.5 and Fig. 4.16), the limiting factor is contrasting for both electrolytes: in the catholyte the charge-transfer loop dominates while mass transport is most critical with the anolyte. Additionally, there are different mechanisms causing the performance degradation of each electrolyte during circulation. Catholyte symmetric cell undergoes a ohmic loss increase from the pollution of the membrane, whereas the anolyte circulation deteriorates with time in the electrode.

The separate analysis of both electrolytes in conditions close to the final RFB system showed its benefits. The materials used and their pretreatment process have a strong impact on the

catholyte performance. The behavior of the anolyte in charge and in discharge differs notably and cautions on the potential of this side is necessary. These learnings would not have been detected by the study of a full RFB cell.

An industrial perspective

Compatibility test between all the components involved in the system is of primary importance. Long-term experiments must be carried out, since the system is dedicated to long operational life. The electrolytes behavior in the cell are contrasting, both in terms of internal limitations and performance degradation during cycling. It is logically inferred that the stack design must not be symmetrical on both sides and that the porous material, the frame design and also the flow rate have to be adjusted accordingly.

Local overpotential can have strong implications, as exemplified with the anolyte. It reveals the necessity of an homogeneous flow distribution between the cells of the stacks and within the electrodes of each half-cell.

5

FULL CELL STUDY

Contents

| | |
|---|------------|
| 5.1 Standard cycling | 138 |
| 5.1.1 Comparison standard / segmented cell | 138 |
| 5.1.2 Parameters evolution during cycling | 143 |
| 5.2 Influence of operating conditions | 157 |
| 5.2.1 Strategy to investigate internal heterogeneity of battery operation . | 158 |
| 5.2.2 Current density | 163 |
| 5.2.3 Flow rate | 169 |
| 5.2.4 Temperature | 178 |
| 5.3 Summary of the parameter study | 185 |
| 5.3.1 Comparison of the impact of the three parameters | 185 |
| 5.3.2 Development of an operational map | 186 |

The previous chapter detailed the separate characterization of each electrolyte, in flow battery conditions. In the forthcoming discussion, the focus is given to the full cell, with the anolyte and the catholyte constituting each half-cell.

In a primary step, a basic cycling was performed in the segmented cell at LEMTA and compared to the standard tests performed at Kemiwatt. This analysis is necessary to confirm the relevance of the test bench developed during the PhD. Afterwards, the operating parameters accessible with the segmented cell were scrutinized during cycling to investigate on the long-term behavior of the battery.

This provides a baseline of knowledge for the second step of the full cell study. Once cycling in standard conditions was reviewed, a parameter study was performed to scan a varied range of operating points, by changing the current density, the flow rate and the temperature successively.

5.1. Standard cycling

The standard cycling of a lab test cell is presented in the following. Firstly, two tests performed in standard cells of 25 cm² used at Kemiwatt and a test conducted in the segmented cell are compared, to validate the equivalence between the two test beds. In a second part, the parameters monitored in the segmented cell can be followed during cycling: it outlines the aging of the battery.

5.1.1. Comparison standard / segmented cell

The major difference between the standard test bed and the segmented set-up (described respectively in Sections 2.1.2 and 2.4) is the geometry of the active surface and the pumps connected to the cell. To compare them, the metrics of flow factor (FF) is defined (sometimes called stoichiometric factor). It represents the ratio between the actual volumetric flow rate and the stoichiometric flow rate \dot{q}_F [78], derived from Faraday's law (1.11):

$$\text{FF} = \frac{\dot{q}}{\dot{q}_F} \quad (5.1)$$
$$\text{with } \dot{q}_F = \frac{I}{zFC_{\text{reactant}}}$$

\dot{q}_F depends on the reactant concentration C_{reactant} , therefore it increases as the reaction progresses. Indeed, a constant inflow makes the flow factor decrease during the process.

The standard lab-test cell used at Kemiwatt is a 25 cm² square cell with feeders positioned diagonally on the porous electrode; there is no flow channel in this small design. The pumps are purposely oversized to get rid of any mass transfer limitation and focus on the influence of the other parameters: materials, electrolyte composition, cycling conditions etc. The flow rate is 200 mL min⁻¹, corresponding to a high FF of 130 (calculated at the start of charge at 40 mA cm⁻²). The flow behavior is studied in larger cells for which pumps are sized equivalently to a real system.

The segmented cell configuration developed in this PhD thesis has a rectangular active surface area of $30 \times 1.4 = 42 \text{ cm}^2$. The flow enters and leaves the active surface through a manifold of same width as the active surface (machined in the frame, as visible in (Fig. 2.9B)). The small width compared to the length makes the flow almost one-dimensional along the cell. The adjustable pumps can give a flow factor between 1 and 40 (calculated at start of charge). This bench allows the investigation of the flow rate impact (as in the parameter study in subsection 5.2.3). In the standard cycling, the flow rate was maintained at its maximum value of 100 mL min⁻¹, that is $\text{FF} = 40$ at start of charge (much lower than in the standard cell).

In Kemiwatt's stack, the average flow rate is 1 L min⁻¹ for each 2000 cm² cell, which would correspond to 15 mL min⁻¹ in the square cell and 30 mL min⁻¹ in the segmented cell when considering the surface ratio.

This section compares two standard cell tests with a third one made in the segmented cell. The three battery cycles, lasting for 300 charge/discharge steps, followed the same protocol:

100 mL of each electrolyte (described in subsection 2.1.1), charge and discharge at constant current (40 mA cm^{-2}) between the standard voltage window $[0.6; 1.5 \text{ V}]$. Each cycle last between 1 and 2 h (depending on the cell used and the aging), giving a total cycling time of 15 – 20 days.

Test 1 occurred in a standard cell with a pristine membrane while the membrane of Test 2 had been pretreated by reflux as described by the procedure in subsection 2.1.2 (test 2 is described by the terms “reflux” in the legends of the following figures). Test 3 used a similar reflux treated membrane, this time in the segmented cell (hence the description in the legends being “reflux, seg” for Test 3).

During a battery cycling, the most basic monitoring is the cell voltage variation with time. The signal recorded for 10 cycles of Test 3 is displayed in Fig. 5.1.

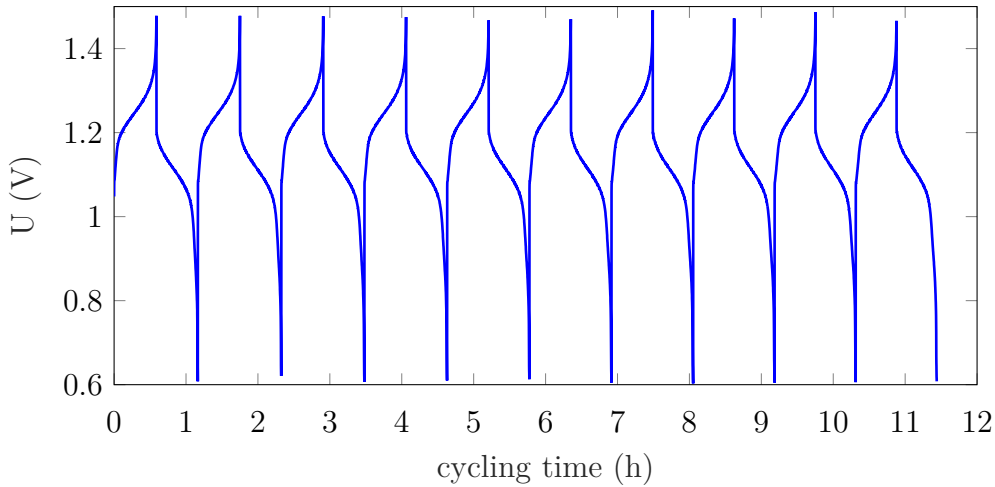


Figure 5.1: Cell voltage record during cycling, Cycles 10-19 of Test 3

This display is not really suggestive in itself; voltage data are postprocessed to derive the capacity retention and the cell efficiency during cycling.

Fig. 5.2 shows the capacity retention of the 3 set-ups versus cycle number, in the form of a percentage of the theoretical capacity $Q_F = 1088 \text{ mA h}^{-1}$, calculated from Faraday’s law (2.3).

The capacity evolution with cycling features an equivalent decreasing shape for all the experiments.

In the standard set-up, the capacity utilization is above 100 % for the first cycles. Several reasons can be speculated to explain this observation, as already listed by [2]:

- ➔ The underestimation of the anolyte capacity is likely and can stem from an error on the solution concentration or on the volume inserted in the set-up.
- ➔ Despite the thorough gas purging step made during the set-up preparation, some residual oxygen could trigger the oxidation of the freshly reduced anolyte species, giving rise to an apparent capacity above the theory. This would be made possible by the excess of catholyte compared to anolyte.
- ➔ Side reactions could also take place concurrently to the charge of the electrolytes. Preliminary tests conducted at Kemiwatt were performed with a micro gas chromatograph. It was connected to the electrolyte tanks and regularly sampled the vapor phase of the tank during cycling. Small amounts of H_2 were detected in both sides of the

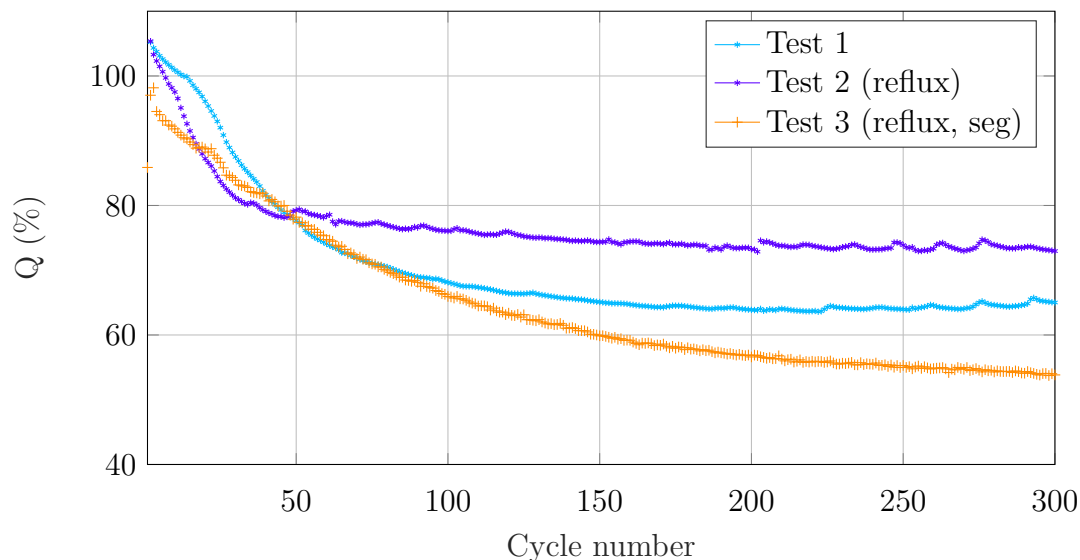


Figure 5.2: Comparison of the capacity utilization in discharge (compared to the theory Q_F) achieved with cycling in Test 1, 2 and 3; $J = 40 \text{ mA cm}^{-2}$

cell. This confirms the occurrence of water electrolysis during cycling. Quantitative tests are necessary for a thorough diagnosis.

- ➔ The carbon felt could also exchange electrons by surface reduction or oxidation, thus contributing to a higher apparent capacity of the set-up [202].

In the standard cell (Test 1 and 2), the capacity utilization dropped fast during the first 100 cycles before reaching a plateau. Test 1 stabilized at 65 % of the initial capacity, whereas Test 2 had the highest capacity retention (73 %). Therefore the membrane pretreatment helps mitigating the initial capacity loss.

The results from the segmented cell follow the same trend with a more pronounced capacity fade and a slower stabilization. The initial capacity achieved is close to theory, and the capacity utilization nearly stabilized after 300 cycles, to a value of 55 %.

The difference between the results in standard and segmented cells likely derives from the flow conditions and the geometrical configuration of the 2 set-ups. The flow factor is much lower at extreme SOC (State Of Charge) in the segmented cell and mass transport limitation leads to both larger capacity loss and slower stabilization during cycling. The capacity loss observed for every test is addressed further by examining the evolution of global and local parameters in subsection 5.1.2.

The efficiency can be assessed by several metrics, defined earlier in subsection 2.2.2. The coulombic and energy efficiencies (CE and EE respectively) are displayed in Fig. 5.3 for the three tests.

CE is close to 100% for all the tests and reveals a reversible chemistry with low species cross-over, no side reaction and correct gas tightness of the set-up (the presence of oxygen would discharge the reduced ARS and impair CE). In particular, the reflux treatment of the membrane does not affect its selectivity regarding active species. The three tests show high energy efficiency EE above 82%, which is of the same order of a VFB [203]. EE compounds moderately with cycling, because of the cell resistance increase and the cell voltage modification:

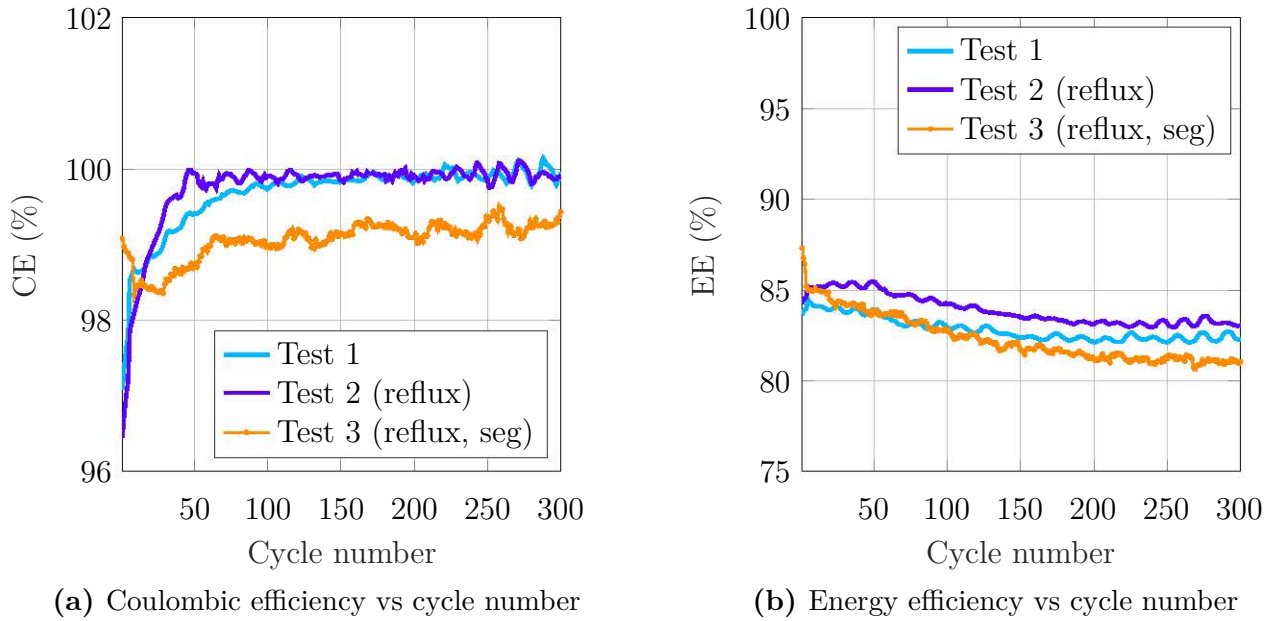


Figure 5.3: Comparison of the efficiencies evolution with cycling for Test 1, 2 and 3

both phenomena are described below and negatively alter the voltage efficiency of the battery. EE is highest for Test 2 thanks to a lower membrane resistance after reflux treatment.

Both CE and EE are slightly reduced in the segmented cell but to an extent that will not query its relevance for the technology study. This could be due to measurement or current control minor errors, since the test benches used for Tests 1/2 and Test 3 are not the same.

The repetitive oscillations observed in the curves of the standard Tests 1 and 2 (for the capacity and the efficiencies) are due to temperature variation over the days; the segmented cell is thermally-controlled and thus the data do not feature a patterned fluctuation. Indeed temperature is commonly known to speed up reactions and decrease the resistance of the system, giving the opportunity to reach more energy capacity and better efficiency.

In the three tests, a polarization curve (PC) was performed every 50 cycles to follow the performance evolution. The cell was half-charged (in comparison to the capacity achieved on the preceding cycle) to reach 50 % SOC. Since the capacity retention evolves with time, the SOC is an *apparent* cell metrics that may not correspond to the actual SOC of each electrolyte. The two electrolytes do not have an equal SOC neither, since side reactions along with active species secondary reactions may occur. Some techniques of SOC monitoring were proposed in the literature. Skyllas-Kazacos investigated the use of conductivity or light absorption measurements to the half-cells of a vanadium redox flow battery [184]. Wei et al. proposed a real-time SOC estimation from an adaptative battery modelling [204, 205]. These methods are however not applicable to the technology of interest or too elaborate to be used in this study. Therefore, the definition of the SOC was limited to the use of the total capacity accessible at one point of the cycle, as the reference of 100 %.

The global PCs and their fit obtained for Test 3 are displayed in Fig. 5.4. Only the region in current of discharge evolved substantially between the cycles. This will be developed further in subsection 5.1.2. A linear fit was done between $[-100; 100 \text{ mA cm}^{-2}]$ for all the PCs, so as to extract the equivalent resistance of the cell called R_{PC} .

The resistance evolution against cycle number is displayed in Fig. 5.5 for the three tests. In all cases, the curve follows an initial increase before stabilizing slowly. This increase could be caused by partial clogging or adsorption on the porous electrode, diminution of the reaction kinetics or membrane pollution. The sole use of PC cannot identify from what stems the resistance increase. EIS technique can help delineating the origin of performance degradation. It was only used in the segmented set-up, whose results are given in the next section.

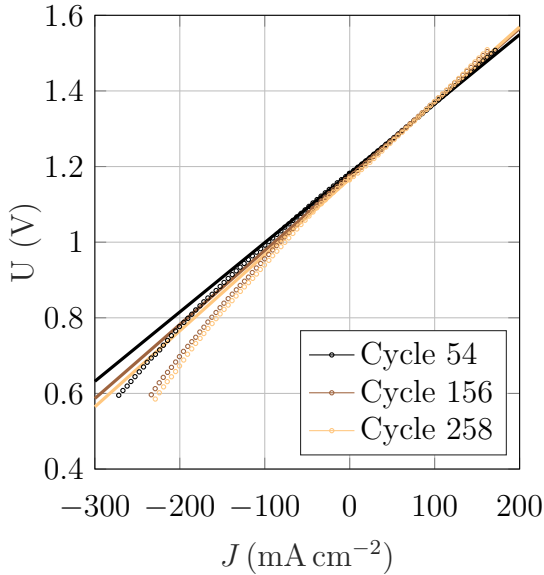


Figure 5.4: 3 PC curves at SOC 50 and fits during cycling of Test 3

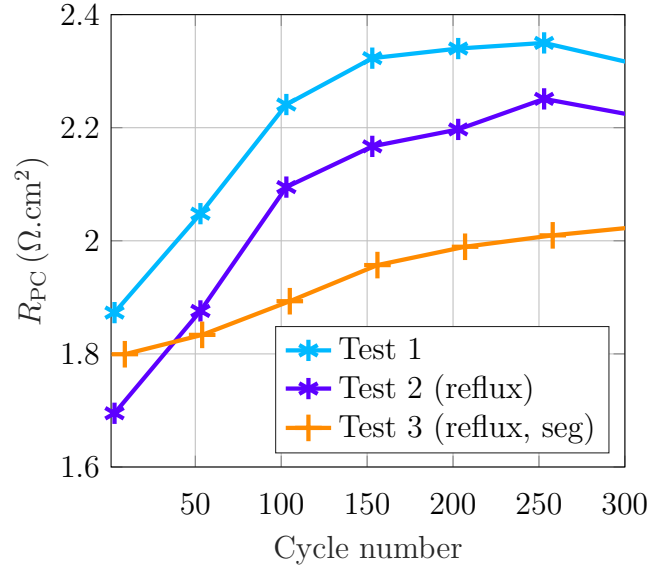


Figure 5.5: Comparison of resistance determined from polarization curves (SOC 50) vs cycle number for Test 1, 2 and 3

The resistive values all lie within 1.7 and $2.4 \Omega \text{ cm}^2$. Test 1 and 2 have a similar trend; the resistance stabilization coincides with the one of the capacity retention, after 100-150 cycles (Fig. 5.2). In Test 2, the use of the reflux membrane mitigates this resistance by 10 %, but does not prevent the performance degradation. In both cases, the cycling resulted in a resistance increase of approximately 20 %. Test 3 displays similar resistance at start but the smallest value after 300 cycles; it only compounded by +10 %. Explaining the difference in performance alteration would have required to decouple the cell resistance by EIS.

Although R_{PC} is lowest for Test 3, it has the worst efficiencies and capacity retention. This is attributed to mass transport issues, arising much sooner during charge or discharge since the FF in the segmented cell is smaller than in standard cells. This phenomenon is not depicted by the slope of the PC since it is performed at SOC 50, a state where no mass limitation have appeared yet.

The comparison of cycles performed in a standard cell and in the segmented test bed developed in the laboratory gives comparable behavior, and the performance is coherent with the specific features of each set-up. It draws several conclusions:

- The battery response in the segmented cell is analogous to the reference tests: segmentation does not affect extensively the performance of the system. In previous works some designs of segmentation could worsen the battery efficiency and therefore be unsuitable for the system study [100].

- Regarding the capacity retention, the standard set-up performs better. Cyclability is not only inherent to a pair of electrolytes but strongly depends on the cell design and the operating conditions of the flow battery. The mass transport seems particularly critical.
- The reflux-pretreatment of the membrane is beneficial for the cycling because it leads to a higher and faster stabilization, along with a lower cell resistance.
- There seems to be a correlation between the stabilization of the cell resistance (deduced from PC curves) and of the capacity. However, the lower R_{PC} of the segmented cell does not give the best efficiency and capacity retention. This underlines that information from PC curves at SOC 50 are incomplete to depict the battery performance.

An industrial perspective

The cycling performance differs from one set-up to another: capacity retention and efficiency are directly related to the cell geometry and the flow conditions. This substantiates the need to be cautious when assessing the suitability of electrolytes to be used in RFB: the testing conditions could mislead the investigation. Similarly, lab-scale cells can falsely depict a promising performance that cannot be reproduced in operational stacks. Indeed, the flow factor used in the standard cells allows rapid system stabilization and satisfactory capacity retention, but is irrelevant for a real size system as it would represent tremendous pumping power.

The ratio between *electrolyte volume / active surface of the cell* is also a design parameter to examine. Indeed a large volume considerably increases the cycling duration and can alter the battery behavior. The study of similar ratios compared to the industrial needs has been started recently with Kemiwatt's small test cells.

5.1.2. Parameters evolution during cycling

The previous analysis of standard and segmented cells confirms that they give comparable results, and that reliable cycling study can be performed with the segmented set-up. The present section focuses on the case of a typical cycling in the segmented cell (Test 3), under standard conditions defined as follows:

- Current, $I = 1.68 \text{ A}$; Current Density, $J = 40 \text{ mA cm}^{-2}$
- Flow Rate, $\dot{q} = 100 \text{ mL min}^{-1}$
- Temperature, $T = 25 \text{ °C}$

The following results capture the interest of using an instrumented test bench and segmented cell to comprehend all the implications from such a complex system. The evolution with cycling of the monitored global and local parameters are given, before examining the characterization results. The results are specifically interpreted to identify the mechanisms of capacity fade and resistance increase observed in Figs. 5.2 and 5.5.

a) Cell voltage

The voltage curve is usually the first and most common curve to be observed when cycling a battery. The ones obtained with the technology under study deserve a special look as they evolve during cycling.

Fig. 5.6 displays the charging and discharging curves of every 20 cycles, normalized in percent of each capacity phase, so as to focus on their shape.

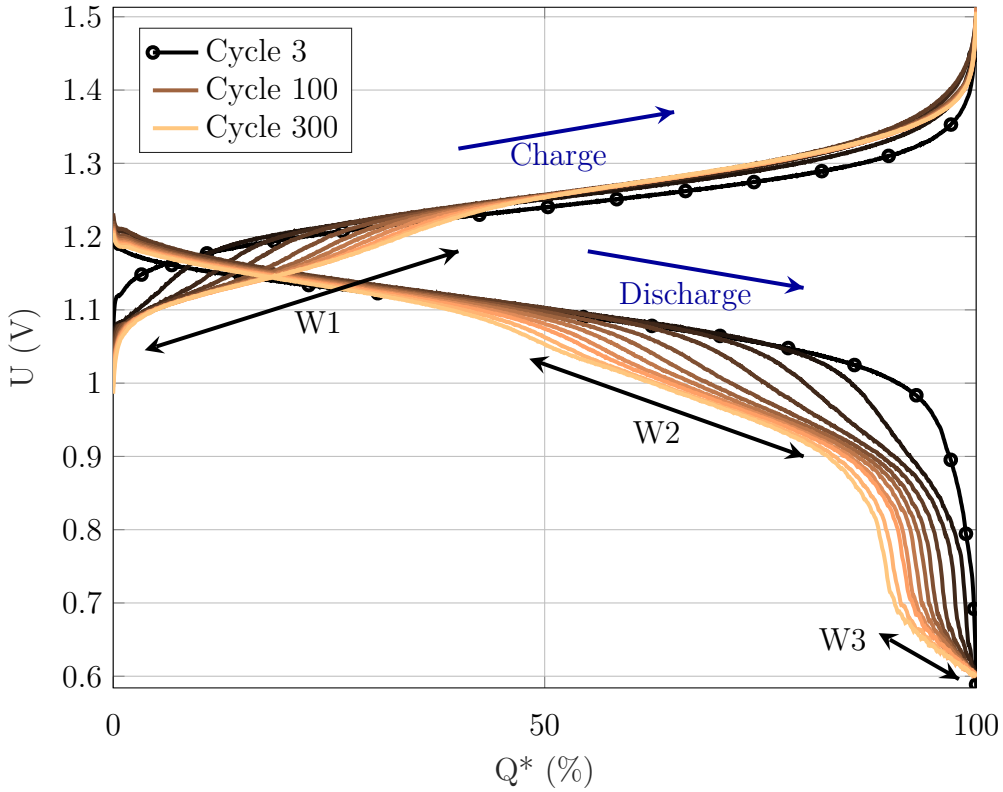


Figure 5.6: Normalized voltage curves evolution with cycling. The arrows pinpoint the 3 waves appearing during cycling

The initial curves in black are very standard. Nevertheless, their form rapidly evolve against cycle number towards the final form of cycle 300, drawn in yellow. The first curves are more dispersed than the last ones, indicating a rapid modification that mitigates with cycling.

The first section of the charge decreases gradually in potential to make a first *wave* (which could also be called a plateau) appear between 0 and 40%, noted W1 in the figure. The rest of the charge is kept unchanged.

What happens early in charge corresponds to the last part of the discharge: between 45 and 100%, the discharge curves drop towards lower potentials to delineate a second wave W2 of increasing significance.

A third zone appears with aging in the last 10% of discharge, outlined by W3 on the figure. In the following, it will be referred to as the *low potential plateau*. Unlike the equivalence between W1 and W2, there is no symmetrical wave to W3, which should be visible at the very start of charge. Such wave will actually be detectable at very low current density (see the parameter study in subsection 5.2.2).

The final voltage characteristics present a two-plateau charge and a discharge divided in three distinct zones.

The appearance of such peculiar features is the signature of successive reactions, accounting for the total charge or discharge of the electrolytes. Thanks to the preliminary half-cell study in Chap. 4, these occurrences are unambiguously attributed to the anolyte. The in-situ local potential measurements were also consistent. They showed that the waves of potentials were detected on the negative side, while the positive side followed a smooth potential signal. Nevertheless, since the potential measurement technique could not be validated during this PhD (see subsection 2.4.4), the local potential results are not presented.

The reduced form of the anolyte is unstable and rapidly evolves into several electrochemical subsystems as evidenced in subsection 4.4.2. One possible aged form of the ARS was proposed from ex-situ characterization of the used solution; it is sketched in Fig. 4.25. The aging seems to occur very early in the cycling and leads to a stabilized system, as the capacity drops until a threshold in Fig. 5.2.

Such capacity fade was already reported in previous papers using the AQDS, a similar anthraquinone molecule [67, 113, 206]. The reactional mechanisms are not clear but several scenarios can be contemplated. Carney and coworkers reported the intermolecular dimerization process of the AQDS molecule that arises at high concentration [207]. This chemical bonding prevents from the reversible storage of two electrons per molecule; its nature and the number of electrons exchanged depends on the pH of the solution.

The chemical modification of the reduced anolyte induced a SOC imbalance between the two half-cells, which was evidenced by ex-situ electrochemical analysis of the solutions during cycling. After a number of cycles, the catholyte actually became limiting in charge while it was initially the anolyte (according to the initial capacity inserted). The anolyte remained limiting in discharge. However, this topic lies beyond the scope of this PhD thesis.

b) Local current density

The monitoring of local currents reveals a non-uniform distribution during charge/discharge phase and changing behavior with cycling. In Fig. 5.7 are compared the local current density records in absolute value for Cycles 1, 20, 80 and 300. In each subplot the dashed lines delimit the charge and the discharge steps: the rest period (60s, no current) between charge and discharge is not represented. The signals of every 2 segments are displayed for better clarity. The curves are plotted versus cumulative capacity of a full cycle (charge + discharge) in Ah.

For all cycles, the general local current distribution presents significant fluctuations around the average value of 40 mA cm^{-2} . The inlet segments (in blue) are always above the average while the outer segments (in orange/red color) exhibit lower values. The highest and lowest values are performed by respectively the first and last segment at any time. The current distribution within the cell also compounds with cycling, as the extreme curves progressively spread away from the average.

The start and end of charge/discharge phases of Cycle 1 are zoomed in for better view in Fig. 5.8.

The charge and discharge essentially present the same pattern. The local current densities exhibit a hump during the first 5% of the step. The most important spike magnitudes are

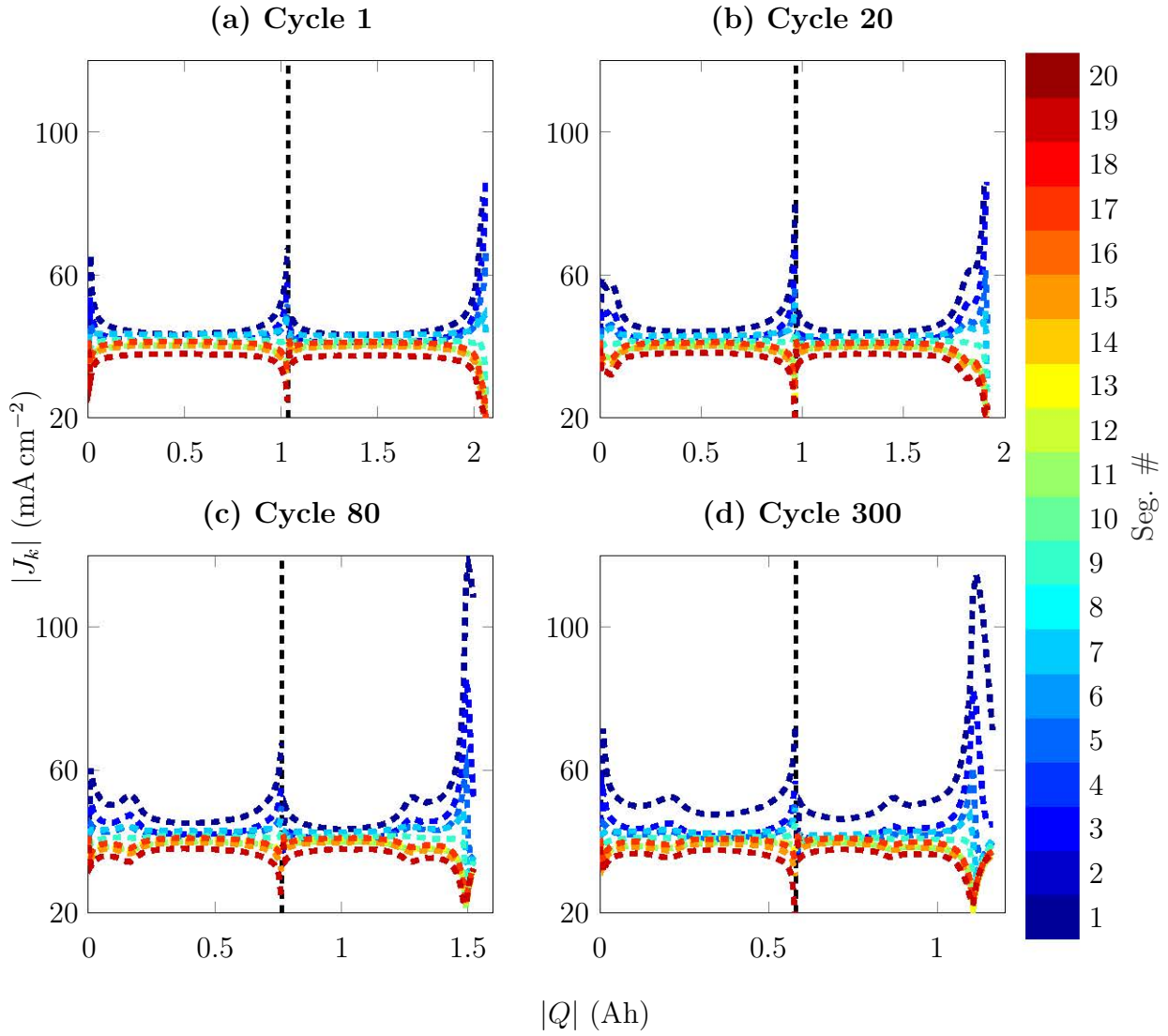


Figure 5.7: Local current evolution for Cycles 1, 20, 80 and 300 (plot of one segment out of two) of test 3, run at $J = 40 \text{ mA cm}^{-2}$, versus the cumulated capacity of one cycle. The dashed line delimits the end of charge and start of discharge

visible for segment #1 and #20 with an opposite shape, as the sum of all local currents is held constant. The local current density in the center of the cell (light blue/green curves) is almost constant and close to the average value.

The current distribution then evolves to be almost uniform during the most part of the charge/discharge phase (subplot (a) of Fig. 5.7). Internal heterogeneity compounds again for the last 5 % of the charge or discharge phase. The stark rise of current at inlet and decrease at the outlet mark the end of the process. The most prominent heterogeneity is recorded at start of charge and end of discharge, that is to say close to 0 % SOC.

The internal behavior indicates that when starting a process, there is always a transient response where inlet segments produce more charge than outlet. This phenomenon certainly derives from the local concentration along the electrode channel: when current is applied, all the segments contain the same reactant concentration: they can deliver the same amount of

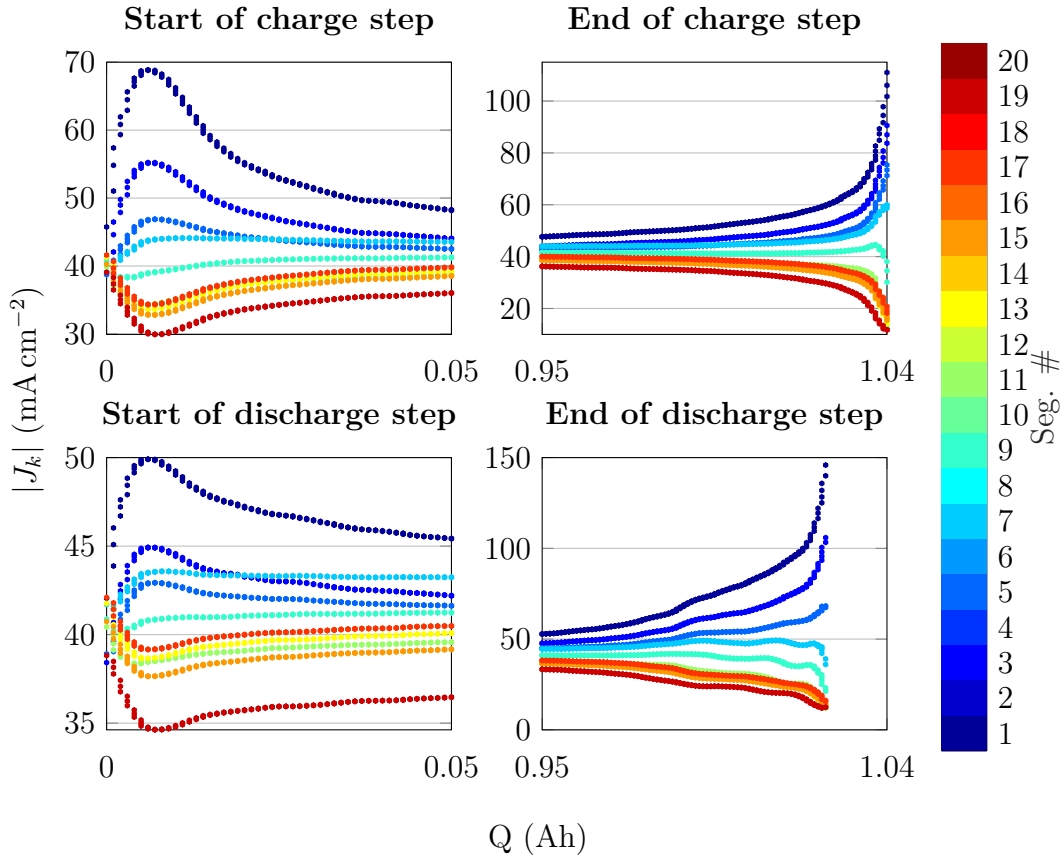


Figure 5.8: Zooms on the local currents at start and end of each phase of Cycle 1 from Fig. 5.7 (a)

charges (indeed all the curves of the left-hand subplots of Fig. 5.8 start from the same point). The outer segments are then fed by the depleted electrolyte that already reacted at the inlet, while the first segments are fed with fresh electrolyte from the tank. For this reason the current at the inlet increases at the expense of the current produced at the outlet. This heterogeneity mitigates after a few percent of charge and the internal operation reaches a steady-state, where the inlet segments keep a superior current value than the last segments.

At the end of the process, an equivalent mechanism derives from the decreasing concentration of active species. The outer segments suffer from reactant depletion first and can no longer sustain the reaction rate; the local current at the inlet in turn increases abruptly to comply with the global current applied to the battery. This critical heterogeneity induces a concentration overpotential that reaches the cut-off voltage, and the process stops.

As depicted by the other subplots of Fig. 5.7, the patterns at start and end of each step are conserved throughout the cycling. However, a second spike rises at the beginning of charge and end of discharge. It is almost hidden in Cycle 20 since it occurs very early in charge and very late in discharge. In Cycle 80, the spikes are observed at 0.15 A h in charge and 1.3 A h in discharge. Their position evolve to 0.2 A h and 0.9 A h in Cycle 300.

Indeed, this contribution widens with cycling and is postponed in the charge process (or is brought forward during discharge). These spikes reveal a symmetry between charge and discharge (according to the vertical dashed line delimiting the two processes).

These peculiar current attributes arising with cycling can be correlated to the cell voltage evolution in Fig. 5.6. Indeed, the appearance of the spikes during charge and discharge coincide with the change of plateau in the voltage curve. For instance in Cycle 300, the jump to the second plateau is visible after 40 % of charge and 50 % of discharge. The position of the spikes in subplot (d) of Fig. 5.7 are close to these values. This would indicate that changing from one form of reactant to another (what is suspected to happen with the second potential plateau) disturbs the local currents, by inducing a higher current at the inlet and lower reaction rate at the outlet. This is exactly the pattern already observed at the start of charge or discharge (Fig. 5.8).

Additionally, the low potential plateau emerging at the end of discharge also affect the current distribution: at the very end of Cycle 300 (Fig. 5.7 (d)) the internal current distribution curbs back to a more uniform operation (this is hardly visible since it occurs only on the last percent of discharge).

As a conclusion, the locally-resolved current distribution unveils that the cell operation is never perfectly homogeneous and compounds at the start and end of each process. More specifically, the beginning of a reaction conveys a transient internal heterogeneity with a sharp spike of inlet current: it is visible at start of both charge and discharge, but also in the middle of the process because of the appearance of a new reactant in the anolyte. The end of the processes are also characterized by a highly heterogeneous current distribution, with most of the reaction concentrated at the cell inlet.

c) Pressure drops

The pressure drops (ΔP) in each side of the segmented cell was monitored during the 300 cycles. The ΔP evolution with time for the two circuits of electrolytes are represented in Fig. 5.9. The measurements are averaged over 500 points (a point was recorded every 0.6 s) to highlight the global evolution. Cycle 1 is not shown but presented later in Fig. 5.10.

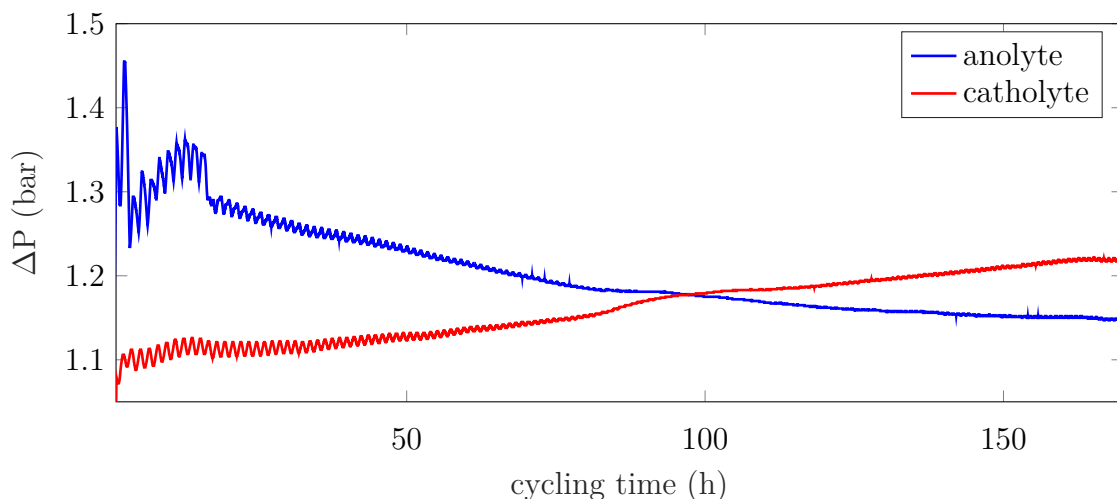


Figure 5.9: Pressure drops over cycling time, $\dot{q} = 100 \text{ mL min}^{-1}$

The overall pressure differential in both sides is between 1.1 bar and 1.5 bar. It is representative of the pressure drops in Kemiwatt's system, being roughly 1 bar. As a comparison, Reed et al. measured 0.3 bar to 0.7 bar in an operating 3-cell VFB stack of 800 cm^2 (and a length of

electrode similar to the segmented cell) using a flow-through design, the same electrode material but a flow rate twice as low [37]. The pressure losses largely depend on the stack design and dimensions, the operating flow rate and the viscosity of the electrolyte.

The initial pressure losses caused by the flow of anolyte is substantial but decreases after a few cycles. It is explained by the change of the rheological behavior of the solution after its use in the battery (subsection 3.2.2). After 15 unsettled cycles, the differential pressures in both sides change almost linearly with time and in the opposite direction; the anolyte pressure decreases while it rises on the catholyte side.

The flow rate monitoring unveiled that the flow was indeed constant with time (fluctuations representing less than 1 %). The average of the flow rate during the 300 cycles is 94.5 mL min^{-1} for the catholyte, and 93.5 mL min^{-1} : it is less than 7 % of divergence from the command given to the pumps (100 mL min^{-1}).

The initial modification of anolyte viscosity is very fast and the maximum value with the fresh solution is never reached again. Fig. 5.10 shows the very start of the cycling: current is applied at the dashed vertical line. The pressure is lower in Fig. 5.10 than in the other figures because the flow rate is set to 50 mL min^{-1} during the first charge. Applying current to the battery produces an immediate decrease of pressure in the anolyte of more than 40 %.

A further test showed that the pressure drop reduction was actually triggered by a constant voltage step of 1 V applied on a new cell. This voltage induces less than 4 mA cm^{-2} and the reduction in pressure is immediate: it means that when the anolyte reaches a characteristic potential threshold it becomes less viscous, and the transformation is not a question of quantity of charge passed in the electrolyte. The underlying mechanism could be the desorption of the anolyte molecules when an overpotential is set at the carbon fibers. This finding proves the necessity to set a low flow rate at start of cycling, in spite of the electrode prewetting with KOH. A preconditioning step of the anolyte could be designed before being circulated it in the end-use stacks.

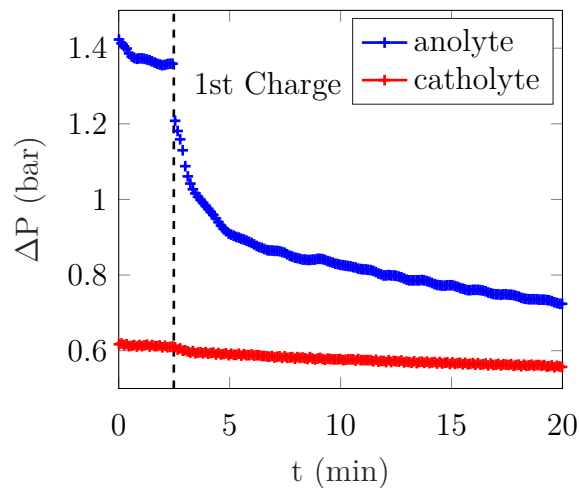


Figure 5.10: Zoom on the pressure drops responses when first applying a current at start of cycling, $\dot{q} = 50 \text{ mL min}^{-1}$

By zooming in on a few cycles in Fig. 5.11 (the 60 s period of rest between charge and discharge is not represented), it becomes obvious that the pressure drops depend on the SOC. A similar pattern is observed in a VFB [102]. During the anolyte charge, ΔP increases and

then goes back down during discharge. The reverse is observed with catholyte. This pattern substantiates the dependence of the electrolytes viscosities according to their respective composition (indeed ionic and active species concentration vary with SOC).

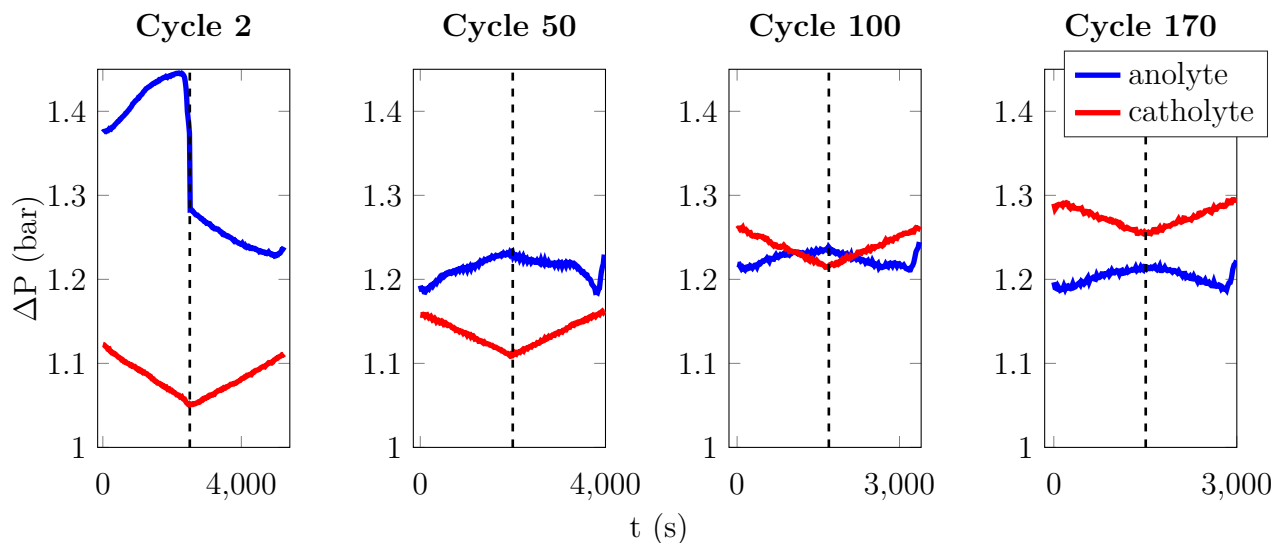


Figure 5.11: Pressure drops at several cycles, $\dot{q} = 100 \text{ mL min}^{-1}$. The dashed line delimits the end of charge and start of discharge

Moreover, the anolyte behavior is clearly modified during cycling. While at the start (Cycle 2) there is a gap between end of charge and start of discharge (the pressure drops evolve during the rest after end of charge), the ΔP curve becomes continuous from Cycle 50. During aging also emerges a spike at the very end of discharge, on the anolyte side. It could derive from the low potential plateau in discharge accessed after many cycles (Fig. 5.6): the reaction of this form of molecules could impede the electrolyte viscosity.

In Fig. 5.11, the variation of the catholyte pressure drop during one cycle is opposite to the anolyte behavior. Furthermore the shape does not evolve with cycling. This agrees with the preliminary study that showed no change of catholyte viscosity after use in the battery (subsection 3.2.2). Therefore a chemical aging cannot account for the global ΔP rise on this side. It could be explained by a decrease in porosity due to species adsorption (as already speculated in subsection 4.3.3) or electrode distortion.

The opposite evolution of the pressures in both compartments could derive from water transfer through the membrane during operation (mechanisms described in subsection 3.3.2). The water flow towards one side would increase the internal flow rate and with it the pressure drops. The flow sensors might not detect these slim variations of flow rate. The water transfer was disregarded during this full cell operation and would necessitate further investigations.

An industrial perspective

Monitoring pressure drops is one of the easiest instrumentation but is deemed as a precious indicator. Three learnings can be retained for the industrial application:

- ➔ The unequivocal change of anolyte viscosity to a potentiostatic input signal paves the way to an appropriate preconditioning method before using this electrolyte in the system. An external pretreatment set-up could be designed to hold the solution at a constant potential during an extended period. The equivalent electrolyte potential (corresponding to 1 V of cell voltage) necessary to precondition the anolyte must be determined.
- ➔ Although the anolyte aging globally alleviates the pressure drop of this half-cell, the fully discharged state leads to a pressure spike. This is likely related to the species formed during the *low potential plateau* in discharge: a higher voltage cut-off could be determined to avoid reaching this small section of the discharge.
- ➔ The pressure drop rise at the catholyte should be scrutinized, to unveil the underlying process. Over the long run, it could represent a threat for the correct supply of electrolyte on this side.

d) Polarization curves

Characterization can be made at several SOC of the battery. Fig. 5.12 presents the global polarization curves (PC) at SOC 20, 50 and 80 obtained during the 150th cycle.

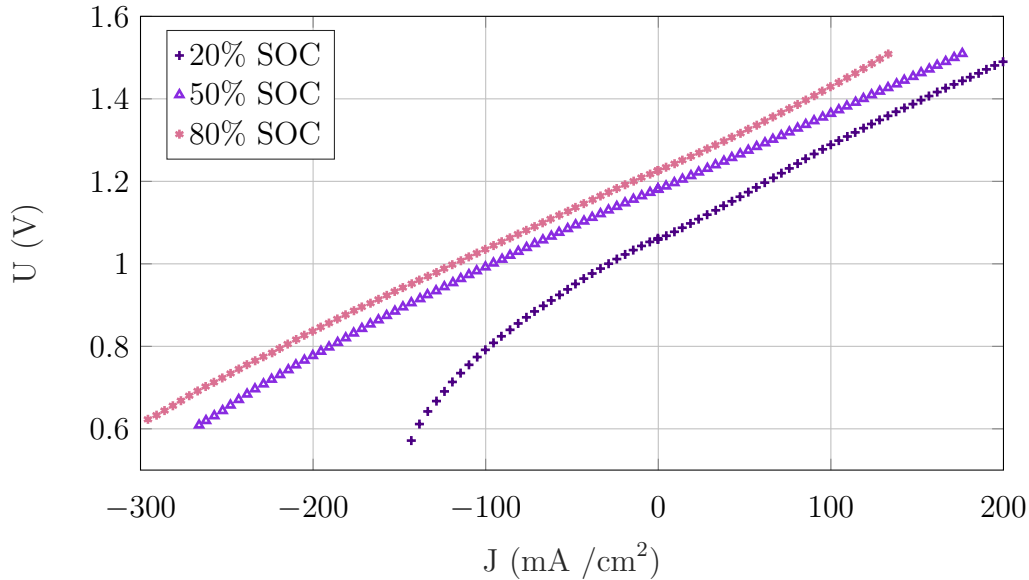


Figure 5.12: Global polarization curves at 20, 50 and 80 % SOC, after cycle 150, $\dot{q} = 100 \text{ mL min}^{-1}$

As expected, the PC are shifted upwards at higher SOC, because the V_{OC} given by Nernst Law increases (1.4). At SOC 50, the curve is almost linear throughout the polarization (a small bent can be observed at very high discharge rates). Its regression analysis gives a line with a slope equalling $1.97 \Omega \text{ cm}^2$. This equivalent resistance, called R_{PC} , depicts the activation,

ohmic and mass transport losses of the system at this SOC (PC contributions detailed in subsection 1.3.1). The PC is continuous in both positive and negative polarization zones. It reveals that charge and discharge essentially induce the same losses.

When the battery is almost discharged at SOC 20, its characteristic is bent in the negative polarization from -50 mA cm^{-2} . Indeed a low material concentration is available for discharge and this lack of reactant establishes a concentration overpotential. If no cut-off voltage was defined, a limiting current would be reached when $U \rightarrow 0$. In the positive region, the plot is essentially linear.

At high SOC (80 %), the characteristic curve is parallel to the PC at half-charge. It features a non-linear part at highly positive currents (from approximately 80 mA cm^{-2}) for the same reasons as at SOC 20. The deviation is nevertheless less marked.

The discrepancy between the PCs at SOC 20 and 80 might be caused by the way the battery SOC is determined: as already mentioned, it is set according to the capacity achieved during the preceding full cycle in standard conditions. This method estimates an apparent cell SOC that certainly does not comply with the SOC of the two half-cells, which could lead to non-symmetrical battery states at apparent SOC 20 and 80.

This difference could also substantiate that the charge is not limited by advective mass transport as much as in discharge. Clement et al. asserted the same for a VFB by observing the local current gradients [101].

It is worth observing that even at SOC 50, the voltage boundaries are not symmetrical around V_{OC} ; larger currents can be reached in discharge than in charge.

The use of segmented cell enables plotting the local PC, by representing cell voltage versus the current density of each segment. The 20 curves at SOC 50 are compared in Fig. 5.13 along with the global PC in black.

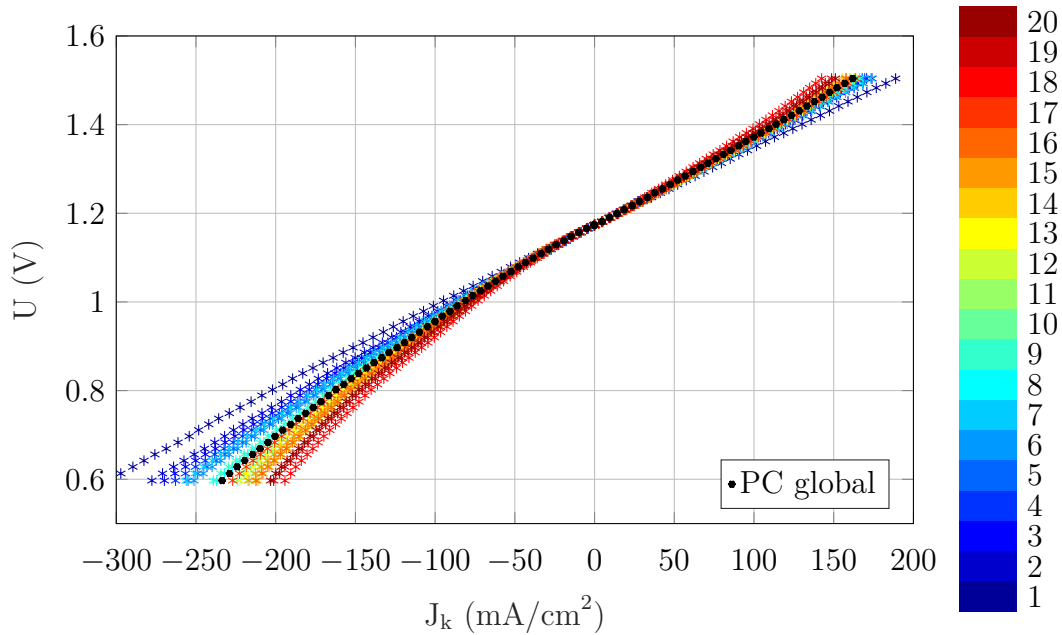


Figure 5.13: Local polarization curves at SOC 50, cycle 150, $\dot{q} = 100 \text{ mL min}^{-1}$. Global PC represented by black dots

The local PC is highly dependent on the position along the length of the cell. The global PC perfectly matches with the PCs of the center segments. As expected, the contribution of all segments influences the cell response that is approximately the average of the local curves. Segment #1 displays a perfectly linear PC: the inlet never suffers from active material starvation. From Segment 2 a region assigned to mass-transport limitation appears at high polarization (both negative and positive) and its significance grows with the position in the electrode channel: this stems from the accumulation of reactant consumption along the cell. Similar localized polarization curves have been reported by Becker et al. [103]. They also highlighted reactant starvation close to the cell outlet during a PC.

The local PCs of Fig. 5.13 can be fitted with linear regression in the range of $\pm 50 \text{ mA cm}^{-2}$. In Fig. 5.17, the slopes of these fits (in $\Omega \text{ cm}^2$) are compared to the resistances determined from EIS measurements.

The cut-off level in discharge allows for higher polarization. When comparing the curves within the symmetric window $[-150; 150 \text{ mA cm}^{-2}]$, the curves are roughly equivalent in charge and in discharge. The study of the flow rate parameter will extend the analysis of local PCs in subsection 5.2.3.

e) EIS

Electrochemical impedance spectroscopy (EIS), described in subsection 2.2.4, is performed along with PC during each characterization cycle. Fig. 5.14 depicts the Nyquist plots of a cell recorded at three SOC: 0, 50 and 100 %. The results were obtained at the 100th cycle of another test performed in the same segmented set-up with operating conditions equivalent to Test 3.

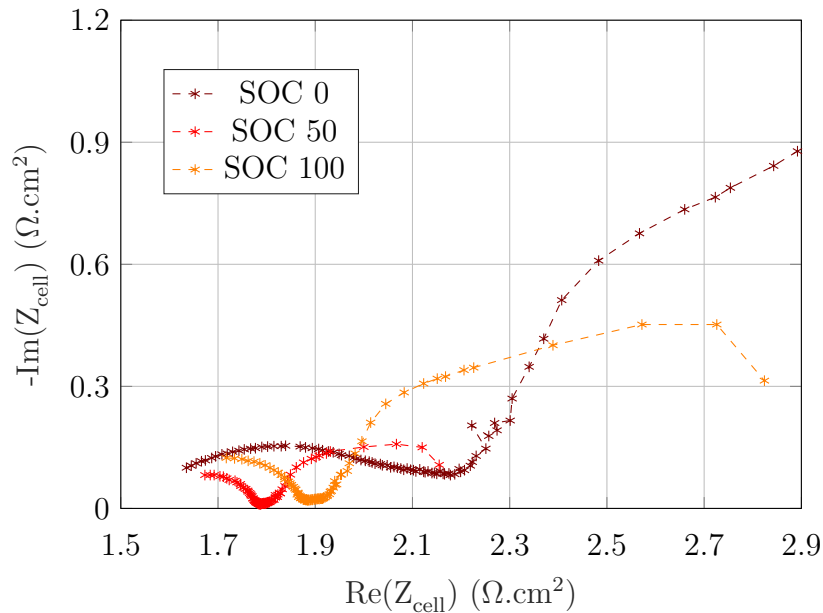


Figure 5.14: Nyquist plots from EIS at 3 SOC (cycle 100 of another set-up) around $J = 0$

The 3 spectra are composed of a small semi-circle at high frequency (HF) and a bigger low-frequency (LF) one (the typical shape of a Nyquist plot is described in subsection 2.2.4). The

data acquisition system and electronic hardware are reliable only over a delimited frequency range that does not permit to observe the full closing of the loops (at very high or very low frequency).

Extending the HF semi-circle would lead to an x-axis intercept that is equivalent for all the spectra. The high-frequency resistance R_{HF} is indeed expected to be independent of the SOC. It was utilized during separate characterization of the components (Chap. 3) for parameter determination. The medium frequency points between the two semi-circles correspond to the charge-transfer resistance R_{CT} added to R_{HF} . It is referred to as R_{MF} for medium-frequency resistance in this section. It equals respectively 1.8, 1.9 and 2.2 $\Omega \text{ cm}^2$ at the 3 SOC (calculated from the formula (4.38)). This indicates that charge-transfer is SOC-dependent: a depletion of active species (at low and high SOC) impairs the reaction at the electrode. The variation of R_{CT} versus SOC was indeed thoroughly examined to characterize each half-cell in Chap. 4. The resistance is more critical at low than at high SOC. This discrepancy could be related to the fact that the SOC of the cell is only an *apparent* state. For SOC 0, there is also a small imaginary component at MF, outlining slight measurement errors. Yet the variation of R_{CT} with SOC is of the same order as in the symmetric cells (Figs. 4.11 and 4.22).

The predominant variation with SOC is the low-frequency semi-circle which expands at SOC 0 and 100. At these states, the EIS hypothesis of linearity is no longer respected for low frequency signals (subsection 2.2.4): because one form of active species is lacking, its relative concentration variation becomes large ($\Delta C/C > 1$). As a consequence, the voltage response from the perturbation is not sinusoidal anymore. It is thus meaningless to perform low frequency EIS at extremes states of charge of the battery.

The evolution of the EIS response at SOC 50 during cycling is represented by the Nyquist plots in Fig. 5.15. The medium-to-high frequency section (left-hand side of the curves) remains almost constant over the cycles; the horizontal drift only accounts for 5 % of the R_{MF} value. On the other hand, the LF semi-circle substantially and regularly expands with the cycle number. This evolution is reminiscent of the anolyte symmetric cell study (Nyquist plots depicted in Fig. 4.16):

- R_{LF} increased by +40 % in the symmetric cell while the evolution in the full cell is +25 %
- R_{CT} also degraded in the symmetric cell, contrarily to the full cell where it is almost constant

These notable differences might be the consequence of dissimilar anolyte conditions during the two tests: in the symmetric case it had been freshly prepared and kept at SOC 50 in circulation, while during the full cell study, the anolyte was cycled between SOC 0 and 100.

The increase of the low-frequency semicircle, most certainly attributed to the anolyte half-cell, is a sign of mass transport compounding during cycling. As already suggested during the anolyte symmetric cell study, it can stem from a reduction of the active surface area of the electrode (due to adsorption or filtration of particles obscuring the pores), the decrease of the active species concentration or of their diffusion coefficients.

The extrapolation of the semi-circle at very low frequencies would give intercept values (called R_{LF}) higher than R_{PC} in Fig. 5.5, for instance 2.4 $\Omega \text{ cm}^2$ after 300 cycles against 2 $\Omega \text{ cm}^2$ according to the PC slope. The comparison between EIS and PC results is commented below.

Thanks to local current measurements along the cell, Nyquist plots can be obtained for each segment. Fig. 5.16 represents the local EIS responses in the segmented cell at SOC 50

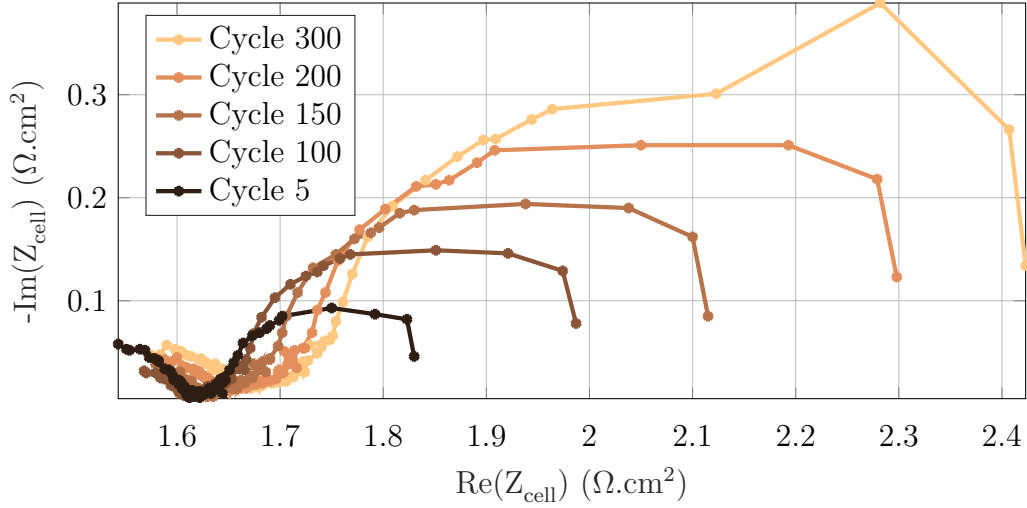


Figure 5.15: Global Nyquist plots of the segmented cell at SOC 50 around $J = 0$, evolution with cycling

during the 150th cycle. The HF loop has been removed for more clarity, only the loop between 100 Hz and low frequency is presented.

The characteristic is gradually modified with the segment position as it was the case for local PCs (Fig. 5.13). There is a progressive expansion of the low-frequency semi-circle towards the flow outlet, which embodies the accumulated material consumption along the electrode. Similarly to the perfectly linear PC of Seg. #1, the Nyquist plot at this position has virtually no low-frequency loop: there is almost no mass transport limitation in this segment.

Fig. 5.17 depicts the local resistances determined from the Nyquist plots of Fig. 5.16. The two ends of the semi-circle at medium and low frequencies give the corresponding resistances R_{MF} and R_{LF} . The latter cannot be determined for Seg.#18-#20 since the intercept of the loop is not available in the plots within the range of frequencies recorded. The slope of the fitted local polarization curves of Fig. 5.13 between $[-50; 50 \text{ mA cm}^{-2}]$ gives R_{PC} . The values represented as Seg.#0 stand for the full cell resistance.

The diagram highlights the quasi-homogeneous value of R_{MF} that was expected to be invariant with the position in the flow channel. The standard deviation of these resistances is 6%. As already mentioned, R_{MF} is composed of:

- ➔ the high-frequency resistance that stays constant at all times (unless if the membrane is getting polluted, as in section 4.3)
- ➔ the charge-transfer resistance that only evolves with SOC (a property that was used during the half-cell characterization in Chap. 4)

R_{PC} embodies the same resistive components, supplemented with the mass transport losses. Therefore this second resistance is also nearly constant for all the segments (the standard deviation is again 6%) and 20% higher than R_{MF} .

The third equivalent resistance displayed in Fig. 5.17 is R_{LF} . It embodies the combination of all the internal losses (purely ohmic, charge transfer and mass transport losses). R_{LF} equates to R_{PC} for the first two segments but their difference exacerbates towards the outflow. Indeed, when the period of the EIS signal becomes lower than the residential time inside

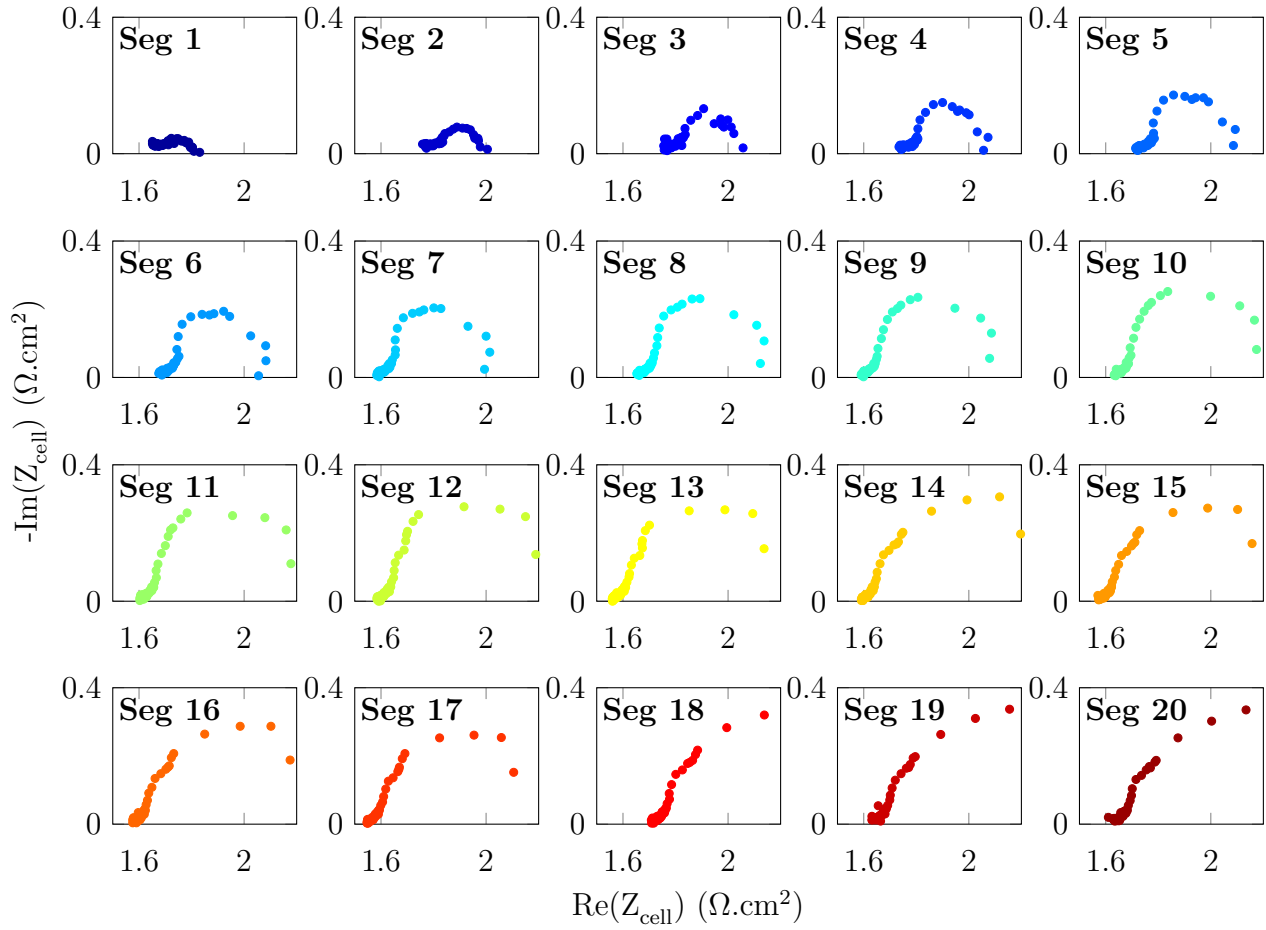


Figure 5.16: Local Nyquist plots from EIS at SOC 50 around $J = 0$, cycle 150

the cell (corresponding to $f < 150$ mHz for 100 mL min^{-1}), a new mechanism appears: the concentration oscillation along the porous electrode can yield an impedance that distorts the local spectra towards the outlet [193]. To get rid of this artifact, the pumps should deliver an oscillating flow rate in phase with the input current.

The standard cycling study in the instrumented test bench leads to key insights for the system aging in operational conditions. All the parameters that could be tracked with this set-up are somehow interrelated and each of them brings a deeper perception of the system behavior.

In light of the locally-resolved measurements, the current distribution is not constant along the length of the cell, contrarily to what is asserted in simple models [83]. High internal gradients are detected at the start and end of a phase. Moreover, the internal heterogeneity seems to compound during cycling.

The battery aging, readily perceptible from the voltage curves, is attributed to the anolyte thanks to the half-cell potentials records. This aging has a direct impact on local current distribution and pressure drops, which all feature an evolution during cycling.

Cycling is also accompanied by a tiny increase of the mid-frequency resistance from EIS (+5%), a small increase of the resistance deduced from PC (+10%) and a much larger

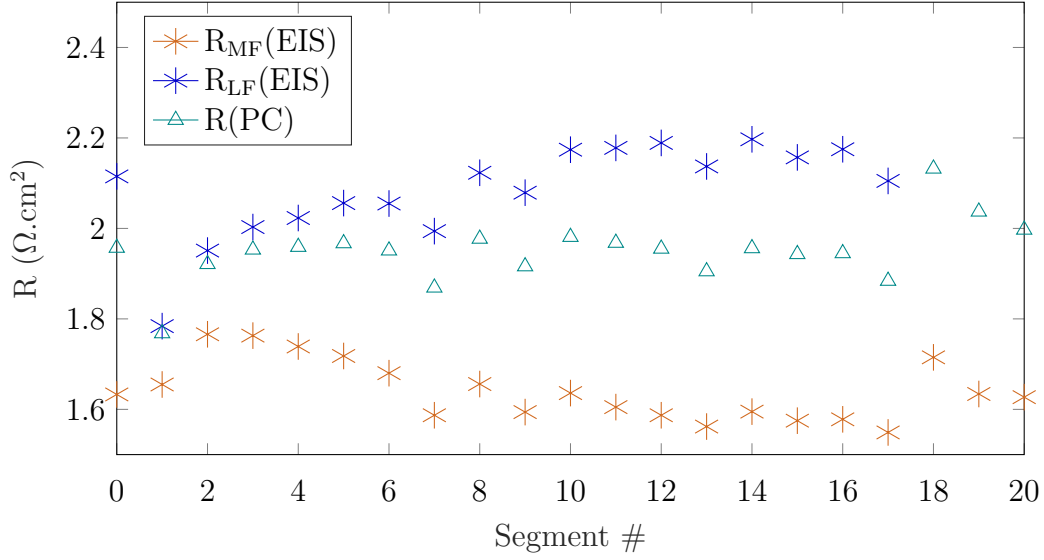


Figure 5.17: Comparison of the local resistances determined at SOC 50 for Cycle 150, by EIS at medium and low frequencies R_{MF} and R_{LF} (two ends of the semi-circles in Fig. 5.16) and from the slopes of the polarization curves: R_{PC} (Fig. 5.13)

compounding of the total resistance from EIS (+25 %). This evidences that performance degradation stems from several mechanisms with a predominant deterioration of the mass transport.

Comparing the resistances deduced from the two characterization processes of PC and EIS is insightful and substantiates that the two characterization procedures complement each other. R_{MF} accounts for ohmic and charge-transfer resistances, while R_{PC} also involves mass-transport losses. These two resistive values are independent from the position along the electrode. The last R_{LF} shows a difference with R_{PC} that can be ascribed to artifacts during EIS (concentration oscillation along the flow). Nevertheless, the LF resistance exhibits a higher increase during cycling than the PC slope. This would suggest that a part of mass transport limitation degrades gradually but its evolution is not detectable by the polarization curve. Further analyses would be required to identify this phenomenon.

A notable difference between charge and discharge is highlighted by the characterizations (PC and EIS): mass-transfer limitation appears prominent in discharge. This aspect is however difficult to deconvolute from the error on SOC. The apparent state of the battery is determined from the total capacity available at a given time in cycling and under standard conditions; it certainly mismatches with the actual SOC of both half-cells (themselves not equal to each other).

5.2. Influence of operating conditions

The previous section related to the standard cell working conditions with a special focus on the influence of the battery SOC and the system aging during cycling. In the following, the impact of the operating parameters on the battery response is addressed. First and foremost, the issue of internal heterogeneity depending on the duty point is introduced, to evidence its

possible negative consequences on the system. In the three subsequent parts, the effect of the parameters I , \dot{q} and T are evaluated one at a time. The final section seeks the optimization of a battery cycle in light of the preceding learnings.

5.2.1. Strategy to investigate internal heterogeneity of battery operation

The segmented set-up developed during this PhD gives an unprecedented insight on the internal behavior of the battery. Thanks to its 1D-like design, the tool focuses on the heterogeneity along the electrolyte flow. In a first part, the homogeneity issue is illustrated by comparing two extreme cases. The approach to evaluate its consequences is brought to light. This leads to set a criterion for acceptable homogeneity and to establish a thorough design of experiments. The latter enables the operating conditions to be efficiently tested in the purpose of diagnosing their influence on the battery operation.

a) Developing criterion to quantify the heterogeneity and its consequences

The segmentation of the RFB cell forces to reassess the standard way of analyzing the battery response. The following paragraphs compare the cycles obtained for the two extremes of flow rate conditions possible with the pumps in use: (100 mL min^{-1} and 10 mL min^{-1}).

The most basic data usually observed during battery cycling is the voltage evolution with time. It is a simple indicator of where the battery is in its charge/discharge stage and reveals the importance of overvoltage induced by the operating state. Fig. 5.18 and Fig. 5.19 compare on the left the voltage responses for both \dot{q} . In the plots at right, the local current current distributions are given at the times visualized by the red dots on the voltage curves. The times are taken as fractions of the charge or discharge duration t_{tot} : 5 %, 50 % and 95 %.

It is immediately apparent from the local current data that the first segments (corresponding to the entry point of the electrolyte solutions) always have a higher local current than the other segments. While this effect is less pronounced as the flow rate is increased, it is still visible at start of charge and end of discharge. When the charge starts, the distribution is surprisingly worse for the high flow rate. It can be clearly seen that in the middle of a charge cycle, the lower flow rate setting corresponds to a more heterogeneous local current profile. Fig. 5.19 shows essentially the same results for the discharge phase, except at the end. Finishing the charge with low flow rate induces a huge variation of the local current along the flow with outlet segments at 0 mA cm^{-2} . At the end of discharge, the segments show on the contrary a nearly uniform current except for Seg.#1 and #2.

The contrasting profiles at the two extreme flow rates are related to the internal distribution of concentration. Close to the end of the stage, the segments towards the outlet are depleted in reagent and cannot maintain the same amount of electrochemical exchanges. The phenomenon is aggravated with low electrolyte flow rate. The justification of heterogeneity at the start of the step is not as intuitive, as the contrast between the end of charge and discharge.

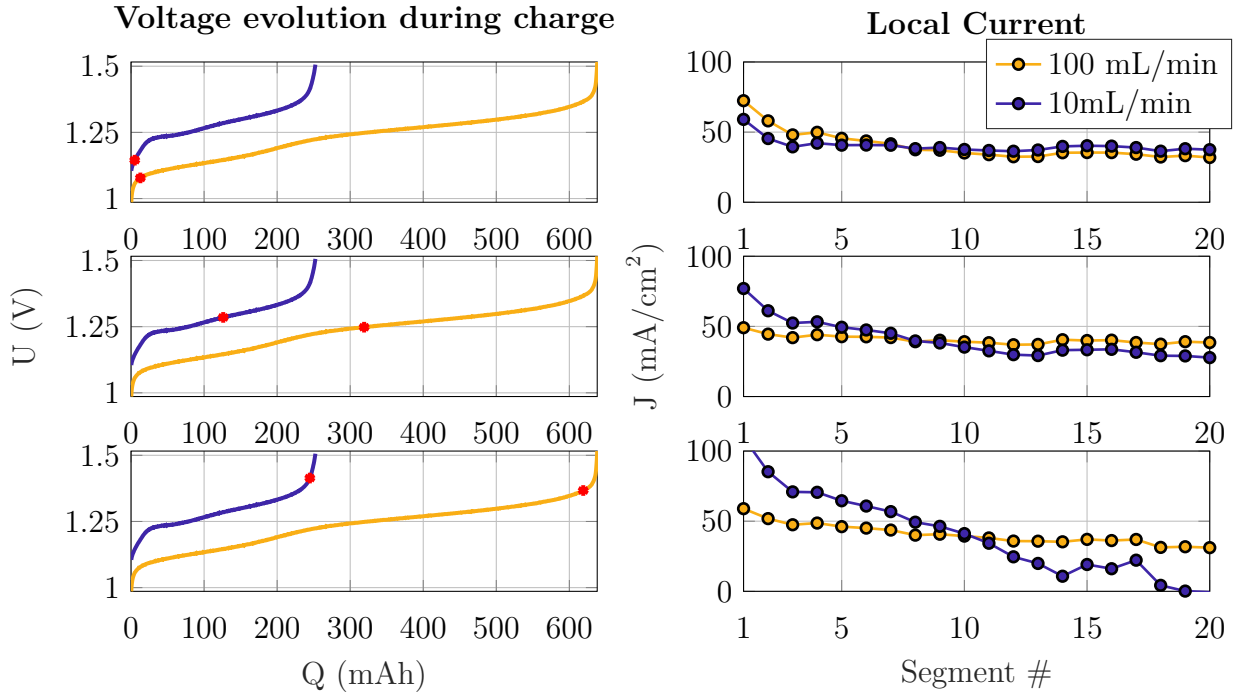


Figure 5.18: Comparison of the cell voltage versus capacity (left) and the distribution of local current (right) at beginning, middle and end of charge stage (the position on the voltage curve is visualized by the red dot) for two flow rates

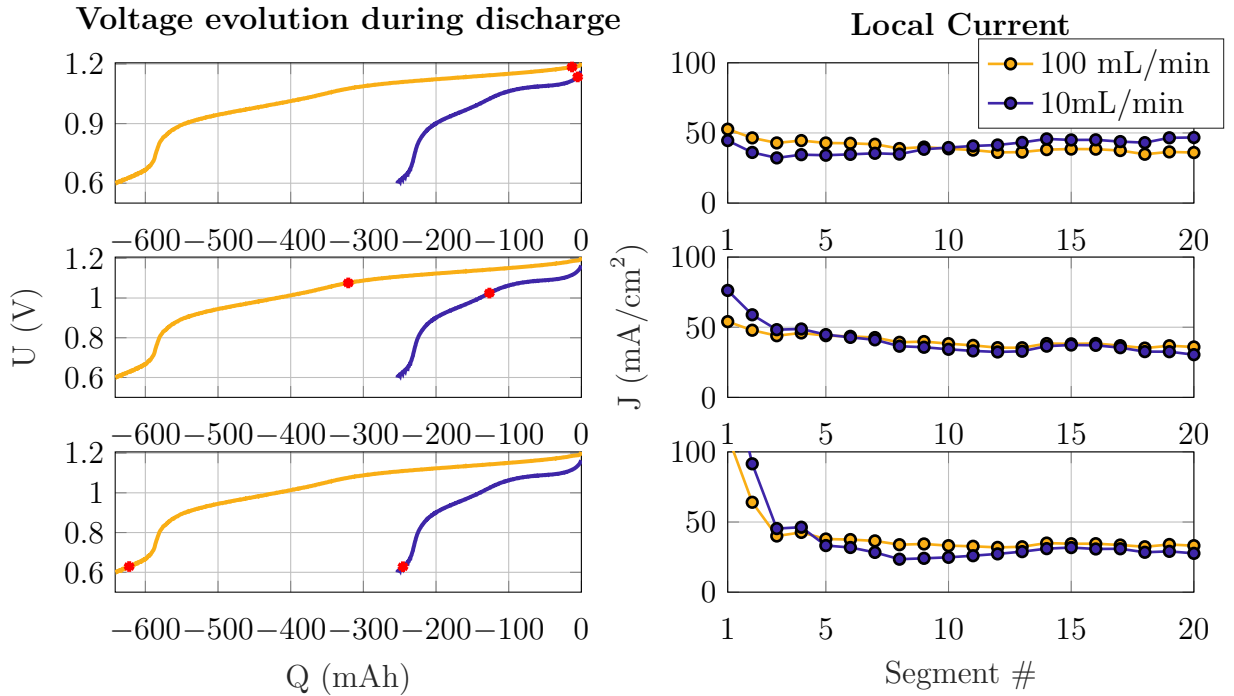


Figure 5.19: Comparison of the cell voltage versus capacity (left) and the distribution of local current (right) at beginning, middle and end of discharge stage (the position on the voltage curve is visualized by the red dot) for two flow rates

It is impossible to conclude on the extent of heterogeneity by visualizing a few snapshots of current profiles. Given that the current distribution varies at each time step and differently with the conditions, it must be regarded more globally to evaluate its impact. To this end, two macroscopic parameters are introduced:

- The first measure is local but covers the full stage: it is the local capacity percentage noted Q_k^* (k stands for the segment number), and is calculated as a fraction of the total capacity according to:

$$Q_k^* = \frac{1}{Q_{\text{tot}}} \int_0^{t_{\text{max}}} j_k \, dt \quad [\%] \quad (5.2)$$

- The second measure is local but instantaneous: the internal current distribution is characterized by its standard deviation. This corresponds to the square root of the second central moment of the distribution; higher moments also exist to describe the dispersion of a set of data. To have a straightforward point of comparison for any cycling condition, the standard deviation was normalized to the average local current $\bar{j} = \frac{J}{20}$. This parameter is noted σ_J^* and is calculated by:

$$\sigma_J^*(t) = \frac{1}{\bar{j}} \sqrt{\frac{1}{20-1} \sum_{k=1}^{20} |j_k(t) - \bar{j}|^2} \quad [\%] \quad (5.3)$$

Using the local currents distribution in charge, the two criteria described above are depicted in Fig. 5.20 for the two flow rates.

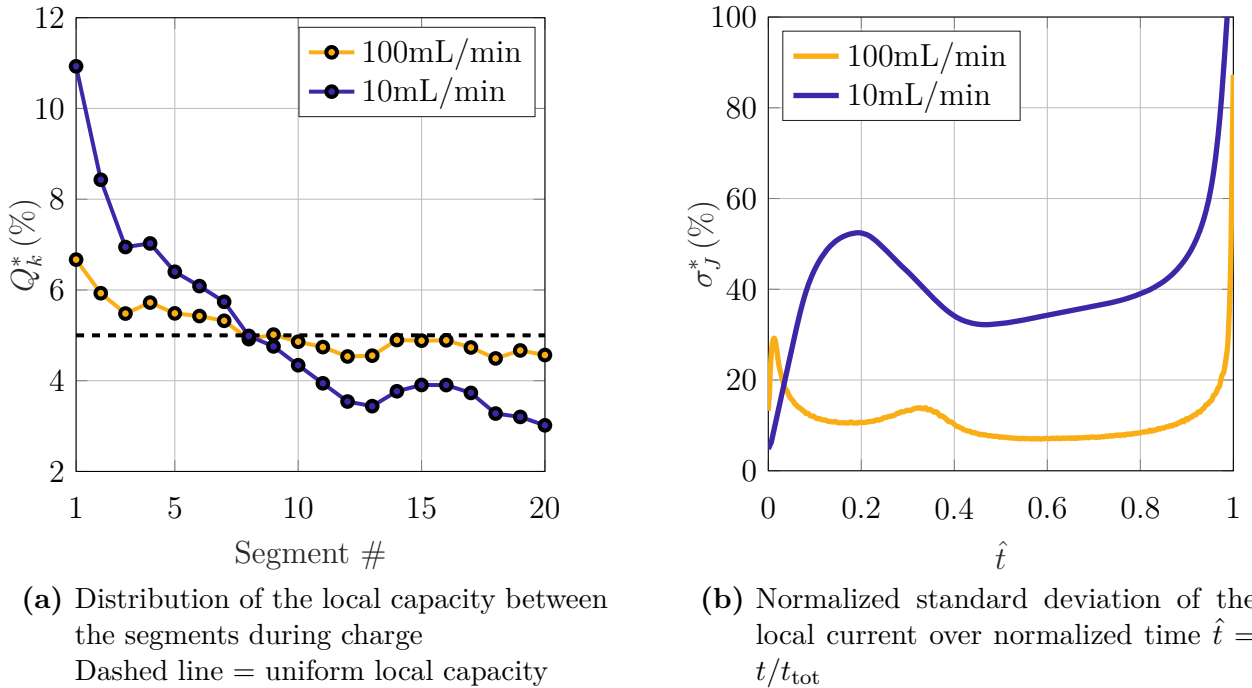


Figure 5.20: Impact of local current distribution on a charge of a flow battery: representation of the local capacity and the standard deviation. Comparison of two flow rates

The dashed line in Fig. 5.20a embodies the ideal case of uniform local capacity. The data points deviation from this level highlights the non-uniformity. At lowest flow rate, the first

segment delivered more than thrice as much capacity as the last one. The same occurred in discharge. It means that the cell is on average always overloaded at the inlet. It was not straightforward from the current profiles of Figs. 5.18 and 5.19 that the contrast over the entire stage would be of this range. A higher flow rate setting mitigates the effect. One can notice that the two profiles cross the average dashed line at the exact same position. Before # 7, the segments are always overloaded, whatever the flow rate.

In Fig. 5.20b, the time is normalized to the total time of the step to compare both conditions. In that case, the symbol \hat{t} is used. The local current distribution clearly varies over time. Two zones of important heterogeneity are drawn at start and end of the charge process. The similar inflection observed after $\hat{t} = 0.9$ for each plot suggests that the end of charge is associated with a huge internal distribution of current. The spike at the onset is brief at high flow rate and the standard deviation regains a low value for the rest of the charge. Low flow rate induces much more heterogeneity over the course of the step. The initial spike lasts over an extended period, after which σ_j^* stays high. The discharge phase presents comparable behaviors and will be scrutinized as well in the next sections.

From the first criterion Q_k^* , it would be concluded that the flow rate should just be raised to achieve more uniform distribution of current. On the other hand, σ_j^* evidences that the response over the course of the step is complex. The present illustration of the phenomenon is based on the comparison of two extreme cases. While the lowest flow rate seems very critical, the maximum value still features uneven distribution. Moreover, this flow rate is unrealistic in comparison to the typical operating conditions expected for large RFB systems. Finally, the use of a high pump power would impact negatively on the overall efficiency of the system, as the effective power output is the difference between battery stack power and the pump power.

This first part exemplifies the heterogeneity of local currents within the cell and evidences its dependency on flow rate and more generally on the working conditions. It becomes clear that a wrong handling of battery operation will affect its performance and lifetime, but at the same time that the optimization process is intricate and depends on numerous aspects.

An industrial perspective

As it yields high local current density, internal heterogeneity in operation will inevitably alter the battery efficiency and robustness. Considering the long operational life the system is designed for, it is preferable that all the parts sustain equivalent loads, to age at a similar pace. Uneven stresses can trigger the local deterioration of one or several components. In a stack configuration, the consequences can be dramatic: for instance, the membrane failure would eventually lead to the mixing of the total volume of the two electrolytes. Moreover, it is impossible to diagnose a local breakdown before it impacts the full system. It would require the monitoring of all the stacks and cells, which adds to capital cost.

b) Design of Experiment (DOE)

The present section describes the strategy developed to investigate the impact of several factors on the global performance and internal homogeneity of the cell during operation. The design of experiment (DOE) endeavors to decouple the influence of each parameter of interest.

First of all, a reference operating point of cycling was chosen to be compared with any

other set of parameters. It corresponds to the settings used in the first part of this chapter (subsection 5.1.2) and is referred to as standard conditions SC. The following values define it:

- Current, $I = 1.68 \text{ A}$; Current Density, $J = 40 \text{ mA cm}^{-2}$
- Flow Rate, $\dot{q} = 100 \text{ mL min}^{-1}$
- Temperature, $T = 25 \text{ }^{\circ}\text{C}$

The goal of the parameter study is to assess the individual impact of I , \dot{q} and T on the current heterogeneity observed along the length of the segmented cell. For this purpose, the DOE presented in Table 5.1 was executed on a single segmented set-up, so that the results are as comparable as possible. The parameters were scanned over a range of typical operating conditions.

Table 5.1: Design of experiment for the parameter study of I , \dot{q} and T

| Test number and description | Fixed parameters | Scanned parameter range |
|-----------------------------|---|--|
| 1: varying current density | $\dot{q} = 10, 50 \text{ or } 100 \text{ mL min}^{-1}$ $T = 25 \text{ }^{\circ}\text{C}$ | $J \in [10 : 150 \text{ mA cm}^{-2}]$ with $\Delta J = 20 \text{ mA cm}^{-2}$ |
| 2: varying flow rate | $J = 40 \text{ mA cm}^{-2}$ $T = 25 \text{ }^{\circ}\text{C}$ | $\dot{q} \in [10 : 100 \text{ mL min}^{-1}]$ with $\Delta \dot{q} = 10 \text{ mL min}^{-1}$ |
| 3: varying temperature | $J = 40 \text{ mA cm}^{-2}$ $\dot{q} = 100 \text{ mL min}^{-1}$ | $T \text{ (}^{\circ}\text{C)} \in [10, 20, 25, 30, 35, 40]$ |

Before performing the parameter study, the cell was run for 50 cycles to stabilize it. Thereafter, polarization curves at all flow rates and 3 SOC (20, 50 and 80 %) were plotted, with 2 full SC cycles (charge+discharge) between each PC to reset the battery. The cell was set at the desired percent of SOC by assuming that the total capacity achieved in the preceding SC cycle corresponded to SOC 100. The PC record protocol is described in subsection 2.2.3.

The next stage of the DOE focused on the cycling ability for all the duty points. 10 cycles were executed at each set of parameters. Due to the aging highlighted earlier (subsection 5.1.2) and since all the tests were performed on the same cell, following the performances in standard conditions was essential. Therefore, 4 cycles in SC were inserted between each operating value tested to get a baseline over cycling. For ease of interpretation, it was chosen to run symmetric cycles in all cases, that being with the same charging and discharging conditions. All the cycling performances, given by the capacity and the energy along with the efficiencies (coulombic, voltage and energy), stabilized after 3 cycles at a given operating point. The performances of the 10th cycle for each setting are presented in the next sections.

c) Reference capacity and apparent SOC

For the specific study of a parameter, the value of the range tested that gives the most accessible capacity is considered as the reference. The most favorable conditions are, as one can expect, the lowest current, or the highest flow rate, or the highest temperature. The maximum capacity achieved for a given parameter study is used to define SOC 100. It is

termed Q_{max}^{ref} , while the capacity reached in less favorable conditions is called Q_{tot} . As an example, for the two tests compared in Fig. 5.18, the reference capacity for the flow rate study is the one accessed with $\dot{q} = 100 \text{ mL min}^{-1}$, that is $Q_{max}^{ref} = 637 \text{ mA h}^{-1}$; it characterizes SOC 100. At $\dot{q} = 10 \text{ mL min}^{-1}$, the achieved capacity is $Q_{tot} = 252 \text{ mA h}^{-1}$. The low flow rate only gives access to 40 % of Q_{max}^{ref} . Then at the end of charge it is considered that the battery is at SOC 40. As a consequence, the 10 cycles at $\dot{q} = 10 \text{ mL min}^{-1}$ run the battery between SOC 0 and 40; this range is called the *apparent* SOC.

However, this is not completely correct when observing the performance of the first cycle at a new operating point. The first discharge actually stops earlier than the charge. In the example, the SOC at the end of a cycle is consequently 20 % at 10 mL min^{-1} . The battery is run between SOC 20 and 60 at this \dot{q} ; this is the *actual* SOC range. Nevertheless this shift at the end of discharge will be ignored for simplicity, which is not detrimental for the qualitative comparison conducted.

In the next parts, the σ_j^* curves obtained for different conditions will be represented as a function of *apparent* SOC, which is immediate in charge. In discharge, the curves need to be shifted by the SOC reached at the end of charge (SOC 40 in the example), for a convenient comparison. Curves of the next section are obtained by this method (Figs. 5.24 and 5.25). The definition of SOC in the parameter study is arbitrary and depends on the state of life of the battery and on the range of values tested. As a consequence, the usable capacity will not be the same for the current density than for the flow rate study, nor the temperature study. This protocol simplifies the representation of the results and allows their qualitative comparison.

An industrial perspective

It was decided to focus on the variables I , \dot{q} and T because they are key in the real application. Indeed, a RFB connected to the grid will undergo continual power load fluctuations during its cycle life since it is assigned to absorb the intermittency caused by renewable sources. Hence studying the current impact is worthwhile. The flow rate is another influential factor for the power output of the battery that depends on the pump consumption. The optimization of this variable must start with appreciating its effect on the internal operation of the battery. Finally, RFBs might be allocated to remote areas and are expected to be operational at all times regardless of the environmental conditions. That is why the temperature study is interesting to give a prediction of the system resiliency.

A well-designed experiment allows to distinguish between the influence of the operating factors. The subsequent sections compile the results related to each parameter of interest J , \dot{q} and T , with special effort to compare information obtained by the characterization methods and during cycling.

5.2.2. Current density

As illustrated in the design of experiment, the current density was scanned over a wide range of values: $J \text{ (mA cm}^{-2}\text{)} \in [10, 30, 50, 70, 90, 110, 130, 150]$. Only the results with a flow rate of 100 mL min^{-1} are presented hereafter, but the two other sets of data (at 10 and 50 mL min^{-1}) will be used at the end of the chapter in section 5.3. All the tests were performed at constant current input. Although it is not representative of the real battery operation in a grid, it gives

an interesting insight of the effect of power on the system behavior. This impact is regarded for the full cell in the first place. Then the internal heterogeneity of the cell is analyzed.

a) Global effect

The voltage charge and discharge curves at several currents are compared in Fig. 5.21. It clearly shows that changing the current density only shifts the voltage curves up or down. The curves are approximately regularly spaced, which confirms the resistive behavior of the battery. The stop in charge is dictated by the voltage cut-off at 1.5 V: if there was no risk of starting undesired second reactions at high voltage, it would be logical to expand the voltage limits accordingly to the operating current. Cycling at higher current density with maintained voltage boundaries shortens the accessed capacity.

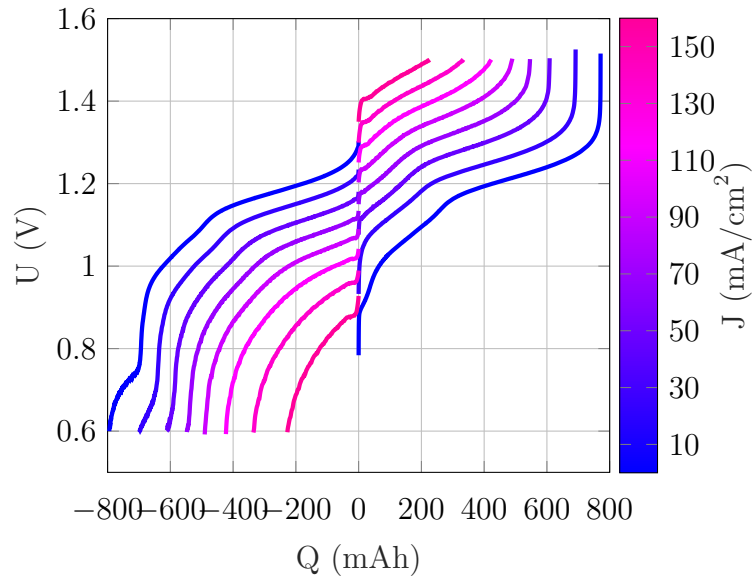


Figure 5.21: Voltage charge and discharge curves as a function of the capacity for all the currents tested, $\dot{q} = 100 \text{ mL min}^{-1}$ and $T = 25^\circ\text{C}$

Fig. 5.22a depicts the total capacity and energy (defined in subsection 2.2.2) in charge and discharge as a function of operating current.

The energy of the cell declines with current intensity. This is justified in the work of Rudolph and coworkers [208] by the squared-dependence of energy on J , as illustrated by their simplified equations:

$$W = JU_{avg} t_{tot} \quad (5.4)$$

$$\text{with } U_{avg} = V_{OC} \pm JR_{cell} \quad (5.5)$$

U_{avg} is the average voltage during the charge/discharge phase, and R_{cell} embodies the equivalent cell resistance which can be estimated by PC or EIS characterizations. The open circuit voltage V_{OC} is SOC-dependent, but is usually taken at SOC 50 for simplification. The energy in charge and in discharge can be seen as the sum of the ideal energy W_{id} (if $R_{cell} = 0$) and the ohmic

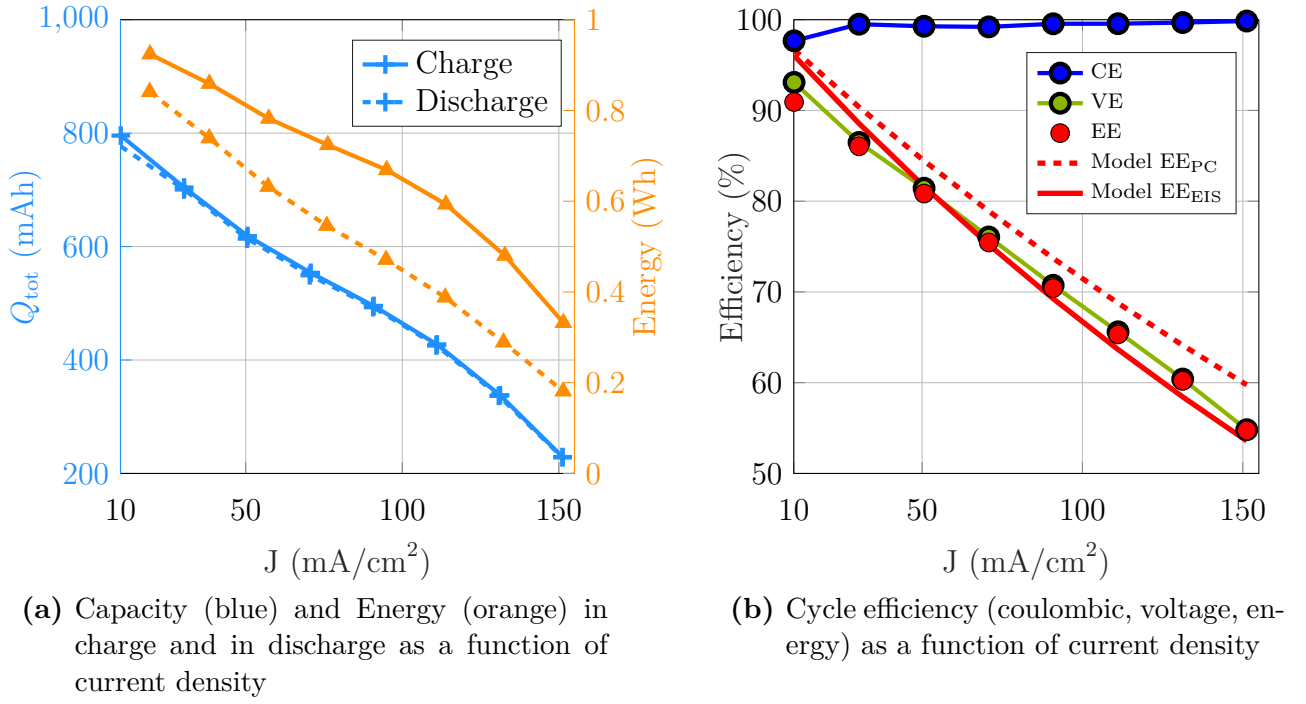


Figure 5.22: Global impact of the total current density on cycling performance

losses ΔW , as:

$$\begin{aligned} W_{ch} &= W_{id} + \Delta W_{ch} \\ &= [V_{OC}J + J^2 R_{cell}] t_{tot} \end{aligned} \quad (5.6)$$

$$\text{and } W_{dis} = [V_{OC}J - J^2 R_{cell}] t_{tot} \quad (5.7)$$

Fig. 5.22b provides a complementary representation by giving the cycling efficiency, in terms of coulombic (CE), voltage (VE) and energy (EE) (defined in subsection 2.2.2). The energy efficiency, represented by the red dots, is very linear with J . The coulombic efficiency looks improved at very high current although it is already satisfactory from 30 mA cm⁻². This is usually substantiated by a shorter cyclic time, thus limiting the active material cross-over and ensuing inefficiency [203]. It is noteworthy that the active molecules used in this work being negatively charged, their permeation through the cation-exchange membrane is minimal (subsection 3.3.2) compared to vanadium cations [209]. This leads to enhanced coulombic efficiency of 99.3% at a typical current density of 60 mA cm⁻², against 90-95% for the vanadium technology with cationic membranes [203]. The CE can be improved to 98% for VFB when using an anion-exchange membrane [210]. On the other hand, the alkaline RFB under study is more resistive than the classic VFB, which implies inferior VE. Overall, one effect balances the other and the global energy efficiency is close to 80% for both technologies (the flow rate is however higher in the vanadium study) [203].

The major contribution to energy efficiency decay is the voltage efficiency loss. It is substantial since the ohmic drop due to high current counts twice, both in charge and in discharge. EE is reduced by almost 40% between the minimum and maximum operating current. On the basis of Eqs. (5.6) and (5.7) and if t_{tot} is considered equal in charge and discharge, which is

consistent with the very high coulombic efficiency, the energy efficiency can be written as:

$$EE = 1 - \frac{2}{1 + \frac{V_{OC}}{JR_{cell}}} \quad (5.8)$$

The formula (5.8) is used to estimate EE, with $V_{OC} = 1.2\text{ V}$ determined during rest at half-charge and R_{cell} estimated either from:

- ➔ the polarization curve, $R_{PC} = 2\ \Omega\text{ cm}^2$ after 300 cycles with the segmented cell (Fig. 5.5)
- ➔ the EIS at low frequency, $R_{LF} = 2.4\ \Omega\text{ cm}^2$ after 300 cycles (Fig. 5.15)

The simulated EE, called EE_{PC} or EE_{EIS} depending on the resistance estimate used, are visible in Fig. 5.22b in red solid or dashed lines. The model accuracy is substantially enhanced when using the resistance estimate from EIS at low frequency. This suggests that this characterization procedure is more meaningful than the PC curve, which does not encompass all the losses during cell operation.

Chen et al. used a similar equation to describe EE in a quinone-bromide flow battery [70]. They estimated the cell resistance from the polarization curve recorded at half-charge, and obtained a satisfactory model accuracy.

The global cell response for various current densities must be correlated to local effects scrutinized below.

b) Local effect

The internal cell operation can be represented by means of the local capacity percentage Q_k^* on one hand and the standard deviation of local currents σ_J^* (5.3) on the other hand, as introduced earlier (subsection 5.2.1).

Fig. 5.23 depicts the capacity of each segment as a ratio of the total cell capacity Q_{tot} versus cycling current density, in charge and in discharge. In charge, the capacity distribution is more disparate at very low J but stabilizes above 50 mA cm^{-2} . The capacity of the first two segments stand out at 6 and 7 %, while the others lie between 4.5 and 5.5 %. The heterogeneity is slightly larger in discharge, where a minimum appears around 100 mA cm^{-2} .

This observation on capacity is actually a direct consequence of the heterogeneity of the local currents. The corresponding standard deviations are given versus the SOC for all currents in Figs. 5.24 and 5.25. The *apparent* SOC was calculated relatively to Q_{max}^{ref} achieved at lowest current (as described in subsection 5.2.1).

The detailed evolution of $\sigma_J^*(t)$ is complex. At the start and end of charge, two areas of high heterogeneity are emphasized.

- ➔ Fig. 5.24b zooms in on the onset of charge. An early spike is conspicuous at low J but is almost absent above 70 mA cm^{-2} . Moreover, the appearance of a second distinct spike only at 10 mA cm^{-2} is certainly correlated to a subsidiary reaction in the anolyte, as predicated in subsection 5.1.2. At lowest J , the signature of an early reaction is detected on σ_J^* but also on the voltage curve (Fig. 5.21) that exhibits a slim wave at the very start of charge, invisible at other values of J .
- ➔ During the rest of the stage, the standard deviations remain below 20 %. For $J \leq 90\text{ mA cm}^{-2}$ the end of charge is accompanied with a vertical rise of σ_J^* ; this is remi-

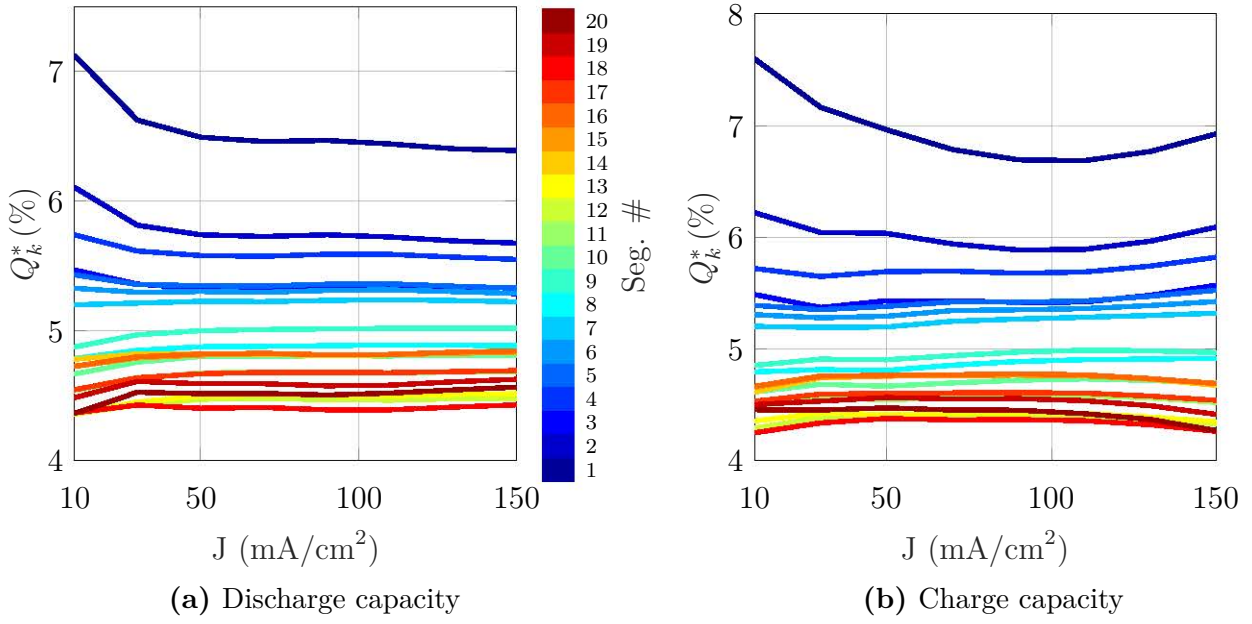


Figure 5.23: Local capacity (percentage of Q_{tot}) versus cycling current density, for all segments

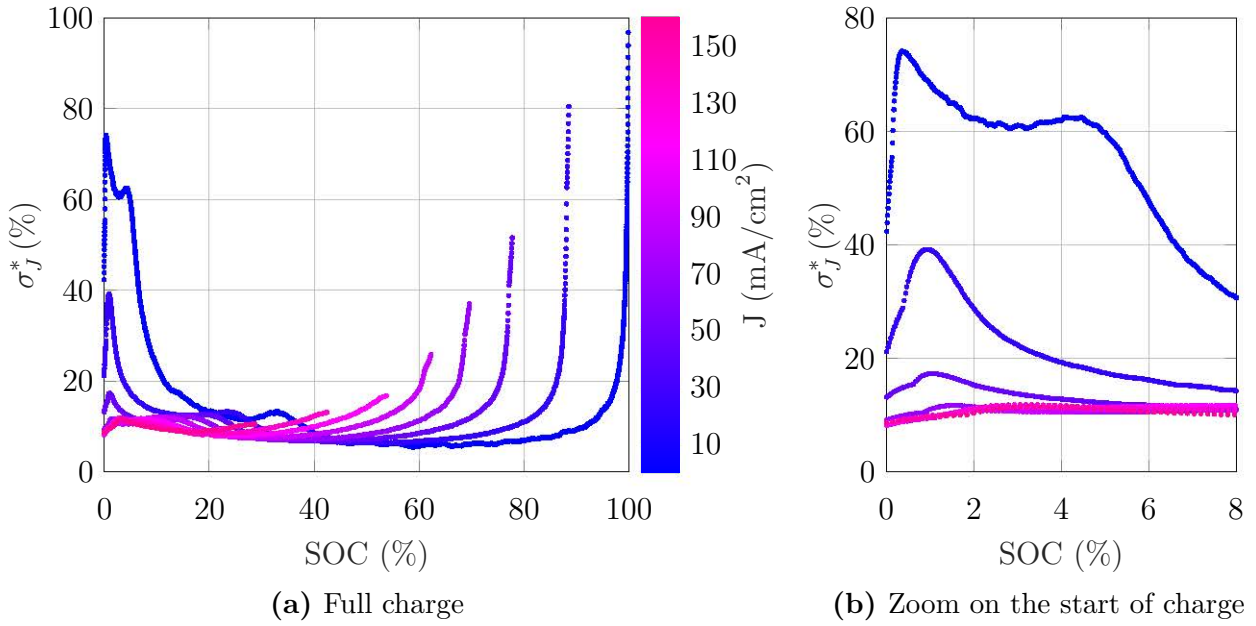


Figure 5.24: Variation of σ_J^* versus SOC during charge, for all cycling current densities tested

niscient of the voltage curve whose inflection at the end is only noticeable for the low currents (Fig. 5.21). σ_J^* increase is this time correlated to a reactant depletion, which is not attained at high current since the voltage cut-off prevented it.

In discharge, the representation versus the *apparent* SOC (defined in subsection 5.2.1) looks adequate since all curves follow the same trend (Fig. 5.25). The arrow illustrates the curve evolution with time of discharge.

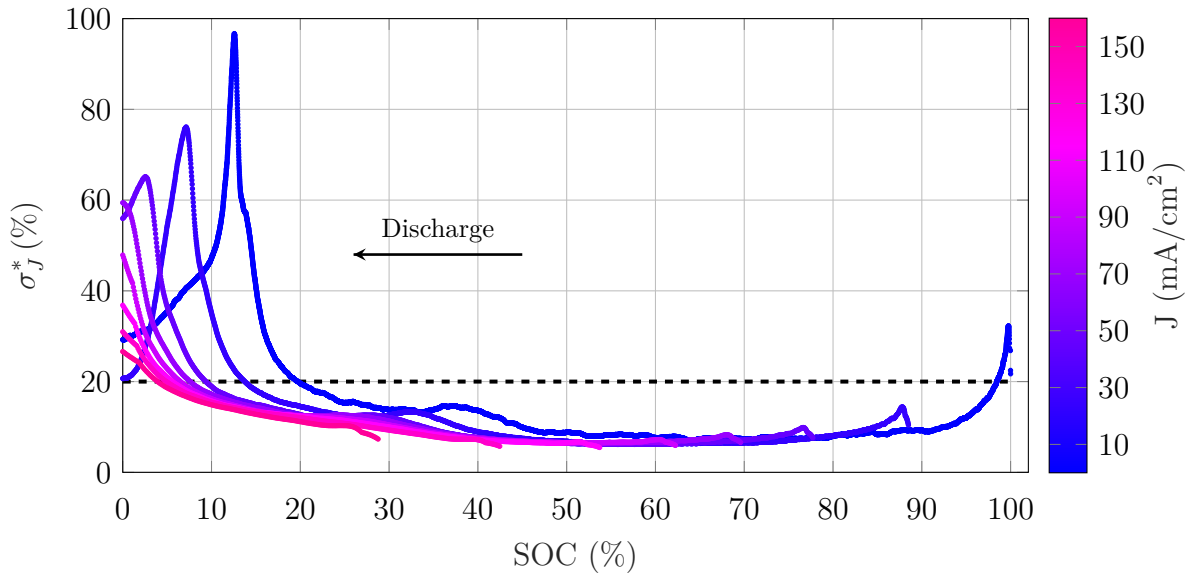


Figure 5.25: Variation of σ_j^* versus SOC during discharge (taking into account the SOC_{tot} at the end of charge), for all cycling current densities tested. The dashed line illustrates the deviation threshold used later to construct an operational map in [section 5.3](#)

- For the three lowest current inputs, a small spike is visible at the start of discharge (right hand of the curve), similar to the occurrence in the respective charge curves (Fig. 5.24b).
- The end of discharge at higher currents outlines a rise of the deviation whose ending value is lower at high J . For $J \leq 50 \text{ mA cm}^{-2}$, this rise is followed by a peculiar reduction of σ_j^* for the last percent of discharge (e.g. between SOC 12 and 0 at 10 mA cm^{-2}). Once again this singularity relates to the anolyte subsidiary reaction that provoked the double spike in charge at lowest J ; this substantiates that this reaction is reversible. The corresponding voltage curves feature the *low potential plateau* in discharge (Fig. 5.21).

As discussed in subsection 5.2.1, the *apparent* SOC in Figs. 5.24 and 5.25 was defined arbitrarily. If plotting σ_j^* against the *actual* SOC (e.g. between SOC 15 and 50 at 150 mA cm^{-2}), the major part of the curves would overlay, independently on the current. This shows that the standard deviation of j_k is predominantly a function of the concentration ratio between oxidizing and reducing species. Some irregularities however appear at start of charge and discharge, and are correlated to the secondary reaction in the anolyte side.

To summarize the current input study, the equivalent cell resistance R_{cell} changes with the current applied: low current generates high resistive response. It also increases with SOC due to the evolution of the concentration ratio. The average of R_{cell} over a full cycle allows the prediction the energy efficiency of the cell versus the current input. The efficiency decreases with J , because of square dependence of the energy losses on current.

Charge and discharge lead to dissimilar behavior; the resistance is always lower in discharge, which implies a generally higher local capacity distribution. Over a full step, the homogeneity is illustrated by the distribution of local capacities Q_k^* . The value generating

the most homogeneous operation is 100 mA cm^{-2} in discharge, while in charge the homogeneity is the same from 50 mA cm^{-2} . Yet the difference between each J input remains small. On the other hand, the instantaneous current heterogeneity represented by σ_J^* varies significantly with the total current. At the start of charge, the highest σ_J^* spikes correspond to lowest currents (for which highest R_{cell} are measured). σ_J^* also depends on the SOC; that explains why at lowest J the spikes at the end of charge and end of discharge are highest: they are caused by a depletion of reactant, only reached when cycling over an extended range of SOC, that is to say at low current.

It stems from these results that accessing the most capacity in the battery inevitably causes temporary heterogeneity. It can be curbed by setting a high current, which in turn involves ohmic losses and thus lower available capacity. In that respect accessing all the capacity while maintaining internal homogeneity is incompatible.

An industrial perspective

In practical applications, the grid dictates the power output requirement: the battery management system continuously adapts the current to the stack voltage to comply with the needs of the grid. This implies a variation of current input instead of ideal constant current cycling as in the experiments. The constraints are strict in discharge, and the battery must deliver the power needed by the external load. Conversely, the power used to charge the battery can be regulated to ensure the smoothest and most effective method of charging. This adjustment is particularly necessary at the start of charge, where lowest currents induce high local heterogeneity. At high SOC, the lowest current should be applied to access the most capacity, but it will be at the expense of local homogeneity. In the middle of charge, the current value does not alter the local operation; high J charging is desirable to shorten the duration and in the meantime the pumping power losses.

5.2.3. Flow rate

A similar parameter study was conducted with flow rate varying in the following range: 10, 20, 30, 40, 50, 60, 70, 80, 90, 100 mL min^{-1} . Temperature and current density were set to their standard value. The flow rate was maintained constant in charge and discharge. The impact of \dot{q} on the cell performance metrics and on its internal heterogeneity is scrutinized in the ensuing discussion.

a) Global effect

The cell voltage versus capacity curves are plotted in Fig. 5.26a. Their modification relative to flow rate is completely different than with current density in Fig. 5.21. The voltage plots keep essentially the same shape for any \dot{q} , only their duration are modified accordingly. When normalized in time (Fig. 5.26b), the voltage profiles are closely superimposed, except at lowest flow rate. It means that the limiting processes are independent on \dot{q} , their occurrence is just delayed with enhanced transport of species. It is rationalized by the concentration overpotential included in the cell voltage (1.17): this term rises faster during operation at reduced flow rate, thus limiting the time of charge/discharge phase.

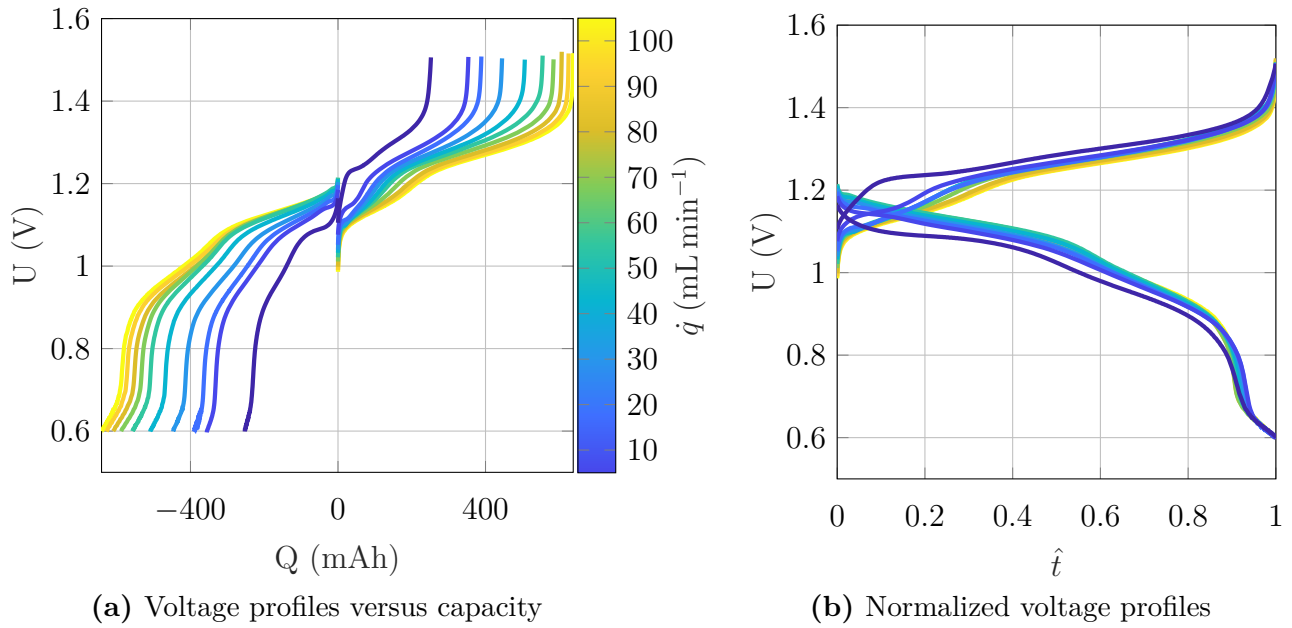


Figure 5.26: Voltage charge and discharge curves for all the flow rates tested, $J = 40 \text{ mA cm}^{-2}$ and $T = 25^\circ\text{C}$

Consequently the capacity accessed decreases with lower electrolyte flow rate. It is more explicitly represented in Fig. 5.27a. The capacity and the accessed energy increase with flow rate. According to the model of Chen et al. [211], it is explained by the competition between mass transport and reaction kinetics limitation: as the flow rate increases, the concentration overpotential diminishes to become negligible compared to activation losses. At sufficiently high supply of active species, the performances reach a plateau only determined by the rate of reactions. The experimental curves of Fig. 5.27a confirm a similar trend: both capacity and energy tend towards a limit that would be reached at flow rates higher than the experimental limit of 100 mL min^{-1} .

The cell efficiency versus flow rate is summarized in Fig. 5.27b. The coulombic efficiency does not show an evident variation pattern but remains constant around 99 %. Therefore the energy efficiency is only a function of voltage efficiency which lies above 80 % from 20 mL min^{-1} . After this value the benefit of flow increase is minimal in terms of efficiency. It implies that unlike the current density (Fig. 5.22) whose impact was paramount on both capacity and efficiency, the flow rate can only slightly ameliorate the accessed capacity. Furthermore, the energy efficiency calculated from (2.10) does not integrate the pump power consumption. Instead the system efficiency encompassing this aspect is heavily influenced by the flow rate input.

Ma et al. reported similar effect of electrolyte flow rate on a VFB stack [212]. The system capacity had a stronger dependence on supply of active material than its efficiency. At similar current density and equivalent flow rate (30 mL min^{-1}), their 15-cell stack displayed 81 % of energy efficiency (against 79.5 % in the present work). At higher current density, their experimental study showed that the flow rate had more impact and that it must be increased to keep an equivalent capacity and efficiency. Their results confirm that combining the variation of several parameters is requisite to comprehend the system performance over all possible working conditions. This will be addressed in section 5.3.

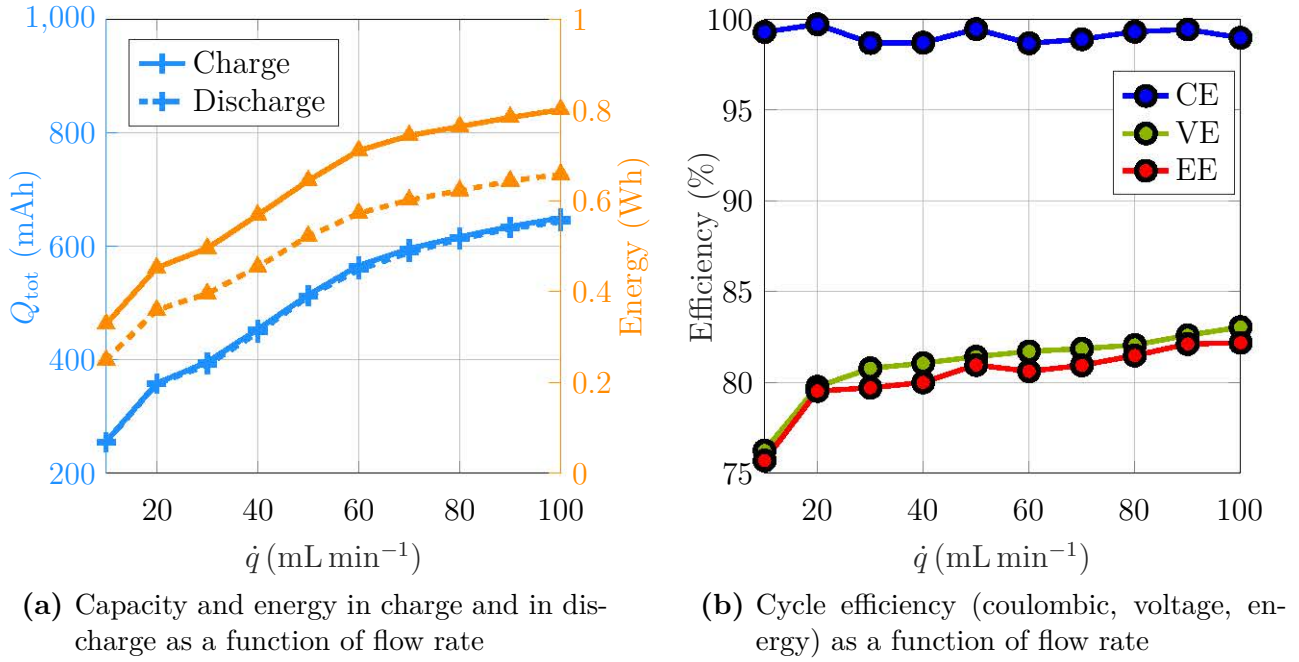


Figure 5.27: Global impact of the flow rate on cycling performance

b) Local effect

Alongside with global effects, the influence of flow rate is even more pronounced on internal homogeneity.

Fig. 5.28 proves that accessing more capacity (made possible at high \dot{q}) is compatible with improved homogeneity, which is opposite to the results with respect to current. Indeed, the slowest electrolyte flow induces a variation of local capacity between 3 and 11 % of the total capacity, while the distribution is confined between 4.5 and 6.5 % at highest flow input. By comparing the variation of local capacity in mAh, it comes that rising the electrolyte velocity from 10 to 100 mL min⁻¹ boosts the production of charges at the outer segments by 75 % (and only by 33 % at the first ones): the outlet is logically more sensitive to mass transport limitation.

The standard deviation of the local capacities, noted $\text{std}(Q^*)$ is plotted in Fig. 5.29. Flow rate has a conspicuous impact over the uniformity of the cell operation, whose average deviation can fall from 40 to 10 % in charge, and from 35 to 15 % in discharge. The influence of \dot{q} is slightly more pronounced in charge than in discharge, which means that the discharging step is more critical in terms of internal homogeneity.

Figs. 5.30 and 5.31 display the homogeneity of internal currents versus SOC in charge and discharge, for all the tested flow rates. The consequence of \dot{q} on instantaneous internal homogeneity is visible throughout the step, while for the current density study in Figs. 5.24 and 5.25, σ_j^* predominantly changed at start of charge and end of discharge. In charge, three parts can be distinguished:

- ➔ Before 2 % of charge, a first spike appears, whose magnitude and position is determined by the flow rate, as shown by the zoom in Fig. 5.30b: the faster the electrolyte flow, the earlier and higher the spike.

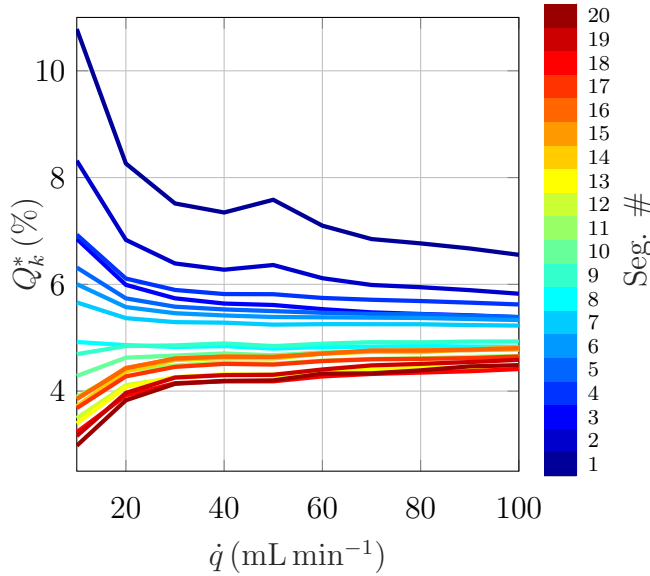


Figure 5.28: Local charge capacity (percentage of Q_{tot}) versus flow rate, for all segments

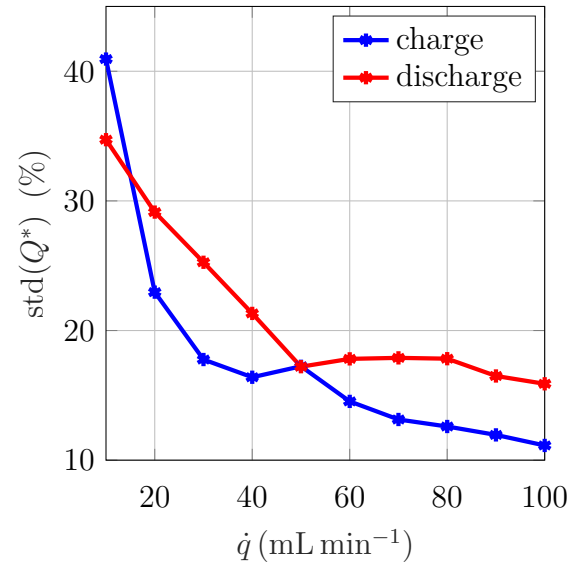


Figure 5.29: Standard deviation of the local capacities in charge and discharge as a function of flow rate

- ➔ After 2 % SOC, a second spike occurs between 10 and 30 % SOC (depending on \dot{q}). The magnitude of the second spike is this time inversely proportional to the flow rate. At 20 and then 10 mL min^{-1} , the two spikes end up merging into a conspicuous wave.
- ➔ After these initial disturbances, the internal distribution recovers homogeneity for a duration depending on \dot{q} . The end of charge matches with a rapid increase of σ_j^* up to 70-80 %.

In discharge (Fig. 5.31), all curves exhibit a humped shape at start which is larger and higher at decreased \dot{q} value. A second wave is visible later in discharge and precedes the inflection caused by mass transport limitation at the end of discharge. The last 10 % of discharge feature a new decrease of σ_j^* as already observed in the current study (Fig. 5.25). This attribute matches the *low potential plateau* of the voltage curves (Fig. 5.26a), induced by a subsidiary reaction in the anolyte side (subsection 5.1.2). This feature expands at higher flow rate, revealing that more species of this anolyte form can react thanks to a mitigated concentration overpotential.

The deviation profiles convey the idea that flow rate could be optimized during each phase while maintaining local current uniformity. The graphs will help to define a threshold where flow rate needs to be adjusted according to the SOC of the battery. The efficiency of such strategy will be assessed later in section 6.2.

From all the cycles at a given duty point arises a difficulty: the operating variables affect the internal homogeneity and in the meantime the SOC range on which the battery can be cycled. The uniformity also evolves with time according to SOC. It is thus challenging to decouple the respective influence of the parameters J or \dot{q} and the SOC on σ_j^* . To refine the study and map all working points, the operating factors should be modified once the SOC has been set to a certain value in standard conditions. It however necessitates rigorous and time-consuming experiments. Maintaining a constant SOC with varying settings is precisely the concept of Polarization Curve. The method of performing it was specially optimized to

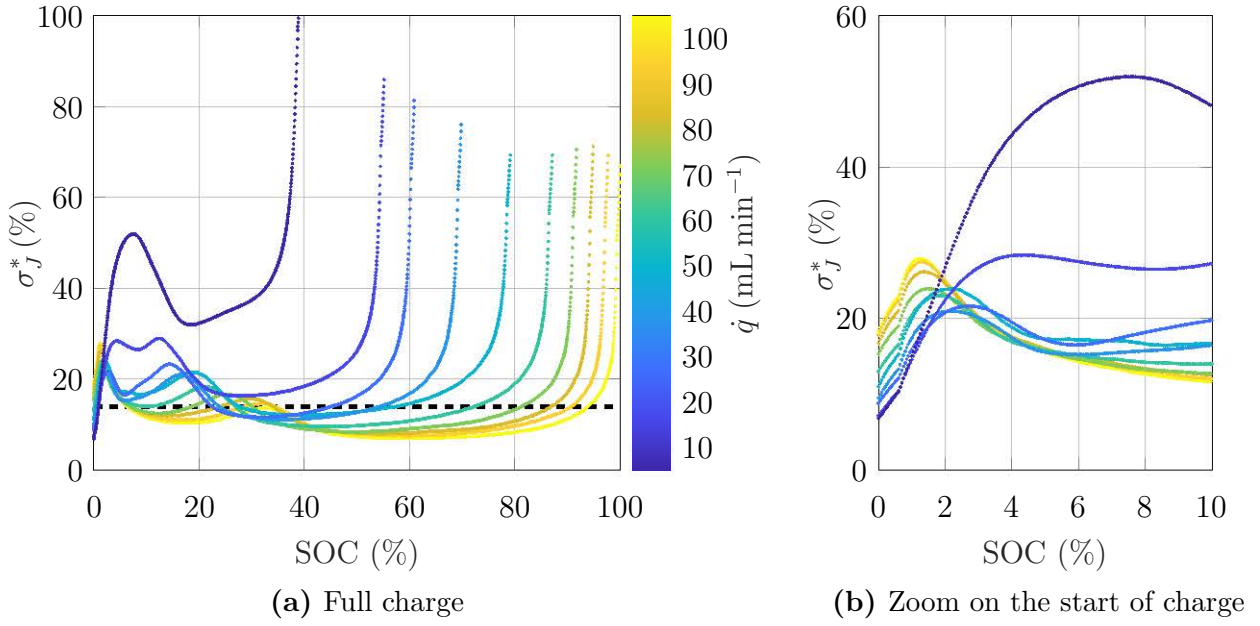


Figure 5.30: Variation of σ_J^* versus SOC during charge, for all flow rates tested. The dashed line in (a) illustrates the deviation threshold used later to construct an operational map in section 5.3

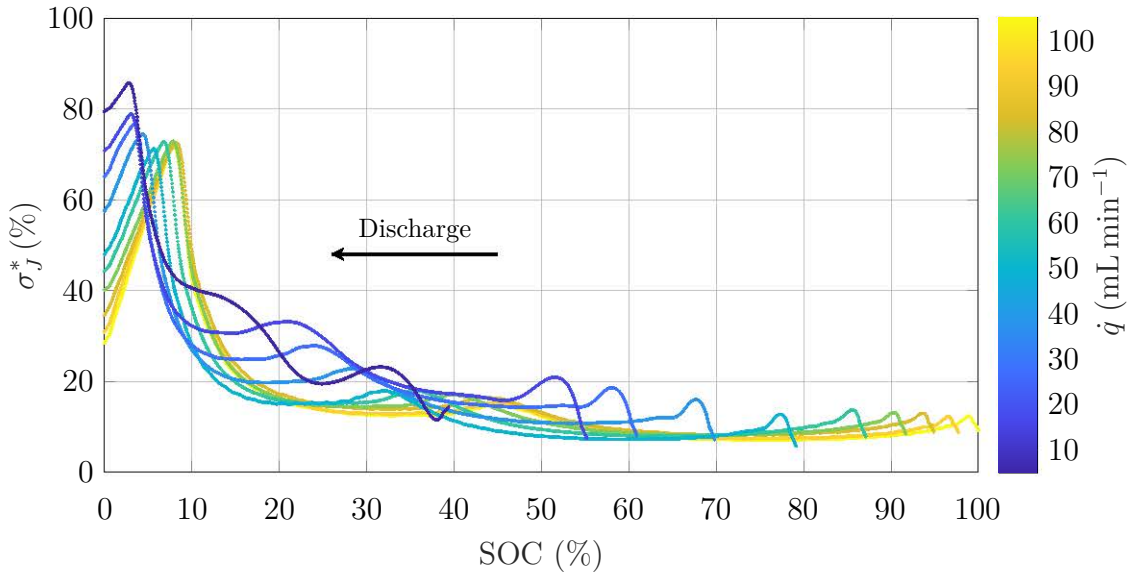


Figure 5.31: Variation of σ_J^* versus SOC during discharge (taking into account the SOC_{tot} at the end of charge), for all flow rates tested

obtain the most relevant characterization (subsection 2.2.3). Learnings provided by PC are illustrated in the next part.

c) PC curves

Polarization curves were performed at SOC 50 unless specified. The global PCs at all flow rates are given in appendix (Fig. 6.17), because they are analyzed only after the post-treatment described hereafter. The segmented set-up allows to record the local polarization of each segment. Fig. 5.32 shows the local PC of Seg.#1 (dashed lines) and #20 (solid lines) for all the flow rates tested. For simplification, the local polarization curve of one segment is noted PC#1 or PC#20.

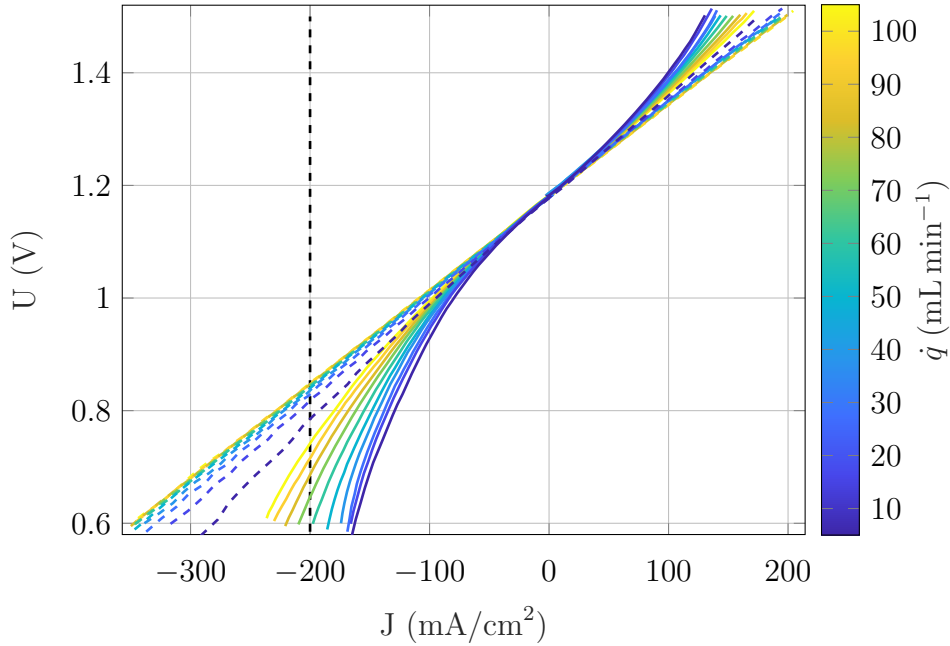


Figure 5.32: Local Polarization Curves of Seg.#1 (dashed lines) and #20 (solid lines) at SOC 50 for all flow rates tested

The inlet segment exhibits a linear characteristic at any flow rate, while the PCs of the last segment are not straight throughout the range of currents scanned. The PCs of the two segments overlap around $J = 0$, and within a narrow current window that depends on the flow rate. Indeed, the deviation of PC#20 from linearity starts from a lower current as the flow rate is decreased. Such a distortion towards increased currents derives from mass transfer limitation, as already explained in subsection 5.1.2. The reactant depletion emerges along the length of the cell, closer to the inlet as flow rate is reduced. This limitation is never observed at the first segment.

When examining the PCs between $[-200; 200 \text{ mA cm}^{-2}]$ to respect symmetry around the open-circuit point, the bows are more pronounced in discharge although they start at higher polarization. This signifies that mass transport becomes limiting later in discharge but compounds faster once started; this effect cannot be explained in a simple way. The modification of PC#20 by the flow rate is also most prominent in the discharge zone.

On the other hand, PCs#1 almost overlap at flow rates between 40 and 100 mL min^{-1} . Only the three lowest flow rates substantially modify the response of #1. To get a clearer view of PC#1 evolution with flow rate, a linear regression is executed within the reduced current window $[-200; 200 \text{ mA cm}^{-2}]$ to get the most accurate fit. Both charging and discharging parts

are fitted simultaneously since the curve is continuous through the two regions and gives the equivalent resistance of the segment noted $R_{PC\#1}$. The PCs#1 at SOC 20 and 80 were also fitted. Unless at SOC 20 and high discharging current, the curves of #1 feature a linear trend throughout the current range applied (as shown in appendix, Figs. 6.18 and 6.19). Fig. 5.33 compares the local resistance of #1 deduced from the fitted PC slope versus the flow rate, for the 3 SOC.

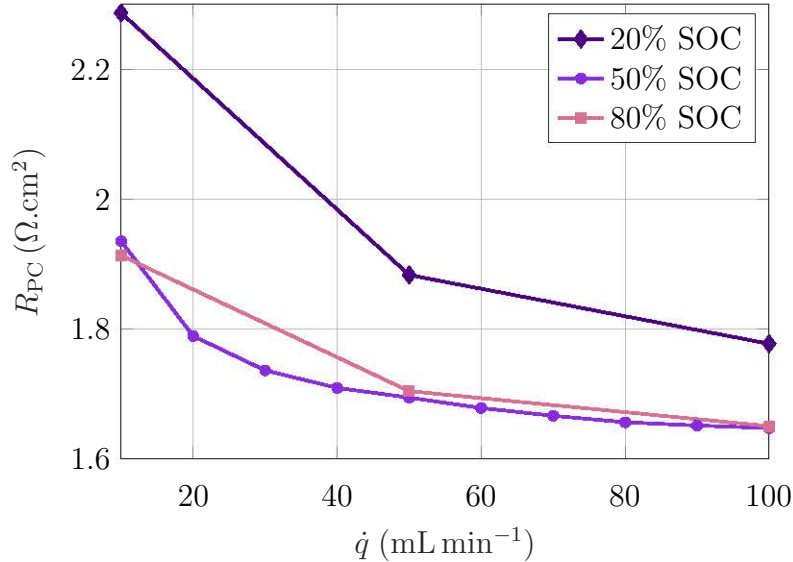


Figure 5.33: Resistance of #1 as a function of \dot{q} . Calculated from the slope of the fitted PCs#1 performed at SOC 20, 50 (Fig. 5.32) and 80.

All curves feature a decreasing trend with flow rate of approximately -15% , with a marked evolution between 10 and 30 mL min⁻¹. The resistance tends to a low limit at high flow rate, similarly to the capacity and energy that evolved towards a maximum (Fig. 5.27a). Even though PC#1 is visually linear whatever the flow rate, the segment resistance is still affected by mass transport. This might underline a phenomenon at pore scale that depends on the advection of the electrolyte. This could also be caused by a measurement error when there is a high current heterogeneity between the segments (which occurs at low flow rate). This would induce a potential gradient along the electrode and migration of charges towards other segments, instead of being collected where they have been produced.

The resistance values are lowest at SOC 50 but do not evolve much at SOC 80. Contrarily, the resistance is raised significantly at SOC 20: by 12% at the slowest electrolyte flow. At this SOC, the low reactant concentration increases the charge-transfer resistance R_{CT} , as already exemplified during the symmetric cell study Chap. 4. Additionally, this lack of reactant compounds the mass transport losses, which seems to have an effect on the PC slope as already mentioned.

The contrast between the resistances at SOC 20 and 80 can be justified by the difference of limiting electrolyte in charge and in discharge (as mentioned in subsection 5.1.2): the catholyte cuts the charge, while the discharging process is stopped by the anolyte. Therefore it can be inferred that the resistance increase by reactant depletion can be different. Moreover, the SOC is calculated from the capacity achieved in standard conditions: it represents an *apparent* SOC for the entire cell, and does not correspond to the *actual* SOC of each electrolyte. The state

imbalance between the two half-cells can also be dissimilar at SOC 20 and 80 which results in unequal resistance values.

The resistance from PCs#1 can be seen as the in-situ indicator of the kinetics and ohmic losses. It was chosen to build the *corrected global* PC by subtracting $JR_{PC\#1}$ to emphasize the mass transfer limitation at the cell level. Since $R_{PC\#1}$ is influenced by \dot{q} and tends towards a limit at high flow rate, the value at 100 mL min^{-1} ($1.65 \Omega \text{ cm}^2$) was used. These corrected global PCs at SOC 50 are compared in Fig. 5.34 for all the flow rate inputs.

This method is an alternative to the correction reported by peers [90, 213]. They use the high-frequency resistance R_{HF} measured by EIS before the polarization to correct the obtained curve. As such, only the ohmic drop is compensated but the kinetic losses remain.

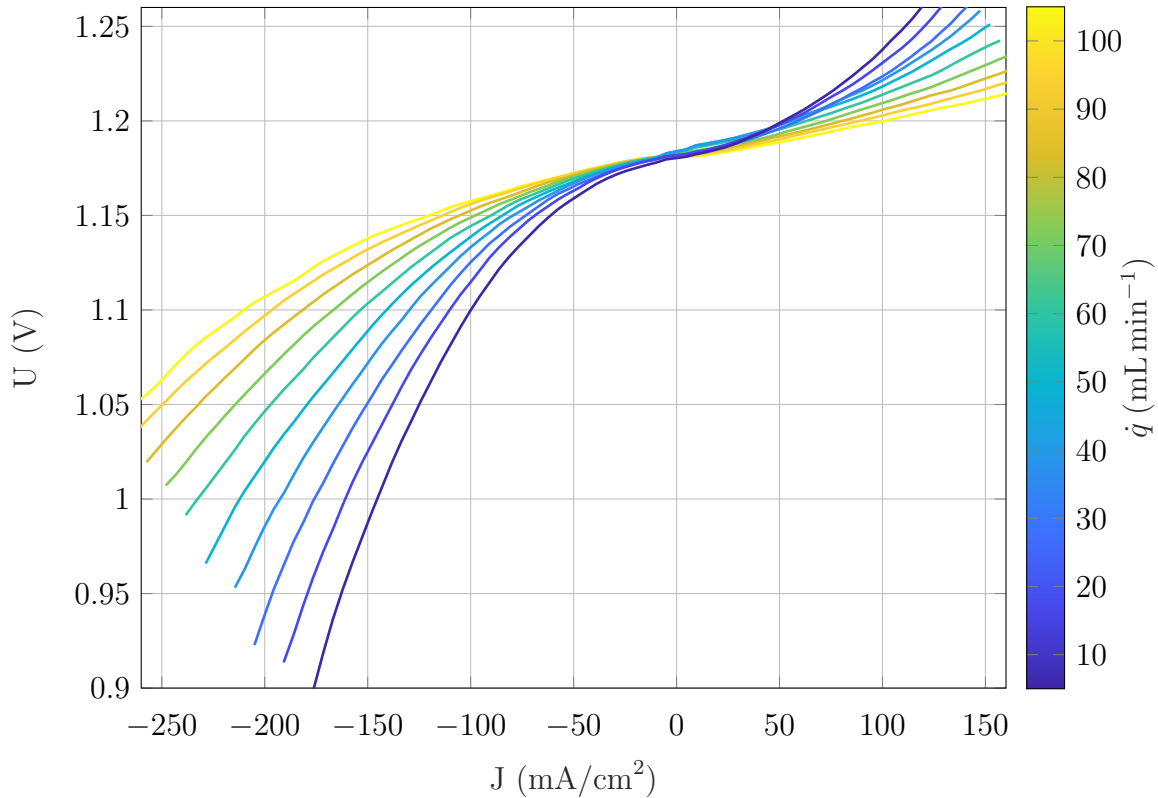


Figure 5.34: Global Polarization Curves corrected with $R_{PC\#1}(100 \text{ mL min}^{-1}) = 1.65 \Omega \text{ cm}^2$, for all flow rates tested

The figure clearly highlights the flow rate effect on the global battery response. It is observed that the mass transport alters the cell operation at almost any current input and the corrected PC curves are regularly distributed according to the flow rate. It means that there is virtually no operating point that prevents the starvation of the electrode outlet, even at highest electrolyte flow. At -100 mA cm^{-2} in Fig. 5.34, the voltage drop equals 80 mV at lowest flow rate and less than 30 mV at highest \dot{q} . Milshtein and coworkers evidenced the same trend by modelling and experiments [90].

In Fig. 5.34, the same current density in charge ($+100 \text{ mA cm}^{-2}$) induces an inferior voltage drop of 60 mV at lowest \dot{q} : this confirms that mass transport limitation is less intense in charge than in discharge.

Similarly to the cycling analysis, the local current distribution can be observed through

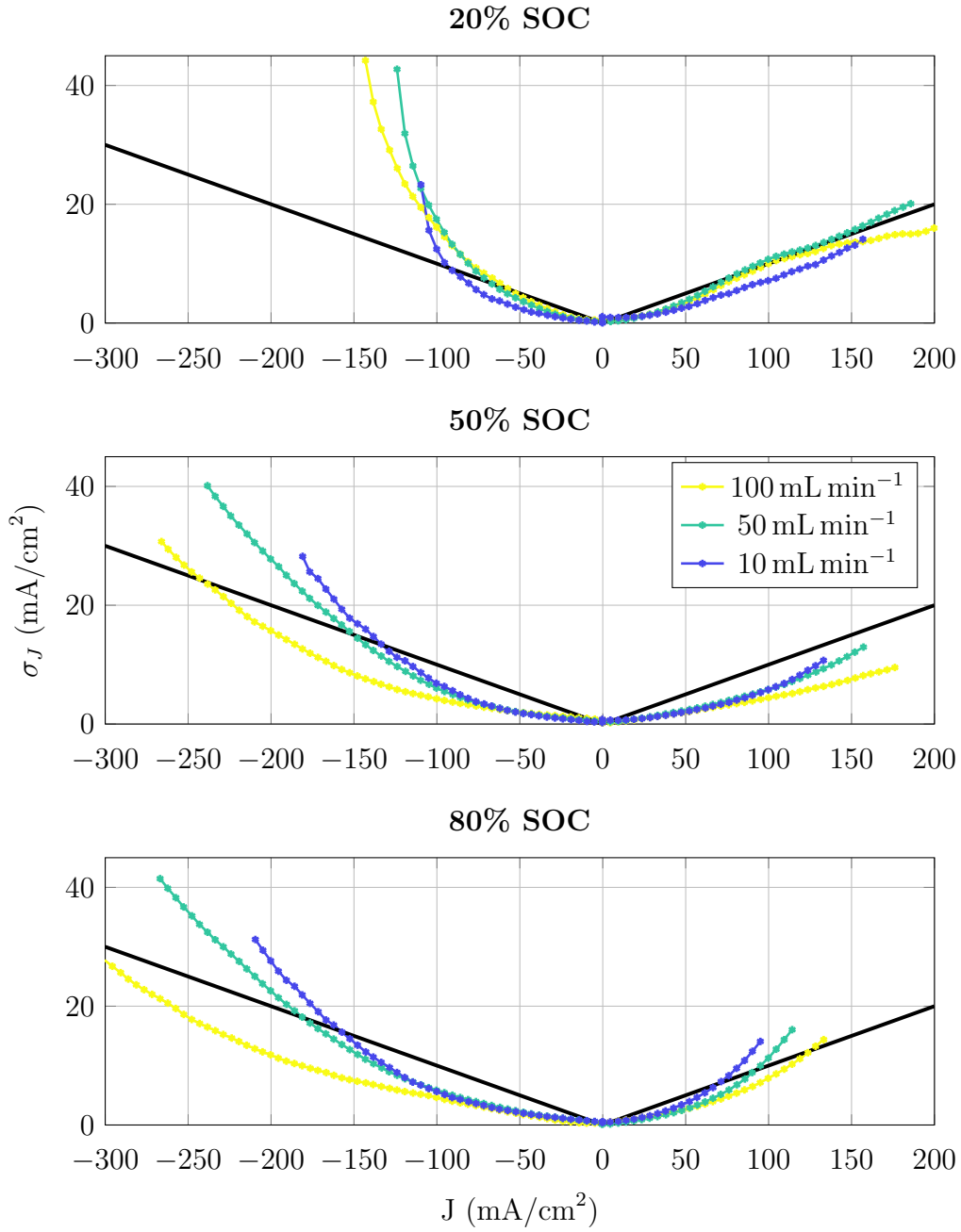


Figure 5.35: Variation of σ_J during Polarization Curves at the 3 flow rates: 10, 50 and 100 mL min⁻¹. Each subplot corresponds to a specific SOC (20, 50 and 80% from top to bottom). Black solid line represents the limit of $\sigma_J^* = 10\%$ of the applied current J .

their standard deviation σ_J during a PC. It is however chosen to represent standard deviation in mA cm⁻² rather than in % of the total J , because it would not be calculable around $J = 0$. Fig. 5.35 illustrates σ_J for global PCs at the three flow rates 10, 50 and 100 mL min⁻¹. The subplots correspond to the 3 SOC: 20, 50 and 80 %. The solid lines represent a local current deviation threshold of 10% of the total current density applied J : below this limit, the cell uniformity is deemed as correct.

At SOC 50 (central subplot), the curves feature a slightly more important deviation in

discharge than in charge, in particular at low \dot{q} . This confirms the findings from the PCs Figs. 5.32 and 5.34: discharge yields more mass transport limitation in comparison to charge. Additionally, σ_J exceeds the 10 % threshold much earlier at low flow rate. As already evidenced with the cycling analysis, the standard deviation of local current is directly linked to mass transport: the slowest advective flow, the more concentration gradient between the inlet and outlet segments and therefore the more internal current heterogeneity. Yet it should be noted that the standard deviation for the three flow rates match exactly within the current range of $[-60; 60]$ mA cm⁻². It is not the case of the three corrected-PC over the same current range in Fig. 5.34: at low flow rate the overpotential is already more important than at high \dot{q} . This demonstrates that the concentration overpotential observed in the PC does not automatically imply a critical heterogeneity within the cell.

The effect of SOC on σ_J is clearly visible. At SOC 20 (resp. at SOC 80), charge (resp. discharge) can be maintained with good uniformity for an extended range of currents, whereas discharge (resp. charge) entails a deviation above 10 % at low current density. The results at SOC 20 and 80 are not perfectly symmetrical: the two lowest flow rates drive the deviation above the threshold from respectively -150 and -180 mA cm⁻², while the highest advection keeps the uniformity acceptable even at -300 mA cm⁻². The dissimilarity between SOC 20 and 80 was already discussed from the values of $R_{PC\#1}$ in Fig. 5.33.

At SOC 20 in discharge, the influence of flow rate on σ_J is insignificant. The low concentration of reactant outweighs the impact of electrolyte flow by causing a rapid increase of σ_J around the same current J for all flow rates. The same phenomenon is visible to a lesser extent at SOC 80 in charge.

The polarization curves give complementary hints on the mechanisms ruling the cell operation. Mass transport limitation is visible on the outer segments, while #1 exhibits a linear PC at any flow rate. However, its equivalent resistance increases with low flow rate. This resistance is also compounded at low SOC. The resulting global PC of the cell heavily depends on \dot{q} : the advective mass transfer losses are influential at almost any current, even at fastest electrolyte flow.

The PCs also outline the unequal response in charge and discharge: discharge generates more serious mass transport limitation that convey higher overpotential at a given operating current.

The internal current standard deviation substantiates that mass transport limitation compounds the heterogeneity of the cell. At the end of charge or discharge, the flow rate can no longer mitigate this heterogeneity: the reactant starvation contributes to the heterogeneity of the internal currents. This trend was foreseen earlier in the cycling analysis, when comparing the evolution with time of voltage curves and standard deviation: a steep voltage variation is always accompanied by a sharp increase in heterogeneity.

5.2.4. Temperature

The third parameter of study is the temperature, thanks to the thermal control of the segmented device. A new temperature value was regulated three hours before starting the cycling, to make sure that the system had stabilized to the desired temperature. The range of values tested is: 10, 20, 25, 30, 35, 40 °C. The other parameters were kept to their standard value. It needs to be specified that the temperature study was performed on a new segmented

set-up with similar features for convenience. This explain the disparate results with the other parameter studies in terms of capacity, because the cell was not at the same state of aging. Moreover, the temperatures higher than 25 °C were tested before the cold conditions (20 and 10 °C) because there was fear of irreversible damage during cycling at low T. The cell actually showed high endurance at all temperatures.

a) Global effect

Fig. 5.36 displays the voltage curves versus capacity at all temperature values. One striking conclusion is the discrepancy between charge and discharge profiles: the charging curves are shifted upwards at lower T, while the discharge curves all overlap. Their only difference is the low voltage section close to the end of the stage. High temperatures enable the access to the *low potential plateau*, corresponding to a subsidiary reaction in the anolyte side (subsection 5.1.2). This capacity plateau actually modifies the SOC window cycled at several T. This is illustrated in Fig. 5.37 that gives the open circuit voltages V_{OC} before charge or discharge for each temperature tested.

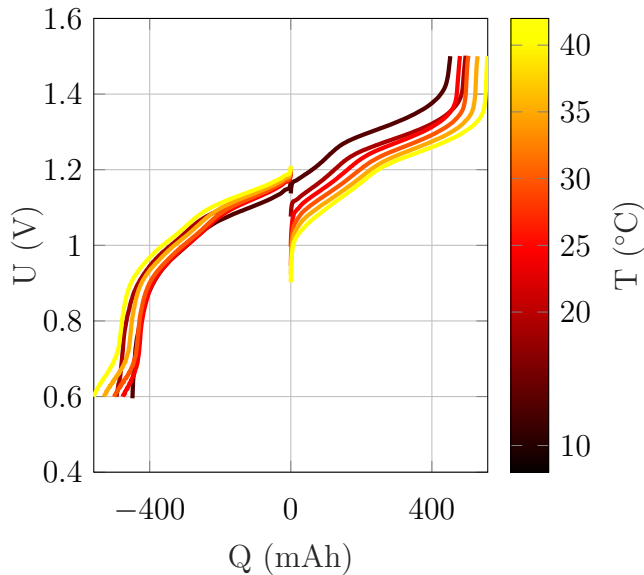


Figure 5.36: Voltage charge and discharge curves as a function of the capacity for the temperature values tested, $\dot{q} = 100 \text{ mL min}^{-1}$ and $J = 40 \text{ mA cm}^{-2}$

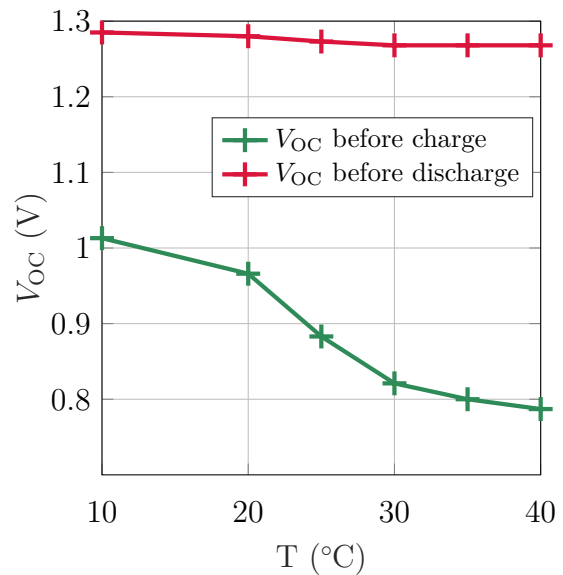


Figure 5.37: Open circuit voltage before charge and discharge for cycles at several temperatures

V_{OC} before charge decreases with T whereas it is maintained constant before discharge. This means that an elevated T runs the battery between SOC 0 and SOC 100 (or between $V_{OC} = 0.8$ and 1.27 V), while low T prevents complete discharge. At 10 °C, SOC varies between 20 and 100 % (the initial SOC=20 % is determined from the ratio of the capacities accessed at the two extreme temperatures).

In charge, the profiles distribution are related to the initial SOC that varies with the operating temperature. In discharge, voltage curves overlap since they all start from the same SOC.

The evidence that increased T gives access to the *low potential plateau* can be attributed to

several reasons. The activation effect of temperature is well-known in electrochemical systems: the reaction rates k_0 are boosted with heat according to the empirical Arrhenius law (1.9). The temperature dependence of the species transport across the membrane are also predicted with an Arrhenius model [214]. The diffusivity of the molecules in the solvent is proportional to T according to Stokes-Einstein's law (3.12). The transport of species is enhanced since the electronic, ionic and membrane conductivities are temperature-dependent. All these aspects contribute to the reduction of the cell resistance at higher temperature, which extends the capacity accessible within a predefined voltage window.

The cycling performance at several T is further highlighted in Fig. 5.38. Temperature ameliorates the capacity accessible along with the energy (Fig. 5.38a). The gain is however not as prominent as with the variation of current (Fig. 5.22a). In terms of efficiency (Fig. 5.38b), the coulombic performance CE diminishes at low T ; it could be partially ascribed to the absence of the low voltage plateau in discharge in the colder and more resistive cell. The overall gain in performance represents a regular increase of 5 % between 10 and 40 °C. The divergent point at 20 °C is due to the order of the temperature values tested. On the other hand, the cold conditions impaired only temporarily the performances and the capacity at standard temperature could be recovered after the study.

It was observed that an elevated temperature changed the water transfer direction between the two tanks; a thorough study with precise monitoring of the volumes should be conducted, to identify the parameters affecting the water transfer.

An industrial perspective

The boosted performances at 40 °C are valuable, because the real-size system operation is expected to maintain this approximate value of temperature (due to heating from the reactions and the pumps). Moreover, the losses at low T being reversible once the cell returns to SC, it signifies the ability of the system to be left idle for an extended period, before being seamlessly turned back on from a low temperature.

Nonetheless, temperature can have downsides on the battery performance. The active material concentration depends on the temperature of the solution. For example in a VFB, vanadium ions used in the anolyte (oxidation states +II and +III) precipitate when the temperature drops, while the precipitation of the vanadium in the catholyte (oxidation state +V) occurs at elevated temperature. Further, the transport of all species is promoted with T , including water and potentially active material through the membrane. If the flow of water is predominant on one direction, one half-cell is being concentrated by the loss of solute. The combination of these mechanisms can cause precipitation of active species, which contributes to capacity decay and possible blocking of the electrolyte channels. No deterioration was observed during the temperature investigation; complications could arise at temperatures higher than 40 °C, or for a longer cycling. Finally, the system was aged before performing the temperature study. The consequences could be detrimental if the first cycles of a new system were launched directly at low temperature. These concerns should be addressed in further studies.

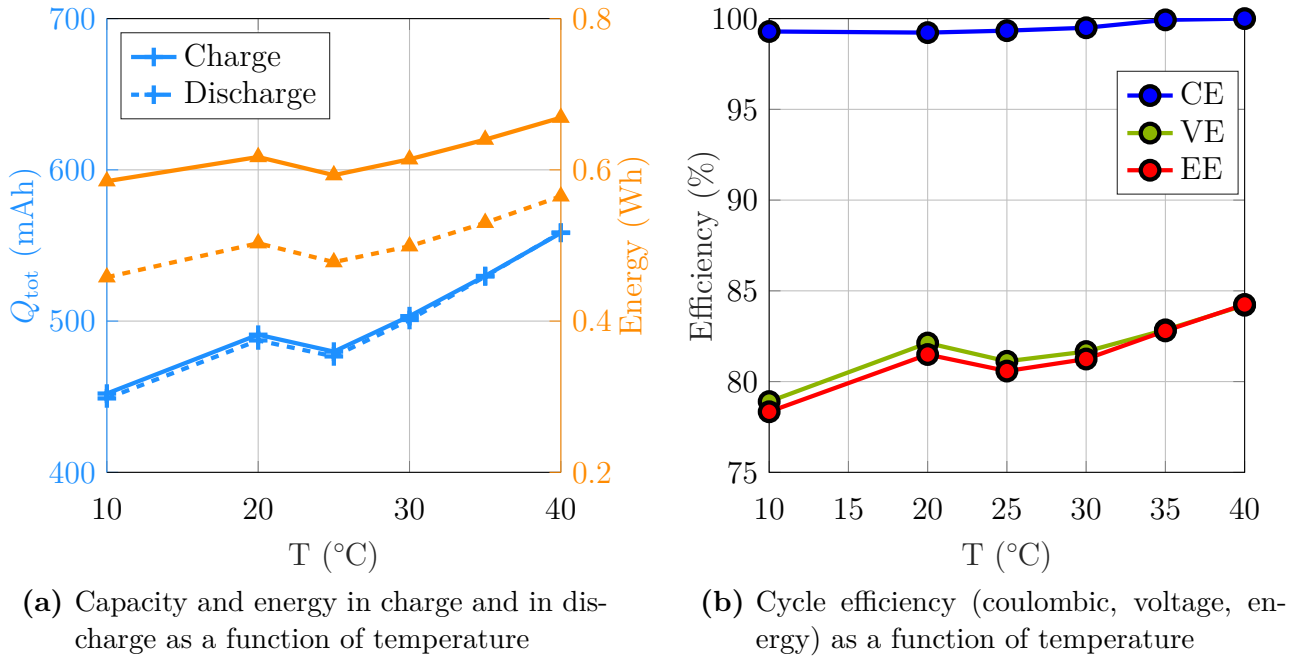


Figure 5.38: Global impact of the temperature on cycling performance

An industrial perspective

Besides the climatic conditions, temperature can also arise from internal sources: heat dissipated due to the Joule effect since the system is resistive, pump heating by friction losses, self-discharge reaction that are exothermic [31]. As such, temperature is closely tied to the current and flow rate conditions. The battery management is more difficult with fluctuations of the system temperature since many factors can be affected by this fluctuation. The water osmosis can be reversed or precipitation can cause the increase of pump power and heterogeneities inside the reaction volume. Internal temperature gradients in a stack also complicates the problem [215]. Additionally, some components must be cooled-down if exposed to heat, especially the electronic devices. Cooling systems add on the energy consumption losses of the battery. Temperature is very influential on the battery internal operation but also on the global system performance. This factor must not be overlooked when developing the technology and its operational management.

b) Local effect

The temperature influence is also assessed on the internal features of the cell.

In Fig. 5.39, the local charging capacity of each segment of the cell is represented versus the temperature. The inlet segments show an increase of their capacity between 20 and 40 $^{\circ}\text{C}$. Seg. #1 gains 1% on the share of the total capacity, which is the most pronounced change. This occurs at the expense of cell homogeneity, which is compounded at elevated temperature.

By looking closely at the local current deviation during charge in Fig. 5.40, it becomes clear that the temperature mostly affects the first part of the charging phase. Indeed, the early spike rises regularly with T , suggesting the development of heterogeneity with heating. It should

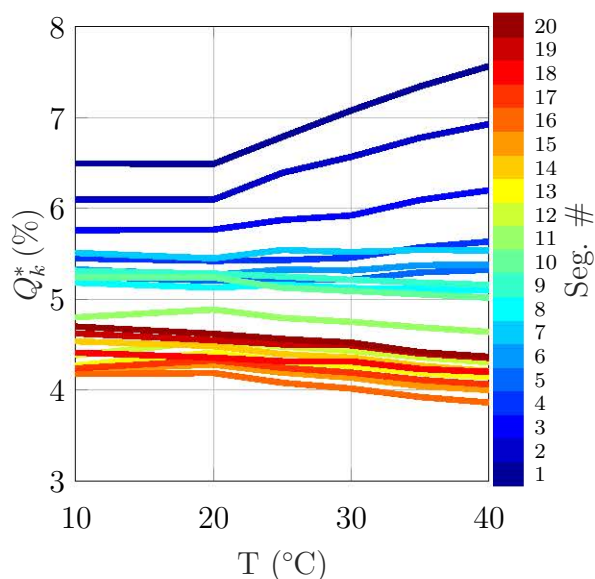


Figure 5.39: Local capacity (percentage of Q_{tot}) versus temperature, for all segments

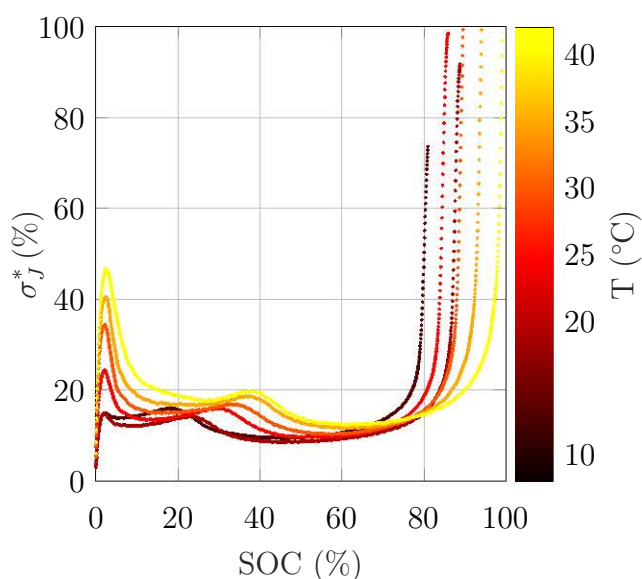


Figure 5.40: Variation of σ_J^* versus SOC during charge, for all temperature values tested

be noted that since the initial SOC differs between each cycle at different T (according to the V_{OC} values in Fig. 5.37), it could also account for a different internal homogeneity at start of charge.

After the first 15 % of SOC, all profiles of σ_J^* lie below 20 % deviation. The heterogeneity steeply rises in the final percent of charge. The local current uniformity evolution is modified similarly by a temperature increase or a current decrease (Fig. 5.24).

The profiles of σ_J^* in discharge (Fig. 5.41) reveal that temperature has a limited effect on the current deviation for the major part of the discharge, between SOC 100 and 20. At start of each discharge (on the right-hand side of the figure), the initial spike is slightly enlarged by a high T .

Below SOC 20, the steep rise caused by reagent depletion is followed by a new decrease for temperatures above 20 °C. As already mentioned in the studies of J and \dot{q} , this drop is associated with the *low potential plateau* observed in the voltage profiles, and is due to a subsidiary anolyte reaction. At the two highest temperatures, this drop reaches a threshold around $\sigma_J^* = 20\%$, from which the deviation curves start again to go up. This might indicate the depletion of this second form of anolyte species. This molecule accounts for approximately 12 % of the total capacity accessed at 40 °C.

The temperature study highlights a prominent influence on the SOC range accessed during cycling: an elevation of temperature gives access to the low potential capacity plateau in discharge. As such, the voltage curves and the profile of local current deviation σ_J^* change only in charge, because the initial SOC is altered with T . The local capacity distribution reveals that an elevated temperature boosts the reactions at the inlet segments. Along with the capacity accessible, the thermal conditions modify the efficiency, being improved at increased temperature. After the temperature study, the cell regained its previous performances which confirms the system robustness towards temperature.

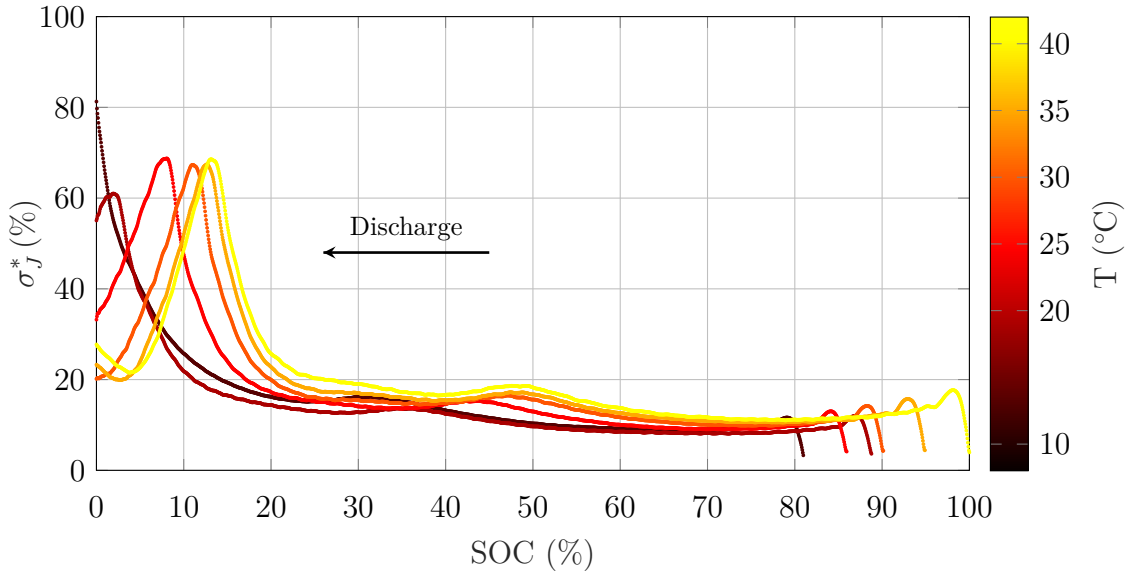


Figure 5.41: Variation of σ_J^* versus SOC during discharge, for all temperature values tested

c) PC curves

The analysis can be narrowed-down by keeping the SOC constant. This is what the polarization curves aim for. They uncover the real influence of the temperature on the cell resistance and on the local current uniformity.

Fig. 5.42 presents the global polarization curves at SOC 50 for 3 tested values of T : 10, 25 and 40 °C. The open circuit voltage (i.e. at $J = 0$) is different at 10 °C: this is due to the approximate method to estimate the SOC of the cell (subsection 5.2.1), and implies that the PC at this T was plotted at a SOC > 50 %. The calculated variation of the equilibrium and standard potentials (E_{eq} and E^0 , (1.4)) with T are too small and not in the good direction to account for this discrepancy.

Between $[-150; 150 \text{ mA cm}^{-2}]$, the linear part of the PCs are fitted. The slopes, given in the legend, show that the low T unambiguously hampers the cell performance while highest T slightly enhances it. In the meantime, the coldest condition provides the most linear PC through the full current range; in the meantime, the voltage limits are reached earlier. At -200 mA cm^{-2} , the higher the temperature, the more concentration overpotential is detected on the PC (by comparing the curve to its linear fit).

The local current standard deviation during PC provides complementary information. As for the flow rate study (Fig. 5.35), the standard deviation σ_J is plotted in mA cm^{-2} according to the applied current density J in Fig. 5.43. It clearly highlights that a higher temperature drives more heterogeneity: this confirms the trend detected in the cycling analysis when observing the local capacity distribution versus T (Fig. 5.39). Elevated temperature boosts the reactions at the inlet and generates an uneven current distribution.

At 40 °C, the heterogeneity cannot be kept under the 10 % limit during discharge, whereas the maximum charging current to comply with the threshold is around 150 mA cm^{-2} . This matches with the preceding conclusion of the flow rate study: charge and discharge processes are not symmetrical. The same effect is visible at other temperature values. The lowest T leads to very good cell uniformity, at the cost of low cell performance.

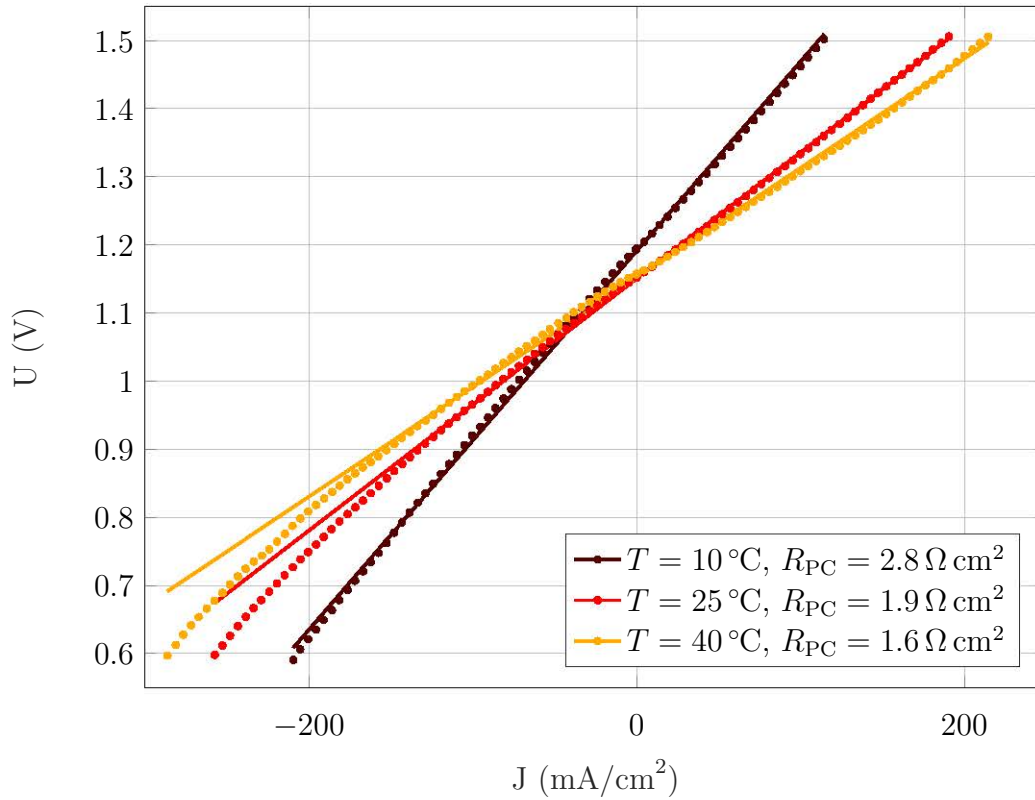


Figure 5.42: Global Polarization Curves (dotted lines) for the three temperatures: 10, 25 and 40 °C, and their fits (solid lines). The slopes of the fits give equivalent resistances R_{PC} reported in the legend

The PC complements the parameter study by uncovering a neat dependence of the cell performance with temperature. Moreover, cell uniformity is clearly impaired by an elevated temperature.

As already evidenced earlier, the charge and discharge are not symmetrical: internal heterogeneity is compounded during discharge.

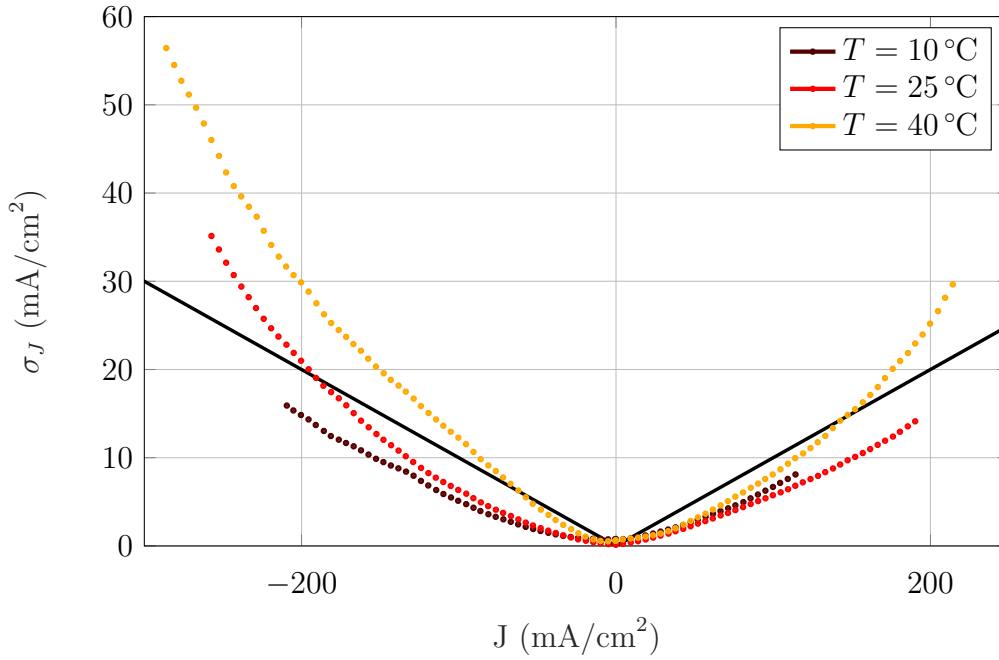


Figure 5.43: Variation of σ_J during the PCs of Fig. 5.42 for the three temperatures: 10, 25 and 40 °C. Black solid line represents the limit of $\sigma_J^* = 10\%$ of the applied current J

5.3. Summary of the parameter study

The parameter studies relative to J , \dot{q} or T unravel not only their substantial but also diverging effect on the system operation. This part synthesizes the separate analyses by combining their results and comparing their outcomes.

5.3.1. Comparison of the impact of the three parameters

The highest current density $J = 150 \text{ mA cm}^{-2}$ (at 100 mL min^{-1}) and lowest flow rate tested $\dot{q} = 10 \text{ mL min}^{-1}$ (and 40 mA cm^{-2}) give access to a similar cycling capacity of 200 mA h (with very different voltage profiles). This enables the comparison of these two extreme duty points. Table 5.2 presents the features of these two cycles: their energy efficiency, the average current uniformity represented by $\overline{\sigma_J^*}$ in charge and in discharge as well as their respective advantages.

Table 5.2: Comparison of the features of two extreme duty cycles that give access to the same capacity 200 mA h

| Extreme point | operating | Energy Efficiency | Current uniformity $\overline{\sigma_J^*}$ | Advantage |
|--|-----------|-------------------|--|----------------------|
| $J = 150 \text{ mA cm}^{-2}$ (and 100 mL min^{-1}) | | 55 % | 10 % in charge 14 % in discharge | fast charge |
| $\dot{q} = 10 \text{ mL min}^{-1}$ (and 40 mA cm^{-2}) | | 75 % | 40 % in charge 35 % in discharge | low pump consumption |

This comparison exemplifies that a similar global metrics (here the accessed capacity) can actually hide very divergent cell operations. High current cycling impairs the cell efficiency but maintains acceptable local current uniformity. Contrarily, a low flow rate is detrimental for the homogeneity of the cell but features better efficiency than high current. In the meantime, pump consumption is mitigated by slow electrolyte flow input, but also by fast charge (provided that the pumps are switched off after full charge). Preferring one duty point over the other is disputable and depends on the criteria taken into consideration. Both operational conditions affect the pump consumption to a certain extent. This must also be regarded when assessing the total efficiency of the system.

The diagram in Fig. 5.44 generalizes how the variation of each parameter impacts the cell. The diminution of the current density, the augmentation of electrolyte flow rate or the temperature increase all yield the same global effects: they give access to more capacity and improve energy efficiency. Nevertheless, it was proven that their specific lever mechanism implies dissimilar consequences at local scale. High electrolyte flow rate makes the current distribution more uniform throughout the cycle. A low current or an elevated temperature maintain a good homogeneity for the most part of the cycle. They however change the SOC window on which the cell is cycled, and with it the local current heterogeneity at start and end of each phase.

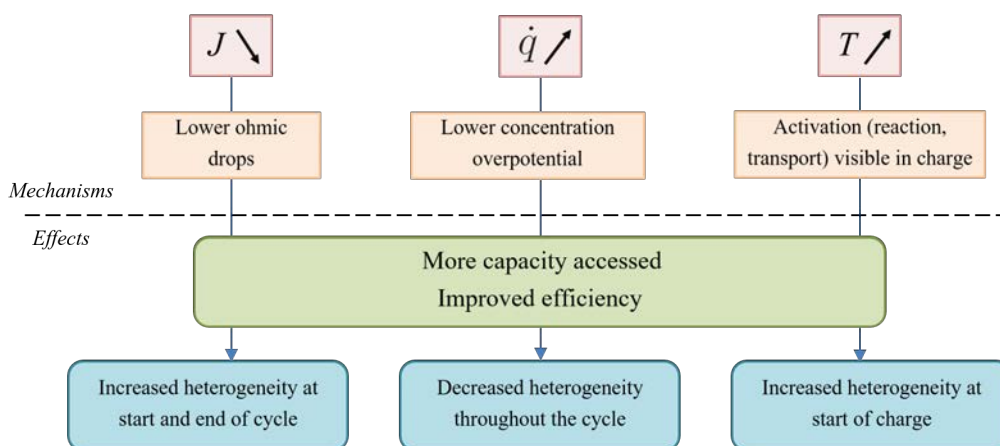


Figure 5.44: Effects of current, flow rate and temperature variation on the global and local cell performances

Table 5.2 and Fig. 5.44 underline that there are several ways to achieve a high capacity and cell efficiency, each of them having their pros and cons. Changing one parameter drives a particular modification of the internal operation of the battery and the global metrics are not sufficient to depict the real consequences. An internal investigation with an equipped set-up such as the segmented cell is crucial to comprehend the system sensitivity to operational conditions. Moreover, the best operating point does not exist and it results in compromises that must be appraised accordingly to the flow battery technology.

5.3.2. Development of an operational map

In practice, the power load is ordered by the grid, while the battery is at a given SOC; the temperature is dictated by the system environment, its operational history and its present state (flow rate, reactions ongoing inside the stacks etc.). The flow rate is actually the only parameter

that can be adapted during cycling. The ensuing discussion presents the construction of a tool that could help to guide the management of the flow rate according to the duty point (SOC, power load, T).

This tool takes the form of an operational mapping, elaborated from the experimental results of the parameter study. It is chosen to focus on studies at 25 °C for which the most data points are available. Since cycling was performed at constant current, the operating conditions are defined with J . The criterion targeted is the local current homogeneity, represented by σ_J^* . The map will help to minimize the electrolyte flow rate, and with it the pump consumption, without compounding the internal uniformity of the cell operation. The results of four data-set, representing in total 37 cycling conditions, can be combined to sketch what the operation chart would look like:

- ➔ 1 test of varying flow rate at constant current $J = 40 \text{ mA cm}^{-2}$
- ➔ 3 tests of varying current at constant flow rate: $\dot{q} = 10, 50 \text{ or } 100 \text{ mL min}^{-1}$

Throughout the tests combined in this section, monitoring the SC capacity confirmed that it stayed constant and that no aging effect would interfere in the comparison. To allow for a relevant combination of data, the definition of the maximum capacity was standardized for all these tests and set to $Q_{max}^{ref} = 637 \text{ mA h}$; it is the capacity reached in standard conditions (SC), as described in subsection 5.2.1. This value is the baseline with which the *apparent* SOC for all cycling conditions was determined. Due to this new reference capacity, the critical SOC values represented in the following maps can be slightly different than the ones read directly in Figs. 5.24, 5.25, 5.30 and 5.31. In discharge, it is assumed that the curves start from SOC 100, which is not strictly the case. To get an accurate operational map, discharges in different working conditions should be tested after a charge in standard conditions so that they could start at the same SOC.

The thresholds of acceptable heterogeneity were determined as $\sigma_J^* = 15\%$ in charge and $\sigma_J^* = 20\%$ in discharge, because discharges always generate more heterogeneity than the charging phases. The thresholds take the form of horizontal lines in the representation of σ_J^* vs SOC; they are illustrated by dashed lines in Fig. 5.25 and Fig. 5.30a.

The crossing point of each curve (σ_J^* vs SOC) with the threshold line defines the critical SOC from which the internal heterogeneity no longer meets the requirements. From this critical state, the flow rate should be increased to alleviate the heterogeneity if the charge or discharge keeps going at the same J . The curves usually cross the threshold line several times during a step, but the initial spikes (within the first 10 % of charge or discharge) are not taken into account in the present analysis.

For a given combination (SOC, J), the minimal flow rate that maintains acceptable internal heterogeneity is mapped in Fig. 5.45 for the charge and in Fig. 5.46 for the discharge. In these maps, the experimental points are reported by the black points. The solid colored lines were extrapolated between the experimental points. For $J = 40 \text{ mA cm}^{-2}$, all the flow rates were tested, giving a continuous horizontal line. For other currents, only 3 values of flow rates were examined. Quadratic polynomials were fitted from these data to infer a continuous extrapolation between the data points. This mapping is sketched in the background with semi-transparent points.

Fig. 5.45 shows that the experimental lines agree with each other and allow the mapping of a coherent and gradual change of flow rate through the operational conditions. The data at lowest flow rate lie below 5 % of SOC on the left of the map, because such a slow electrolyte

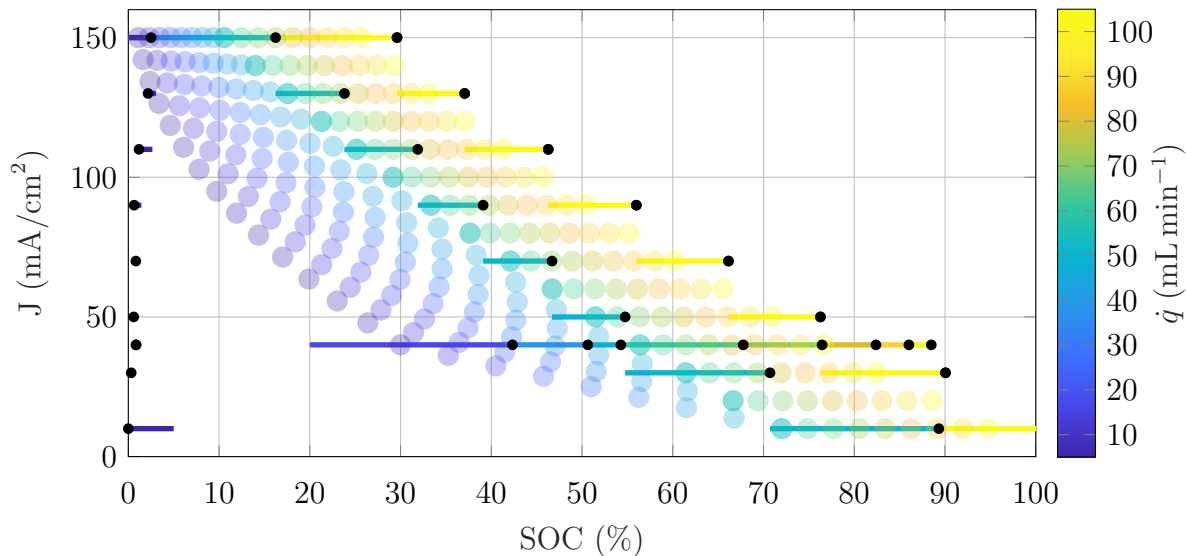


Figure 5.45: Operational map giving the flow rate necessary to keep acceptable internal homogeneity ($\sigma_J^* < 15\%$) according to the operating point (SOC, J) in charge. Constructed from 4 tests of the parameter study. The raw data points are displayed in black and the solid lines connect these points, the transparent circles were extrapolated between the 4 data sets.

flow induces an heterogeneity above the threshold from the start of the phase.

There is a blank area between SOC 0 and 30 for which no condition can comply with the prerequisite uniformity. It is related to the spikes observed at the start of charge in Figs. 5.24a and 5.30a. This operating zone is peculiar: the highest local current deviations are obtained at lowest flow rates or lowest current inputs. Therefore the strategy to follow is contrasting with the rest of the charge and must be examined separately.

The mapped region substantiates that the more current density is applied, the less capacity can be charged in uniform conditions. Further, as the SOC increases at a given current, the flow must be raised to maintain acceptable homogeneity. The diagonal line in yellow demarcates the limit beyond which the charge cannot be performed at an acceptable σ_J^* due to pump limitation of 100 mL min^{-1} . This zone contains the high currents coupled with high SOC.

The map for the discharge (Fig. 5.46) is almost symmetrical to the charge. At high SOC, a low flow rate is sufficient to ensure good homogeneity. There is almost no blank area, because the start of discharge does not feature as critical spikes as during charge (Figs. 5.25 and 5.31). As the cell is further discharged, the electrolyte flow needs to be sped up. At 150 mA cm^{-2} , the cell cannot be discharged below 70 % SOC; it tallies with the limit of 30 % SOC in charge. The upper diagonal limit in yellow is positioned slightly higher in discharge than in charge.

As already discussed earlier in subsection 5.2.1, the maps of Figs. 5.45 and 5.46 are disputable since they are constructed with an *apparent* SOC, calculated with respect to the capacity available at this cycle life of the cell in the standard conditions defined. Nevertheless they confirm that such analysis can provide insightful diagrams for battery management purpose.

The operational maps constructed in this study can be compared to the work of König et al. [216]. They proposed equivalent maps delimiting the required flow rate at a given duty point (SOC, J) based on an innovative optimization of the instantaneous efficiency of the RFB

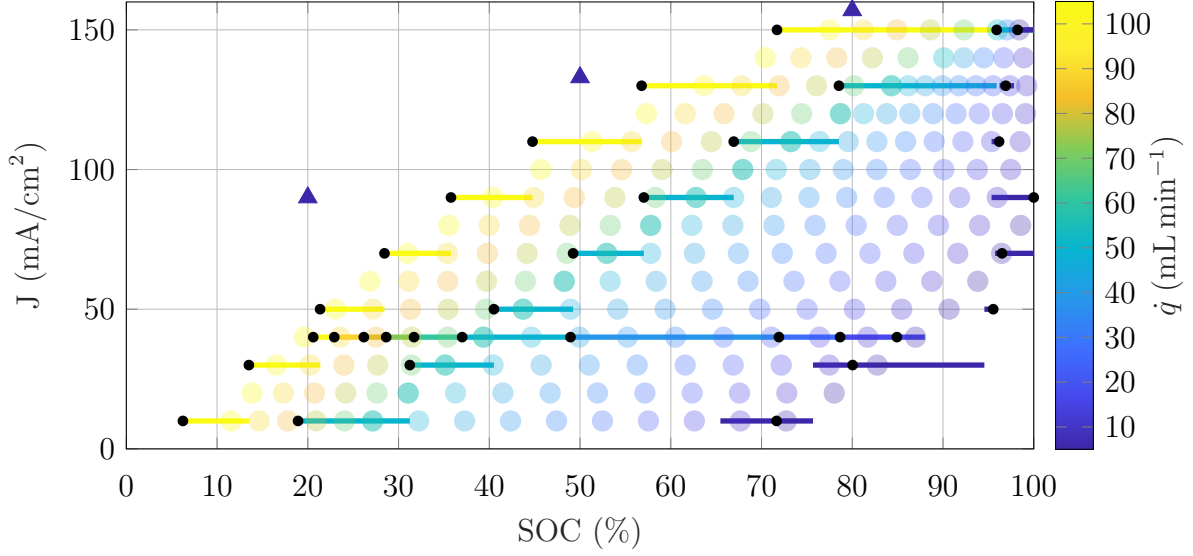


Figure 5.46: Operational map giving the flow rate necessary to keep acceptable internal homogeneity ($\sigma_J^* < 20\%$) according to the operating point (SOC, J) in discharge. Constructed from 4 tests of the parameter study. The raw data points are displayed in black and the solid lines connect these points, the transparent circles were extrapolated between the 4 data sets. The triangles represent the data extracted from the PC characterization at 10 mL min^{-1} (from the deviation curves of Fig. 5.47)

system (which was evaluated by modelling in their work). The overall aspect is similar, even though it was not constructed on an equivalent analysis.

Kim et al. also performed a parameter study on the VFB system to analyze the influence of the current and the flow rate [217]. They established an empirical equation relating the flow rate and the SOC to the energy efficiency of the cell (including pump consumption). This expression was used to map the energy efficiency according to the duty point (SOC, flow factor) for a given current density. They showed that EE could gain up to 8 % with a flow factor changed from 1 to 3 (definition of flow factor given in (5.1)).

Similarly to during cycling, the standard deviation of local current can also be observed during the Polarization curves, as it was already done during the flow rate and temperature studies. It is insightful to compare the data from cycling and from this characterization. To this end, Fig. 5.47 displays σ_J vs J during the PC at $\dot{q} = 10 \text{ mL min}^{-1}$ obtained for the 3 SOC. The deviation threshold of 10 % is given by the solid line.

The plots relative to PC evidence that the internal uniformity heavily depends on the SOC and on the sign of current: at SOC 20, the cell can withstand high charging current without reaching the limit while it is restricted to a maximum of $J = 90 \text{ mA cm}^{-2}$ in discharge. The reverse applies at SOC 80. This trend complies with the maps built from cycling in charge and in discharge Figs. 5.45 and 5.46. Nonetheless, the operating points deduced from PC data would not tally with these maps. For example, the limiting currents in discharge that obey the threshold of $\sigma_J^* \leq 10\%$ (Fig. 5.47) are illustrated by the triangles in Fig. 5.46. Even with a limiting criterion lower than the one used for the cycling analysis (that was $\sigma_J^* \leq 20\%$), the points do not match the mapping and underestimate the current distribution induced during discharge. For instance at SOC 50, any current below $J = 130 \text{ mA cm}^{-2}$ would

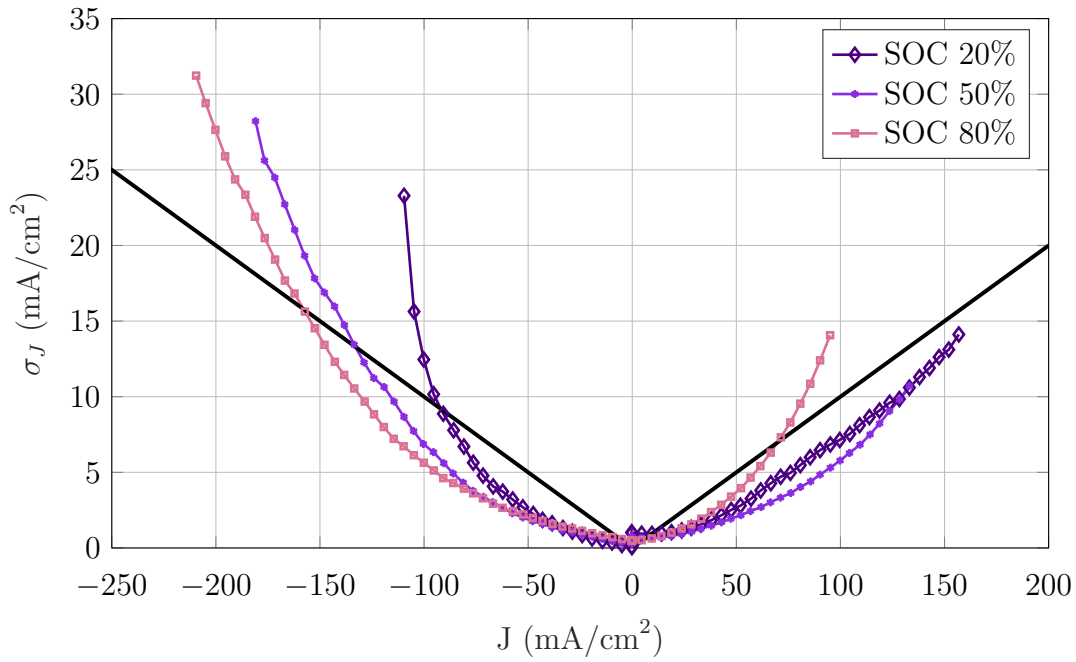


Figure 5.47: Variation of σ_J^* versus J during PC at $\dot{q} = 10 \text{ mL min}^{-1}$ for SOC 20, 50 and 80 %

lead to an acceptable heterogeneity at lowest \dot{q} : cycling data conversely affirm that above $J = 110 \text{ mA cm}^{-2}$, no flow rate can comply with the homogeneity criterion.

This means that the PC is not representative of the real cycle conditions, and its results are of limited significance for the cell operation. This diagnosis tool cannot substitute the full cycle analysis, which was already concluded by Zheng and coworkers [218]. Indeed, they unravelled that only the voltage efficiency could be properly assessed from the polarization curves, but the energy efficiency and accessible capacity could not be determined. The maximum power density that is sometimes extracted from PC is not meaningful either in practical conditions.

An industrial perspective

The maps combining several experimental data sets convey the possibility to optimize the electrolyte flow rate, in order to sustain homogeneous operation of the battery. The tool developed from the segmented cell results can be extended to the industrial stacks provided a validation phase (to assess the homogeneity over the full size electrode and between the stacked cells) and some adjustments (flow rate range of the stack, power control rather than current control). A difficulty lies in the influence each factor has over one another. In particular, the internal temperature is partly determined by the current and the flow rate, and in turn reshapes the internal current distribution.

The three parameter studies substantiate that all J , \dot{q} and T factors dictate the global cell performance along with the internal current distribution. Through specific lever mechanisms, each parameter influences differently the internal current uniformity of the cell. The evolution of the standard deviation of local currents σ_J^* with time is a relevant variable to examine. It

exhibits several distinct zones:

- At the very start of charge, a first spike appears. It is exacerbated at low current, high flow rate, or high temperature.
- At the end of charge, the steep increase of the deviation correlates with the voltage rise; it is attributed to mass transport limitation due to reactants starvation.
- In discharge, σ_j^* also features an early hump enlarged by a small current input, a low flow rate or an increased temperature. The discharge ends with a stark rise of current deviation. In the conditions that give access to the low potential plateau, the deviation falls back down during the last percent of discharge.

However, two main challenges arise from this parameter study:

- The operating conditions alter the SOC window accessed during cycling. As a consequence, it is difficult to compare the voltage or σ_j^* curves for several parameter values, since the battery SOC is also modified. The effects of the parameter value and the SOC cannot be entirely isolated. In particular, the early spike of current deviation in charge is most critical at lowest current and highest temperature. It can only stem from a very low initial SOC (because the cell is fully discharged in these two extreme conditions) or also be caused by the extreme parameter values themselves.
- The voltage curves as well as the current deviation curves are distorted by the convoluted anolyte characteristics. A spike arises in the middle of the charge or discharge phase and a plateau of additional capacity can be reached at the end of discharge, under propitious conditions (e.g. low current or high T). These particularities sometimes complicate the results analysis.

The Polarization curves complements the diagnosis from cycling. They convey similar trends to the charge-discharge tests results: the influence of flow rate but also of SOC is prominent on the internal cell heterogeneity. Moreover, PCs clearly substantiate that discharge is more critical in terms of current uniformity than charge. As such, the two steps of a cycle must therefore be managed differently, which justifies the need of an operational map both for charge and discharge. Ultimately, the PCs overestimate the cell performance by displaying more uniform internal operation. This tool cannot comprehensively depict the practical battery behavior. The charge-discharge analysis remains essential during the RFB investigation.

To complement the study, several prospects can be envisioned. The long-run operation under unfavorable conditions for cell uniformity (such as high current, low flow rate or high temperature) would unravel whether the distribution evolves with aging. The impact of heterogeneous operation on material degradation (membrane and electrode) could be assessed by post-mortem characterization. The mapping could be based on refined experiments where the SOC is adjusted in standard conditions before changing one parameter value. In this way, all the duty points could be analyzed and the effects of SOC and operating conditions on the cell uniformity could be properly decoupled.

They operational maps based on the parameter study will be tested in cycling conditions in the next chapter to investigate experimentally their relevance (section 6.2).

6

INDUSTRIAL CELL STUDY

Contents

| | |
|---|------------|
| 6.1 Hydraulic study | 194 |
| 6.1.1 Model development | 194 |
| 6.1.2 Computational results | 197 |
| 6.1.3 Clear flow cell experiment | 201 |
| 6.2 Flow rate optimization | 206 |
| 6.2.1 Strategy | 206 |
| 6.2.2 Results | 208 |
| 6.3 Conclusion | 212 |

This final chapter proposes further investigative steps to take into consideration the industrial size stack. The previous chapter presented the use of the lab-scale test bench to examine the battery cycling and identify the influence of several operational parameters. The results were obtained from the segmented set-up, whose length equates to the short side of the stack manufactured at Kemiwatt (35 cm). Since the width of the segmented cell is marginal compared to its length, the flow could be readily considered one-dimensional along the flow channel. Unlike this ideal case, the cells constituting a stack are two dimensional with a wide electrolyte inflow at the bottom of each cell. As a consequence, a strategy must be developed to ensure an homogeneous supply of the large electrode area.

A typical stack configuration used in a RFB system is depicted in Fig. 6.1. The layers composing a cell are piled up together: end plate, negative electrode, membrane, positive electrode, bipolar plate, negative electrode, and so on. The bipolar plates are called as such because they constitute the end of one cell and the start of the next one. Through these bipolar foils, usually made of graphite, the individual cells of the assembly are electrically connected in series. This ensures a high voltage between the two ends plates of the reactor. All half-cells of the same polarization (positive or negative half-cells) are hydraulically connected in parallel. The corresponding electrolyte (respectively catholyte or anolyte) is pumped from the tank to the stack through a large-diameter manifold. A channel is machined in each plastic frame encasing the electrode and transports the liquid flowing in the manifold to the half-cell reaction

volume. The electrolyte is then flowed through the porous electrode (in contrast with flow-by design that require a flow field on the bipolar plate) and a symmetric channel gathers the reacted electrolyte outwards the stack through an outlet manifold. Depending on the design, the inflow/outflow manifolds can be located on the same side of the stack or opposite to each other (as visible on the end plate of Fig. 6.1).

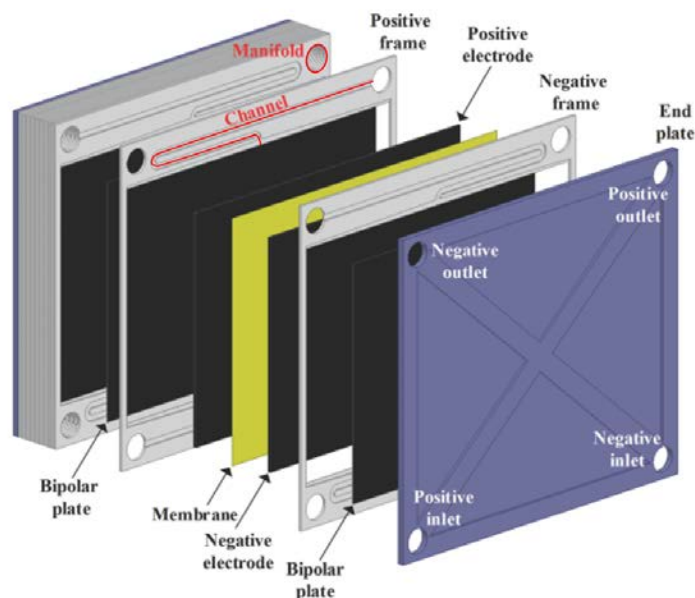


Figure 6.1: Exploded view of a typical stack configuration used in a RFB system with flow-through carbon felts. Adopted from [219]

The ensuing discussion addresses the hydrodynamic aspects of the RFB system. As a first step, a modeling and then an experimental flow visualization is conducted to examine the electrolyte flow through the half-cell of a stack (channel + porous electrode). The second step consists in testing an optimization of the electrolyte flow during cycling to moderate the pumps consumption.

6.1. Hydraulic study

The hydraulic study was carried out at the University of New South Wales (UNSW) in Australia during a practicum visit of 3 months. Under the supervision of Dr Chris Menictas and the expert advice from Emeritus Professor Maria Skyllas-Kazacos, this study undertook the development of both a computational and an experimental method to outline the hydrodynamics aspects in a large RFB cell. Particularly, the influence of the channel design was broached.

6.1.1. Model development

The tool developed for the hydraulic study is a 3D-stationary model describing the electrolyte flow inside a half-cell of the large scale stack. The model was computed using the COMSOL Multiphysics® package.

a) Governing equations

The electrolyte flow is assumed to be laminar, isothermal and incompressible. The liquid and solid properties are considered isotropic. The influence of gravity is neglected. As mentioned in Chap. 3 the rheological behavior of the electrolyte can be complex; nevertheless it is described as a single phase Newtonian fluid in the simulation.

The domain of simulation consists in the inlet/outlet distribution channels machined in the frame and the porous electrode. The simultaneous flow through pure-fluid and porous domains is described based on the approach of Le Bars and Worster [220]. The Navier-Stokes equation governs the flow in the open regions of the channels:

$$\rho (\vec{u} \cdot \nabla) = -P + \nu [\nabla \vec{u} + (\nabla \vec{u})^T] \quad (6.1)$$

\vec{u} is the velocity field, ρ and ν the density and dynamic viscosity of the liquid phase. P represents the liquid pressure.

Thanks to the incompressible flow assumption, the continuity equation has the following form:

$$\nabla \cdot \vec{u} = 0 \quad (6.2)$$

Darcy's law defines the average fluid velocity in a mesoscopic control volume of the porous medium, according to the applied pressure gradient (or pressure drop) ∇P [221]:

$$\vec{u} = \frac{-k}{\nu} \nabla P \quad (6.3)$$

The permeability k (m^2) describes the capacity of a porous material to transmit a fluid; it is largely dependent on its structure (shape and size of the pores). It is usually described by the Kozeny-Carman expression:

$$k = \frac{d_f^2}{K} \frac{\varepsilon^2}{(1 - \varepsilon)^2} \quad (6.4)$$

K is the Kozeny-Carman coefficient, d_f the mean fiber diameter and ε the porosity of the solid phase. Experimental data of the permeability are available from the electrode supplier (see Fig. 2.2). For the electrode compression ratio used in the design studied (35 %), the value is $k = 6.6 \times 10^{-11} \text{ m}^2$.

From (6.2) and (6.3), it comes the following pressure equation in the porous electrode:

$$\frac{-k}{\nu} \Delta P = 0 \quad (6.5)$$

This set of equations contains the fields of velocity and hydraulic pressure as variables: they are resolved in parallel for the free-flow and the porous media.

The input parameters used for the hydraulic modeling are listed in Table 6.1.

Table 6.1: Input parameters used in the hydraulic model

| Parameter | k (m ²) | ε | ν (mPa s) | ρ (kg m ⁻³) |
|-----------|-----------------------|---------------|---------------|------------------------------|
| | $6.6e - 11$ | 0.9 | 1.3 | 1100 |

b) Computational domain

The domain used in this simulation accurately represents a real half-cell configuration used and tested at Kemiwatt. The geometry illustrated in Fig. 6.2 was sketched in a CAD software from the technical drawing before being imported into COMSOL®. The inflow and outflow channels design is represented in light grey. It consists of a four-level channel that divides progressively to feed a network of $4 \times 16 = 64$ ports that interfaces with the base of the porous electrode, illustrated in dark grey. Its dimensions are 35×55 cm which equate to 1925 cm^2 of active surface. The porous felt is compressed to 3 mm. The channel section varies to a small extent between the layers; it remains approximately equal to 15 mm^2 (with a constant depth of 2.5 mm). The outlet channel mirrors the inlet, with feeders both on the same side of the half-cell. The manifold connecting the half-cells is not considered here, as there is a change of flow direction in its section that pointlessly complicates the model.

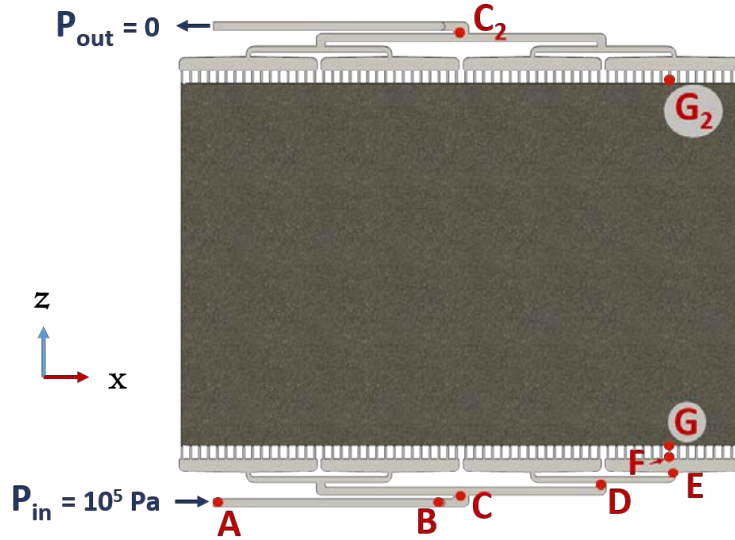


Figure 6.2: Computational domain of the hydraulic model: flow paths of the frame and porous electrode

The boundary conditions are applied as a pressure differential between the two feeders as represented in Fig. 6.2, such that:

$$P_{in} - P_{out} = 10^5 \text{ Pa} \quad (6.6)$$

This value corresponds to the pressure drop measured between the inlet and outlet of Kemiwatt's industrial stack, in typical flow rate conditions. Indeed the industrial system is equipped with pressure sensors upstream and downstream from the stack, as they are cheaper

and more reliable than flow rate sensors. The frequency of the pumps are regulated to comply with the desired pressure gradient in the stack.

A normal flow direction is defined at the boundaries. All the other boundaries are defined with no-slip conditions and no flux.

The pressure values used in this model are relative: they do not take into account the atmospheric pressure.

A preliminary mesh refinement study permitted to optimize the meshing to get convergence of the results without unnecessary resolution: in the porous electrode, the mesh is coarse with unstructured elements, while it is refined with rectangular elements and high inflation ratio in the narrow channels.

Nevertheless, the domain meshing remains complex because the frame was sketched identically to the real object. It could be simplified with right-angled corners. This modification could save computation time without affecting the model relevance (in light of the results described hereafter).

6.1.2. Computational results

The main results and related learning of the 3D-stationary model are presented. The velocity plots of this section are sketched at the mid-plane of the simulated domain ($y = 1.5 \text{ mm}$).

The computation was first conducted by replacing the porous electrode by a pure-fluid region. The simulation was run again by taking into account the porous matrix. Fig. 6.3 maps the simulated contour of velocity magnitude $|u|$ in the domain without porous electrode (Case 1: left) and then with porous electrode (Case 2: right). The same velocity colorbar was used for both maps.

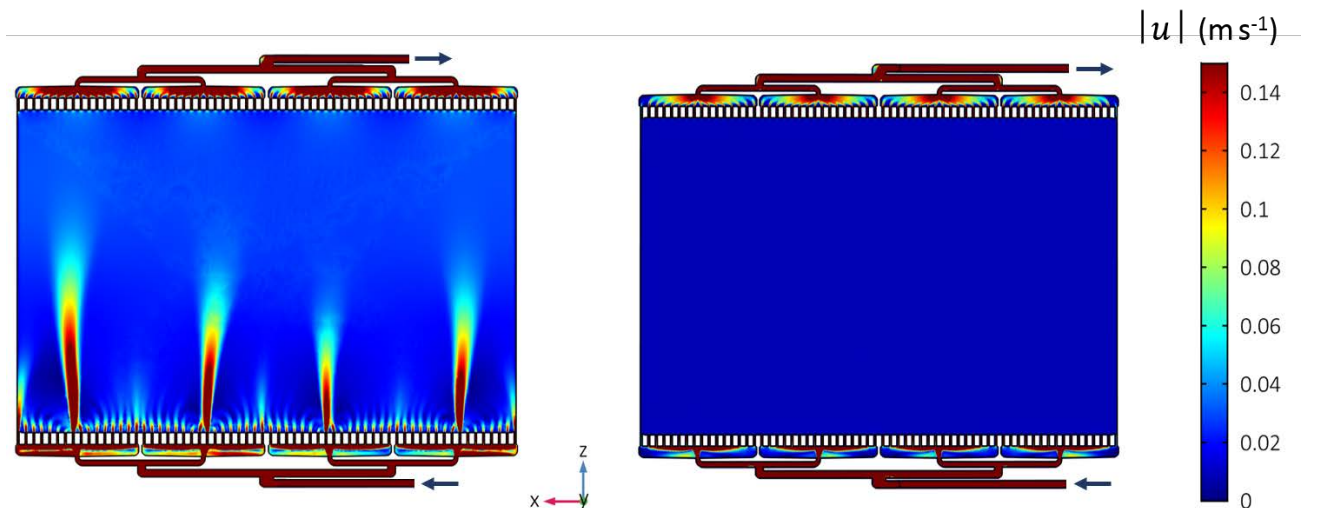


Figure 6.3: Simulated velocity contour plots without porous electrode (Case 1: left) and with porous electrode (Case 2: right)

In both cases, there is a high velocity variation between the inlet/outlet and the middle of the domain. Since the same quantity of fluid is transported in the narrow channel and

then disperses into the wide surface area of the electrode, the velocity is highly reduced in the electrode region. At the inlet, the Reynolds number Re , defined for a pipe flow by (6.7) can be determined:

$$Re = \frac{u\rho D_H}{\nu} \quad (6.7)$$

D_H is the hydraulic diameter of the channel, and equates to $4A/P$ for a non-circular channel section (A being the cross-sectional area and P the wetted perimeter). According to the geometry of the inlet channel ($D_H = 2.2\text{ mm}$) and the velocity magnitude of 0.15 m s^{-1} , $Re = 280$, which is largely inferior to the critical value of $Re_c = 1700 - 2000$ [222]. This proves that the entire flow is laminar in the problem.

The contrast between Case 1 and 2 is obvious. Without porous matrix, the liquid follows four main flow paths that face the outlets of the third branches constituting the channel. Outside the preferential streams the velocity is very low. The design of 4-layered channel connected to the multiple inlet ribs is not sufficient to evenly distribute the electrolyte flow through the large active area.

Once the porous electrode fills the middle of the domain, the flow distribution is much more even in this region. The porous matrix has an effect of flow distributor, but in turns decreases the resulting velocity by constituting additional pressure drop.

Other depictions of the simulation of Case 2 are considered to better understand what happens in the presence of porous electrode.

The computed flow path was divided into small sections to observe the pressure gradient between the probes labelled with letters in Fig. 6.2. The distribution of the pressure drop (ΔP) in each section is represented in Fig. 6.4. The figures above the bars give the portion of the partial ΔP relative to the overall pressure drop.

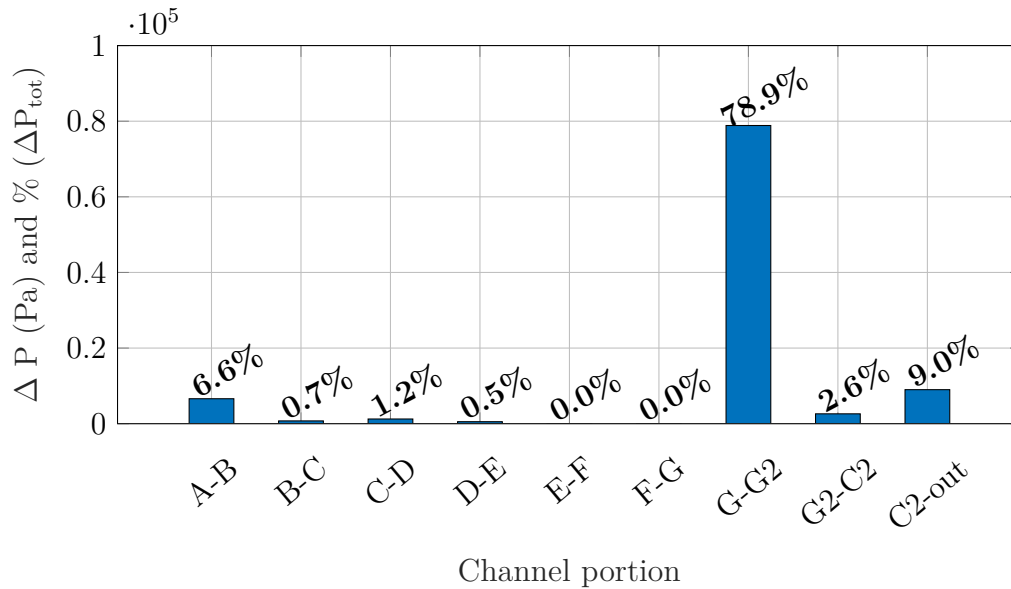


Figure 6.4: Pressure drops distribution along the flow path in the sections represented in Fig. 6.2, Case 2

This representation unambiguously unveils that most of the pressure drop happens between

G and G2, that is through the porous electrode. This justifies the even flow distribution in Case 2. The porous matrix being highly resistive to the electrolyte stream, it is responsible for almost 80 % of the total pressure drop and permits an homogeneous electrolyte supply through the large active surface area.

An industrial perspective

The high hydraulic resistance of the porous electrode is unfavorable for the pump consumption in the RFB system. Several strategies could be contemplated to mitigate the pressure losses in the active surface area:

- An alternative is the use of thinner carbon electrode, called carbon paper, associated with a flow field design embedded in the bipolar plate (this configuration was briefly studied in subsection 3.4.3). This *flow-by* electrode concept is widely considered at laboratory scale [36, 90], but is not easily scalable to industrial stack configuration. Indeed it would require thick bipolar plates that reduce the compactness of the reactor. Moreover, this layout might worsen the concentration polarization because of lower convective mass transport rates [90].
- Another strategy is the stacking of several layers of carbon felts to create zones of different porosity inside the active surface, without affecting the design of the bipolar plate. Two possibilities are illustrated by Cases A and B in Fig. 6.5. Case A combines several stripes of electrode gradually added towards the outlet to compensate the reactant depletion by an increased electrode/electrolyte interface area. To produce a similar effect, Gurieff et al. proposed to vary the half-cell thickness along the flow so that electrode compression increases at the outlet [86]. Case B consists in adding small pieces of a second felt onto the first layer, to emulate flow field designs embossed in the bipolar plate. This type of arrangement was tested experimentally by Reed et al. in a 3-cell 1 kW stack [37]. Their interdigitated flow pattern cut directly into a carbon felt sheet showed promising results.
- Alternatively, the use of two layers with different porosity could be utilized; the higher density electrode lying close to the membrane [131]
- Finally, the electrode itself can be modified. Dennison et al. tested electrode perforation of carbon paper [223]. They obtained substantial improvement of cell performance and reduction of pressure losses with a perforated electrode. Another approach would be cutting channels directly onto the graphite felt as represented in Case C; Bhattarai et al. have tested several types of groove geometries and recorded a few percent of efficiency increase [131].

These options offer flexibility to the stack designer in terms of materials properties or channel geometry and sizes, as illustrated in the patent [224]. Easy to implement in an already existing stack configuration, they could lead to substantial improvement of reactant delivery towards the active surface while reducing the pump consumption.

Another observation from Fig. 6.4 is the asymmetry between the upstream and downstream channel, accounting for 9 % and 11.6 % of ΔP_{tot} respectively. The influence of the meshing and the convergence criterion must be investigated to conclude about this difference.

In practice, the viscosity is modified during a charge/discharge phase because of molecule reaction and exchange of cations through the membrane. Therefore the variation of electrolytes

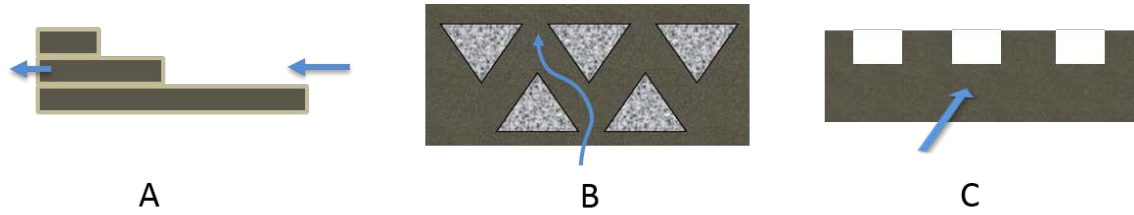


Figure 6.5: Strategies for mitigation pressure drop in the porous electrode of an industrial stack; flow direction represented by the blue arrows. Case A: porous electrode stacking along the electrolyte flow, Case B: flow field design built with a second layer of porous electrode added on top of the first one, Case C: electrode embossing by heat-treatment or electrode compression.

viscosity should be taken into consideration in a combined hydraulic-electrochemical model. Xu et al. showed that this approach led to a more realistic simulation[225].

Finally, it is visible that most pressure drop happens in the extreme parts of the channels (between A-B and C2-out). This is expectable as only this portion of the channel collects the total amount of fluid in circulation.

The inlet and outlet channels in the presence of the porous electrode (Fig. 6.3, Case 2) are zoomed in to represent the velocity streamlines with a color code illustrating the magnitude $|u|$. This depiction is given in Fig. 6.6.

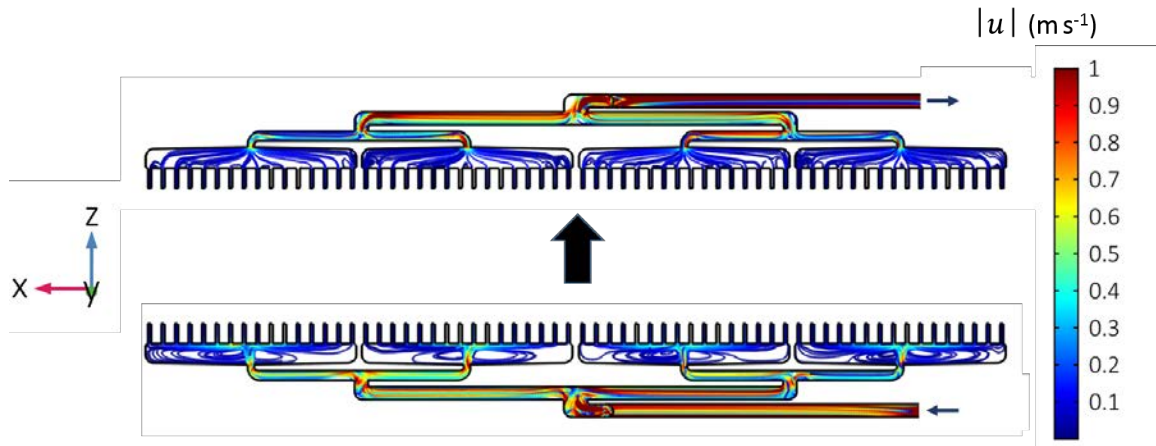


Figure 6.6: Simulated velocity streamlines and magnitude in the inlet (bottom) and outlet channels (top), Case 2

In the upstream region (at the bottom of the figure), the velocity progressively diminishes as the flow divides into the sub-channels. It starts from 1 m s^{-1} in the first channel, between A-B, inducing the highest pressure gradient in Fig. 6.4. Then the velocity declines until 0.1 m s^{-1} in the last channel levels connected to the 64 small ports. In this part, the velocity streamlines evidence stagnant zones where the electrolyte recirculates instead of entering the ribs. This is caused by the abrupt opening of the third-level channel with straight edges, towards the large and rectangular last channels. Instead, the design could be rethought by using funnel-shape edges, to force the flow towards the ports by a progressive increase of the section. This solution will be explored experimentally in the following section.

An industrial perspective

Stagnant zones must be avoided in the final design, because they could lead to solid build-up that can eventually block one or several sub-channels. It would entail a high heterogeneity in the distribution pattern, and potential side reactions or material corrosion in the dead zones of the electrode.

In the downstream region, the velocity increases towards the outlet, with similar magnitudes as the inlet channel. However, no electrolyte stagnation is observed in the sub-channels after the ports. The unlike upstream and downstream flow patterns explain the difference in the corresponding ΔP observed previously (Fig. 6.4). This also suggests that the need can be different upstream and downstream of the electrode, so that the best channel design is not necessary symmetrical between the two ends.

This 3D model depicts the hydrodynamic behavior in a real-size half-cell RFB. It unraveled that the flow distribution was uniform thanks to the presence of the porous matrix. This is at the expense of important pressure losses in this zone. As a consequence, this preliminary study points out that the porous electrode surface must be rearranged in the hope of minimizing pump consumption.

The next development of the stack-level model would couple the electrochemical aspect to depict the dynamic response of a full cell, and simulate how the flow pattern affects the reaction and the cell efficiency. Such comprehensive model was already developed in the RFB field, as the one described by Blanc and Rufer [226]. With this multiphysics tool, Gurieff et al. investigated new electrode geometries to increase the velocity along the cell by reducing the cross-section to compensate the reactant depletion. The radial electrode geometry showed promise for adapting the stoichiometric ratio along the flow path while also preventing any stagnant region [227]. The downside of this design is increased pressure loss.

Once the design is optimized at the single-cell level, the whole stack and its related challenges should be considered to investigate the flow distribution between the parallel cells and take into account the shunt current problems, arising from the hydraulic connection of the cells by means of the conductive electrolyte. Xing et al. were the first to model shunt currents at stack-level RFB with the circuit analog approach [228]. They showed in particular that increasing the resistance of the channels end manifolds were viable developments to decrease the shunt current loss.

The higher-level modeling approach would include the pumping power to effectively address the total RFB system performance, by taking into account the losses from the pump consumption. This would open the way for a global optimization of stack design. For example, Xu et al. introduced a power-based efficiency criterion and evidenced that the optimal flow rate depended on the flow design of the cell [229].

6.1.3. Clear flow cell experiment

To complement the modelling study, an experimental set-up was developed to get a flow visualization of the electrolyte in the half-cell of a stack.

A clear cell was designed at reduced scale (1:5) and was composed of two acrylic end plates enclosing a frame that was 3D-printed by the UNSW-owned company Perdix [230] and by the

Lorraine Fab Living lab (LF2L). The frames were printed by stereolithography in the equipment pictured in the left-hand side of Fig. 6.7, from computational objects. The principle of this additive technique is the polymerization of the object layer by layer from a vat of resin [231]. The raw material used was a mix of polymer mixture that provides a sturdy object with a clear aspect. This process allows for great freedom of designs with high precision. A printed frame still on its supporting structure is displayed in the right-hand side of Fig. 6.7. The object was separated from the support and then polished to obtain a smooth surface.

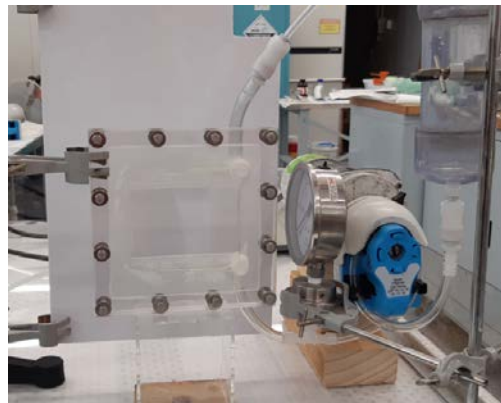


Figure 6.7: Stereolithography printer used to manufacture the clear frames. On the right-hand side, example of frame just after printing.

Figure 6.8: Clear cell set-up used for flow visualization

The frames were sketched on a CAD software (Fusion 360 from Autodesk) before being sent to the printer. Several channel designs, based on the possibilities explored at Kemiwatt, were examined. The computed frames are presented in Fig. 6.9:

- Frame A is the configuration studied in the hydrodynamic model that includes four levels of channel.
- Frame B is a modification of the first layout: the channels were redrawn with funnel-shape openings to avoid the recirculation highlighted by the simulation (Fig. 6.6) and no outer ribs.
- Frame C is a simplified design also tested at Kemiwatt, including only one level of channel in the form of a funnel feeding a network of ribs.

The central open region embodies the active surface containing the compressed porous electrode in the operational battery. The 3D-printed frames do not include any seal, since the tightness of the clear cell was ensured by spreading transparent silicon on the frame before assembly. This protocol can lead to irregularities of the silicon layer, and thus small defects in the channel. The set-up used is pictured in Fig. 6.8. The frame was connected to a tank and a peristaltic pump by transparent pipes. It was held vertically to mimic the real position of the stacks, with a flow from bottom to top. The test always begun by flowing water through the circuit at a high flow rate of 100 mL min^{-1} . The flow was then reduced to 25 mL min^{-1} , corresponding to $u = 10 \text{ cm s}^{-1}$ and $\text{Re} = 153$ in the inlet channel; this is representative of the flow in a large cell (subsection 6.1.2). A drop of dye was added in the tank, and the flow of the coloured liquid through the set-up was captured by filming the clear cell.

Snapshots of the videos of flow are presented and discussed below.

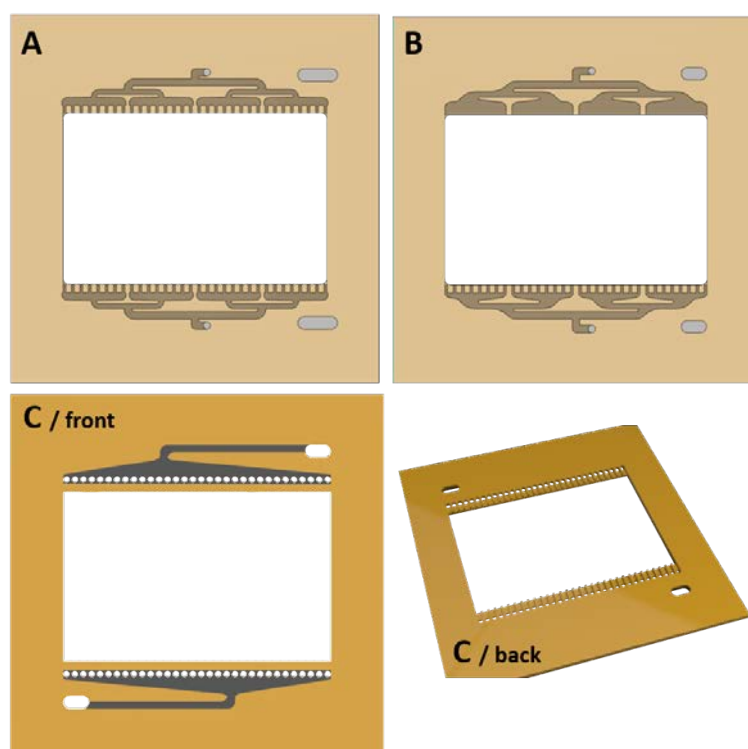


Figure 6.9: Designs of the 3 frames A, B and C printed and tested in the clear set-up

A global view of the flow distribution with the three frames is displayed in Fig. 6.10. All pictures feature preferential streamlines of the liquid inside the open region. For frames A and B, it is clearly influenced by the position of the inflow and outflow, both on the right-hand side of the frame. This entails a low supply of liquid on the upper-left corner.

This drawback was taken into account in the frame C where the feeders were diagonally opposed. Nevertheless, there still is a preferred direction of flow, between the two openings of the inlet and outlet channels.

In frame A, numerous bubbles trapped inside the half-cell can be observed. The Frame B was developed consequently by removing the outer ribs. The visualization proved that this design facilitated the release of these bubbles out of the cell.

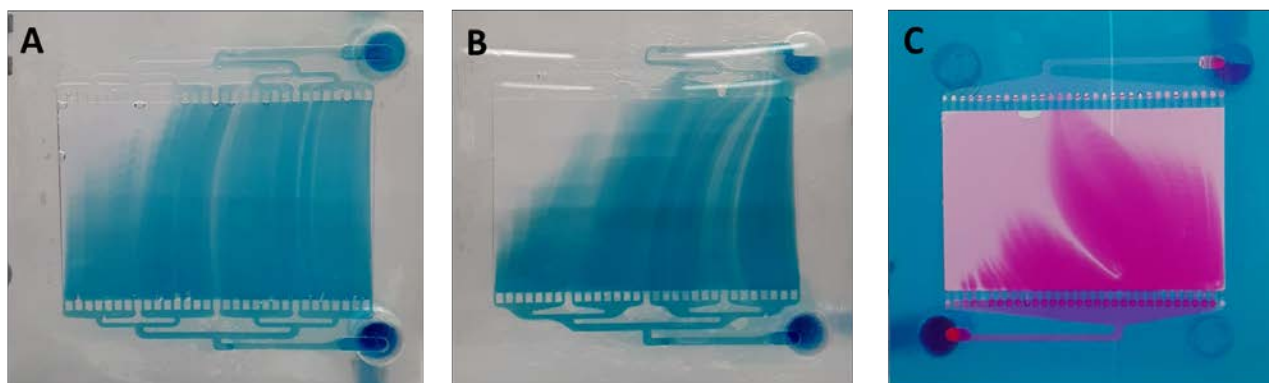


Figure 6.10: Global flow visualization in the clear cell with the three frames, flow of water at 25 mL min^{-1}

These outcomes highlight a non-ideal flow distribution throughout the open region, despite sophisticated channel configurations. This confirms the simulation results presented in [subsection 6.1.2](#), which outlined preferred flow paths in the absence of porous electrode in the active surface. Furthermore, the influence of the feeder positions is key: they should be placed diagonally to enhance the distribution.

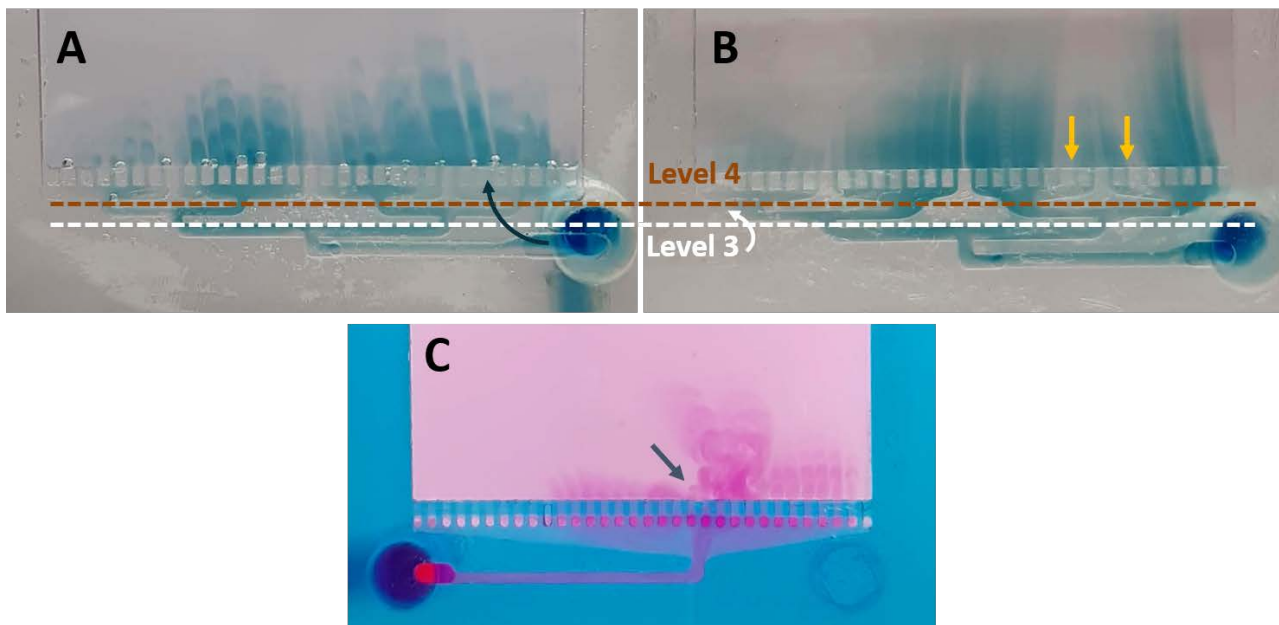


Figure 6.11: Flow visualization in the inlet channels of the three frames, flow of water at 25 mL min^{-1} . The arrows outline some features mentioned in the text.

Fig. 6.11 gathers early snapshots zoomed in on the channel inlets, for the three frames. Frame B was developed in light of the results obtained with Frame A. The flow distribution inside the inlet channel is compared on top of Fig. 6.11. The flow is not uniform from Level 3 of Frame A and is more intense in the central parts of the channel. Level 4 induces further heterogeneity with a preferred path facing the openings of Level 3. The modified Frame B visibly ameliorates the distribution at the third level. Nevertheless, the funnels of Level 4 are too much oriented towards one side, hence a lack of supply of the furthest ribs (highlighted by the yellow arrows). For Frame A and B, the poor supply of the left-end side is clearly visible in the zooms. As already exemplified by Frame B, the use of a funnel-shape channel in Frame C is not sufficient to provide homogeneous flow. Indeed, the ribs on the far left are not supplied in dye while it already penetrated a third of the active surface in front of the channel opening. There is also a neat streamline inside the funnel that seems to create a recirculation zone on the left, delaying the supply on the left of the main path; this is pointed out by the dark arrow in Frame C. The consequences of this defect are observed in Fig. 6.10 where an uncolored line materializes in the middle of the open region.

Additionally, a by-pass was detected for several tests, from the feeder to the open region as depicted by the dark arrow in Frame A (Fig. 6.11). This bias was caused by a leakage between the surface of the frame and the clear end plates, due to uneven spreading of the silicon before assembly. Unlike in the clear cell, the industrial frames do contain gaskets around the active surface and around the channels, to avoid any by-pass. In this regard, the tightness of the clear set-up could be improved to emulate the real configuration.

The flow visualization was tested with the presence of a porous electrode (similar to the graphite material used in the real cell) in the open region. Fig. 6.12 compares the observation before and after adding the porous matrix in the case of Frame B, with zooms on the inlet and outlet channels. It must be noted that the material had the same thickness as the clear frame (3 mm) was indeed not compressed in the set-up. Its porosity was similar to the electrode used in the battery (95 %). Water was flowed at 100 mL min^{-1} for 1 h before using the dye, to force the wetting of the porous electrode.

In spite of the porous electrode, the same pattern is observed in the inlet and outlet channels. This substantiates that the porous electrode may not perfectly homogenize the flow distribution, as opposed to what predicated the simulation (subsection 6.1.2). The porous electrode being opaque, the visualization was not possible in this zone.

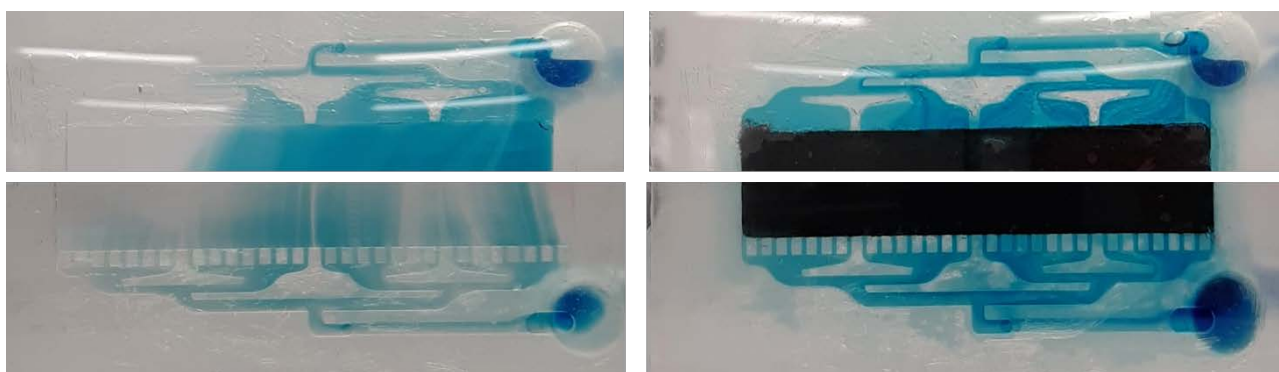


Figure 6.12: Flow visualization in the inlet and outlet channels of frame B, with or without porous electrode (no compression). Flow of water at 25 mL min^{-1}

The test was performed again with the electrode compressed to the same ratio as in the real system (35 %), but the results were not conclusive: many bubbles stayed trapped inside the clear cell and a by-pass was observed on one side of the electrode. This unravels the difficulty to wet the hydrophobic electrode and the need to improve the tightness of the clear cell set-up so that the liquid is forced to flow through the porous matrix.

An industrial perspective

Similarly as in the clear cell, the removal of air bubbles can be an issue for the industrial stack. Initially present in the half-cell, they appear to be difficult to expel:

- They can stay trapped inside the pores, even after a long duration of circulation. This was revealed by the IRM study in Fig. 5.27.
- If dislodged from the porous structure, they might still block some parts of the channel (as visible in Fig. 6.10 for Frame A and C). This could create dead zones or recirculation and hamper the pressure drop.

To overcome this issue, several strategies can be contemplated. The porous electrode could be pretreated to increase its wettability, the channels could be enlarged and designed to facilitate the release of air (as it was made with Frame B), or the stack could be placed under vacuum before starting the flow of liquid (which is certainly the most effective solution but least adaptable to battery manufacturing).

The flow visualization tests performed during this PhD were preliminary but showed that the clear cell was an efficient tool to diagnose the flow behavior inside the half-cell of a RFB. It shows the importance of the channel designs on the uniformity of the flow and pinpoints the problem of electrode wetting and air bubbles removal.

The clear cell tightness could be improved by adding gaskets in the vicinity of the channels or securing the silicon spreading to avoid any irregularity.

The experimental study could be complemented by using specific fluids instead of pure water, such as highly viscous liquids or suspensions, to mimic the characteristics of the anolyte (subsection 3.2.2). A part of the inlet channel could also be intentionally clogged to examine the consequences on the downstream flow distribution.

The cross-sectional flow inside the porous electrode at a local level could be observed with the NMR study in subsection 3.4.2. A further development could be considered to investigate the flow distribution inside the entire porous electrode of the clear cell platform. A fluorescent tracer could be added to the real electrolyte, since the liquid would not necessarily be transparent anymore. The workability of this method was already validated at the laboratory: the clear cell permits the detection of the tracers excited by a laser beam inside the porous electrode, because this material does not fluoresce. Using a high-resolution camera could even allow microfluidic studies thanks to pore-scale imaging. Such diagnostic tool would yield crucial highlights for the RFB technology development.

6.2. Flow rate optimization

As substantiated in the hydraulic study, the flow-through configuration of a RFB stack induces a substantial pressure drop through the porous electrode. This inevitably causes pumping losses that impair the global efficiency of the system. While several modifications of the porous structure could reduce the pressure losses, a straightforward method is the optimization of the flow rate itself during cycling. This section explores the relevance of such strategy.

6.2.1. Strategy

The study of flow rate optimization is based on the results of the preceding parameter study (section 5.3) and is conducted on the segmented cell. Variable profiles (VPs) of flow rate are constructed from the operational maps in Figs. 5.45 and 5.46 for charge and discharge. As such, the \dot{q} VPs integrate the σ_j^* criterion to ensure a good current uniformity throughout the cycle.

These profiles are plotted versus SOC in Fig. 6.13a. The discharge VP is plotted against 100–SOC to be similar to the one in charge. They are compared to the conventional flow rate control used in the literature [232], defined relative to the stoichiometric flow rate and multiplied by a flow factor (FF) of 4 (Eq.(5.1)). Indeed as the reaction advances, stoichiometric ratio would decrease with a constant volumetric flow rate.

The charge and discharge are slightly different, in the fact that the step at 50 mL min^{-1} must be set earlier during discharge and lasts over a wider range of SOC, because the middle of the discharge phase coincides with hampered local current homogeneity Fig. 5.31. The profiles are very close to the optimal flow rate dictated by the stoichiometry with a FF

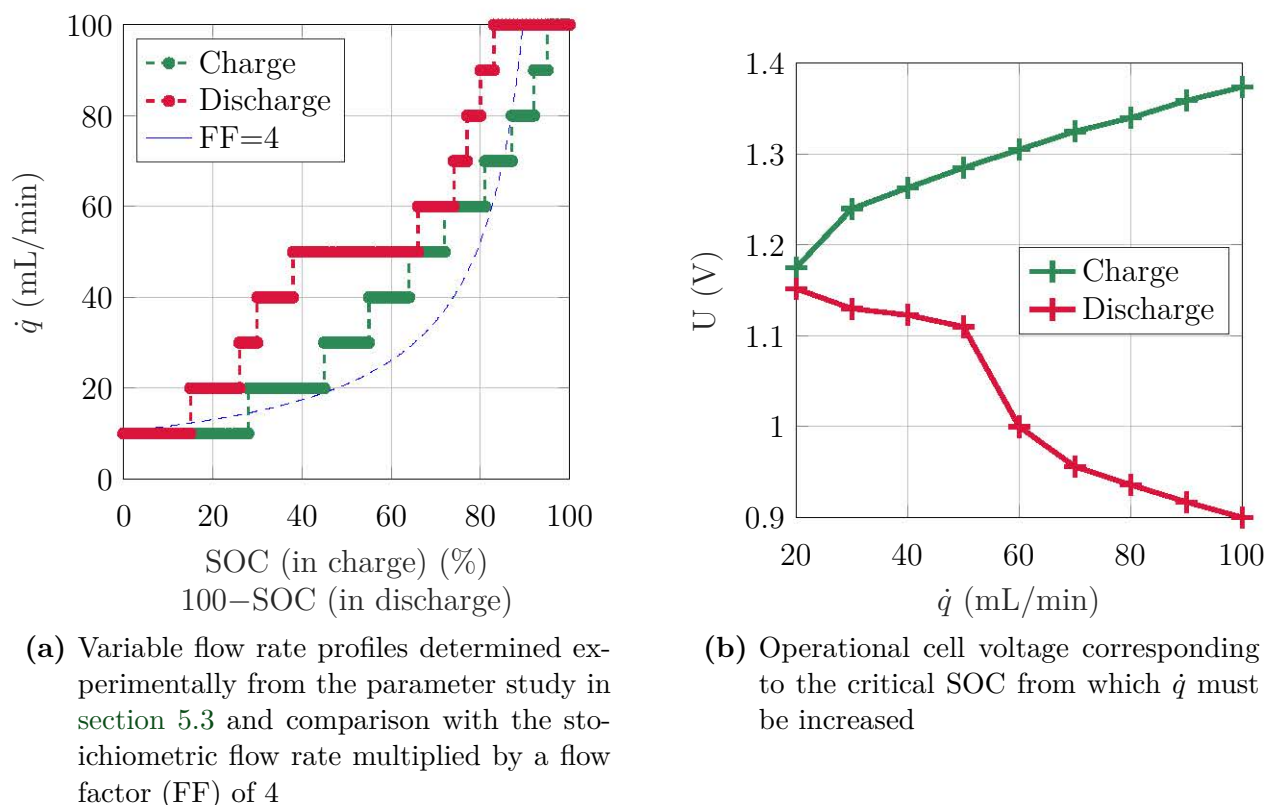


Figure 6.13: Proposed flow rate optimization deduced from the parameter study (section 5.2): flow rate variation versus SOC and corresponding operational cell voltage at the critical SOC

of 4. This shows the relevance of the criterion based on current uniformity, and confirms that the reactant depletion is directly correlated to the increasing heterogeneity observed during a cycle.

The operational voltage corresponding to the critical SOC of Fig. 6.13a is reported against the flow rate in Fig. 6.13b. It exhibits a progressive variation versus \dot{q} especially in charge, which emphasizes the possibility to adapt the flow rate accordingly to the cell voltage.

An industrial perspective

The flow optimization according to the SOC can easily be implemented to the industrial level since there is an unambiguous correlation between the optimal flow rate and the cell voltage. The control voltage must be adapted to the stack size by multiplying the unit cell value to the number of cells composing the stack, provided that the flow is uniform throughout the stack. The strategy presented here is only valid for a current density of 40 mA cm^{-2} , but could be extended to other cycling currents according to the operational maps of the previous chapter.

The flow rate optimization was studied on the segmented cell subsequently to the parameter study of section 5.2. A cycle was performed with the VPs applied to charge and discharge. The same profile was operated concurrently on the catholyte and the anolyte. Two VPs were tested, interspersed with 5 cycles in standard conditions (i.e. $\dot{q} = 100 \text{ mL min}^{-1}$):

- ➔ VP1 strictly corresponded to the profiles given in Fig. 6.13a.
- ➔ VP2 was essentially the same but the step at 10 mL min^{-1} was skipped to start each phase of the cycle from 20 mL min^{-1}

6.2.2. Results

Figs. 6.14 and 6.15 present the results in charge and in discharge respectively. The flow rate, the cell voltage and the standard deviation of the local currents σ_J^* are charted in three subplots. The two VPs are compared to the data of constant flow rate cycles at 10 mL min^{-1} and 100 mL min^{-1} (standard conditions, noted SC). The low flow rate cycle comes from the parameter study conducted earlier on the set-up while the SC cycle was recorded just before launching the VP profiles. It can be mentioned that the small fluctuations of flow rates are detected because of the diaphragm pumps.

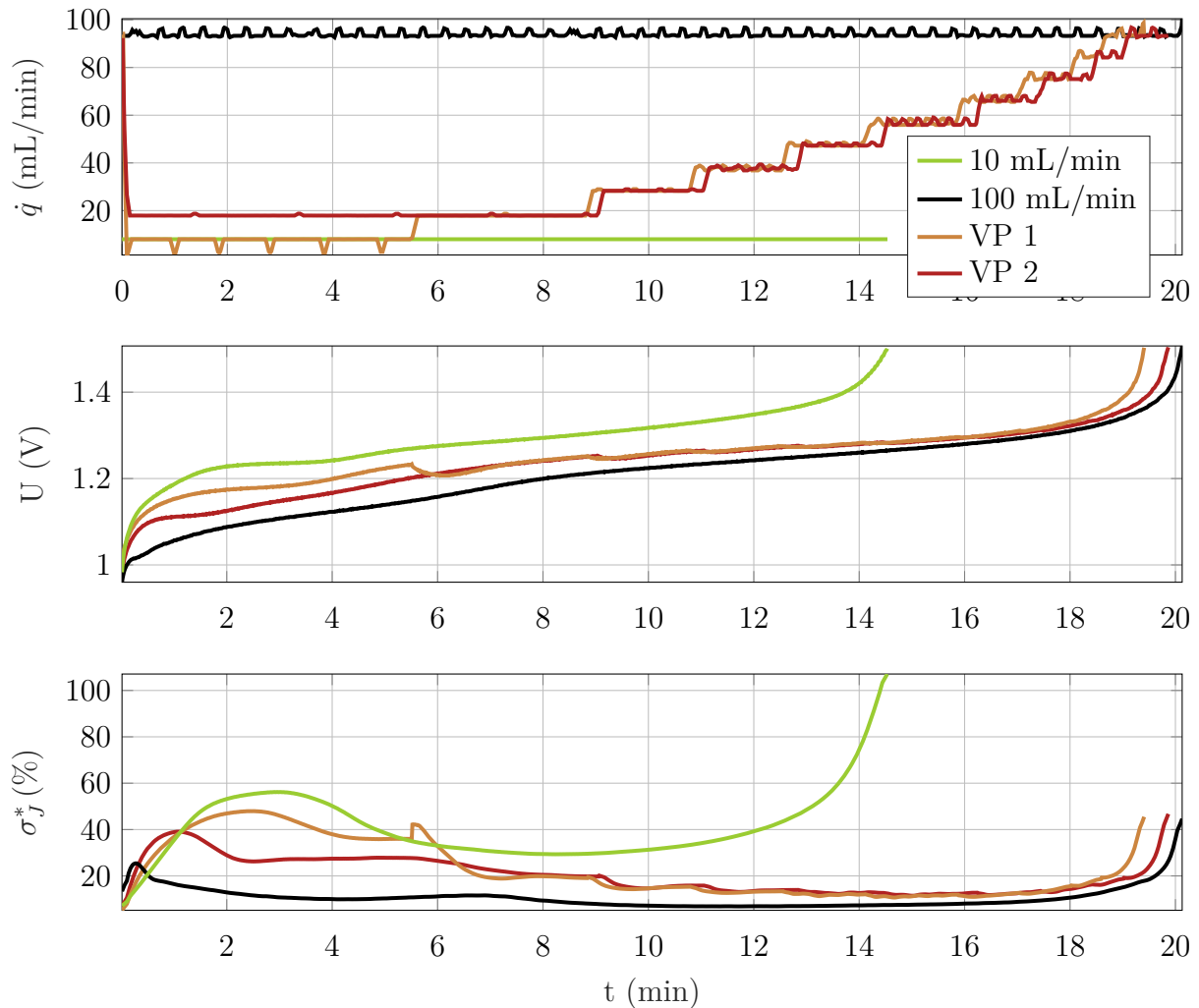


Figure 6.14: Charge data (flow rate profile, cell voltage and standard deviation of local current) for cycles at 10 and 100 mL min^{-1} and the two variable profiles, cycles at 40 mA cm^{-2} and 25°C

The most promising observation is the comparable capacity accessed with VPs or with the

reference cycle at 100 mL min^{-1} . VP 1 gives access to 95 % of the reference capacity, while VP2 represents 99 %. This outlines the great opportunity of adapting the flow rate with SOC.

The cell voltage is marked by the change of flow rate, especially at low flow rate. The first portion of $U(\text{VP1})$ is slightly lower than the curve corresponding to 10 mL min^{-1} , which is ascribed to the aging of the test that occurred between these two cycles, as already illustrated in Fig. 5.6. From 20 mL min^{-1} , VP1 gives the same voltage response as VP2. The VPs allow the leveling of the cell voltage evolution during charge. At the end of charge, from 15 min, the voltage of the two VPs meet the one in SC. This shows that the choice of flow rate only affects temporarily the cell voltage, but has no consequence on U once \dot{q} is increased.

The standard deviations of current are as expected: VP1 exhibits a high hump at start of charge, close to the characteristic of the cycle at low flow rate. After the step at 10 mL min^{-1} performed in VP1, the current uniformity follows the same evolution for the two VPs. It is generally higher than at 100 mL min^{-1} . As already revealed in the parameter study (subsection 5.2.3), the spike of σ_j^* at start of the process cannot be avoided but is most prominent and extended at low flow rate. As a consequence the target deviation threshold of $\sigma_j^* < 20 \%$ cannot be achieved before 8 min (the first 40 % of the charge).

Similar observations can be retained from the discharge phase in Fig. 6.15. The discharge capacity is also satisfying for the two VPs. The coulombic efficiency calculated over the full cycle is 98 % for both VPs, against 99 % in SC. The global energy efficiency equals 80 % with the two variable profiles of flow rate, which is close to the efficiency in SC (85 %).

During the step at 10 mL min^{-1} , VP1 exhibits similar voltage and standard deviation of current than the discharge at this flow rate. The rest of the discharge is identical for VP1 and 2. Unlike in charge, the voltage signals with VPs never meet the voltage curve in SC. This shows that low flow rates set early in the stage affect to a larger extent the end of this stage in discharge than in charge.

Concerning the cell uniformity, the VPs are effective in maintaining σ_j^* below 20 % during most of the discharge.

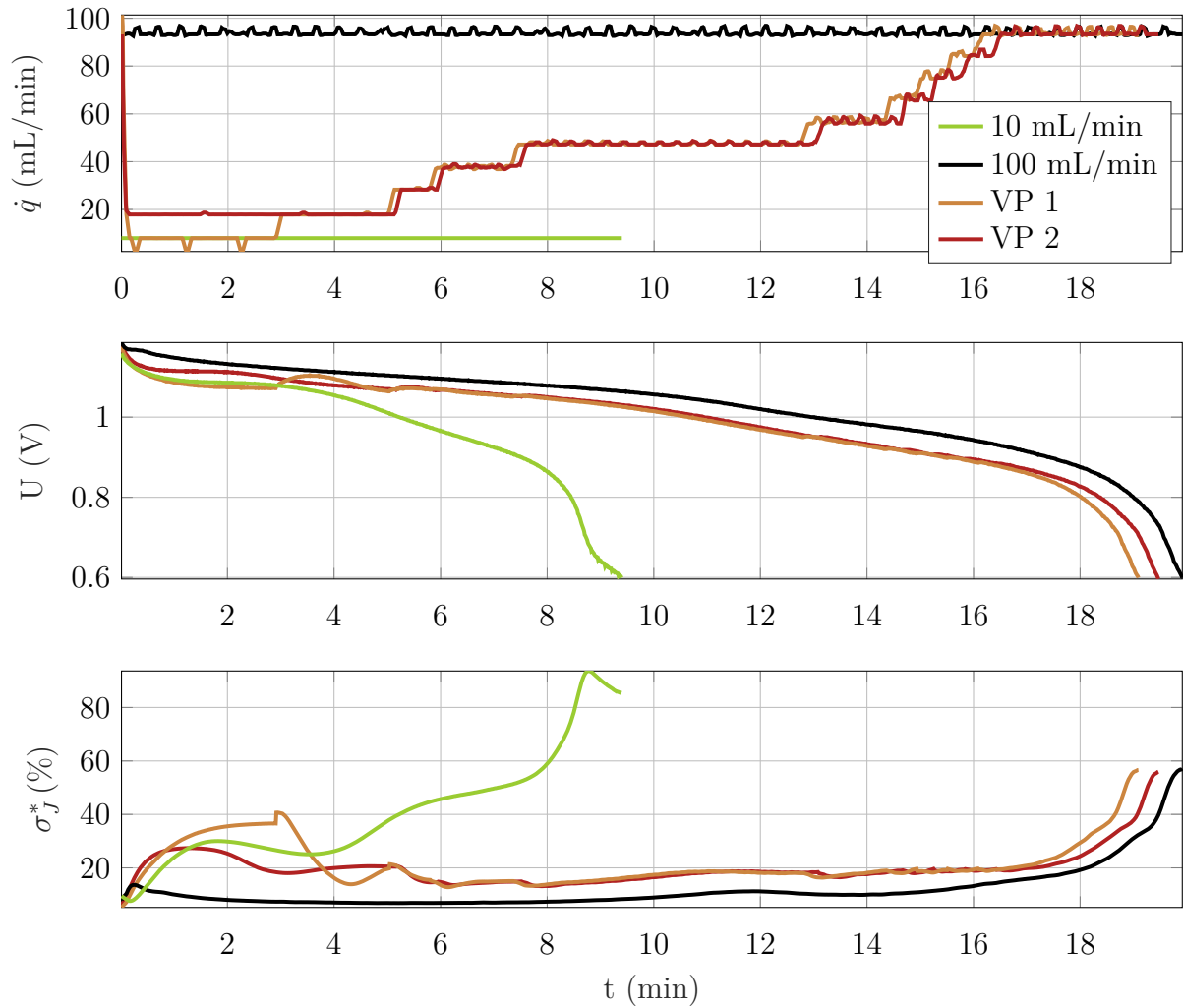


Figure 6.15: Discharge data (flow rate profile, cell voltage and standard deviation of local current) for cycles at 10 and 100 mL min⁻¹ and the two variable profiles, cycles at 40 mA cm⁻² and 25 °C

An industrial perspective

The variable profiles of flow rate yield good energy efficiency and accessed capacity. These performance metrics must be correlated to the pumping power efficiency to quantify the global gain of such strategy on the RFB system. The range of flow rate used in the segmented set-up is not entirely representative of the flow conditions in the final system, therefore the optimized profiles should be adapted consequently.

By comparing the charge and discharge data, it can be observed that the cell homogeneity is generally better in discharge than in charge with VPs. It is particularly critical at start of charge. To mitigate this effect, it was proposed to delay the variable profile by beginning the charge at 100 mL min⁻¹ for a brief period (5 % of charge). The results for VP2 with or without this delay are presented in Fig. 6.16 for the charge step. The curves are plotted against SOC to focus on the effect of the delay on the signals. It is noteworthy that the two tests yielded an equivalent access to capacity.

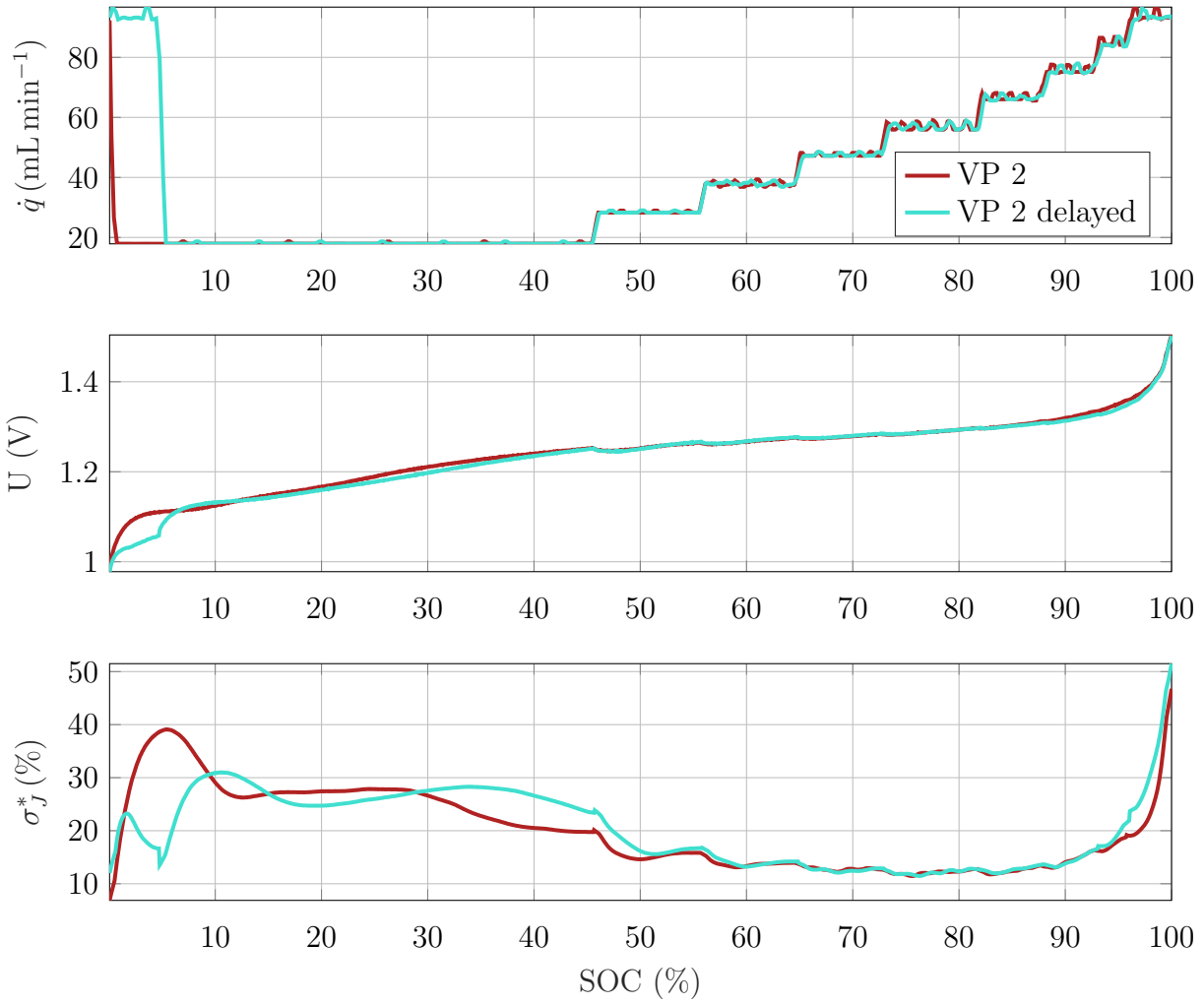


Figure 6.16: Charge data (flow rate profile, cell voltage and standard deviation of local current) for the variable profile 2 with or without an initial step at 100 mL min^{-1} (5 % of the charge)

The initial step at high flow rate has a prominent impact on both the cell voltage and the standard deviation. The cell heterogeneity is interestingly reduced thanks to this strategy, and the spike at $\sigma_j^* = 40\%$ is avoided. After the delay at 100 mL min^{-1} , the standard deviation increases but does not exceed 30%. VP2 and VP2 with delay follow the same evolution for the rest of the charge. The discharge phase was improved similarly by the delayed VP.

Ma et al. tested a comparable strategy on a kilowatt-classe module of VFB, by increasing the flow rate at a given stack voltage in charge and in discharge [212]. The stack voltage was affected in the same fashion as the cell voltage presented in Figs. 6.14 and 6.15. they evaluated an improvement of 8 % of the system efficiency, with a sustained cycling capacity.

Ling et al. explored the strategy of pulsating electrolyte flow (pumps alternately on and off) on a small VFB cell [233]. They also outlined an increased energy efficiency but at the expense of higher concentration polarization. Their approach certainly drives undesirable internal heterogeneity that can be deleterious in the lung run.

The flow rate optimization gives promising results: the profiles tested ensure an energy efficiency and accessed capacity almost as good as the cycle at highest flow rate. This high-

lights that the flow rate can easily be adapted to the SOC of the battery without impairing the performance. Moreover, such strategy substantially mitigates the system losses due to pump consumption. The global efficiency including this aspect could not be assessed during this study, since the pump sizing was not comparable to the industrial RFB system.

6.3. Conclusion

This last chapter was an introduction of the challenges related to the hydrodynamic aspects of the RFB technology. Three separate diagnostic studies were performed, all of each drawing complementary and meaningful conclusions.

The simple hydraulic model revealed the critical pressure drop induced by the presence of the porous electrode. Several suggestions could be envisioned to mitigate this effect.

The experimental clear cell technique showed interesting insights and pinpointed the importance of the channel design on the flow distribution. The results also raised questions about the electrode wetting and the removal of air bubbles from the inside of the stack. The combination of fluorescence technique was proposed to extend the relevance of this device.

The third study focused on a strategy of flow optimization by adapting the flow rate according to the SOC and to the direction of current (charge or discharge), based on the insights of the parameter study (section 5.2). The results were encouraging and revealed the possibility to minimize the pump consumption without affecting the battery performance.

All these highlights must be assessed in regard to the whole RFB system, by taking into consideration the cycling conditions, the aging of the system, the effect of shunt currents in the stack, and the global efficiency of the whole plant.

CONCLUSIONS AND OUTLOOK

Given the exigency to find solutions for a more sustainable society, energy storage arises as a crucial challenge that has not been solved yet, despite the intensifying research efforts. The Redox Flow Battery is an appealing technology that might be able to tick the low-cost, sustainable, long-life and easy-operation requirements for the widespread commercialization of such system. The collaboration of LEMTA and Kemiwatt through this PhD work intended to develop a strong knowledge baseline of the technology being industrialized at the company. Furthermore, there was a desire of comprehending how the selected chemistry would impact the operation of the battery.

Summary

This PhD thesis strived to address the RFB intricacy by analyzing the system at all levels. The degree of complexity was progressively increased to deconvolute the influence of each component and to conclude on specific precautions to be taken for the correct operation of the battery. The work being carried out at a multidisciplinary lab and in collaboration with the renowned RFB team at UNSW, several unique characterization techniques and analytical platforms could be integrated to the study.

First, all the components of the cell were assessed separately: the actives species, the membrane and the electrode. A thorough electrochemical analysis was performed on the concentrated electrolytes and showed converging results although the theory was first developed for dilute solutions. Several membrane pretreatments were examined by Fourier-transform infrared spectroscopy before evaluating the impact of the cationic content of the electrolyte on the membrane resistance. The latter investigation was conducted on a specific cell set-up and also served for the characterization of the porous carbon electrode. The flow behavior in the electrode was observed at a microscopic scale by magnetic resonance imaging.

The next step proposed was the half-cell characterization of the RFB. The electrolytes were independently examined in operating conditions of the RFB, by making use of a symmetric cell configuration. This technique helped to bridge the gap between ex-situ characterization and full RFB cell operation. The two-step study consisted in observing the cell resistance evolution (by electrochemical impedance spectroscopy) during circulation and then during cycling, so that a calendar effect could be decoupled from the cycling-related evolution. Contrasting responses were observed from the two electrolytes. Important mass-transfer losses emerged with the anolyte circulation, while the catholyte featured increasing charge-transfer losses. These observations were reinforced by the use of inverse problem methodology to determine

in-situ key features, namely the reaction rate constant and the membrane resistance. The effect of active species concentration on the cell performance was also addressed in the symmetric cell.

The full-cell level was tackled by the development of an instrumented test bench, where the major operating parameters could be accurately monitored and tuned: the flow rate and the internal pressure drop, the temperature and the current density. Moreover, the internal current distribution could be followed by means of the segmented cell. A concerted effort was put into securing the local potential probing in the segmented cell, but it was proved impossible in the present cell arrangement.

A validation case was first performed in standard conditions, before examining the battery performances over 300 cycles. The full-cell study was pursued by a thorough parameter study comprising the current density, the flow rate and the temperature. Cycles along with Polarization Curves unraveled how these three operating parameters alter the global response of the system. Thanks to the spatially-resolved measurement available in the segmented cell, the global behavior could be related to local processes. The distribution of the local currents was mostly evaluated through the standard deviation metric. This investigation gave unprecedented insight of the internal operation of a RFB, with peculiar features appearing at the start of the charge or discharge process. Some aspects of the local current distribution could be unambiguously attributed to the anolyte successive reactions, in light of the preceding outcomes of the half-cells characterization.

By combining the results of the parameter study and defining a threshold of acceptable internal heterogeneity during cell operation, an empirical operational map was proposed: it allows the control of the flow rate depending on the mode of operation (charge or discharge and current density magnitude) and the state of charge of the system. The strategy was tested for three cycles and showed maintained capacity with satisfactory internal homogeneity, while the pump consumption was greatly reduced.

The last part focused on the hydraulic challenge arising from a stack-level perspective. A simple hydrodynamic model highlighted the major impact of the porous electrode on flow homogeneity, at the expense of high pressure drop. The design of the frame holding the electrode could also be investigated, by flow visualization in a clear cell platform. The combined techniques unveiled the importance of the half-cell design, and optimization strategies could be suggested.

At all stages of the investigation, an unconventional approach was proposed and showed a real interest for improved understanding.

Learnings and future directions

The PhD work was restricted to a predefined chemistry, along with lab-scale experiments, but the outcomes hold great significance for the industrial development of the technology and the research community.

- * The major conclusion is that *the organic/organo-metallic species combination under study is suitable for the RFB system*. It exhibits promising performances of energy efficiency and cycling lifetime. The organic ARS molecule shows peculiar features with a reactive initial form that rapidly evolves into a stable “aged” configuration during cell

cycling. This generates the coexistence of two electrochemical reactions during charge and discharge of the battery. The underlying degradation process could be partly identified. Relating to this mechanism, the electrolyte rheological behavior changed notably between the fresh and the used solution.

The degradation mechanism of the ARS is particular to this molecule. Other organic species reported in the literature or tested at Kemiwatt did not show the exact same behavior, but can face similar challenges of instability and high viscosity in one of the two forms (charged or discharged molecule). As such, the thorough study of this specific active material draws essential conclusions about the system management and how to handle phenomena such as successive reactions or viscous solutions.

- * The specific anolyte behavior greatly affects the system response as observed in the parameter study. This complicated the analysis and interpretation of phenomena but is a compelling example of the interest to investigate thoroughly each component involved in the technology. *Underlying processes are not to be disregarded and are essential to designing robust and competitive energy storage systems.*
- * Another essential learning is that *the compatibility between the components of the battery is not straightforward and must be addressed carefully*. If not, unexpected interaction can occur in the full system, and is impossible to identify at that level of complexity. Since the energy storage system is expected to have a long lifetime (current claim is 20 years), the compatibility tests should be run over an extended period to detect any long-term undesirable degradation. Examination of the materials post-mortem could be used to identify the degradation mechanisms. Furthermore, the scenarios of system failure should also be anticipated alongside their respective consequences. External factors effects (such as light, oxygen) must also be taken into account when developing the system.
Cell components engineering is an essential point to be discussed with the suppliers. For instance, membrane pretreatment proved essential to be compatible in the system under study.
- * The half-cell characterization proposed *brought further knowledge on the ferri/ferro redox couple*, today widely adopted with an organic anolyte. Indeed this active species takes part into many RFB systems described in the literature, while its own performance into a flow battery is only scarcely reported.
- * This work completes the methods of characterization already described in the literature by *proposing new analytical platforms*; they could be integrated to the systematic assessment procedure followed for the development of any RFB chemistry. As already mentioned in the document, the investigation benches could be improved. The monitoring of local electrode potentials were not included in the segmented cell tests, because the internal electrode reference was not reliable. The bench configuration could be rethought to install a reliable potential measurement, which would give complementary insights of the local phenomena.
The clear cell from the hydraulic study also offers many possibilities to leverage it. An interesting idea is the combination with fluorescence technique that would allow the flow visualization inside the porous material. This technique could also be proposed

at the industrial cell scale.

- * The operational map, optimizing the flow rate according to the duty point, should be adapted and tested on an industrial stack. Indeed, *questions can arise about the relevance of the lab-scale tests for the system level*. The flow strategy proposed was based on keeping a satisfactory internal homogeneity of the cell. Nevertheless, the outcome of highly-heterogeneous operation should be properly quantified over the long run, to validate if this is really critical for the system and after how many cycles. In addition to examining the cell internal uniformity, the battery efficiency should also be evaluated. It would encompass the other sub-systems, such as the pumps and inverters, and would allow an adequate optimization strategy at the system level.
- * Two aspects of the multiphysics RFB technology have been examined by modelling: the electrochemical and hydraulic parts. A shunt current model was also started but was not sufficiently advanced to be presented in this document. These tools should now be combined to *build a reliable multiphysics system level model*, accounting for all the convoluted loss mechanisms occurring in the battery.

The PhD work developed the building blocks constituting an in-depth analysis of Kemiwatt's technology. The effort of combining them into a reliable optimization approach will be pursued at the company to meet the next challenge of industrialization large-scale industrial implementation.

APPENDICES

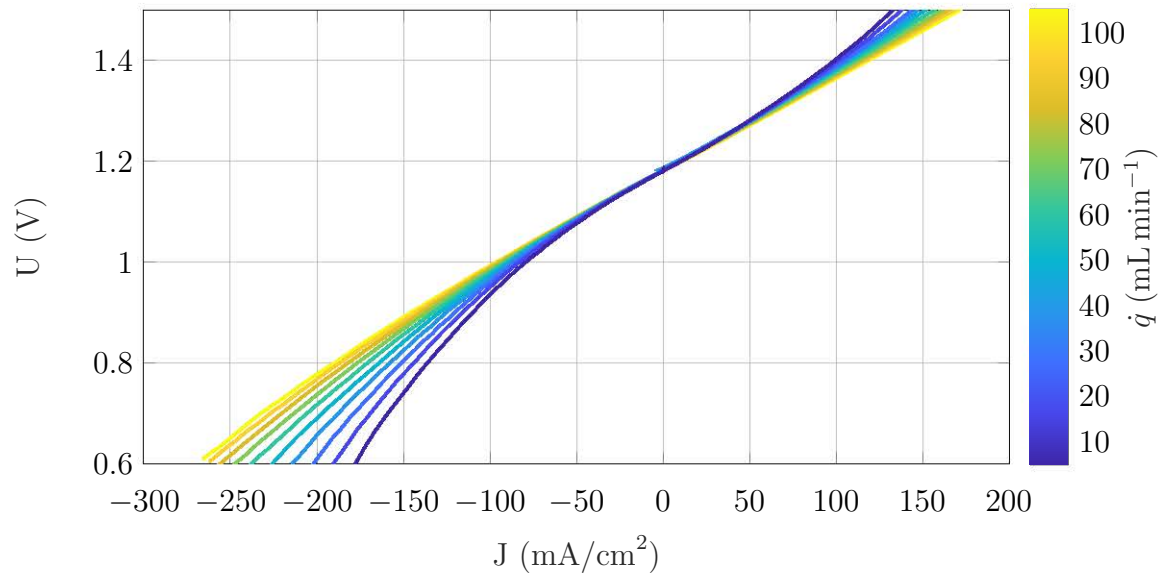


Figure 6.17: Global Polarization Curves for all flow rates tested, performed during the parameter study in [Chap. 5](#)

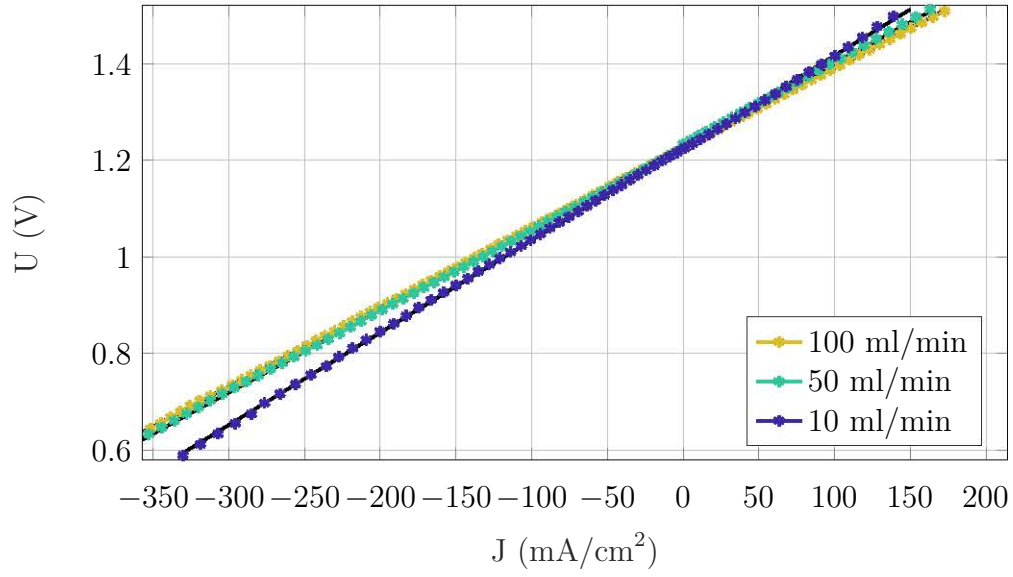


Figure 6.18: Local Polarization Curves of Seg.#1 at SOC 20 for three flow rates performed during the parameter study in Chap. 5

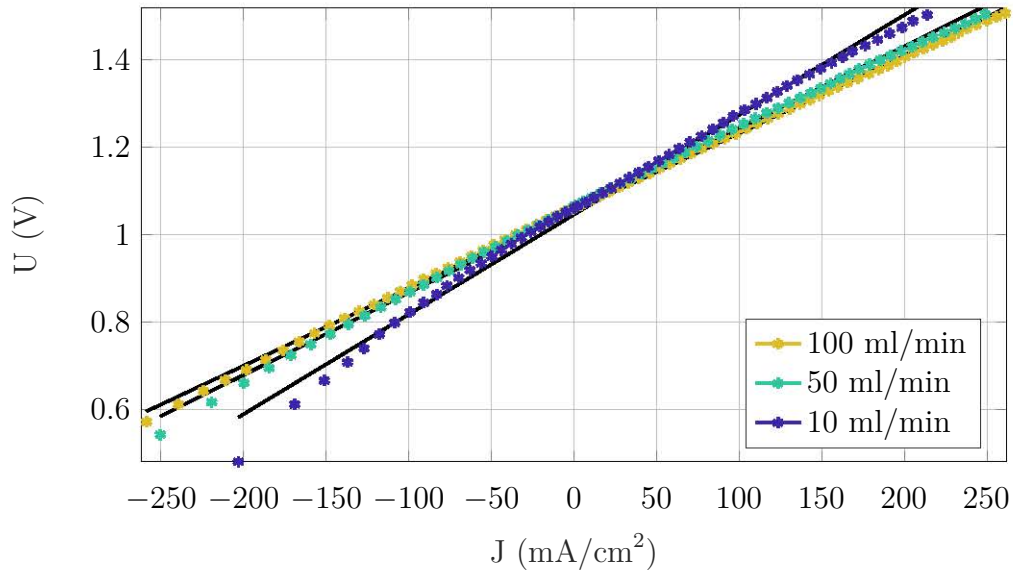


Figure 6.19: Local Polarization Curves of Seg.#1 at SOC 80 for three flow rates performed during the parameter study in Chap. 5

BIBLIOGRAPHY

- [1] Adam Z. Weber et al. Redox flow batteries: A review. In: *Journal of Applied Electrochemistry* 41.10 (2011), pp. 1137–1164.
 - [2] Aurore Lê. “Electrolytes with organic-based active species for aqueous redox flow battery”. PhD Thesis. Université de Rennes 1, 2018.
 - [3] Mark Peplow. Cheap battery stores energy for a rainy day. In: *Nature.com* (2014).
 - [4] Maria Skyllas-Kazacos. *All-Vanadium Redox Battery*. 1988.
 - [5] John S Newman and Charles W Tobias. Theoretical Analysis of Current Distribution in Porous Electrodes. In: *Journal of The Electrochemical Society* 109.12 (1962), pp. 1183–1191.
 - [6] Sofyane Abbou. “Phénomènes locaux instationnaires dans les PEMFC en mode bouché”. PhD Thesis. Université de Lorraine, 2015.
 - [7] Max Roser, Hanna Ritchie, and Esteban Ortiz-Ospina. *World Population Growth*. 2019. URL: <https://ourworldindata.org/world-population-growth>.
 - [8] BP p.l.c. *BP Energy Outlook 2035*. 2015.
 - [9] Paul W Graham et al. GenCost 2018 Updated projections of electricity generation technology costs. In: December (2018).
 - [10] Richard Martin. *Germany Runs Up Against the Limits of Renewables*.
 - [11] Sören Amelang and Kerstine Appunn. *The causes and effects of negative power prices / Clean Energy Wire*. 2018.
 - [12] Jeff St. John. *Global Energy Storage to Double 6 Times by 2030, Matching Solar’s Spectacular Rise / Greentech Media*. 2017.
 - [13] Piergiorgio Alotto, Massimo Guarnieri, and Federico Moro. Redox flow batteries for the storage of renewable energy: A review. In: *Renewable and Sustainable Energy Reviews* (2013).
 - [14] Rachel Carnegie et al. *Utility Scale Energy Storage Systems*. Tech. rep. 2013.
 - [15] Chi-Jen Yang and Robert B. Jackson. Opportunities and barriers to pumped-hydro energy storage in the United States. In: *Renewable and Sustainable Energy Reviews* (2011).
 - [16] Energy Storage Association. *Flow batteries*. Tech. rep. 2015.
 - [17] D M Davies et al. Combined economic and technological evaluation of battery energy storage for grid applications. In: *Nature Energy* (2018), pp. 1–15.
-

- [18] Ilja Pawel. “The cost of storage - How to calculate the levelized cost of stored energy (LCOE) and applications to renewable energy generation”. In: **Energy Procedia**. Vol. 46. 2014, pp. 68–77.
- [19] Kristina Wedege et al. Organic Redox Species in Aqueous Flow Batteries: Redox Potentials, Solubility and Chemical Stability, Supplementary information. In: **Nature Publishing Group** December (2016), pp. 1–13.
- [20] Manasseh Obi et al. Calculation of levelized costs of electricity for various electrical energy storage systems. In: **Renewable and Sustainable Energy Reviews** 67 (Jan. 2017), pp. 908–920.
- [21] O Schmidt et al. The future cost of electrical energy storage based on experience rates. In: **Nature Energy** 2.8 (2017), p. 17110.
- [22] Imre Gyuk et al. **Grid Energy Storage - U.S. Department of Energy**. Tech. rep. 2013.
- [23] Olivier Teller, Jean-Philippe Nicolai, and Marcos Lafoz. **European Energy Storage Technology Development Roadmap Towards 2030**. Tech. rep. 2017, p. 108.
- [24] Grigorii L Soloveichik. Flow Batteries: Current Status and Trends. In: **Chemical Reviews** 115.20 (2015), pp. 11533–11558.
- [25] C. Ponce de Leon et al. Redox flow cells for energy conversion. In: **Journal of Power Sources** 160.(1) (2006), pp. 716–732.
- [26] Minjoon Park et al. Material design and engineering of next-generation flow-battery technologies. In: **Nature Reviews Materials** 2.1 (2016), pp. 1–18.
- [27] Y. Ashraf Gandomi et al. Critical Review—Experimental Diagnostics and Material Characterization Techniques Used on Redox Flow Batteries. In: **Journal of The Electrochemical Society** 165.5 (2018), A970–A1010.
- [28] See Min-Sik Park et al. A technology review of electrodes and reaction mechanisms in vanadium redox flow batteries. In: **Journal of Materials Chemistry A** 3.33 (2015), pp. 16913–16933.
- [29] Chenxi Sun et al. Investigations on transfer of water and vanadium ions across Nafion membrane in an operating vanadium redox flow battery. In: **Journal of Power Sources** 195.3 (2010), pp. 890–897.
- [30] Zhiping Luo et al. Electro-osmotic drag coefficient and proton conductivity in Nafion membrane for PEMFC. In: **International Journal of Hydrogen Energy** 35.3120–3124 (2010).
- [31] Ao Tang et al. Thermal modelling and simulation of the all-vanadium redox flow battery. In: **Journal of Power Sources** 203 (Apr. 2012), pp. 165–176.
- [32] L F Arenas, C. Ponce de León, and F C Walsh. Engineering aspects of the design, construction and performance of modular redox flow batteries for energy storage. In: **Journal of Energy Storage** 11 (2017), pp. 119–153.
- [33] Craig R Horne and Sheri Nevins. **Long-duration, grid-scale iron-chromium redox flow battery systems**. Tech. rep. 2014.
- [34] Christian Blanc. “Modeling of a vanadium redox flow battery electricity Storage System”. PhD thesis. Ecole Polytechnique Fédérale de Lausanne, 2009.

-
- [35] X L Zhou et al. Critical transport issues for improving the performance of aqueous redox flow batteries. In: *Journal of Power Sources* 339 (2017), pp. 1–12.
- [36] Robert M Darling and Mike L Perry. The Influence of Electrode and Channel Configurations on Flow Battery Performance. In: *Journal of The Electrochemical Society* 161.9 (2014), pp. 1381–1387.
- [37] David Reed et al. Stack Developments in a kW Class All Vanadium Mixed Acid Redox Flow Battery at the Pacific Northwest National Laboratory. In: *Journal of The Electrochemical Society* 163.1 (Nov. 2016), A5211–A5219.
- [38] Maria Skyllas-Kazacos et al. The Mechanism and Modelling of Shunt Current in the Vanadium Redox Flow Battery. In: *ChemistrySelect* 1.10 (July 2016), pp. 2249–2256.
- [39] F T Wandschneider et al. A multi-stack simulation of shunt currents in vanadium redox flow batteries. In: *Journal of Power Sources* 261 (2014), pp. 64–74.
- [40] Cong Yin et al. Numerical and experimental studies of stack shunt current for vanadium redox flow battery. In: *Applied Energy* (2015), pp. 237–248.
- [41] Robert M. Darling et al. The Relationship between Shunt Currents and Edge Corrosion in Flow Batteries. In: *Journal of The Electrochemical Society* 164.11 (2017), E3081–E3091.
- [42] Michael Schimpe et al. Energy efficiency evaluation of a stationary lithium-ion battery container storage system via electro-thermal modeling and detailed component analysis. In: *Applied Energy* 210 (2018), pp. 211–229.
- [43] Sarah Roe, Chris Menictas, and Maria Skyllas-Kazacos. A High Energy Density Vanadium Redox Flow Battery with 3 M Vanadium Electrolyte. In: *Journal of The Electrochemical Society* 163.1 (July 2015), A5023–A5028.
- [44] John Fitzgerald Weaver. *World’s largest battery: 200MW/800MWh vanadium flow battery – site work ongoing*. 2017. URL: <https://electrek.co/2017/12/21/worlds-largest-battery-200mw-800mwh-vanadium-flow-battery-rongke-power/>.
- [45] 2017. URL: <https://hornsdailepowerreserve.com.au/>.
- [46] Williams, Georgia. *Vanadium Outlook 2019: After the “Year of Vanadium,” What’s Next?* 2018.
- [47] P Leung et al. Recent developments in organic redox flow batteries: A critical review. In: *Journal of Power Sources* 360 (2017), pp. 243–283.
- [48] Rylan Dmello et al. Cost-driven materials selection criteria for redox flow battery electrolytes. In: *Journal of Power Sources* 330 (2016), pp. 261–272.
- [49] Robert M Darling et al. Pathways to low-cost electrochemical energy storage: A comparison of aqueous and nonaqueous flow batteries. In: *Energy and Environmental Science* 7.11 (2014), pp. 3459–3477.
- [50] Aishwarya Parasuraman et al. Review of material research and development for vanadium redox flow battery applications. In: *Electrochimica Acta* 101 (2013), pp. 27–40.
- [51] Bo Yang et al. An Inexpensive Aqueous Flow Battery for Large-Scale Electrical Energy Storage Based on Water-Soluble Organic Redox Couples. In: *Journal of The Electrochemical Society* 161.9 (2014), pp. 1371–1380.
-

- [52] Andrew N. Jansen et al. “Organic non-aqueous cation-based redox flow batteries”. 2016.
- [53] Tino Hagemann et al. A bipolar nitronyl nitroxide small molecule for an all-organic symmetric redox-flow battery. In: (2016).
- [54] **ViZn Energy Systems / GS200® Energy Storage**. URL: <https://www.viznenergy.com/product-gs200/>.
- [55] **Redflow Energy Storage Solutions**. URL: <https://redflow.com/>.
- [56] **EnSync Energy Systems**. URL: <https://www.ensync.com/agile-flow-battery>.
- [57] **The Elestor Solution - Elestor**. URL: <https://www.elestor.nl/technology-the-elestor-solution/>.
- [58] **Kemiwatt’s technology**. URL: <https://kemiwatt.com/>.
- [59] Lena Hooper-Burkhardt et al. A New Michael-Reaction-Resistant Benzoquinone for Aqueous Organic Redox Flow Batteries. In: **Journal of The Electrochemical Society** 164.4 (2017), A600–A607.
- [60] Tianbiao Liu et al. A Total Organic Aqueous Redox Flow Battery Employing a Low Cost and Sustainable Methyl Viologen Anolyte and 4-HO-TEMPO Catholyte. In: **Advanced Energy Materials** 6.3 (2016).
- [61] Bo Hu et al. Improved radical stability of viologen anolytes in aqueous organic redox flow batteries. In: **Chemical Communications** 54.50 (2018), pp. 6871–6874.
- [62] Bo Hu et al. Long-Cycling Aqueous Organic Redox Flow Battery (AORFB) toward Sustainable and Safe Energy Storage. In: **Journal of the American Chemical Society** 139.3 (2017), pp. 1207–1214.
- [63] Eugene S. Beh et al. A Neutral pH Aqueous Organic–Organometallic Redox Flow Battery with Extremely High Capacity Retention. In: **ACS Energy Letters** (2017), pp. 639–644.
- [64] Aaron Hollas et al. A biomimetic high-capacity phenazine-based anolyte for aqueous organic redox flow batteries. In: **Nature Energy** 3.6 (2018), pp. 508–514.
- [65] Jian Luo et al. Unprecedented Capacity and Stability of Ammonium Ferrocyanide Catholyte in pH Neutral Aqueous Redox Flow Batteries. In: **Joule** 3.1 (Jan. 2019), pp. 149–163.
- [66] Shijian Jin et al. A Water-Miscible Quinone Flow Battery with High Volumetric Capacity and Energy Density. In: **ACS Energy Letters** 4 (2019), pp. 1342–1348.
- [67] Brian Huskinson et al. A metal-free organic-inorganic aqueous flow battery. In: **Nature** 505.7482 (2014), pp. 195–8.
- [68] Tobias Janoschka et al. An aqueous, polymer-based redox-flow battery using non-corrosive, safe, and low-cost materials. In: **Nature** 527.7576 (2015), pp. 78–81.
- [69] Tino Hagemann et al. An aqueous all-organic redox-flow battery employing a (2,2,6,6-tetramethylpiperidin-1-yl)oxyl-containing polymer as catholyte and dimethyl viologen dichloride as anolyte. In: **Journal of Power Sources** 378 (2018), pp. 546–554.
- [70] Qing Chen, Louise Eisenach, and Michael J Aziz. Cycling Analysis of a Quinone-Bromide Redox Flow Battery. In: **Journal of The Electrochemical Society** 163.1 (2016), A5057–A5063.

-
- [71] Arthur J. Esswein and Steven Y. Reece. “Aqueous redox flow batteries featuring improved cell, design characteristics”. 2016.
- [72] **ViZn Energy Systems / GS200® Energy Storage**. URL: <https://www.cmblu.com/organic-electrolytes/>.
- [73] Tomasz R biś, Ting Yang Nilsson, and Olle Inganäs. Hybrid materials from organic electronic conductors and synthetic-lignin models for charge storage applications. In: **Journal of Materials Chemistry A** 4.5 (2016), pp. 1931–1940.
- [74] Yeni Moon and Young Kyu Han. Computational screening of organic molecules as redox active species in redox flow batteries. In: **Current Applied Physics** 16.9 (2016), pp. 939–943.
- [75] Alan M. Pezeshki et al. The Cell-in-Series Method: A Technique for Accelerated Electrode Degradation in Redox Flow Batteries. In: **Journal of The Electrochemical Society** 163.1 (Nov. 2016), A5202–A5210.
- [76] John S. Newman and Karen E. Thomas-Alyea. **Electrochemical systems**. Ed. by Inc. John Wiley & Sons. Third Edition. 2004, p. 647.
- [77] Allen J Bard and Larry R Faulkner. **Electrochemical methods - Fundamentals and Applications**. Ed. by Inc John Wiley & Sons. 1980.
- [78] Yifeng Li, Maria Skyllas-Kazacos, and Jie Bao. A dynamic plug flow reactor model for a vanadium redox flow battery cell. In: **Journal of Power Sources** 311 (Apr. 2016), pp. 57–67.
- [79] Doug Aaron et al. Polarization curve analysis of all-vanadium redox flow batteries. In: **Journal of Applied Electrochemistry** 41.10 (Oct. 2011), pp. 1175–1182.
- [80] Q. Xu and T. S. Zhao. Fundamental models for flow batteries. In: **Progress in Energy and Combustion Science** 49 (2015), pp. 40–58.
- [81] A A Shah, M. J. Watt-Smith, and F C Walsh. A dynamic performance model for redox-flow batteries involving soluble species. In: **Electrochimica Acta** 53.27 (2008), pp. 8087–8100.
- [82] Adam Z Weber and John Newman. Modeling transport in polymer-electrolyte fuel cells. In: **Chemical reviews** 104.10 (2004), pp. 4679–4726.
- [83] Dongjiang You, Huamin Zhang, and Jian Chen. A simple model for the vanadium redox battery. In: **Electrochimica Acta** 54.27 (Nov. 2009), pp. 6827–6836.
- [84] Yasser Ashraf Gandomi et al. In Situ Potential Distribution Measurement and Validated Model for All-Vanadium Redox Flow Battery. In: **Journal of The Electrochemical Society** 163.1 (2016), A5188–A5201.
- [85] Kyeongmin Oh et al. Three-dimensional, transient, nonisothermal model of all-vanadium redox flow batteries. In: (2014).
- [86] Nicholas Gurieff, Victoria Timchenko, and Chris Menictas. Variable Porous Electrode Compression for Redox Flow Battery Systems. In: **Batteries** 4.4 (Oct. 2018), p. 53.
- [87] Jarrod D. Milshtein et al. High current density, long duration cycling of soluble organic active species for non-aqueous redox flow batteries. In: **Energy Environ. Sci.** 9.11 (2016), pp. 3531–3543.
-

- [88] Robert M Darling and Mike L Perry. Half-Cell, Steady-State Flow-Battery Experiments. In: *ECS Transactions* 53.7 (2013), pp. 31–38.
- [89] C.-N. Sun et al. Resolving Losses at the Negative Electrode in All-Vanadium Redox Flow Batteries Using Electrochemical Impedance Spectroscopy. In: *Journal of the Electrochemical Society* 161.6 (Apr. 2014), A981–A988.
- [90] Jarrod D Milshtein et al. Quantifying Mass Transfer Rates in Redox Flow Batteries. In: *Journal of The Electrochemical Society* 164.11 (2017), pp. 3265–3275.
- [91] Ke Gong et al. All-Soluble All-Iron Aqueous Redox-Flow Battery. In: *ACS Energy Letters* 1 (2016), pp. 89–93.
- [92] Jian Luo et al. Unraveling pH dependent cycling stability of ferricyanide/ferrocyanide in redox flow batteries. In: *Nano Energy* 42. September (2017), pp. 215–221.
- [93] Jarrod D. Milshtein et al. 4-Acetamido-2,2,6,6-Tetramethylpiperidine-1-Oxyl As a Model Organic Redox Active Compound for Nonaqueous Flow Batteries. In: *Journal of Power Sources* 327 (2016), pp. 151–159.
- [94] Mohd Ruslim Mohamed, H. Ahmad, and M. N. Abu Seman. Estimating the state-of-charge of all-vanadium redox flow battery using a divided, opencircuit potentiometric cell. In: *Elektronika ir Elektrotechnika* 19.3 (Mar. 2013), pp. 37–42.
- [95] Alan M. Pezeshki et al. Elucidating effects of cell architecture, electrode material, and solution composition on overpotentials in redox flow batteries. In: *Electrochimica Acta* 229 (2017), pp. 261–270.
- [96] M Zago and A Casalegno. Physically-based impedance modeling of the negative electrode in All-Vanadium Redox Flow Batteries: insight into mass transport issues. In: *Electrochimica Acta* 248 (2017), pp. 505–517.
- [97] Marc-antoni Goulet and Michael J Aziz. Flow Battery Molecular Reactant Stability Determined by Symmetric Cell Cycling Methods. In: *J. Electrochem. Soc.* (2018).
- [98] Sofyane Abbou et al. Time evolution of local potentials during PEM fuel cell operation with dead-ended anode. In: *ECS Transactions* 58.1 (2013), pp. 1631–1642.
- [99] J Dillet et al. Impact of flow rates and electrode specifications on degradations during repeated startups and shutdowns in polymer-electrolyte membrane fuel cells. In: *Journal of Power Sources* 250 (2014), pp. 68–79.
- [100] Wen-Yen Hsieh. Measurement of local current density of all-vanadium redox flow batteries. In: *Journal of Power Sources* 271 (2014), pp. 245–251.
- [101] Jason T. Clement, Douglas S. Aaron, and Matthew M. Mench. In Situ Localized Current Distribution Measurements in All-Vanadium Redox Flow Batteries. en. In: *Journal of The Electrochemical Society* 163.1 (Nov. 2015), A5220–A5228.
- [102] Purna C Ghimire et al. A comprehensive study of electrode compression effects in all vanadium redox flow batteries including locally resolved measurements. In: *Applied Energy* 230 (2018), pp. 974–982.
- [103] Maik Becker et al. Polarization curve measurements combined with potential probe sensing for determining current density distribution in vanadium redox-flow batteries. In: *Journal of Power Sources* 307 (2016), pp. 826–833.

-
- [104] Qing Chen, Michael R Gerhardt, and Michael J Aziz. Dissection of the Voltage Losses of an Acidic Quinone Redox Flow Battery. In: *Journal of The Electrochemical Society* 164.6 (2017), pp. 1126–1132.
- [105] Joachim Langner et al. Determination of Overpotentials in All Vanadium Redox Flow Batteries. In: *ECS Transactions* 58.37 (2014), pp. 1–7.
- [106] Edgar Ventosa et al. Operando studies of all-vanadium flow batteries: Easy-to-make reference electrode based on silver–silver sulfate. In: *Journal of Power Sources* 271 (Dec. 2014), pp. 556–560.
- [107] H. Hewa Dewage, V. Yufit, and N. P. Brandon. Study of Loss Mechanisms Using Half-Cell Measurements in a Regenerative Hydrogen Vanadium Fuel Cell. In: *Journal of The Electrochemical Society* 163.1 (2016), A5236–A5243.
- [108] C.-N. Sun et al. Probing Electrode Losses in All-Vanadium Redox Flow Batteries with Impedance Spectroscopy. In: *ECS Electrochemistry Letters* 2.5 (Feb. 2013), A43–A45.
- [109] B. Le Gorrec. *Thermodynamique et cinétique expérimentale*. Tech. rep. Grenoble INP: Universite Joseph Fourier, 2005.
- [110] X. Wei et al. An Aqueous Redox Flow Battery Based on Neutral Alkali Metal Ferri/ferrocyanide and Polysulfide Electrolytes. In: *Journal of the Electrochemical Society* 163.1 (2015), A5150–A5153.
- [111] Christo S Sevov, Koen H Hendriks, and Melanie S Sanford. Low-potential pyridinium anolyte for aqueous redox flow batteries. In: *Journal of Physical Chemistry C* 121.39 (2017).
- [112] Zhengjin Yang et al. Alkaline Benzoquinone Aqueous Flow Battery for Large-Scale Storage of Electrical Energy. In: *Advanced Energy Materials* 8.8 (2018), pp. 1–9.
- [113] Kaixiang Lin et al. Alkaline quinone flow battery. In: *Science* 349.6255 (2015), pp. 1529–1532.
- [114] David G Kwabi et al. Alkaline Quinone Flow Battery with Long Lifetime at pH 12. In: *Joule* (2018).
- [115] Shu Zhang, Xin Li, and Dandan Chu. An Organic Electroactive Material for Flow Batteries. In: *Electrochimica Acta* 190 (2016), pp. 737–743.
- [116] Stefano Radice et al. Aquivion PerfluoroSulfonic Acid ionomer membranes: A micro-Raman spectroscopic study of ageing. In: *Polymer Degradation and Stability* 98.6 (2013), pp. 1138–1143.
- [117] A. Ghielmi et al. Proton exchange membranes based on the short-side-chain perfluorinated ionomer. In: *Journal of Power Sources* 145.2 (2005), pp. 108–115.
- [118] Ahmet Kusoglu and Adam Z. Weber. New Insights into Perfluorinated Sulfonic-Acid Ionomers. In: *Chemical Reviews* 117.3 (2017), pp. 987–1104.
- [119] Kolja Bromberger, Johannes Kaunert, and Tom Smolinka. A Model for All-Vanadium Redox Flow Batteries: Introducing Electrode-Compression Effects on Voltage Losses and Hydraulics. In: *Energy Technology* 2 (2014), pp. 64–76.
- [120] Tien Chan Chang, Jun Pu Zhang, and Yiin Kuen Fuh. Electrical, mechanical and morphological properties of compressed carbon felt electrodes in vanadium redox flow battery. In: *Journal of Power Sources* 245 (2014), pp. 66–75.
-

- [121] SGL Carbon. *Battery felts and bipolar plates for redox flow batteries*.
- [122] R. Schweiss Woehner, S., O. Oettinger, and C. Hillesheim. *Sigracell cell sets – composite electrodes for flow batteries*. Tech. rep. Germany: SGL Carbon GmbH, pp. 2–5.
- [123] Jochen Friedl and Ulrich Stimming. Determining Electron Transfer Kinetics at Porous Electrodes. In: *Electrochimica Acta* 227 (2017), pp. 235–245.
- [124] Richard L. McCreery. Advanced carbon electrode materials for molecular electrochemistry. In: *Chemical Reviews* 108.7 (2008), pp. 2646–2687.
- [125] Doug Aaron et al. Kinetic enhancement via passive deposition of carbon-based nanomaterials in vanadium redox flow batteries. In: *Journal of Power Sources* 366 (2017), pp. 241–248.
- [126] Julia Mainka. “Local impedance in H₂/air Proton Exchange Membrane Fuel Cells (PEMFC) Theoretical and experimental investigations”. PhD thesis. 2011, p. 248.
- [127] Zhijiang Tang et al. “Proton Exchange Membrane Performance Characterization in VRFB”. In: 2012, pp. 25–34.
- [128] R. Eckl, R. Grinzinger, and W. Lehnert. Current distribution mapping in polymer electrolyte fuel cells — A finite element analysis of measurement uncertainty imposed by lateral currents. In: *Journal of Power Sources* 154.1 (Mar. 2006), pp. 171–179.
- [129] J. T. Clement, T. A. Zawodzinski, and M. M. Mench. Measurement of Localized Current Distribution in a Vanadium Redox Flow Battery. In: *ECS Transactions* 58.37 (Apr. 2014), pp. 9–16.
- [130] Matti Noponen et al. Measurement of current distribution in a free-breathing PEMFC. In: *Journal of Power Sources* 106.1-2 (2002), pp. 304–312.
- [131] Arjun Bhattarai et al. Advanced porous electrodes with flow channels for vanadium redox flow battery. In: *Journal of Power Sources* 341 (Feb. 2017), pp. 83–90.
- [132] Gäel Maranzana et al. A multi-instrumented polymer exchange membrane fuel cell: Observation of the in-plane non-homogeneities. In: *Journal of Power Sources* 180 (2008), pp. 748–754.
- [133] S++. *Current Density Distribution Measurement in large fuel cells and fuel cell stacks*. URL: <http://www.splusplus.com/measurement/en/csclin.html>.
- [134] Jan Hendrik Ohs et al. The Effect of the Reference Electrode Position on the Measurement of Half Cell Polarization in Proton-Exchange Membrane Fuel Cells. In: *Journal of The Electrochemical Society* 159.7 (2012), F181–F186.
- [135] Zhenyu Liu et al. Positioning the reference electrode in proton exchange membrane fuel cells: Calculations of primary and secondary current distribution. In: *Electrochimica Acta* 49.6 (2004), pp. 923–935.
- [136] Wensheng He and Trung Van Nguyen. Edge Effects on Reference Electrode Measurements in PEM Fuel Cells. In: *Journal of The Electrochemical Society* 151 (2004), A185–A195.
- [137] T Gaumont et al. Measurement of protonic resistance of catalyst layers as a tool for degradation monitoring. In: *International Journal of Hydrogen Energy* 42.3 (2017), pp. 1800–1812.

-
- [138] Hubert H. Girault. *Electrochimie physique et analytique*. Presses polytechniques et universitaires romandes, 2008.
- [139] Noémie Elgrishi et al. A Practical Beginner's Guide to Cyclic Voltammetry. In: *Journal of Chemical Education* 95.2 (2018), pp. 197–206.
- [140] L. Wei et al. In-situ investigation of hydrogen evolution behavior in vanadium redox flow batteries. In: *Applied Energy* 190 (2017), pp. 1112–1118.
- [141] Christine Lefrou, Pierre Fabry, and Jean-Claude Poignet. *Electrochimie: Concepts fondamentaux illustrés*. 1. 2007.
- [142] György Inzelt et al. *Handbook of Reference Electrodes*. Springer, 2013.
- [143] Aurora Turcanu and Thomas Bechtold. pH Dependent redox behaviour of Alizarin Red S (1,2-dihydroxy-9,10- anthraquinone-3-sulfonate) - Cyclic voltammetry in presence of dispersed vat dye. In: *Dyes and Pigments* 91.3 (2011), pp. 324–331.
- [144] Els Tourwé et al. Extraction of a quantitative reaction mechanism from linear sweep voltammograms obtained on a rotating disk electrode. Part II: Application to the redoxcouple $\text{Fe}(\text{CN})_6^{3-/4-}$. In: *Journal of Electroanalytical Chemistry* 609 (2007).
- [145] Francisco J Vidal-Iglesias et al. Errors in the use of the Koutecky-Levich plots. In: *Electrochemistry Communications* 15.1 (2012), pp. 42–45.
- [146] Dale A.C. Brownson and Craig E. Banks. *The Handbook of Graphene Electrochemistry*. 2014.
- [147] Richard S. Nicholson. Theory and Application of Cyclic Voltammetry for Measurement of Electrode Reaction Kinetics. In: *Analytical Chemistry* 37.11 (1965), pp. 1351–1355.
- [148] Dan Dragu, Mihai Buda, and Teodor Vişan. Cyclic voltammetry simulation using orthogonal collocation: Comparison with experimental data and measuring the electrochemical rate constant. In: *UPB Scientific Bulletin, Series B: Chemistry and Materials Science* 71.3 (2009), pp. 77–90.
- [149] Christian Rüssel and Walther Jaenicke. Rate constants, activation free enthalpies and activation entropies of the electrochemical reduction of 1,4-diazines in DMF. In: *Electrochimica Acta* 27.12 (1982), pp. 1745–1750.
- [150] Soeren Schumacher et al. Alizarin Red S as an electrochemical indicator for saccharide recognition. In: *Electrochimica Acta* 56.19 (July 2011), pp. 6607–6611.
- [151] Stephen Fletcher. The theory of electron transfer. In: *Journal of Solid State Electrochemistry* 14.5 (2010), pp. 705–739.
- [152] Holger Fink, Jochen Friedl, and Ulrich Stimming. Composition of the Electrode Determines Which Half-Cell's Rate Constant is Higher in a Vanadium Flow Battery. In: *Journal of Physical Chemistry C* 120.29 (2016), pp. 15893–15901.
- [153] C Beriet and D Pletcher. A microelectrode study of the mechanism and kinetics of the ferro/ferricyanide couple in aqueous media: the influence of the electrolyte and its concentration. In: *Journal of Electroanalytical Chemistry* 361 (1993), pp. 93–101.
- [154] X Zhang, Johna Leddy, and Allen J Bard. Dependence of rate constants of heterogeneous electron transfer reactions on viscosity. In: *J. Am. Chem. Soc. Gas Phase Ion Chemistry* 107.3 (1985), pp. 3719–3721.
-

- [155] Investigations of the ferricyanide-ferrocyanide system by pulsed rotation voltammetry. In: *Anal. Chem.* 50. Copyright (C) 2010 American Chemical Society (ACS). All Rights Reserved. (1978), pp. 476–479.
- [156] P. H. Daum and C. G. Enke. Electrochemical Kinetics of the Ferri—Ferrocyanide Couple on Platinum. In: *Analytical Chemistry* 41.4 (1969), pp. 653–656.
- [157] Chongmok Lee and Fred C Anson. Inhibition of the electroreduction of $\text{Fe}(\text{CN})_6^{3-}$ at microelectrodes in the absence of supporting electrolyte Mediation of the inhibited reduction by methyl viologen *. In: *J. Electroanal. Chem. Elsevier Sequoia S.A* 323 (1992), pp. 381–389.
- [158] Marc-Antoni Goulet, Maria Skyllas-Kazacos, and Erik Kjeang. The importance of wetting in carbon paper electrodes for vanadium redox reactions. In: *Carbon* 101 (2016), pp. 390–398.
- [159] W. Du et al. A Surrogate-Based Multi-Scale Model for Mass Transport and Electrochemical Kinetics in Lithium-Ion Battery Electrodes. In: *Journal of the Electrochemical Society* 161.8 (2014), E3086–E3096.
- [160] Xin Li. Modeling and simulation study of a metal free organic-inorganic aqueous flow battery with flow through electrode. In: *Electrochimica Acta* 170 (2015), pp. 98–109.
- [161] Xin You, Qiang Ye, and Ping Cheng. The Dependence of Mass Transfer Coefficient on the Electrolyte Velocity in Carbon Felt Electrodes: Determination and Validation. In: *Journal of The Electrochemical Society* 164.11 (June 2017), E3386–E3394.
- [162] Yongfu Zhao, Shihui Si, and Cui Liao. A single flow zinc//polyaniline suspension rechargeable battery. In: *Journal of Power Sources* 241 (2013), pp. 449–453.
- [163] Glyn William Arnold Foster. “The action of light on potassium ferrocyanide”. In: *Exhibition Scholar, Manchester University*. Vol. 44. 2, pp. 130–139.
- [164] Miriam Shirom and Gabriel Stein. Excited State Chemistry of the Ferrocyanide Ion in Aqueous Solution. II. Photoaquation. In: *The Journal of Chemical Physics* 55.7 (1971), pp. 3379–3382.
- [165] David D. Kuhn and Thomas C. Young. Photolytic degradation of hexacyanoferrate (II) in aqueous media: The determination of the degradation kinetics. In: *Chemosphere* 60.9 (2005), pp. 1222–1230.
- [166] Carlos Antonio Pineda Arellano and Susana Silva Martínez. Effects of pH on the degradation of aqueous ferricyanide by photolysis and photocatalysis under solar radiation. In: *Solar Energy Materials and Solar Cells* 94.2 (2010), pp. 327–332.
- [167] M Reinhard et al. Photooxidation and photoaquation of iron hexacyanide in aqueous solution: A picosecond X-ray absorption study. In: *Structural Dynamics* 1.2 (2014), p. 24901.
- [168] MW Fuller et al. The Photolysis of Aqueous-Solutions of Potassium Hexacyanoferrate(III). In: *Australian Journal of Chemistry* 39.9 (1986), p. 1411.
- [169] J.F. De Wet and R. Rolle. On the Existence and Auto-reduction of Iron(III)-hexacyanoferrate(III). In: *Z. anorg. allg. Chem.* 336.111 (1965), pp. 96–103.
- [170] Fuel Cell Store. *NAFION® Hydrogen-Form Membrane Expansion*. Tech. rep. Technical Information Bulletin 93-01, pp. 1–2.

-
- [171] Bo Jiang et al. Insights into the Impact of Nafion Membrane Pretreatment Process on Vanadium Flow Battery Performance. In: *ACS Applied Materials & Interfaces* v (2016), pp. 1–32.
- [172] Maria-Chiara Ferrari et al. FTIR-ATR Study of Water Distribution in a Short-Side-Chain PFSI Membrane. In: *Macromolecules* 45.4 (2012), pp. 1901–1912.
- [173] F. Xu et al. Chemical Modification of Perfluorosulfonated Membranes with Pyrrole for Fuel Cell Application: Preparation, Characterisation and Methanol Transport. In: *Fuel Cells* 5.3 (2005), pp. 398–405.
- [174] Department of Chemistry and Michigan state university. *The Nature of Vibrational Spectroscopy*.
- [175] M. Zatoń, J. Rozière, and D. J. Jones. Current understanding of chemical degradation mechanisms of perfluorosulfonic acid membranes and their mitigation strategies: a review. In: *Sustainable Energy & Fuels* 1.3 (2017), pp. 409–438.
- [176] Jose L G Fierro, Jose M Campos-martin, and Gema Blanco-brieva. Hydrogen Peroxide Synthesis : An Outlook beyond the Anthraquinone Process Angewandte. In: *Angewandte Chemie - International Edition* 45 (2006), pp. 6962–6984.
- [177] Shouwen Shi, Adam Z Weber, and Ahmet Kusoglu. Structure-transport relationship of perfluorosulfonic-acid membranes in different cationic forms. In: *Electrochimica Acta* 220 (2016), pp. 517–528.
- [178] I. A. Stenina et al. Ion mobility in Nafion-117 membranes. In: *Desalination* 170.1 (2004), pp. 49–57.
- [179] David Aili et al. Porous poly(perfluorosulfonic acid) membranes for alkaline water electrolysis. In: *Journal of Membrane Science* 493 (2015), pp. 589–598.
- [180] R. M. Darling et al. The Influence of Electric Field on Crossover in Redox-Flow Batteries. en. In: *Journal of the Electrochemical Society* 163.1 (July 2015), A5014–A5022.
- [181] Petr Vanysek. “Ionic Conductivity and Diffusion at Infinite Dilution”. In: *CRC Handbook of Chemistry and Physics, 93rd Edition*.
- [182] Simon Malifarge, Bruno Delobel, and Charles Delacourt. Determination of Tortuosity Using Impedance Spectra Analysis of Symmetric Cell. In: *Journal of The Electrochemical Society* 164.11 (2017), E3329–E3334.
- [183] Wei Xie, Robert M Darling, and Mike L Perry. Processing and Pretreatment Effects on Vanadium Transport in Nafion Membranes. In: *Journal of The Electrochemical Society* 163.1 (2015), A5084–A5089.
- [184] Maria Skyllas-Kazacos and Michael Kazacos. State of charge monitoring methods for vanadium redox flow battery control. In: *Journal of Power Sources* 196.20 (2011), pp. 8822–8827.
- [185] Robert Darling et al. Transport Property Requirements for Flow Battery Separators. In: *Journal of The Electrochemical Society* 163.1 (July 2016), A5029–A5040.
- [186] J González-García et al. Characterization of a carbon felt electrode: structural and physical properties Experimental details. In: *Journal of Materials Chemistry* 9 (1998), pp. 419–426.
-

- [187] Thomas J Rabbow and Adam H Whitehead. Deconvolution of electrochemical double layer capacitance between fractions of active and total surface area of graphite felts. In: *Carbon* 111 (2017), pp. 782–788.
- [188] Eiichi Fukushima. Nuclear magnetic resonance as a tool to study flow. In: *Annual Review of Fluid Mechanics* 31.1 (Jan. 1999), pp. 95–123.
- [189] Deisy Lizeth et al. Membrane contactors for process intensification of gas absorption into physical solvents : Impact of dean vortices. In: *Journal of Membrane Science* 530.December 2016 (2017), pp. 20–32.
- [190] Donald W. Marquardt. An Algorithm for Least-Squares Estimation of Nonlinear Parameters. In: *Journal of the Society for Industrial and Applied Mathematics* 11.2 (June 1963), pp. 431–441.
- [191] K Kunimatsu. Study of the ferricyanide/ferrocyanide redox system on Pt by EMIRS Part I. Infrared spectra of the intermediates in the charge transfer. In: *J. Electroanal. Chem.* 262 (1989), pp. 195–209.
- [192] A. F. Holleman, Egon Wiberg, and Nils Wiberg. *Inorganic Chemistry*. Ed. by Academic Press. 2001, p. 1884.
- [193] Gaël Maranzana et al. A proton exchange membrane fuel cell impedance model taking into account convection along the air channel: On the bias between the low frequency limit of the impedance and the slope of the polarization curve. In: *Electrochimica Acta* 83 (2012), pp. 13–27.
- [194] Igor Derr et al. Degradation of all-vanadium redox flow batteries (VRFB) investigated by electrochemical impedance and X-ray photoelectron spectroscopy: Part 2 electrochemical degradation. In: *Journal of Power Sources* 325 (2016), pp. 351–359.
- [195] L Fernández Macía, M Petrova, and A Hubin. ORP-EIS to study the time evolution of the $[\text{Fe}(\text{CN})_6]^{3-}/[\text{Fe}(\text{CN})_6]^{4-}$ reaction due to adsorption at the electrochemical interface. In: *Journal of Electroanalytical Chemistry* 737 (2014), pp. 46–53.
- [196] M Stieble and K Jiittner. Surface blocking in the redox system $\text{Pt}/[\text{Fe}(\text{CN})_6]^{3-}, [\text{Fe}(\text{CN})_6]^{4-}$: An ac impedance study. In: *J. Electroanal. Chem. Elsevier Sequoia S.A* 290 (1990), pp. 163–180.
- [197] Jan Kawiak, Teresa Jedral, and Zbigniew Galus. A reconsideration of the kinetic data for the $\text{Fe}(\text{CN})_6^{3-}/\text{Fe}(\text{CN})_6^{4-}$ system. In: *J. Electroanal. Chem* 145 (1983), pp. 163–171.
- [198] Herman E. Zittel and T. M. Florence. Voltammetric and Spectrophotometric Study of the Zirconium-Alizarin Red S Complex. In: *Analytical Chemistry* 39.3 (Mar. 1967), pp. 320–326.
- [199] Larissa Brentano Capeletti et al. Encapsulated alizarin red species: The role of the sol-gel route on the interaction with silica matrix. In: *Powder Technology* 237 (Mar. 2013), pp. 117–124.
- [200] Bitu Dadpou and Davood Nematollahi. Electrochemical Oxidation of Alizarin Red-S on Glassy Carbon Electrode: Mechanistic Study, Surface Adsorption and Preferential Surface Orientation. In: *Journal of The Electrochemical Society* 163.7 (Apr. 2016), H559–H565.

-
- [201] Silvina Pirillo et al. Horseradish peroxidase and hematin as biocatalysts for alizarin degradation using hydrogen peroxide. In: *Industrial and Engineering Chemistry Research* 49.15 (Aug. 2010), pp. 6745–6752.
- [202] S Tiwari and J Bijwe. Surface Treatment of Carbon Fibers - A Review. In: *Procedia Technology* 14 (2014), pp. 505–512.
- [203] M R Mohamed, P K Leung, and M H Sulaiman. Performance characterization of a vanadium redox flow battery at different operating parameters under a standardized test-bed system. In: *Applied Energy* 137 (2015), pp. 402–412.
- [204] Zhongbao Wei et al. Adaptive estimation of state of charge and capacity with online identified battery model for vanadium redox flow battery. In: *Journal of Power Sources* 332 (Nov. 2016), pp. 389–398.
- [205] Zhongbao Wei et al. Online state of charge and model parameter co-estimation based on a novel multi-timescale estimator for vanadium redox flow battery. In: *Applied Energy* 172 (June 2016), pp. 169–179.
- [206] Bo Yang et al. High-Performance Aqueous Organic Flow Battery with Quinone-Based Redox Couples at Both Electrodes. In: *Journal of The Electrochemical Society* 163.7 (2016), A1442–A1449.
- [207] Thomas J. Carney et al. Concentration-Dependent Dimerization of Anthraquinone Disulfonic Acid and Its Impact on Charge Storage. In: *Chemistry of Materials* 29.11 (2017), pp. 4801–4810.
- [208] S. Rudolph et al. “Unexpected” behaviour of the internal resistance of a vanadium redox flow battery. In: *Journal of Power Sources* 306 (2016), pp. 394–401.
- [209] Chenxi Sun et al. Investigations on transfer of water and vanadium ions across Nafion membrane in an operating vanadium redox flow battery. In: *Journal of Power Sources* 195.3 (2010), pp. 890–897.
- [210] Arjun Bhattarai et al. Novel Approaches for Solving the Capacity Fade Problem during Operation of a Vanadium Redox Flow Battery. In: *Batteries* 4.4 (2018), p. 48.
- [211] Ching Liang Chen, Hak Koon Yeoh, and Mohammed Harun Chakrabarti. An enhancement to Vynnycky’s model for the all-vanadium redox flow battery. In: *Electrochimica Acta* 120 (2014), pp. 167–179.
- [212] Xiangkun Ma et al. An optimal strategy of electrolyte flow rate for vanadium redox flow battery. In: *Journal of Power Sources* 203 (2012), pp. 153–158.
- [213] D. S. Aaron et al. Dramatic performance gains in vanadium redox flow batteries through modified cell architecture. In: *Journal of Power Sources* 206 (2012), pp. 450–453.
- [214] Rajagopalan Badrinarayanan et al. Extended dynamic model for ion diffusion in all-vanadium redox flow battery including the effects of temperature and bulk electrolyte transfer. In: *Journal of Power Sources* 270 (2014), pp. 576–586.
- [215] Yitao Yan et al. Modelling and simulation of thermal behaviour of vanadium redox flow battery. In: *Journal of Power Sources* 322 (2016), pp. 116–128.
- [216] S. König, M R Suriyah, and T Leibfried. Innovative model-based flow rate optimization for vanadium redox flow batteries. In: *Journal of Power Sources* 333 (2016), pp. 134–144.
-

- [217] Dong Kyu Kim et al. Parametric study and flow rate optimization of all-vanadium redox flow batteries. In: *Applied Energy* 228 (2018), pp. 891–901.
- [218] Qiong Zheng et al. Investigation on the performance evaluation method of flow batteries. In: *Journal of Power Sources* 266 (2014), pp. 145–149.
- [219] Sebastian König. “Model-based Design and Optimization of Vanadium Redox Flow Batteries”. PhD thesis. 2017.
- [220] M. Le Bars and M. Grae Worster. Interfacial conditions between a pure fluid and a porous medium: Implications for binary alloy solidification. In: *Journal of Fluid Mechanics* 550 (2006), pp. 149–173.
- [221] Manolis M Tomadakis and Teri J Robertson. Viscous permeability of random fiber structures: Comparison of electrical and diffusional estimates with experimental and analytical results. In: *Journal of Composite Materials* 39.2 (2005), pp. 163–188.
- [222] Kerstin Avila et al. The onset of turbulence in pipe flow. In: 333.6039 (2011), pp. 192–196.
- [223] C R Dennison et al. Enhancing Mass Transport in Redox Flow Batteries by Tailoring Flow Field and Electrode Design. In: *Journal of The Electrochemical Society* 163.1 (2016), A5163–A5169.
- [224] Makoto Inoue; Masaru Kobayashi. *Electrode material for flow-through type electrolytic cell, wherein the electrode comprises carbonaceous material having at least one groove*. 1997.
- [225] Q. Xu, T. S. Zhao, and C. Zhang. Effects of SOC-dependent electrolyte viscosity on performance of vanadium redox flow batteries. In: *Applied Energy* 130 (Oct. 2014), pp. 139–147.
- [226] Christian Blanc and Alfred Rufer. “Understanding the Vanadium Redox Flow Batteries”. In: *intechopen*. Dr Artie N. 2010. Chap. Paths to S.
- [227] N Gurieff et al. Performance enhancing stack geometry concepts for redox flow battery systems with flow through electrodes. In: *Journal of Energy Storage* 22 (2019), pp. 219–227.
- [228] Feng Xing, Huamin Zhang, and Xiangkun Ma. Shunt current loss of the vanadium redox flow battery. In: *Journal of Power Sources* (2011), pp. 10753–10757.
- [229] Q Xu, T.S. Zhao, and P.K. Leung. Numerical investigations of flow field designs for vanadium redox flow batteries. In: *Applied Energy* 105 (2013), pp. 47–56.
- [230] URL: <https://www.perdix.com.au/>.
- [231] Charles W Hull. “Apparatus for production of three-dmensonal objects by stereolithography”. March 1986. 1986.
- [232] Ao Tang, Jie Bao, and Maria Skyllas-Kazacos. Studies on pressure losses and flow rate optimization in vanadium redox flow battery. In: *Journal of Power Sources* 248 (2014), pp. 154–162.
- [233] C Y Ling et al. Pulsating electrolyte flow in a full vanadium redox battery. In: *Journal of Power Sources* 294 (2015), pp. 305–311.

Development of Analytical Techniques for the Investigation of an Organic Redox Flow Battery using a Segmented Cell

Redox Flow Batteries (RFBs) are a promising solution for large-scale and low-cost energy storage necessary to foster the use of intermittent renewable sources. This work investigates a novel RFB chemistry under development at the company Kemiwatt. Based on abundant organic/organo-metallic compounds, this new technology promises the deployment of sustainable and long-lived systems. The study undertakes the building of a thorough knowledge base of the system by developing innovative reliable analytical tools. The investigation started from the evaluation of the main factors influencing the battery performance, which could be conducted ex-situ on each material composing the cell. The two electrolytes were then examined independently under representative operating conditions, by building a symmetric flow cell. Cycling coupled with EIS measurements were performed in this set-up and then analyzed with a porous electrode model. This combined modeling-experimental approach revealed unlike limiting processes in each electrolyte along with precautions to take in the subsequent steps (such as membrane pretreatment and electrolyte protection from light). A segmented cell was built and validated to extend the study to the full cell system. It provided a mapping of the internal currents, which showed high irregularity during cycling. A thorough parameter study could be conducted with the segmented platform, by varying successively the current density, the flow rate, and the temperature. The outcome of this set of experiments would be the construction of an operational map that guides the flow rate adjustment, depending on the power load and the state of charge of the battery. This strategy of flow rate optimization showed promising outcomes at the lab-cell level. It can be easily adapted to real-size systems. Ultimately, an overview of the hydrodynamic behavior at the industrial-cell level was completed by developing a hydraulic modeling and a clear cell as an efficient diagnostic tool.

Keywords: Redox flow battery, Organic compound, Battery cycling, Impedance model, Symmetric cell, Segmented cell

Développement d'outils d'analyse et d'une cellule segmentée pour l'étude d'une batterie redox organique à électrolyte circulant

Les batteries à électrolyte circulant ou redox flow batteries (RFB) représentent une technologie prometteuse pour répondre aux besoins grandissants de stockage d'énergie. Elles seraient particulièrement adaptées aux réseaux électriques qui comptent une part grandissante d'énergie d'origine renouvelable, produite en intermittence. L'objet de ce travail est l'étude d'un nouveau type de RFB, actuellement développé par l'entreprise Kemiwatt. Il repose sur l'utilisation de molécules organiques, qui sont abondantes et recyclables. Le but de cette étude est d'améliorer la compréhension fondamentale de la batterie grâce à l'utilisation d'outils d'analyse précis et innovants. Chaque composant du système a d'abord été analysé via des moyens expérimentaux ex-situ. Les deux électrolytes composant la batterie ont ensuite été étudiés séparément en conditions réelles de circulation dans une cellule symétrique. Couplées à un modèle d'électrode volumique, les données ont été analysées pour identifier les facteurs limitants de chaque solution. La batterie entière a ensuite été étudiée dans un dispositif segmenté, permettant l'accès à la distribution interne du courant. Une étude paramétrique, réalisée avec la cellule segmentée a permis d'observer les effets du courant, du débit et de la température sur le fonctionnement de la cellule, puis d'établir une cartographie des conditions de fonctionnement idéales, suivant la puissance et l'état de charge de la batterie. L'aspect hydrodynamique du système a finalement été abordé en développant un modèle fluide ainsi qu'une maquette expérimentale de cellule transparente pour visualiser l'écoulement.

Mots-clés: Batterie à électrolyte circulant, Composé organique, Cyclage de batterie, Modèle d'impédance, Cellule symétrique, Cellule segmentée